UNIVERSITÀ DEGLI STUDI DI NAPOLI FEDERICO II

Scuola Politecnica e delle Scienze di Base

Ph.D. Course in Chemical Sciences

XXXI Cycle

Adsorption of H_2S and HCHO on new generation materials based on composite Zn-Cu sorbents and surface active carbon materials: effect of physico-chemical properties on the process performance

Giacomo de Falco

Tutors: *Prof. Fabio Montagnaro*

Dr. Stefano Cimino

Dr. Luciana Lisi

Supervisor: *Prof. Vincenzo Busico*

Ph.D. Course Coordinator: *Prof. Luigi Paduano*

2015–2018

Acknowledgements

I would like to express my personal, heartfelt gratitude to a number of people. Firstly, I wish to thank my supervisor, Prof. Fabio Montagnaro, for his support and guidance over the last three years. He provided a direction when I couldn't see one and his charism has inspired the way I will continue to approach research in chemistry.

I would also like to thank Dr. Cimino and Dr. Lisi for their assistance during the time spent in their lab.

I am very grateful to Dr. Marco Balsamo and Dr. Alessandro Erto for their generous advice concerning this body of work along with their daily supervision and constant moral support.

During my PhD I spent time in New York (USA), working in the lab of Prof. Teresa Bandosz. I warmly thank her and all the members of her group for their extraordinary kindness and generous contributions of knowledge, not to mention the informal and pleasant moments we shared.

Finally, I would like to thank my family and my closest friends, no personal achievement would have any value without the possibility to share it with them.

Table of Contents

A mia Madre,

a mia Sorella,

a mio Padre,

Grazie per il vostro continuo Sostegno.

Introduction

Nowadays, air pollution is one of the most challenging issues worldwide for the potential damage of our environment and health risk to humans. Pollutants are produced by some different sources in order to supply the increase of global energy demand due to the rapid development of the economy and booming population growth. Air pollution can be classified in two different types: indoor and outdoor pollution.

Outdoor air pollutants mainly consist in the emission of CO_x, NO_x, SO_x, H_2S and particulate matter (PM). These pollutants are manly produced by anthropogenic sources because our society still heavily relies on fossil fuels for various applications such as electricity generation, transportation, industrial and domestic heating. In particular, in the fossil fuels and in biogas it is possible to find H_2S that contributes to increase the formation of SO_x connected with the acid rains (O'Neill, 1993). Moreover, outdoor air pollutants have become a public concerned problem in modern metropolises. A good urban design can tackle the accumulation of air pollutants allowing their dispersion (Santamouris, 2001).

On the other hand, the issues of indoor air pollution are stimulating the interest of many scientists because people usually spend most of their time in indoors (Jenkins et al., 1992; Brasche and Bischof, 2005). According to the World Health Organization (WHO), around 3 billion people in the world still cook and heat their home using dirty solid fuels (such as waste wood, char-coal, coal, dung, crop wastes) on open fire places, which generate large amount of air pollutants (such as SO_2, O_x, CO, and PM). The main indoor pollutants are volatile organic compounds (VOC) such as formaldehyde and terpenes. We can suppose that indoor air quality is better than outdoor air quality due to the possible installation of ventilation and air cleaning devices but, for example, the pollutants may accumulate in the indoor environment if the indoor air is not well ventilated, which seriously affects the health of the inhabitants. However, for combined indoor and outdoor air quality studies in literature, many found indoor air pollutant concentration higher than outdoor (Chen and Chao, 2011). As an example, Fung at al. (2014) found some traces of diesel exhaust being it extracted into a

mechanically ventilated building from unloading trucks, which is a quite common phenomenon for those fresh air intakes designed at low level. Consequently, in order to solve both categories of air pollutions (indoor and outdoor), some solutions must be developed. It is important to underline that a way to reduce outdoor pollution can be of removing the pollutants before using fossil fuels (e.g. removing H_2S). Instead, this type of solution cannot be developed for indoor pollution.

Adsorption can be considered a very favourable technique for removing both indoor and outdoor pollutants with respect to other technologies (e.g. absorption, membrane separation and scrubbing) in view of its comparatively low cost, wide range of applications, simplicity of design, easy operation, low harmful secondary products and facile regeneration of the adsorbents (Sjostorm et al., 2011; Samanta et al., 2012). Many sorbents can be used to remove the pollutants from air such as zeolites, mesoporous materials and activated carbons (AC). In air pollution control, activated carbon is the most widely used adsorbent because it offers the advantages to have high surface area and volume of pores, and a variety of chemical properties on its surface. In addition, there are a lot of simple techniques for introducing surface modifications on AC in order to increase the adsorption capacity of target pollutant.

This PhD Thesis in Chemical Sciences aims at a deep understanding of the intertwining among materials properties, experimental conditions and adsorption outcomes, with the focus on an experimental research activity dealing with the removal of two target pollutants that contribute to increase 1) outdoor pollution (hydrogen sulphide) and 2) indoor pollution (formaldehyde), by adsorption on materials of various nature.

Experimental tests have been performed in lab scale plants under realistic operating conditions in terms of, e.g., temperature, pressure and typical flue gas composition. Regeneration studies have been conducted on the samples. The intertwining among raw solids properties and properties of the functionalised samples has been investigated by comparing adsorption results with outcomes obtained from porosimetric, thermogravimetric and spectroscopic analyses. In

particular, the first chapter of this Thesis is centered around the main theoretical aspects concerning both thermodynamics and kinetics of the adsorption phenomenon, and a literature survey to deeply study the state of the art onto adsorption of H_2S and HCHO. Chapter 2 describes the experimental protocols adopted for the functionalisation of the samples, solids characterisation and adsorption experiments; furthermore, a description of the lab scale plants, built and optimised for the execution of adsorption experiments, is also provided. Chapters 3 and 4 report the main results obtained from adsorbents characterisation and adsorption tests on H_2S and HCHO. The part concerning H_2S adsorption was carried out in the framework of a funded cooperation with the Institute for Research on Combustion of the Italian National Research Council in Naples (IRC-CNR; supervisors Dr. Stefano Cimino and Dr. Luciana Lisi). The part concerning HCHO adsorption was carried out during an internship spent at City College of New York, supervisor Prof. Teresa Bandosz (the internship was co-funded by the PhD Course in Chemical Sciences, University of Naples Federico II, and by the Short Term Mobility Program of IRC-CNR, CUP B53C17001430005). Conclusions and future developments are reported in Chapter 5. The Appendix embodies the scientific articles published on Journals by the candidate in relationship with this PhD Thesis, here listed:

1) M. Balsamo, S. Cimino, G. de Falco, A. Erto, L. Lisi. ZnO-CuO supported on activated carbon for H_2S removal at room temperature. **Chemical Engineering Journal** 2016, 304, 399–407.
2) S. Cimino, L. Lisi, G. de Falco, F. Montagnaro, M. Balsamo, A. Erto. Highlighting the effect of the support during H_2S adsorption at low temperature over composite Zn-Cu sorbents. **Fuel** 2018, 221, 374–379.
3) G. de Falco, M. Barczak, F. Montagnaro, T.J. Bandosz. A new generation of surface active carbon textiles as reactive adsorbents of indoor formaldehyde. **ACS Applied Materials & Interfaces** 2018, 10, 8066–8076.

4) G. de Falco, F. Montagnaro, M. Balsamo, A. Erto, F.A. Deorsola, L. Lisi, S. Cimino. Synergic effect of Zn and Cu oxides dispersed on activated carbon during reactive adsorption of H_2S at room temperature. **Microporous and Mesoporous Materials** 2018, 257, 135–146.
5) G. de Falco, W. Li, S. Cimino, T.J. Bandosz. Role of sulfur and nitrogen surface groups in adsorption of formaldehyde on nanoporous carbons. **Carbon** 2018, 138, 283–291.

Chapter 1 –

Overview/state of the art on the aspects of interest for this PhD Thesis in Chemical Sciences

In this chapter it will be discussed: the main theoretical aspects concerning both thermodynamics and kinetics and the typical samples used for the adsorption phenomenon and the state of art on the adsorption of H_2S and HCHO, with an emphasis on the applications of activated carbons as they are of major interest for this PhD project.

1.1 Adsorption process

The phenomenon by which molecules (adsorbate) of gas (Balsamo et al., 2013; Erto et al., 2015; Montagnaro et al., 2015; Balsamo et al., 2018) or liquid (Montagnaro and Santoro, 2009; Balsamo et al., 2010; Balsamo et al., 2011) phase adhere to a solid surface (adsorbent) is called adsorption (Ruthven, 1984; Do, 1998). There are two types of adsorption: physisorption and chemisorption, according to the nature of the interaction between adsorbate and adsorbent. The physical adsorption occurs when adsorbate molecule is attached to the adsorbent surface by weak forces without being chemically modified (van der Waals, London or dispersion forces). The latter have a very low binding energy (heat of adsorption equal to or less than 40 kJ mol^{-1}). As the involved forces are not strong, the adsorption process may be easily reversed. On the other hand, chemisorption involves the formation of chemical bonds (heat of adsorption higher than 40 kJ mol^{-1}) that can be either ionic or covalent with the adsorbate being chemically modified.

Most of adsorption processes are carried out in fixed bed column in which the concentration in the fluid and solid phase changes with time, as well as with the position in the bed (McCabe et al., 2005). The characterisation of the adsorption process can be done either from a thermodynamic point of view, in order to have information about adsorption capacity and its dependence on the main process parameters, or by a kinetic standpoint, focusing on fluid-dynamic characterisation, mass transport from fluid to solid phase and, more in general, on the rate of the overall process.

1.1.1 Adsorption theory

Adsorption is a spontaneous process ($\Delta G<0$) and is characterised by a decrease in the entropy as a substance in fluid phase is adsorbed and incorporated into the surface of a solid compound ($\Delta S<0$). Note that, at constant temperature and pressure, $\Delta G=\Delta H-T\Delta S$: it is easy to deduce that adsorption is an exothermic process. These observations are generally valid when physical adsorption is considered. This entails that physical adsorption is thermodynamically favoured at low temperatures. The thermodynamic study of adsorption processes is carried out through the adsorption isotherm, experimental curves obtained by the relationship between the concentration of the adsorbate in the fluid phase and the concentration of the adsorbate in the adsorbent particles at a given temperature and under equilibrium conditions (McCabe et al., 2005). In Fig. 1.1a the typical shapes of adsorption isotherms are shown: isotherms can be classified on the basis of their shapes (another way to categorise the adsorption isotherms is that following the IUPAC classification, see Fig. 1.1b). It is possible to observe that favourable isotherms are convex upward because we obtain in this case a high loading of particles captured by the adsorbent at low concentration in the fluid phase. Instead, unfavourable isotherms are concave upward, which means that relatively low solid loadings are obtained at high concentration in the fluid. The irreversible isotherm is characterised by a constant amount of pollutant captured on the sorbent, also increasing the concentration in the fluid phase. In the linear isotherm case, the amount adsorbed is proportional to the concentration in the fluid.

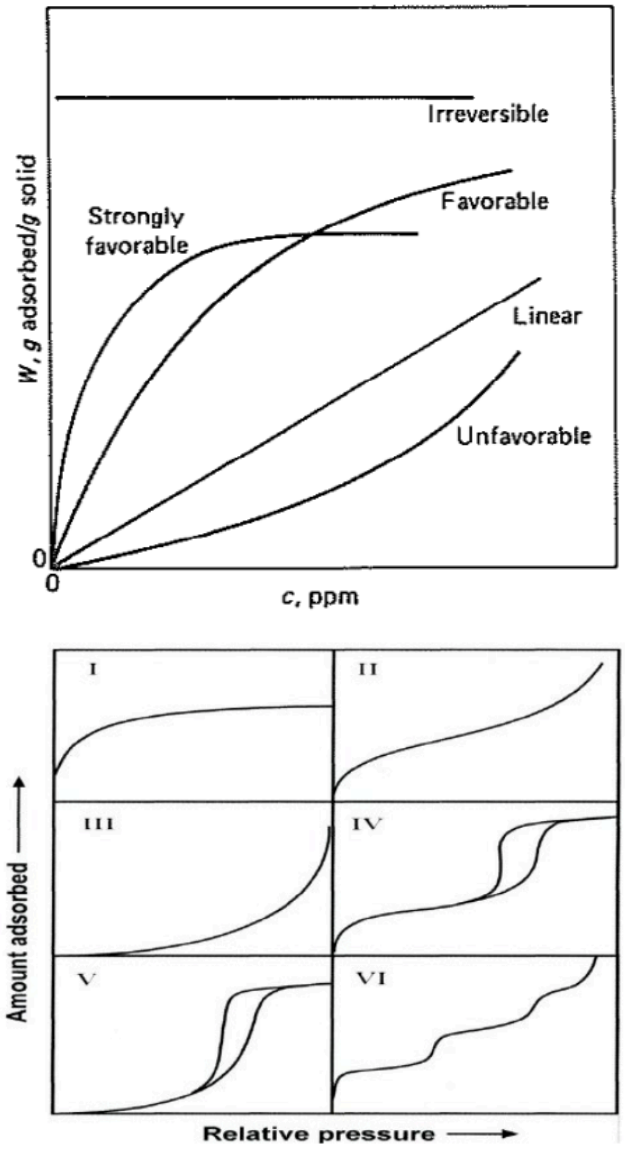

Fig. 1.1. a-up) Adsorption isotherms (McCabe et al., 2005). b-down) Classification of adsorption isotherms following IUPAC.

Many mathematical models have been developed based on the interpretation of adsorption isotherms to describe the mechanism involved during the process. The first successful model describing adsorption process is Langmuir model based on the following assumptions: i) the solid surface is composed of a two-dimensional array of energetically homogeneous sites; ii) only a monolayer

can occur and only one molecule can adsorb on a site; iii) the adsorption is localised and there is no adsorbate-adsorbate interaction; iv) all sites are energetically equivalent.

The general form of the Langmuir isotherm can be expressed as:

$$\omega_{eq} = \frac{\omega_{max} K_L P_{eq}}{1 + K_L P_{eq}} \quad (1.1)$$

where ω_{eq} [mmol g^{-1}] and P_{eq} [bar] are the adsorbent specific molar adsorption capacity and the equilibrium gas partial pressure of the adsorbate, respectively; K_L [bar^{-1}] and ω_{max} [mmol g^{-1}] represent the Langmuir equilibrium constant and the maximum adsorption capacity of the adsorbed species, respectively. The hypothesis of monolayer adsorption is one of the most restrictive assumptions of Langmuir's theory. In fact, adsorption frequently takes place in multilayer (i.e. molecules arrange themselves on the solid surface in more than one layer). However, although with somewhat restrictive assumptions, this model allows for an accurate description of the phenomenon when the adsorbed quantity is low and in the case of no interaction with the solvent.

At low adsorbate partial pressure, the adsorption process can be described by a linear relationship expressed as:

$$\omega_{eq} = K_H P_{eq} \quad (1.2)$$

where K_H [mmol g^{-1} bar^{-1}] is the Henry equilibrium constant. Another most widely used model is the Freundlich isotherm. Compared with the Langmuir isotherm, the Freundlich isotherm does not have much limitation, it can deal with physical and chemical adsorption and the surface heterogeneity. Especially, this model frequently succeeds in depicting the adsorption behavior of organic compounds and reactive matter. The Freundlich isotherm is expressed as:

$$\omega_{eq} = K_F P_{eq}^{\frac{1}{n}} \quad (1.3)$$

K_F [mmol g^{-1} $bar^{-1/n}$] and $1/n$ [–] are the Freundlich constant and the heterogeneity parameter, respectively (both generally temperature-dependent) (Do, 1998) to be determined.

Brunauer, Emmett and Teller (1938) studied a new descriptive model in order to improve the Langmuir theory taking into account a multilayer adsorption of gases on a porous and non-porous solid. In addition to the assumptions proposed by Langmuir, it also assumes that the energy of adsorption of the second and subsequent layers of molecules is equal to that of liquification, and the total amount adsorbed is the amount on all layers. The BET equation is usually expressed in a linear form:

$$\frac{P}{n(P_0-P)} = \frac{1}{n_m c} + \frac{P(c-1)}{n_m c P_o} \tag{1.4}$$

in which P_0 is the saturation vapor pressure, n is the molar amount adsorbed at pressure P, n_m is the molar amount of adsorbate required for complete monolayer coverage and c is a dimensionless constant which relates to adsorption energy and expressed in an exponential form. The plot of $\frac{P}{n(P_0-P)}$ versus $\frac{P}{P_0}$ gives a straight line with intercept of $\frac{1}{n_m c}$ and slope of $\frac{c-1}{n_m c}$.

The BET equation is one of the most used model for the interpretation of isotherms obtained from the adsorption of nitrogen at –186°C in order to determine the surface area, but in particular it is not useful for highly microporous carbons. Dubinin and Radushkevich gave us a model for the estimation of micropore volume from the low and medium part of an adsorption isotherm:

$$\frac{V}{V_0} = \exp\left[\left(\frac{A}{E}\right)^2\right] \tag{1.5}$$

where V is the volume of adsorbate in the micropores per unit mass of the solid, V_0 is the maximum specific volume that the adsorbate can occupy (obtainable

from porosimetric analyses), E is a characteristic energy (related to the adsorption strength between adsorbate and adsorbent, and specific per unit mole) and A is obtained by:

$$A = RT\ln\left(\frac{P}{P_0}\right) \tag{1.6}$$

A was originally termed, by Polanyi, the adsorption potential, but Dubinin preferred the designation "differential molar work of adsorption". Once V and V_0 are known, the solid molar adsorption capacity ω and the saturation uptake ω_{max} can be calculated assuming a liquid-like adsorbed phase according to the Gurvitsch rule (Do, 1998).

In conclusion, it is possible to obtain the isosteric heat of adsorption (q_{st}), a parameter for the degree of energetic heterogeneity of gas–solid interactions, through the determination of the adsorption isotherms at various temperatures. It can be retrieved using the Clausius–Clapeyron equation (Do, 1998).

1.1.2 Adsorption: kinetics

Adsorption processes are characterised by complex kinetic phenomena that can be divided in several elementary steps:

1) fluid phase mass transfer including convective mass transfer and molecular diffusion;

2) interface diffusion between fluid phase and the exterior surface of the adsorbent (i.e., film diffusion);

3) intra-pellet mass transfer involving pore diffusion and surface diffusion;

4) the adsorption-desorption reaction (Crittenden and Weber, 1978; Crittenden et al., 1986).

In particular, there are three main resistances that can delay the whole kinetic process, and the slowest of them represents the limiting step and therefore determines the overall rate of adsorption:

1) external transport: transport through the layer (film) more directly in contact with the solid particle;

2) internal diffusion: transport within the adsorbent pores until the solute reaches the active site;

3) adsorption: formation of the bond between the adsorbent solid and the adsorbate.

The kinetic study of adsorption phenomena and the influence of the characteristic parameters of the process is commonly performed using a process configuration in pilot scale, e.g., a fixed bed column and through the realisation of experimental breakthrough curves as reported in Fig. 1.2.

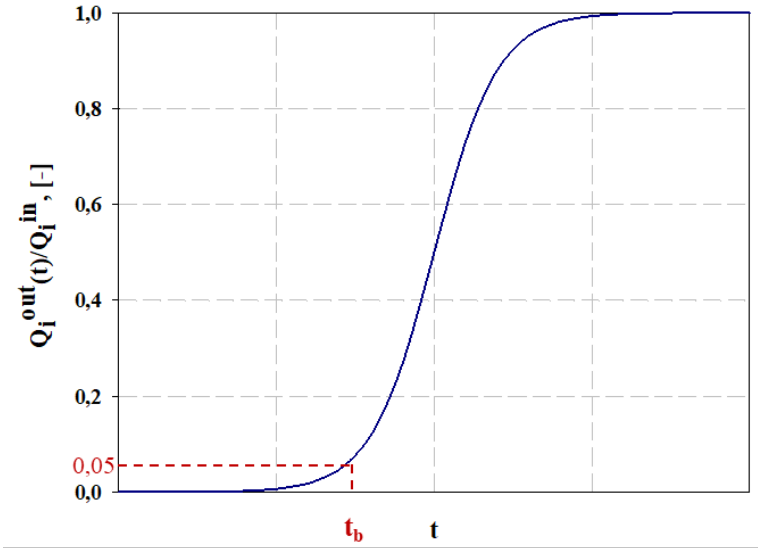

Fig. 1.2. Breakthrough curve in a fixed bed reactor.

A breakthrough curve has a sigmoidal shape and it represents an experimental relationship between the concentration of the pollutant in the gas flow exiting the column, and time. In particular, at the beginning the pollutant is completely adsorbed, then its concentration at the outlet increases up to the inlet level when the solid is completely saturated. The value of time at which the concentration of the pollutant in the outlet gas is, say, 5% of the value at the inlet, is called *breakpoint* time (t_b in Fig. 1.2). It is a clue of the beginning of saturation for the solid adsorbent and, in the industrial practice, it usually represents a

limiting working condition corresponding to regulation emission limit (McCabe et al., 2005).

It can be demonstrated that the area above the breakthrough curve is proportional to the total amount of pollutant captured by the adsorbent; as a matter of fact, in order to evaluate the solid adsorption capacity, a mass balance on *i* (pollutant) species over the adsorption column is required as reported in Eq. (1.7):

$$\frac{Q_i^{in}\rho_i \mathrm{d}t - Q_i^{out}(t)\rho_i \mathrm{d}t}{M_i} = m\mathrm{d}\omega \tag{1.7}$$

where Q_i [L s^{-1}] is the volumetric flow rate of the *i* species, ρ_i [mg L^{-1}] is the pollutant density at the operative temperature and pressure, M_i its molecular weight, m [g] is the adsorbent mass and dω [mmol g^{-1}] the differential solid adsorption capacity. By rearranging Eq. (1.7) and integrating between zero and time t^* for which the out/in ratio of the volumetric flow rate of the *i* species is practically unitary (complete solid saturation), it is possible to evaluate the solid total adsorption capacity ω_{eq}, as reported in Eq. (1.8):

$$\omega_{eq} = \frac{Q_i^{in}\rho_i}{mM_i}\int_0^{t^*}\left(1 - \frac{Q_i^{out}(t)}{Q_i^{in}}\right)\mathrm{d}t \tag{1.8}$$

1.1.3 Common adsorbents

The realisation of an efficient adsorption system starts from the choice of an appropriate solid adsorbent, whose properties should be tuned on the particular compound(s) to be removed. It is important to highlight that sorbents can be also functionalised with active phases. If the latter have a high affinity towards the chemical to remove, the adsorption capacity of the whole system can grow considerably.

The main solid substrates used for adsorption processes are presented in the following.

Alumina

Aluminum oxide (Al_2O_3) is one of the most important ceramic materials widely used as electrical insulator, with exceptional high resistance to chemical agents, excellent performance as catalyst or as catalytic support for several dispersed active phases. It is widely used for structural, microelectronic, membrane applications and water and wastewater treatment (Rahmani et al., 2010). The most common form of crystalline Al_2O_3 is known as *corundum* or α-alumina. Alumina also exists in other phases, including the cubic γ and η phases, the monoclinic θ phase, the hexagonal χ phase, the orthorhombic κ phase and the δ phase, that can be tetragonal or orthorhombic (Levin and Brandon, 1998; Paglia, 2004). In particular, γ-Al_2O_3 has important technical applications, such as good porosity and average surface area (0.45 cm^3/g and 238.9 m^2/g, respectively, according to Fuhrman et al., 2007) which make γ-Al_2O_3 appealing as a solid support. Alumina cannot compete in terms of capacity or selectivity with other sorbents such as molecular sieves, although its superior mechanical strength is important in moving-bed applications (Coulson and Richardson, 2005).

Zeolites

Zeolites are microporous, alumino-silicate minerals that have been considered for separation and purification of gases thanks to their characteristic ability for polar compounds adsorption. Zeolites are built of a periodic array of SiO_4 and AlO_4 tetrahedra-based groups (Ruthven, 1984). Zeolites used to capture molecules are known as molecular sieves (Ozekmekci et al., 2015). Molecular sieves are highly porous and have lattice structures composed of tetrahedral of silica and alumina arranged in various ways. The capturing effect is given by the formation of a cage-like structure with windows which admit only molecules smaller than a certain size (Coulson and Richardson, 2005). By using various source materials and proper conditions of manufacture, it is possible to produce a range of molecular sieves with access dimensions of 0.3 nm^{-1}. Zeolites are effective for the removal of specific compounds such as water and H_2S. Natural

zeolites usually require previous activation and packaging steps which not always makes their use economical.

Mesoporous silica

Ordered mesoporous silicas (e.g., MCM-41, SBA-15, TUD-1, HMM-33 and FSM-16) are a class of silica materials characterised by various cage structures (such as hexagonal, cubic and lamellar). Their narrow and uniform pore size, coupled with their high surface area, make them suitable for the development of novel solid catalysts (Pourzolfaghar and Ismail, 2013). For instance, mesostructured SBA-15 silica is a high-surface area (up to 1000 m^2/g) material, with 6–7 nm-wide regular channels and thick (3–4 nm) pore walls. Especially due to its thick walls, SBA-15 provides thermal stability and this, together with its high surface area, makes it an ideal support for active phases (Sun et al., 2006).

Activated carbons

Activated carbons are carbonaceous materials with a common structure made up of an assembly of defective graphene layers that have high capture potentiality, thanks to a complex structure. The latter is characterised by micropores that determine high surface area for adsorption, but also meso and macropores which can facilitate the diffusion of the adsorbate to the inner porosity (Marsh and Rodríguez-Reinoso, 2006; Whaby et al., 2010; Sayari et al., 2011). Activated carbons are prepared in two steps: carbonisation and activation.

- *carbonisation*- In this first step, naturally occurring carbonaceous materials such as coal, wood, coconut shells or bones are decomposed in an inert atmosphere at a temperature of about 800 K;

- *activation*- The products of carbonisation are not porous enough, hence it is needed an additional treatment or activation to generate a system of fine pores. The carbon may be produced in the activated state by treating the raw material with chemicals, such as zinc chloride or phosphoric acid, before carbonising (i.e. chemical activation). The chemicals involved in chemical activation promote the formation of micropores (i.e. pores with diameters smaller than 2 nm) and

chemical activation generates carbons with a good porosity (Choi et al., 2008). Alternatively, the carbon from the carbonisation stage may be activated at temperatures higher than 1000 K in atmospheres of various gases, such as steam or carbon dioxide (i.e. physical activation, Balsamo et al., 2012, 2013).

Activated carbon has a typical surface area of 500-2000 m^2/g, mostly associated with a set of pores of variable dimensions, commonly classified as micropores (i.e. pores with diameters smaller than 2 nm), mesopores (i.e. pores with diameters between 2 and 50 nm) and macropores (i.e. pores with diameters larger than 50 nm).

Metal oxides

An oxide is a chemical compound that contains at least one oxygen atom and one other element in its chemical formula. Metal oxides typically contain an anion of oxygen in the oxidation state of −2. In the present context, an ideal metal oxide sorbent should have the following characteristics:

- potential of regenerating the metal complex formed upon adsorption into the parent metal oxide;
- extremely reactive toward the compound to be removed;
- appropriate morphology and porosity of the pellet to increase the diffusion capability and reactivity;
- minimised undesired reactions in adsorption and regeneration conditions.

Much of the research concerns metal based materials as sorbent, that are presumed to remove e.g. H_2S at low temperatures according to the general reaction: $H_2S+MeO \rightarrow MeS+H_2O$, where MeO is the parent metal oxide sorbent and MeS is the metal sulphide after the reaction.

1.2 H_2S adsorption

1.2.1 General information

Hydrogen sulphide (H_2S) is a colourless gas with a characteristic odor of rotten eggs. In Table 1.1, some physical and chemical properties are listed.

Table 1.1. Some physical and chemical properties of H_2S.

Molecular weight	34.08
Vapor pressure	1740 kPa (at 21°C)
Density	1.5392 g/L at 0°C, 1 atm
Boiling point	–60°C
Melting point	–82°C
Dipole moment	0.97 D
Dissociation constants	pK_{a1}=7.04; pK_{a2}=11.96
Threshold limit value (TLV)	1 ppm
Immediate danger limit	100 ppm

H_2S is extremely toxic, corrosive and flammable in nature. It causes irritation to nose, throat and eyes at a concentration less than 5 ppm, and at 1000 ppm it causes instant death (United States Department of Labor, 2018). H_2S is perceived by humans at concentrations as small as 0.5–2 ppbv (Gabriel and Deshusses, 2003). H_2S occurs naturally, at various concentration, in different hydrocarbon sources such as crude petroleum, natural gas, liquefied petroleum gas (LPG), off-gases of industrial catalytic hydrodesulphurisation (HDS) upgrading heavy petroleum (bitumen) and biogas. In Table 1.2 it is listed the concentration range of H_2S in various gaseous streams (Samokhvalov and Tatarchuk, 2011). It is also formed by the hydrolysis reaction of metal sulphides present in volcanic rocks. Landfills, rotten vegetation, and composting sites can also contribute to H_2S generation due to anaerobic respiration of sulphate-

reducing bacteria: these organisms breathe sulphate to derive energy and release sulphide as waste.

Table 1.2. Concentration of H_2S in some gaseous streams (Samokhvalov and Tatarchuk, 2011).

Stream	H_2S content, ppmv
Natural gas (sour)	50 ppmv–100 vol%
Natural gas (pipeline quality)	4–16
Raw syngas of IGCC	1700–14 000
Biomass-derived raw syngas	20–600
Desulfurized syngas from IGCC-GCS plant	*ca.* 10
Syngas for industrial synthesis	*ca.* 0.06
Reformate from JP-5 jet fuel	*ca.* 300
Reformate from liquid propane gas (LPG)	*ca.* 0.5
Gas from anaerobic biodigester of organics	50–5000

The international environmental regulations for gas emission by industries have become more and more stringent with respect to the release of gas containing sulphur. Hydrogen sulphide is known to be a major source of acid rain when oxidised in the atmosphere to SO_2. The acceptable H_2S levels can be quite different depending on the end use; for example, 5−15 ppm H_2S is acceptable in natural gas depending on the Country of use, but <1 ppm H_2S is required for fuel cell applications.

1.2.2 State of the art

The first adsorbents used for removing H_2S from syngas, coal gas, etc. at high temperature (T>100°C) were bulk metal oxides. Westmoreland and Harrison (1976) studied, at high temperature (400−1200°C), the desulphurisation potential of oxides of 28 elements with computational free energy minimisations using temperature-dependent free energies from the literature. Fe, Zn, Mo, Mn, V, Ca, Sr, Ba, Co, Cu, and W, showed thermodynamic feasibility (at least 95% desulphurisation and solid stability) for high-temperature desulphurisation. Elseviers and Verelst (1999) observed, with a computational work, that Zn, Mo,

Mn, W, Sn, Co, Cu, Ni, and Fe oxide should be successful in reducing the residual H_2S content to 0.03, 0.6, 2.5, 3.4, 19, 24, 39, 41, and 91 ppm, respectively, with a feed gas containing 12.5% CO_2, 42.5% CO, 32.175% H_2, 12.5% H_2O, and 3250 ppm H_2S at 400°C.

Among these bulk metals oxides, CuO and ZnO are the most studied (Novochinskii et al., 2004; Dhage et al., 2010; Yang and Tatarchuk, 2010). According to Yang et Tatarchuk (2010), the main advantage of the Cu-based sorbents is the highly favoured sulphidisation thermodynamics for copper in the oxidation states of +2 and +1. However, copper compounds (oxides and sulphides) have relatively low melting points and are prone to thermally induced sintering that rapidly lowers the efficiency of the sorbent. Furthermore, CuO sorbents suffer from other limitations such as oxide reduction, loss in surface area and porosity (Erzos et al., 2006; Dhage et al., 2010; Yang and Tatarchuk, 2010). For these reasons, CuO is more likely dispersed onto a suitable support.

Baird et al. (1992) observed stoichiometric adsorption of H_2S on ZnO at 350°C, but it falls off rapidly as the temperature is reduced. Additionally, Novochinskii et al. (2004) and Dhage et al. (2010) tested pure ZnO for H_2S adsorption. Dhage et al. (2010) comparatively examined two types of pure ZnO absorbents (i.e. 3 mm-extrudates and a wash-coated monolith). Despite the higher space velocity for the test with the wash-coated monolith, the outlet H_2S concentration was lower than that with the extruded material. Therefore, the use of a ZnO wash-coated monolith led to a better performance. These tests were conducted at 300–400°C. In this temperature range, ZnO has been widely used to remove H_2S because of its high equilibrium constant (for ZnS formation). In particular, it is important to underline that recent studies carried out by Neveux et al. (2012) showed that the ZnO sulphidation model is characterised by an outward rather than inward growth mechanism for the formation of ZnS (Fig. 1.3). Decreasing the reaction temperature to 200–300°C brings a severe decrease of the sulphidation rate of pure ZnO and this, consequently, reduces its efficiency (Balichard et al., 2014). In fact, the reactions between sulphur species and metal oxide sorbents at low temperatures are confined only in the outer layer of the

sorbent particles. Hence, due to increase of the molar volume in ZnO–ZnS transformation, a ZnS layer is formed, which hinders the further reaction of ZnO and determines a decrease in the overall reactivity and transformation rate (Balichard et al., 2014). Moreover, the transport through the layer is considerably slower at low than at high temperatures, and so it is the sulphur capacity (Yan et al., 2002).

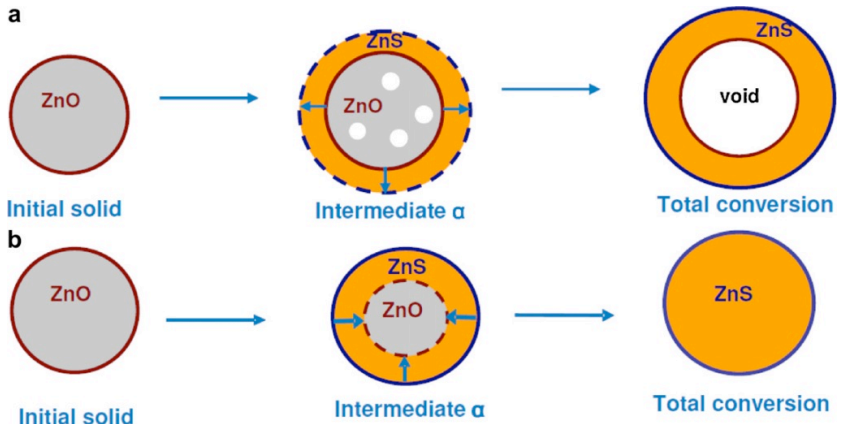

Fig. 1.3. Schematic representation of an outward (a) and an inward (b) growth of ZnS phase during the ZnO sulphidation reaction (Neveux et al., 2012).

A possible way to overcome this difficulty is to use another zinc compound such as $ZnCO_3$, which has a density higher than the corresponding sulphur reaction products (Balichard et al., 2014), or varying the ZnO morphology that involves doping with other metallic species. For example, Skrzypski et al. (2011) studied mixed Cu−Zn oxides and found a 6-fold increase in capacity at 200°C by doping with 6 mol% Cu. Jiang et al. (2010) studied Cu−Zn and Cu−Zn−Al mixed metal oxides prepared via co-precipitation (cp) or multi-precipitation (mp) methods at 80°C. Better dispersion by aluminum results in smaller mean crystalline sizes and higher specific surface area of Al-containing sorbents; breakthrough sulphur capacities also improve as a result of reducing the thickness of sulphide shell so reducing as well the diffusion path length.

As already mentioned, using the metal oxide or mixed metal oxide at relative low T (<200°C) is limited due to kinetic restrictions, which can lead to

rather low utilisation factors. Therefore, current research efforts are devoted to develop high performance sorbents capable to work at low temperature (down to room temperature): a promising approach is to disperse nano-sized metal oxides onto highly porous supports, such as zeolites, mesoporous silicas and activated carbons, or in composites with graphite oxides So far, also unfunctionalised activated carbons have been found to have good removal properties of H_2S when the concentration of pollutant is in the range of ppm or less (Bagreev and Bandosz, 2005). This is the result of unique surface properties of carbonaceous adsorbents such as high surface area and pore volume, along with surface chemistry, which promotes the catalytic oxidation of H_2S in the presence of even small amounts of oxygen and high moisture contents. Both physical adsorption and chemisorption play an important role in the H_2S capture mechanisms on activated carbons. Chemisorption is rapid and mostly occurs at the carbon surface, whereas physical adsorption is relatively slow and mostly takes place at the inner pores of carbon (Yan et al., 2002).

The mechanisms of H_2S adsorption on activated carbon are influenced by the presence of other species such as CO_2 (Bagreev and Bandosz, 2005) and H_2O (Huang et al., 2006). In dry conditions (i.e. absence of humidity in the feed gas stream), H_2S is captured by physical adsorption and it is supposed to occur following the mechanism called micropore filling (Adib et al., 1999, 2000; Feng et al., 2005). When other species besides H_2S are involved in adsorption, both chemical and physical mechanisms can occur. As an example, O_2, adsorbed on the surface of the adsorbent, oxidises H_2S to sulphur or SO_2. It is likely that atoms present in the small pores act as a catalyst for oxygen activation causing hydrogen sulphide oxidation (Nguyen-Thanh and Bandosz, 2005). Moreover, if humidity is present in the gas stream, sulphuric acid might be formed (Nguyen-Thanh and Bandosz, 2005).

The mechanism of H_2S removal in the presence of humidity can be very complex and it depends on many parameters. Huang et al. (2006) humidified activated carbons under various relative humidity (RH) conditions (RH=40–50% or 70–80%) at 323 K for 24 h. After cooling down to room temperature, the

absorbed water vapour condensed to a water film in the pores of the activated carbon. They affirmed that, in such conditions, the H_2S dissolved and dissociated to produce H+ and HS− ions into the water film. This is followed by a dissociative adsorption (Adib et al., 1999, 2000) and in some cases by oxidation that brings to the formation of sulphur, SO_2 or sulphur polymeric structures (Bagreev et al., 2004). Therefore, the absorption of H_2S into the water film increased the adsorption capability of the pre-moistened activated carbon (Huang et al., 2006). Choi et al. (2008) found that the adsorption capacity was not highly dependent on relative humidity in absence of oxygen. However, the adsorption capacity of hydrogen sulphide at constant oxygen concentration (2% vol) was considerably increased by relative humidity.

Another important parameter is the pH occurring in the carbon pores due to water adsorption. If $pH<pKa(H_2S)$, the oxidation brings to the formation of sulphur. Contrarily, if $pH>pKa(H_2S)$, SO_2 and sulphuric acid are preferentially formed (Adib et al., 1999, 2000; Yan et al., 2002).

Previously mentioned, the functionalisation treatment, with metal oxide or other active phases, leads to an increase of adsorption of hydrogen sulphide. The impregnation of basic groups such as KOH (Tsai et al., 2001; Yan et al., 2002), KI (Choi et al., 2008), urea and melamine (Bagreev et al., 2004) determines appreciable results. However, the use of impregnation with these compounds is limited by their low ignition temperature, which could cause undesired autoignition in the bed. Tsai et al. (2001) explored the adsorption of H_2S on alkaline impregnated activated carbons. Generally, the length of unused bed (LUB) of the impregnated alkaline activated carbon was less than in the case of activated carbon, because the alkaline reacted with H_2S and enhanced the adsorption rate. NaOH was selected as the most effective alkaline additive. Moreover, finer adsorbent particle sizes enhanced the adsorption rate. The reaction between H_2S and NaOH can be proposed as follows: H_2S is a diproton acid that reacts with a hydroxide (i.e. $H_2S+AOH \rightarrow AHS+H_2O$) of basic chemicals.

Furthermore, Bagreev et al. (2004) revealed that carbons modified with nitrogen-containing species and heat-treated at 850°C have a hydrogen sulphide

removal capacity exceeding more then 10 times the capacity of unmodified samples. In fact, nitrogen within the carbon matrix can cause an increase in the number of basic groups and changes the charge distribution within carbon layers. Another interesting application of activated carbon functionalisation is the use of metal oxides and hydroxides, such as those based on Cu (Huang et al., 2006) and Zn (Hernandez et al., 2011a,b). Recent studies (Lau et al., 2015) also report cerium oxide as an efficient active phase. Among metal oxides, zinc oxide is the most employed for H_2S adsorption. Rosso et al. (2003) found that ZnO has the highest equilibrium constant for sulphidation, yielding H_2S removal down to even fractions of 1 ppm. The Gibbs free energy of sulphidation of ZnO is $\Delta G = -91607.18+15.16T$ (J mol^{-1}). Therefore, conversion of ZnO to ZnS can easily take place at low temperatures, including room temperature (Samokhvalov and Tatarchuk, 2011). For these applications, the functionalised materials are mainly prepared by means of the precipitation method (Hernandez et al., 2011a,b), that is one of the most easy and economic method to functionalise a support. For instance, biogas desulphurisation tests have pointed out that an activated carbon functionalised with 10% ZnO has a higher H_2S adsorption capacity (≈47%) than the commercial raw activated carbon material, due to the presence of well dispersed ZnO nanoparticles on the surface of the activated carbon (Hernandez et al., 2011a,b). Also in the case of using nanodispersed active phase onto a support at $T \approx 250$°C, the reaction between ZnO and H_2S leads to the formation of ZnS (Rosso et al., 2003). However, the reaction between ZnO and H_2S is affected by the presence of other compounds. For instance, some studies observed that CO_2 can accelerate the reaction between ZnO and H_2S, while H_2O inhibits the reaction due to the desulphurisation reaction (i.e. $ZnO+H_2S \rightleftharpoons ZnS+H_2O$) that brings to the production of water. Hence the presence of H_2O promotes the equilibrium towards the reagent direction (Elseviers and Verels, 1999). Additionally, H_2 accelerates the reaction of H_2S in the presence of H_2O, whereas CO inhibits the reaction (Sasaoka et al., 1994).

Hernandez et al. (2011a,b) explored various ZnO percentage loading on activated carbons ranging from 10 to 30% wt. As a general trend, the H_2S

adsorption capacity increases with the percentage of loading. This tendency reaches a maximum at which the trend is then opposite. In fact, the higher dimension of the dispersed phase (ZnO) due to the increase in the loading percentage determines a reduction in the exposed area so decreasing the dispersion of the active phase on the support. In addition, the functionalised carbon has to be frequently substituted because at high loading percentage it is only partially regenerable (Bagreev et al., 2002).

There are few studies regarding the use of inorganic support as adsorbent without a functionalisation treatment, most of the applications found in the literature make use of these solids as support for the dispersion of an active phase. In a similar way observed for AC, ZnO active phase may be dispersed onto a suitable, high surface area support such as inorganic porous sorbents. Among the latter, amorphous silicates or mesoporous silica are the most studied (Yang et al., 2002;; Hussain et al., 2012; Mureddu et al., 2012; Montes et al., 2013).

For instance, Wang et al. (2008b) studied the H_2S removing capacity of mesoporous silica SBA-15 with adding zinc oxide (ZnO) nanoparticles through incipient wetness impregnation and ultrasonic method. ZnO functionalised mesoporous materials have shown better adsorption capacities than activated carbon-based adsorbents (Wang et al., 2008b; Hussain et al., 2012). As an alternative, Kang et al. (2008) use alumina as a support. The latter is quite effective for H_2S removal thanks to the presence on its surface of hydroxyl groups. In contrast with pure ZnO, pure Al_2O_3 has a high surface area and total pore volume, hence combining Al_2O_3 support and ZnO sorbent; the surface area and total pore volume of composite sorbent can sharply increase in comparison to pure ZnO. This result suggests that, using the ZnO–Al_2O_3, composite sorbents can show a better performance than pure ZnO for H_2S adsorption due to the higher surface area and pore volume (Tajizadegan et al., 2013).

Ozekmekci et al. (2015) tested zeolites for the removal of hydrogen sulphide. The adsorption capacity of H_2S by zeolites, without any functionalisation treatment, is low compared to other sorbents such as activated carbons, because the AC can promote an adsorption–catalytic oxidation

mechanism for H_2S (leading to elemental S, SO_2, sulphates, sulphuric acid, apart from metal sulphides) in the presence of even small amounts of oxygen and high moisture content. However, advantages of zeolite adsorption involve low cost, long-term chemical and thermal stability of adsorbents, (partial) regeneration via thermal (oxidative) treatments and, most importantly, high selectivity for H_2S separation (Yaşyerli et al., 2002). This is crucial because, as mentioned in *Chapter 2*, biogas is made up of several compounds. Cosoli et al. (2008) tested a hydrophilic (i.e. LTA) and an hydrophobic (i.e. MFI) zeolite for H_2S adsorption. The main results of this work indicate that hydrophilic zeolites are more suitable for H_2S adsorption. In fact, electrostatic interactions between the H_2S polar molecule and the framework are more favourable in hydrophilic zeolites.

Moreover, selectivity factors are generally very high in hydrophilic zeolites while MFI shows much lower selectivity for H_2S (Cosoli et al., 2008). Zeolites can be also modified in order to increase their adsorption capacity (Ozekmekci et al., 2015). For instance, Liu et al. (2015) used a hybrid TiO_2/zeolite composite which exploits at the same time the features of zeolite adsorption and TiO_2 photocatalysis action. The performance of TiO_2/zeolite was slightly affected by the high level of CO_2 and favoured by the presence of moisture in the feed gas, especially in the photocatalytic stages.

Before studying other types of adsorbents (with various active phases on a support), some studies focused on the regeneration of the sorbent. Bagreev et al. (2002) tested the regeneration of spent activated carbons by washing with cold water or by means of a thermal treatment (for example by heating the samples at 300°C for 120 min in air). After applying both the regeneration methods, the samples, previously completely exhausted, revealed some capacity to remove hydrogen sulphide. However, the measured capacity was much lower than that for the initial sample, which indicates low efficiency of regeneration, in both the cases. This occurs because some species such as sulphur or sulphuric acid bond irreversibly on the active sites (Huang et al., 2006).

Regeneration efficiencies typically vary in a wide range of 50–80% (Aslam et al., 2015). Differently, Lew et al. (1989) studied regeneration of pure ZnO

sorbents with 10% of air and 90% of N_2 (molar compositions), at 700°C. The regenerability of ZnO is affected by a loss of surface area (due to sintering phenomena) at high regeneration temperatures and by the formation of stable zinc sulphate at low regeneration temperatures. However, since a low oxygen concentration (≈2%) was used in regeneration of the spent sorbent, zinc sulphate formation was not observed. On the other hand, after many sulphidation regeneration cycles, sintering (starting at temperatures of ≈250°C, Samokhvalov and Tatarchuk, 2011) and loss of volatile zinc by reduction of the zinc oxide sorbent will cause a noticeable decrease in the conversion of the sorbent to ZnS, based on the original amount of ZnO. In fact, the non-supported sorbents based on Zn oxides are known to work efficiently for only a small number of sulphidisation regeneration cycles (Dhage et al., 2010).

Further studies reveal that ZnO impregnated alumina shows low efficiencies of regeneration (Yang et al., 2007). In fact, during regeneration of $ZnO–Al_2O_3$ composite sorbents, the active phase and the support interact and produce zinc products that can decrease the adsorption of H_2S because is inactive species for H_2S adsorption, especially at high regeneration temperature. The incomplete regeneration is the real disadvantage of sorbents such as activated carbons and alumina. In fact, the chemical H_2S removal processes are expensive (3.85 €/kg_{H2S}) due to chemical requirements, energy and disposal costs if confronted for instance to biological desulphurisation (0.1–0.25 €/kg_{H2S}) (Sun et al., 2015). This is the reason why an effective regeneration is crucial for economic sustainability of the process. The choice of regenerable sorbents has been often directed toward other sorbents such as zeolites, SiO_2 particles, mesoporous silica and copper oxides. For instance, according to Yang and Tatarchuk (2010), CuO sorbents are favoured as regenerable sorbents. However, according to Ozekmekci et al. (2015), the regeneration of zeolites is much easier, efficient, and also low-cost. In fact, zeolite adsorption involves the reversibility of the adsorption-desorption processes. Moreover, Liu et al. (2015) report that the regenerated hybrid TiO_2/zeolite composite showed a good adsorption and photocatalysis capacity as the fresh one. Finally, with the appropriate support, metal oxide

impregnated sorbents can also achieve high regeneration efficiencies. For instance, Wang et al. (2008a) affirm that ZnO functionalised mesoporous silica sorbents can be easily regenerated at mild conditions (temperature range of 75–100°C) and have excellent stability. Moreover, Yang and Tatarchuk (2010) found that the SiO_2 inert sorbent support is very efficient for regenerable desulphurisation applications at moderately low temperatures (300–500°C). Hence, SiO_2 is developing as support for both ZnO and CuO active phases.

Another way to improve H_2S adsorption is to functionalise sorbents by using mixed metal oxides. In fact, it is well known that the presence of a second metal in a metal oxide matrix can improve the activity and catalytic properties of the single metal oxides. This synergistic effect can be the result of particular metal–metal or metal–oxygen–metal interactions when the "right" combination of metals is chosen. Mabayoje et al. (2013) studied combinations of mixed zinc/cobalt hydroxides. Furthermore, many studies of CuO and ZnO combinations have been made in literature using various supports such as mesoporous SiO_2 and alumina (Kang et al., 2008; Yang and Tatarchuk, 2010; Montes et al., 2013; Elyassi et al., 2014). Montes et al. (2013) use CuO and ZnO supported on mesoporous silica. The maximum efficiency in H_2S removal was observed at zinc loading of 10% wt and copper loading of 20% wt. Higher loadings of ZnO and CuO implicate a decrease in H_2S removal. This is ascribed to the formation of a comparatively less reactive aggregate form of copper or zinc, which decreases both the uniform dispersion of these metal oxides on the support and the specific area and pore volume, caused by many factors (Liu et al., 2012): pore blockage, damage and possible collapse of the pores, as well as the formation of large agglomerates at high loadings of ZnO or CuO. Another factor to be considered is that in coarse metal oxide nanoparticles only the external surface is available to react with H_2S, leaving the inner part of the nanoparticle intact so lowering efficiency and adsorption capacity. The reaction mechanism can be explained based on acid–base reaction. Both Cu^{2+} and Zn^{2+} are moderate acids while sulphur is a soft base, therefore the formation of CuS and ZnS is very favoured (Montes et al., 2013). Due to the use of highly porous supports, ZnO supported on SiO_2

(ZnO/SiO_2) demonstrated a high sulphur capacity and almost complete ZnO utilisation indicating minimised intraparticle mass transfer resistance. However, the practice of using mixed sorbents has not been optimised yet and very few are the studies regarding their interaction with other species present in fuel gas streams and biogas such as H_2O, CO_2 and CH_4.

1.3 Formaldehyde adsorption

1.3.1 General information

Formaldehyde, HCHO, is one of the most common toxic pollutants found in indoor air. HCHO is produced on a large scale by the oxidation of methane or methanol in the presence of a catalyst (Reuss et al., 2002). At ambient conditions, it is a flammable and colourless gas of a pungent distinct odour. Its boiling point is –19°C. The HCHO molecule is polar with a dipole moment of 1.85 D and pK_a of 13.27. The compound is soluble in water, ethanol, diethyl ether, and acetone. Formaldehyde is commonly purchased as a 37% solution in water, known as formalin, with 10% methanol as a stabiliser. The annual production of 37% formaldehyde is about 20 million tons worldwide (Hauptmann et al., 2006). Even though small amounts of formaldehyde are produced naturally by plants, animal, and humans, its main source is anthropogenic. It is introduced to the atmosphere through a combustion process, industrial production or as a component of the resins used in furniture and building materials. Furthermore, its most common sources are pressed woods and particle boards (USA Consumer Products Safety Commission). Based on its toxicity, formaldehyde is classified as a known human carcinogen (Formaldehyde and Cancer Risk NIH, 2018). For example, only in the USA up to 2 million workers are exposed every day to it (Zhang et al., 2009). HCHO is considered as one of the most dangerous gases for the respiratory system (Medinsky and Bond, 2001). In indoor air, formaldehyde is found in carpet cleaners, medicines, cosmetics, adhesives, paper and plastics. Moreover, pressed wood products containing formaldehyde resins are often a significant source of formaldehyde. Exposure to only 4 ppm HCHO causes irritation to nose, throat, and eyes. The high solubility of formaldehyde in water causes rapid absorption in

the respiratory and gastrointestinal tract. Here, it can be oxidised to form formate and exhaled as carbon dioxide or incorporated in biological matrices. According to a report published by “Health Canada”, which is based on human clinical studies and animal experiments, the primary effects of acute exposure to formaldehyde are irritation of the mucosa of the upper respiratory tract and the eyes (Health Canada, 2005). Fig. 1.4 shows the common health effects related to HCHO inhalation. As a consequence, the World Health Organization (WHO) has established its exposure limit at 0.08 ppm for 30 min. Furthermore, US Consumer Products Safety Report of 1997 lists its either indoor or outdoor concentration limit at the level of 0.03 ppm.

1.3.2 State of the art

There are only few reports addressing adsorption of formaldehyde on activated carbons. Through their studies on AC without functionalisation, Kumagai et al. (2008) evaluated the adsorption capacity of AC derived from rice husks (RH) and, for comparison, the experiments were carried out on commercial coconut shell AC. The experimental apparatus was a closed bag of 5 L containing AC in the presence of 1 ppm of HCHO vapour at room temperature. The results showed that an increase in the carbonising temperature of RH AC, from 250°C to 800°C, led to an increase in the HCHO adsorption rate.

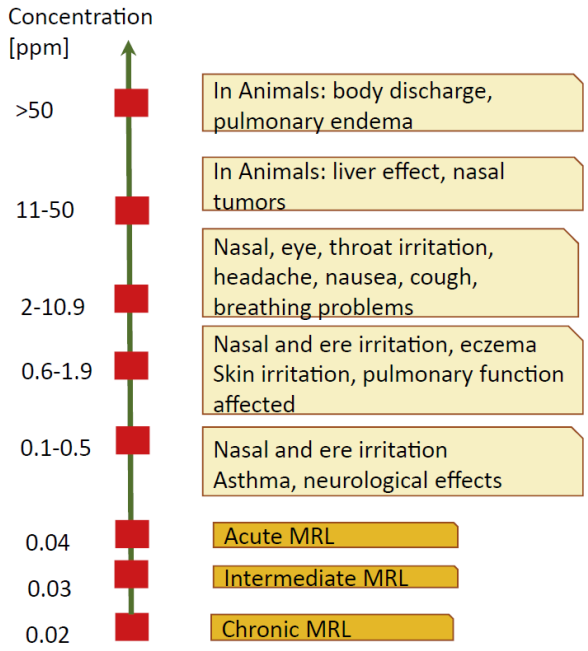

Fig. 1.4. Health effects of formaldehyde exposure (Suresh and Bandosz, 2018).

In the case of samples treated at lower temperature (250°C), it required more than 100 min to reduce the HCHO concentration to 0.5 ppm while the sample treated at 800°C decreased the HCHO concentration to 0.5 ppm after 10 min. The rice husks have a better adsorption of HCHO compared with coconut AC. The authors suggested that RH AC show better adsorption for a high surface basicity that enhances the adsorption of HCHO. The basicity was connected to the presence of inorganic K and Ca compounds. Wen et al. (2011) evaluated the adsorption performance of three commercial AC, derived from coconut shells, wood and coal. The measured formaldehyde adsorption capacities were between 7 to 8 mg g^{-1} at a HCHO concentration of 0.41 mg m^{-3}. Carter et al. (2011) studied the HCHO adsorption isotherm of three carbon based sorbents, ACF cloth and two granular activated carbons, GAC, derived from bituminous coal. The maximum adsorption capacity at 20 ppm of HCHO was obtained for ACF carbon cloth. The comparison of the HCHO adsorption isotherms on the investigated samples indicated that the affinity of HCHO to the adsorbents surface depended on the surface chemistry. It is important to underline that water adsorption isotherm

obtained by the same AC sorbents are similar compared to HCHO isotherm (Fig. 1.5).

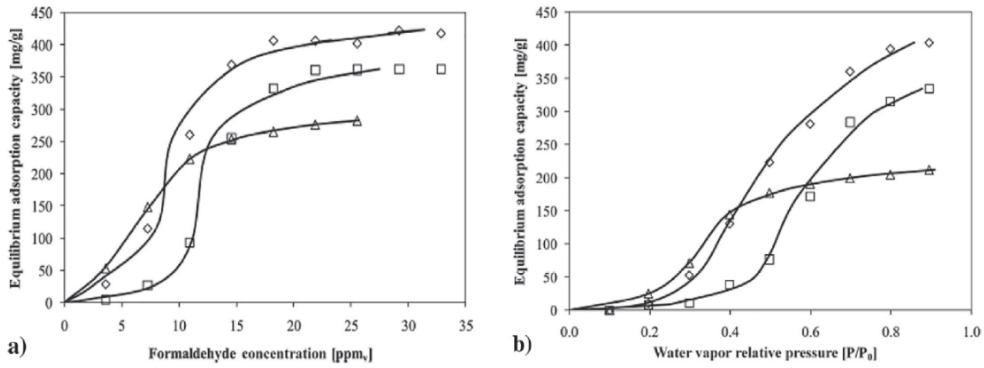

Fig. 1.5. HCHO adsorption isotherms for ACF (◊), GAC1 (□), and GACF (△). Solid lines are fitted adsorption isotherms using Q-L model. (a) HCHO, (b) Water (Carter et al., 2011).

The authors also investigated the density of acid and basic groups on the surface of the sorbent, to find a correlation with the amount of adsorbed HCHO as formaldehyde can behave as either Lewis acid or Lewis base. It was concluded that, at low HCHO concentration, the amount of formaldehyde adsorbed depended on the density of both acidic and basic groups, although the effect of the latter seemed to be stronger.

Rong and coworkers (2002, 2003) investigated the dynamic adsorption of HCHO vapour using rayon-based activated carbon fibers (ACF). The feed gas was generated by HCHO solution in water, and the total flow rate was 0.5 cm^3/s. The sorbents were treated in air oxidised in a temperature range between 350 and 450°C for various periods of time (1–3 h). The sample oxidised at 420°C for 1 h was found to be the one with the highest surface area among all the samples tested, and the adsorption capacity was equal to 583.4 mL g^{-1}. The authors highlighted the competitive adsorption of HCHO and water vapour, because in the same experimental conditions it was found that the sorbents adsorbed a high amount of water. Rong and coworkers also studied the effect of various heat treatment

conditions on the same samples. The temperature range was between 350 and 850°C. The best sample was obtained at 450°C for 0.5 h. In particular, they noticed that this heat treatment increases the selectivity toward HCHO. Finally, they established some relevant aspects to increase the adsorption of HCHO on heat treated rayon activated carbon fiber: 1) presence of acidic carboxylic groups, 2) cooperative interaction of dipole–dipole interaction and hydrogen bonding.

Tanada et al. (1999) measured formaldehyde adsorption isotherms from its water solutions onto untreated and treated AC. The carbon was oxidised with concentrated nitric acid and/or sulphuric acid for 24 h (mass ratio 1:1), and then reduced with iron powder and washed with HCl for 30 min and 60 min. They observed that the adsorption capacity increased from 0.4 mg g^{-1} for the initial sample to 0.8 mg g^{-1} for the modified samples, during adsorption tests at 15°C and 35 mg/L as initial HCHO concentration. At 25°C, it was observed a two-fold increase in the capacity of the sorbent. It was concluded that this was due to the specific interactions between formaldehyde and the surface of AC, by introducing amino groups on the surface of treated samples.

As seen above, in order to increase the adsorption of HCHO, modification by incorporation of basic groups, in particular nitrogen compounds, was the most explored technique. Boonamnuayvitaya et al. (2005) investigated the removal of HCHO vapours using carbons obtained by coffee residues activated with $ZnCl_2$, CO_2 and steam. The best sample was the carbon activated with $ZnCl_2$ under a nitrogen flow (CZn-N_2). On the basis of the collected results, it was concluded that, for HCHO adsorption on activated carbon, surface chemistry is more important than textual features. The kinetics of formaldehyde adsorption (2.3 ppm) at 45% relative humidity and at 30°C on microporous ACs prepared from poly (ethylene terephthalate) and polyacrylonitrile (PAN) was investigated by László (2005). The oxygen content was less than 10% and PAN-derived carbon had 5.3% nitrogen on the surface. The latter sample was found as having the highest formaldehyde uptake per unit surface area. It was concluded that the high oxygen content yielded a greater affinity towards water, as did the presence of nitrogen functionalities in the PAN-derived samples. An et al. (2005) studied

mesoporous AC treated with sulphuric acid and ammonia for removing indoor HCHO (1 ppmv). The adsorption capacity of the samples modified by acid was comparable to that relative to the parent one, despite its smaller specific surface area. Ammonia modified sorbents showed the highest HCHO adsorption capacity, attributed to the presence of nitrogen groups and an increase of surface area. Furthermore, Song et al. (2007) investigated adsorption of low concentration formaldehyde on various ACFs, such as pitch-based, rayon-based, and PAN-based. The initial formaldehyde concentration was 20 ppm. The samples markedly differed in surface areas and pore volumes. The measured adsorption capacities were between 0.01 mmol g^{-1} and 0.478 mmol g^{-1}. Since all PAN-based ACFs showed higher formaldehyde adsorption capacity and longer breakthrough time than did pitch-based or rayon-based ACFs, it was concluded, by XPS analysis, that abundant nitrogen-containing groups in the PAN-derived fibers, and especially pyrrolic, pyridonic, pyridinic, and quaternary groups, promoted the adsorption of formaldehyde. It is important to underline that the authors concluded that the surface area is not a main factor governing HCHO adsorption, but that abundant nitrogen-containing groups in the PAN-derived fibers promote the HCHO retention. In humid condition, however, the HCHO adsorption capability of the PAN-based ACFs drastically dropped because of the competitive adsorption of HCHO and water. Similarly, Lee and coworkers (2010) studied pitch-based ACF (referred as ACNF) and PAN-based ACF (referred as FE series) at 11 ppm of formaldehyde initial concentration in dry and moist conditions (90% RH). They observed (Fig. 1.6) that in dry conditions the amount of HCHO adsorbed is two times more comparing to the amount adsorbed in dry condition for ACNF sorbents.

Another way to increase the HCHO removal performance of AC is modifying the surface with inorganic compounds. Shin and Song (2011) investigated the combined effect of adsorption and catalytic oxidation of HCHO on granular AC modified by introducing silver nanoparticles (batch and dynamic conditions). The dynamic experiments were carried out at 10 ppm formaldehyde in air flow. Results suggested that the catalytic oxidation played a significant role

in increasing the amount of HCHO adsorbed, even though the silver nanoparticles coverage decreases the porosity of AC.

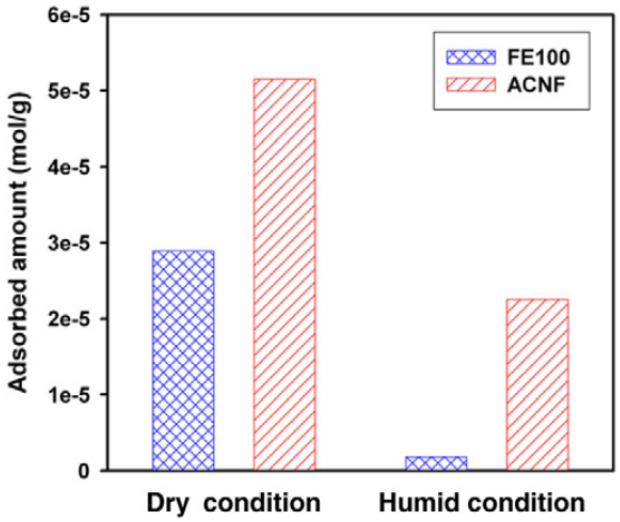

Fig. 1.6 Comparison of formaldehyde adsorption amount at the breakthrough time in dry or humid condition between FE100 and ACNF, Lee et al. (2010).

Rengga et al. (2013, 2017) studied the removal of formaldehyde using AC modified by silver or copper nanoparticles (AC-Ag and AC-Cu, respectively) at initial HCHO concentration equal to 8 ppmv. The incorporation of silver and copper nanoparticles lead to a decrease of initial BET area of 9 and 29%, respectively (BET area of virgin AC was 753 m^2/g). AC-Ag was the best sorbent with HCHO removal of 0.425 mg/g, while the original activated carbon adsorbed 0.264 mg/g. They also prepared another HCHO adsorbent functionalising with silver nanoparticles the surface of bamboo-based activated carbon. The authors investigated the effects of flow rate (350, 400, 450 and 500 mL/min) and HCHO concentration in the feed gas (100, 200, 300, 500, 750 and 1000 ppm). At 1000 ppm, the sorbent exhaustion time (for which the outlet HCHO concentration was as high as 95% the inlet value) was 305 min, and at 100 ppm it extended to 540 min. Under the latter conditions, for comparison, the parent carbon reached the exhaustion at 320 min. The authors indicated that an increase in the inlet concentration of HCHO caused the acceleration of the physical adsorption

through an increase in the diffusion of the adsorbate into the pores, which resulted in a decrease of the time needed to reach equilibrium. Moreover, with an increase in the mass transfer flux from bulk gas to the nanoparticles surface, the driving force (concentration gradient) also increased resulting in a fast equilibrium approach [Suresh and Bandosz, 2018].

Chapter 2 –

Experimental

The following chapter describes the samples used for the experimental runs, along with the experimental protocol that was adopted for their functionalisation, and the techniques for the characterisation of the samples. The description of the lab scale plants used in the execution of the adsorption/desorption tests and their corresponding experimental procedures can be found here as well.

2.1 H_2S adsorption tests

2.1.1 Materials

Two commercial solid sorbents were selected for the experimental tests of H_2S adsorption from a gas stream simulating a combustion flue gas, namely:

- Alumina: γ-Al_2O_3 spheres (abbreviated Als);
- Activated carbon: Darco Norit (abbreviated AC).

Table 2.1 summarises the main properties of these two sorbents, with AC being characterised by finer dimension, far larger BET area, and smaller pores.

Table 2.1. Particle diameter, BET specific surface area and mean pore dimensions for the two sorbents under investigation.

Adsorbent	**Producer**	**Particle diameter (mm)**	**BET specific surface area (m^2/g)**	**Mean pore dimensions (Å)**
Als	SASOL	1.0 spheres	174	80 (monomodal)
AC	NORIT	0.42–0.85 granular	641	15; 35 micro; meso pores

The sorbents were tested as raw and after functionalisation processes, performed with the aim of dispersing on the solid surface: ZnO or CuO or a mix of ZnO/CuO particles adopting the combination of a wet impregnation technique followed by Zn- and Cu-precursors calcination. In particular, in order to analyse the possible synergic effect due to the simultaneous presence of two metals and

optimise the composition of the active phase, several sorbents were prepared. The sorbents are distinguished by various Cu:Zn molar ratios: 0:100, 5:95, 10:90, 25:75, 50:50 and 100:0. For all the functionalised sorbents, the nominal loading of the active phase is 10% wt. of the functionalised sorbent, assuming that all copper and zinc are in their oxide forms.

The impregnation was carried out starting from aqueous solutions of nitrates of Zn ($Zn(NO_3)_2 \cdot 6H_2O$, 99.3%, provided by Sigma Aldrich) and Cu ($Cu(NO_3)_2 \cdot 5/2H_2O$, 98.6%, provided by Sigma Aldrich). The amount of solution per gram of substrate to be used within functionalisation runs was calculated through preliminary wettability tests (i.e. evaluation of the amount of water required for the appearance of a liquid film within the particles) of the substrate itself. The pH of the impregnating solutions is 3.5. Table 2.2 summarises the experimental conditions adopted for the sorbents preparation.

The alumina-based sorbents were later on calcined in air in a heating furnace for 2 h at 240°C, to obtain the decomposition of nitrate precursors and the formation of zinc and copper oxides.

Differently, for activated carbon supported solids, the calcination was carried out in a quartz tubular reactor (ID 20 mm) with N_2 flux. The reactor was placed in a cylindrical oven with PID control, that increases the temperature from approximately 100°C to 250°C at 10°C/min heating rate and then keeps the system at 250°C for 2 h. The temperature of the sorbent packed bed (supported by a Feralloy lather disc placed in the quartz tube) was measured by means of a K-type thermocouple (d=1 mm) placed in the middle of the bed. The gas produced during the thermal treatment was continuously sampled (after water removal by a $CaCl_2$ trap) using a specific analyser for CO_2, CO, NO, CH_4 (IR sensor) and O_2 (electrochemical sensor). More in detail, measurements during these tests were carried out by a continuous GAS 3000 Flue Gas Analyser by GEIT Europe, equipped with an electro-chemical selective sensor for O_2 and operating in the concentration range of 0–25% vol. This analyser also comes with an infrared sensor to measure the CO_2 (0–10% vol.), CO (0–9999 ppm), NO (0–1000 ppm), and CH_4 (0–9999 ppm) concentration.

Table 2.2. Quantities of precursor used to prepare the sorbents, and solid denomination. Percentages for Zn and Cu are on molar basis, and are expressed with respect to the sum Zn+Cu.

Support	Zn %	Cu %	Zn nitrate g mL^{-1}	Cu nitrate g mL^{-1}	Solid denomination
Als	100	0	0.51094	0	Zn/Als
Als	95	5	0.48593	0.02014	$Cu_{0.05}Zn_{0.95}$/Als
Als	90	10	0.46088	0.04032	$Cu_{0.10}Zn_{0.90}$/Als
Als	75	25	0.38537	0.10115	$Cu_{0.25}Zn_{0.75}$/Als
Als	50	50	0.25837	0.20344	$Cu_{0.50}Zn_{0.50}$/Als
AC	100	0	0.51130	0	Zn/AC
AC	95	5	0.48628	0.02015	$Cu_{0.05}Zn_{0.95}$/AC
AC	90	10	0.46120	0.04035	$Cu_{0.10}Zn_{0.90}$/AC
AC	75	25	0.38564	0.10122	$Cu_{0.25}Zn_{0.75}$/AC
AC	50	50	0.25856	0.20358	$Cu_{0.50}Zn_{0.50}$/AC
AC	0	100	0	0.40000	Cu/AC

2.1.2 Solids characterisation techniques

In order to verify the possible residual presence of nitrates after calcination at 250°C on alumina- and activated carbon-based sorbents, Temperature Programmed Desorption tests of nitrogen oxides (named TPD-NO_x tests) were carried out

The actual content of metals in the sorbents was determined by Inductively Coupled Plasma (ICP) spectrometry using an Agilent 7500 ICP-MS instrument, after microwave-assisted digestion of samples in nitric/hydrochloric acid solution.

The textural properties of the sorbents were determined by N_2 adsorption tests at 77 K with a Quantachrome Autosorb 1-C instrument, after degassing the samples for 2 h at 150°C. The Brunauer–Emmett–Teller (BET) method was adopted for the calculation of the specific surface area. Furthermore, the micropore volume (V_M) and the total pore volume (V_{TOT}) were respectively

computed by means of the Dubinin–Astakov and Gurvitsch's rule (Leofanti et al., 1998) applied to the N_2 amount adsorbed at P/P_0=0.99. Finally, the Pore Size Distribution (PSD) was evaluated *via* the Quenched Solid Density Functional Theory (QSDFT) or by means of the Barrett–Joyner–Halenda (BJH) desorption method for mesopores and the Dubinin–Astakov (DA) method for micropores.

X-Ray Diffraction (XRD) tests were performed on powder samples with a Bruker D2 Phaser diffractometer (operated at diffraction angles ranging between 10 and 80°2θ with a scan velocity equal to 0.02°2θ s^{-1}). This technique allows identifying the mineralogical phases of the prepared solid sorbents.

Diffuse Reflectance Infrared Fourier Transform Spectroscopy (DRIFT) experiments were performed on a Perkin Elmer Spectrum GX spectrometer equipped with a liquid-N_2 cooled MCT detector with a spectral resolution of 4 cm^{-1}, averaging each spectrum over 50 scans. The sorbent samples were diluted in KBr (2%) and about 0.1 g of finely grounded powder was placed in the DRIFT cell equipped with a ZnSe window and connected to gas lines. Spectra were collected at 40°C, following a pre-treatment at 120°C for 40 min under flowing Ar.

The total sulphur content in spent sorbents was determined with a LECO SC 144-DR analyser.

Scanning Electron Microscopy (SEM) analysis was carried out with a FEI Inspect microscope equipped with an Energy Dispersive X-ray (EDX) probe. This analysis allowed determining the distribution of the active phases on the support.

X-ray Photoelectron Spectroscopy (XPS) analysis was carried out on a XPS PHI 5000 Versa probe apparatus, using a band-pass energy of 187.85 eV, a 45° take off angle and a 100.0 μm diameter X-ray spot size for survey spectra. High-resolution spectra were recorded in the following conditions: pass energy of 20 eV, resolution of 1.1 eV, and step of 0.2 eV. Sample charging effects were eliminated by correcting the line shift of the C 1s signal from its binding energy value of 284.6 eV. The spectra were analysed by means of a commercial software (CasaXPS, version 2.3.16), by applying mixed Gaussian–Lorentzian (70–30%)

profiles. The assignation of XPS signals was based on the NIST compilation of spectral data (Wagner et al., 2003), unless otherwise stated.

The amount of sulphur released from spent materials in aqueous phase as sulphate ions (ω_{aq}) was evaluated by contacting 0.05 g of each sorbent, previously saturated with H_2S at 3000 ppm, with 0.1 L of distilled water at 60°C. The supernatant solution was analysed for times ranging from 3 to 480 h by means of a 883 Basic IC Plus ionic chromatograph (Metrohm).

2.1.3 Adsorption test rig

H_2S adsorption tests were carried out in two lab scale plants, one for tests at high concentration of pollutant (more than 200 ppm of H_2S in the feed gas), the second one at low concentration of pollutant (less than 200 ppm of H_2S in the feed gas). In particular, the adsorption tests at low concentration were carried out for AC sorbents.

Fig. 2.1 shows a schematic representation of the experimental apparatus for adsorption tests at high concentration.

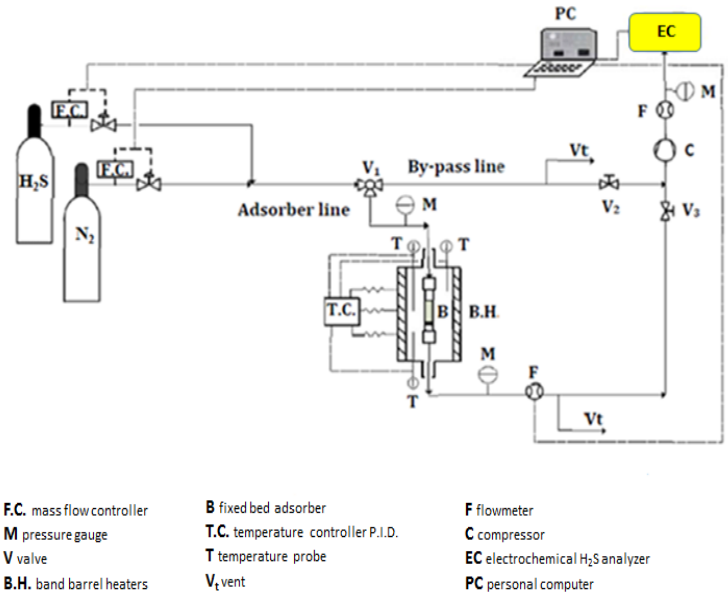

Fig. 2.1. Layout of the experimental apparatus – tests at high H_2S concentration.

The feed gas composition (N_2+H_2S) was determined via mass flow controllers (series El Flow Bronkhorst 201-CV), which allow to generate gas streams simulating typical biogas compositions (i.e. 500–3000 ppm H_2S). H_2S adsorption tests on the investigated sorbents were carried out in a fixed bed column (length=13 cm; inner diameter=2 cm) made up of Pyrex glass, equipped with a 45 μm porous septum and composed of two units for adsorbent charging/discharging operations. The fixed bed temperature was controlled by means of an appropriate heating system, arranged coaxially with the adsorber unit. It consists of three 500 W cylindrical shell Watlow band heaters, enveloped in a thermal insulating layer of ceramic fibers, and connected to EZ PM PID controllers (Watlow).

The performances of the investigated sorbents for H_2S capture have been explored under the following experimental conditions:

• Sorbent dose: 5 g for raw activated carbon and Al_2O_3 (both raw and impregnated), and 2.5 g for impregnated activated carbon.

• Total gas flow rate: 90 L h^{-1} (from now on, gas volumes are expressed as evaluated at T=20°C and P=1 bar);

• H_2S inlet concentration: 500–3000 ppm, balance N_2;

• Temperature: 30°C and total gas pressure: 1 bar.

Hydrogen sulphide concentration measurements during adsorption tests were carried out by a continuous GAS 3240 R BIOGAS gas analyser (GEIT Europe), equipped with an electrochemical selective sensor for H_2S and operating in the concentration range of 0–10000 ppm. Data acquisition and elaboration were performed by interfacing the analyser with a PC unit by means of SCADA monitoring software.

H_2S adsorption capacity at saturation, ω_s [mmol g^{-1}], was determined through a material balance on H_2S over the adsorption column, leading to the following expression:

$$\omega_s = \frac{Q^t C_{H_2S}^{in} \rho_{H_2S}}{M_{H_2S} m} \int_0^{t^*} \left(1 - \frac{C_{H_2S}^{out}(t)}{C_{H_2S}^{in}}\right) \mathrm{d}t \qquad (2.1)$$

where Q^t [L s^{-1}] is the total gas flow rate, $C_{H_2S}^{in}$ [–] is the H_2S volumetric fraction in the gas feed, $C_{H_2S}^{out}$ [–] is the H_2S volumetric fraction at the bed outlet, ρ_{H_2S} is H_2S density (1370 mg L^{-1} at 30°C and 1 bar) while M_{H_2S} [mg $mmol^{-1}$] is its molecular weight; m [g] is the sorbent dose and t^* [s] represents the time required to reach 99% recovery of the initial inlet concentration of H_2S. The resolution of Eq. (2.1) allowed determining the adsorption isotherm, under the verified assumption of constant total flow during the test.

Some adsorption tests, for AC sorbents, were run under identical conditions but substituting part of N_2 flow with either CO_2 or CH_4 with inlet concentration of 40% vol.

Fig. 2.2 schematically shows the lab scale plant with the corresponding analytic equipment used for adsorption tests at low concentration.

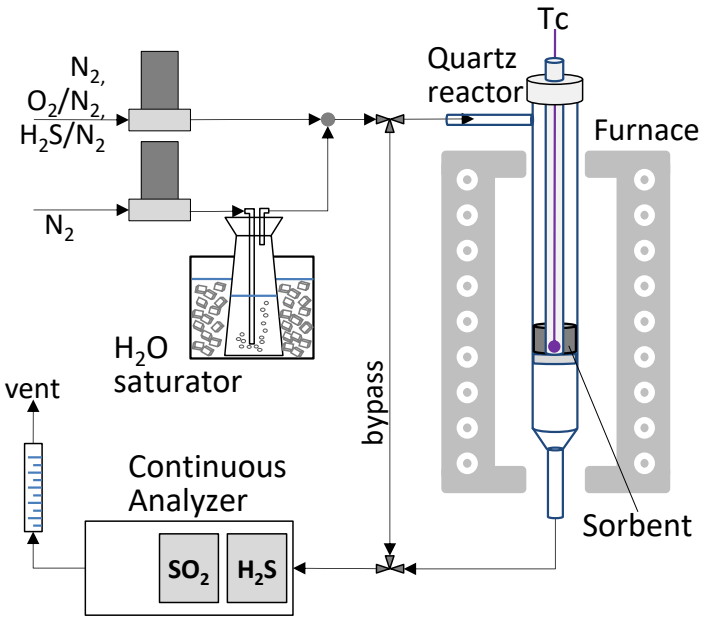

Fig. 2.2. Layout of the experimental apparatus – tests at low H_2S concentration.

A weighted amount of sorbent (20 mg for functionalised materials, if not otherwise reported; 80 mg for raw AC) with a particle size range of 125–200 μm was mixed with quartz to obtain a total bed mass of 200 mg. The sorbent was loaded in a cylindrical quartz reactor with an annular section (OD 10 mm, ID 6mm), supported by a layer of quartz. The temperature of the sorbent was measured by means of a K thermocouple placed in the centre of the fixed bed. The feed gas composition was determined by means of two independent mass flow controllers. The inlet concentration of H_2S ($C_{H_2S}^{in}$) was varied in the range 100–193 ppm (100 ppm as base-case). On the line of auxiliary N_2 and before the reactor inlet, a water vapour saturator made of a gurgler and immersed in a thermostatic bath is placed. This system allows to feed a water-saturated gas stream to the reactor, at atmospheric pressure. The total flow rate of gas during adsorption varied in a range of 20–40 L h^{-1}, corresponding to contact times of 3.4–6.8 ms as referred to the volume of functionalised sorbent. In the case of wet adsorption tests, the H_2S concentration was fixed at 100 ppm, the gas flow rate was 20 L h^{-1}

and the relative humidity was 48%. The adsorption tests, in this case, were stopped at $C_{H_2S}^{out}(t)/C_{H_2S}^{in}$=0.9.

Some adsorption tests were stopped at different times before saturation (corresponding to different levels of H_2S capture) in order to investigate the nature of sulphur species progressively formed during the process.

2.1.4 TPD and TPO tests

Temperature Programmed Desorption and Temperature Programmed Oxidation (TPD/TPO) tests were carried out in the same lab scale plant described in Fig. 2.2. TPD tests were carried out in order to analyse the residual presence of nitrates on the fresh calcined sorbents (TPD-NO_x) and to shed light on the species formed upon the sulphidation process, while evaluating the thermal regenerability of the spent sorbents. TPO tests were also performed on spent sorbents in order to further explore their thermal regenerability. A known sorbent amount (20–150 mg) was heated at 10°C min^{-1} up to 800°C for alumina sorbents, while up to 620°C for AC sorbents, under N_2 flow (20 L h^{-1}). For both kind of samples, the maximum temperature during TPD-NO_x was 620°C. TPO tests were performed under a flow of air, only in the case of alumina based sorbents, or O_2 (5000 ppm) in N_2. The gas analysis was performed by means of two continuous analysers with cross sensitivity corrections: i) ABB Optima Advance Limas 11 UV for NO and NO_2; ii) ABB Optima Advance Limas 11 UV for the simultaneous measurement of H_2S (0–300 ppm) and SO_2 (0–100 ppm) concentrations.

2.2 HCHO adsorption tests

2.2.1 Materials

This part specifically refers to the activity carried out during an internship spent at City College of New York (see Introduction for details). Granular activated carbons and carbon cloths were selected for HCHO adsorption tests. The choice for these two adsorbent materials was suggested from the most interesting results reported in the literature (Tanada et al., 1999; Rong et al., 2002; Rong et al., 2003; Boonamnuayvitaya et al., 2005; Laszlo, 2005; Song et al., 2007; Lee et

al., 2010; Carter et al., 2011; Ma et al., 2011; An et al., 2012). As concerning the used of carbon textile, it was received from the U.S. Army Natick Soldier Research, Development & Engineering Center. It is composed of an inner porous carbon layer and outer nylon layer. In order to eliminate the outer nylon layer, the textile was placed in boiling water for 30 min and then the nylon is manually removed. The remaining inert carbon layer is referred to as CC. The functionalised CC was obtained by immersing the CC swatches in 40 mL of an aqueous solution containing 1 g of four precursors: dicyandiamide (D), penicillin G (P), thiourea (T), or urea (U) with mass ratio of CC:precursor (1:2) for 72 h. Then the textile swatches were dried overnight at 80°C and heated in a horizontal furnace at 800°C (20°C min^{-1}) for 40 min in N_2 flow (180 mL min^{-1}). The obtained samples are referred to as: CC-D, CC-P, CC-T and CC-U, where the last letter represents the modifier. A CC swatch, without functionalisation process, was thermally treated at 800°C in the same operation conditions as the modified samples. It is referred to as CC-HT. This sample is used as a heat treated standard to evaluate the extent of changes in surface chemistry caused by the chemical modifications.

As concerning the granular activated carbons, two commercial granular carbons were used: S208 (coconut shell-based carbon-Waterlink Barnabey and Sutcliffe, indicated as S208) and BAX-1500 (wood-based carbon-Westvaco, indicated as BAX). BAX was dispersed in a melamine suspension, mass ratio=1.5:1, in 25 mL of ethanol for 5 h under stirring at room temperature. Then, the mixture was boiled until complete evaporation of ethanol and then oven dried at 100°C. The next step was a thermal treatment of the sample at 950°C in an inert atmosphere (nitrogen) for 30 min. The heating rate was set to 10°C min^{-1}. Then the sample was washed in a Soxhlet apparatus to remove all the water-soluble compounds and dried in oven at 100°C. This carbon is referred to as BAX-M. To be modified with thiourea, BAX was dispersed in a thiourea solution obtained by dissolving thiourea in 25 mL of water; mass ratio=1:1. After stirring overnight at room temperature, the same steps were carried out as for the preparation of BAX-M. The obtained carbon is referred to as BAX-T.

Finally, it was used a polymer derived carbon, referred to as PSC, that was obtained from poly(sodium 4-styrenesulphonate) carbonised at 800°C, heating rate 10°C min^{-1}, for 40 min under nitrogen flow (300 mL min^{-1}) in a horizontal furnace. The carbon was extensively washed after synthesis to remove the excess of sodium. The spent samples exposed to HCHO under dry conditions are referred to with the letter "s".

2.2.2 Solid characterisation techniques

The surface area and the porosity of the adsorbents were determined from N_2 adsorption isotherms measured on an ASAP 2020 (Micromeritics). All the samples were degassed at 120°C to a constant vacuum (10^{-4} Torr, around 10^{-2} Pa). The specific surface area was determined by the BET method. The total pore volume, V_{TOT}, was calculated from the last point of the isotherms based on the volume of adsorbed nitrogen. The micropore volume, V_M, and the pore size distribution were calculated using the nonlinear density functional theory, 2D-NLDFT, which assumes the heterogeneity of the pore sizes (Jagiello, 2012; Jagiello and Olivier, 2013a, 2013b).

ThermoGravimetric (TG) and Differential TG (DTG) curves were measured on a Q600 thermal analyser (TA Instruments). The samples were heated up to 1000°C at a rate of 10°C min^{-1} in He flow (100 mL min^{-1}). The *m*/*z* thermal profiles of the exhausted gases/vapours, for *m*/*z* 17 (NH_3), 18 (H_2O), 28 (CO), 29 (HCO), 30 (HCHO/NO), 44 (CO_2) and 48 (SO) were collected using a mass spectrometer (MS, Omnistar GSD 320, Pfeiffer Vacuum).

Potentiometric titration of samples was performed on an 888 Titrando automatic titrator (Metrohm). A mass of 0.1 g of carbon textiles was placed in a vessel and dispersed in $NaNO_3$ 0.1 M solution. The solution was maintained at a constant stirring overnight. The pH was recorded and adjusted to about 3.2 by adding HCl 0.1 M and the suspension was titrated with NaOH (0.1 M) up to pH≈10. The proton binding curves, *Q* (Bandosz et al., 1993), were derived from the titration data. The pK_a distributions (Jagiello, 1994), $f(pK_a)$, of the surface acidic groups were calculated by finding a stable solution of the Fredholm integral

equation that relates Q to f(pK_a). For this, the SAIEUS procedure was used (Jagiello et al., 1994).

XPS analyses were performed on virgin carbon cloths by means of a Multi-Chamber Analytical System (PREVAC) with monochromatic 450 W Al Kα X-ray radiation source (1486.6 eV) (Gammadata Scienta). The vacuum in the analysis chamber was 8×10^{-9} Pa. The Binding Energy (BE) scale was referenced against C 1*s*=284.7 eV line. Deconvolutions of the spectra were done using MultiPak software. XPS analyses on virgin granular activated carbons were carried out by Physical Electronics PHI 5000 VersaProbe II spectrometer with a monochromatic Al Kα (1486.6 eV) radiation operating at 15 kV and 50 W. Prior to analysis, all the samples were outgassed until 10^{-8} Torr (around 10^{-6} Pa) at room temperature. High-resolution spectra of powdered samples were detected with the constant pass energy values of 29.35 eV, and a 200 μm diameter analysis area with a take-off angle of 45°, 117.4 eV pass energy, was used for the survey spectra. The detailed amounts of each element were calculated from the individual spectra. The spectrometer energy scale was calibrated using Cu $2p_{3/2}$, Ag $3d_{5/2}$, and Au $4f_{7/2}$ photoelectron lines at 932.7, 368.3, and 84.0 eV, respectively. The SmartSoft-VP2.6.3.4 software package was used for acquisition and data analysis, and MultiPak software was used to fit photoelectron spectra. A Shirley-type background was subtracted from the signals, and recorded spectra were fitted using Gauss–Lorentz curves in order to determine the binding energy of the different element core levels.

2.2.3 Adsorption test ring and tests

Adsorption of HCHO under dynamic conditions was carried out at ambient pressure and T=25°C. Fig. 2.3 shows a schematic representation of the experimental apparatus.

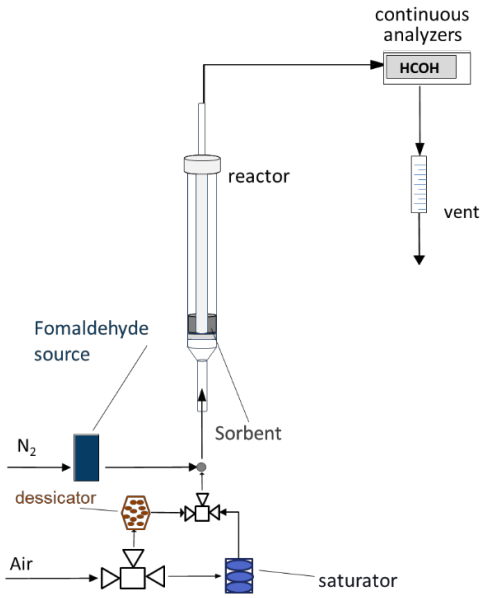

Fig. 2.3. Schematic representation of the HCHO adsorption plant.

A glass column of ID=9 mm was filled with 130 mg of carbon textiles cut in little pieces, or the same amount of PSC (1–2 mm in size). The adsorbent mass was instead 300 mg for the activated carbons (functionalised and not).

Formaldehyde was generated by a calibrated formaldehyde permeation tube (Metronics, Inc.) using a Dynacalibrator (Model 150, Metronics, Inc.) operated at 8°C with 100 mL min^{-1} nitrogen as carrier gas. The outlet flow from the generator, before reaching the testing column, was mixed with 400 mL min^{-1} of air, dry (passing through $CaSO_4$ to totally remove any humidity) or moist of 70% humidity (passing through a water bed). The inlet flow rate of gas was equal to 500 mL min^{-1}, the inlet concentration of formaldehyde (C_{HCHO}^{in}) was set to 1 ppm. Before running experiments in the moist conditions, the adsorbent bed was prehumidified for 1 h with moist air (500 mL min^{-1}). The samples after exposure to moist air were weighted and the weight difference represents the amount of adsorbed water.

The gas analysis was performed with a continuous analyser equipped with an electrochemical sensor (RM 16 Interscan Corporation) with accuracy of 2% of the reading value (working range of analyser: 0–2 ppm of formaldehyde).

The specific adsorption capacity of HCHO at saturation, termed ω_{ads} [mg g^{-1}], was determined through the integration of the area above the breakthrough curve. All the adsorption tests, in the case of granular AC, were stopped at $C_{HCHO}^{OUT}(t)/C_{HCHO}^{IN}$=0.8, where $C_{HCHO}^{OUT}(t)$ is the outlet concentration of formaldehyde. In the case of the carbon textiles, the adsorption tests were stopped at $C_{HCHO}^{OUT}(t)/C_{HCHO}^{IN}$=0.95. These values were arbitrarily chosen for the simulation of near-to-saturation conditions, since the saturation was not reached for some carbons even after very long experimental time.

Chapter 3

Adsorption of H_2S on Zn-Cu modified materials: results and discussion

A portion of this chapter has appeared in print:

1) M. Balsamo, S. Cimino, G. de Falco, A. Erto, L. Lisi. ZnO-CuO supported on activated carbon for H2S removal at room temperature. Chemical Engineering Journal 2016, 304, 399–407. (copyright permission obtained)

2) S. Cimino, L. Lisi, G. de Falco, F. Montagnaro, M. Balsamo, A. Erto. Highlighting the effect of the support during H2S adsorption at low temperature over composite Zn-Cu sorbents. Fuel 2018, 221, 374–379. (copyright permission obtained)

3) G. de Falco, F. Montagnaro, M. Balsamo, A. Erto, F.A. Deorsola, L. Lisi, S. Cimino. Synergic effect of Zn and Cu oxides dispersed on activated carbon during reactive adsorption of H2S at room temperature. Microporous and Mesoporous Materials 2018, 257, 135–146. (copyright permission obtained)

3.1 Results and discussion for alumina sorbents

Table 3.1 shows the BET surface area, total porosity and average pore size for raw and functionalised alumina sorbents.

Table 3.1. BET surface area, total porosity and average pore size for raw Als and Cu_xZn_{1-x}/Als.

Sorbent	BET surface area [$m^2\ g^{-1}$]	Specific pore volume [$cm^3\ g^{-1}$]	Average pore size [Å]
Als	174	0.45	80
$Cu_0Zn_{1.0}$/Als	156	0.37	80
$Cu_{0.05}Zn_{0.95}$/Als	156	0.36	80
$Cu_{0.1}Zn_{0.9}$/Als	157	-	-
$Cu_{0.25}Zn_{0.75}$/Als	157	-	-
$Cu_{0.5}Zn_{0.5}$/Als	157	0.37	80

For sorbents supported on mesoporous alumina, the deposition of active phases determines a slight reduction of the BET surface area with respect to the raw sample. This is in line with the weight increase due to the insertion of 10% wt. of active phase, which causes a decrease in the surface area. Furthermore, the compositions of active phase in terms of Cu/Zn ratio have no effect on the sorbent final properties.

Fig. 3.1 shows the PSD for both raw alumina and $Cu_{0.5}Zn_{0.5}$/Als sorbents.

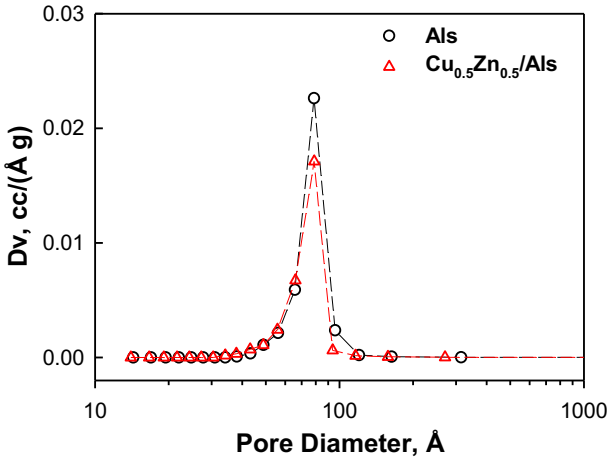

Fig. 3.1. BJH pore size distribution for the raw alumina spheres (Als) and $Cu_{0.5}Zn_{0.5}$/Als sorbent.

The results underline that the functionalisation treatment does not determine great variations in the pore size distribution and only induces a minor reduction of pore volume, thus confirming a homogenous dispersion of the active phases onto the mesoporous alumina.

ICP analysis was carried out to confirm the insertion of the desired percentage of Cu/Zn active phase. The results showed that the overall weight content of Zn+Cu in the active phase is constantly in the range of 8-1–8.4%, in fair agreement with the nominal value of the loaded active phase (10% wt. of ZnO+CuO, corresponding to approximately 8% wt. of metals).

Fig. 3.2 shows the results of SEM-EDX analysis carried out onto $Cu_{0.5}Zn_{0.5}$/Als.

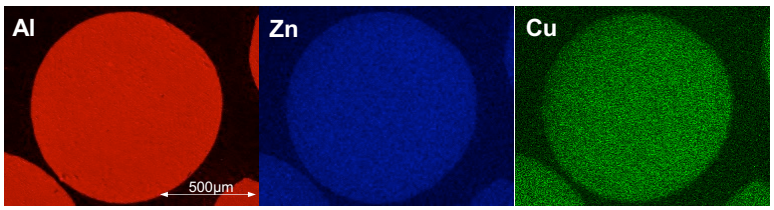

Fig. 3.2. SEM-EDX maps in false colours showing the distribution of the elements (Al, Zn and Cu) across the section of a spherical particle of $Cu_{0.5}Zn_{0.5}$/Als sorbent.

Evidently, the distribution of both elements of the active phase (Zn and Cu) is extremely homogeneous. This confirms that the adopted method of impregnation allows a good penetration of metals in the mesoporous alumina particle.

XRD spectra of virgin raw and functionalised alumina samples, together with the diffraction spectrum of the $Cu_{0.5}Zn_{0.5}$/Als sample after saturation with H_2S at 3000 ppmv and 30°C, are shown in Fig. 3.3. The spectrum of the raw sample is typical of γ-alumina. The XRD patterns for $Cu_0Zn_{1.0}$/Als and $Cu_{0.05}Zn_{0.95}$/Als are equivalent to the one of the parent substrate, probably due to the low content of the active phases flanked with a high dispersion and/or poor crystallinity. Increasing the copper content leads to the formation of two new peaks at 2θ=12.9° and 25.7°, ascribable to $Cu_2(OH)_3NO_3$ (ICDD: 45-594) and to a minor contribution of $Cu(OH)_2$ (ICDD: 42-746). Please note that the presence of Zn hydroxy-nitrate (ICDD: 70-1361) is also possible, being it characterised by a spectrum quite similar to the corresponding Cu phase. For the spent $Cu_{0.5}Zn_{0.5}$/Als sorbent, the Cu-related peaks disappear due to the reaction with H_2S during adsorption though there is no clear evidence of the formation of new crystalline phases, such as ZnS, CuS, $ZnSO_4$, $CuSO_4$.

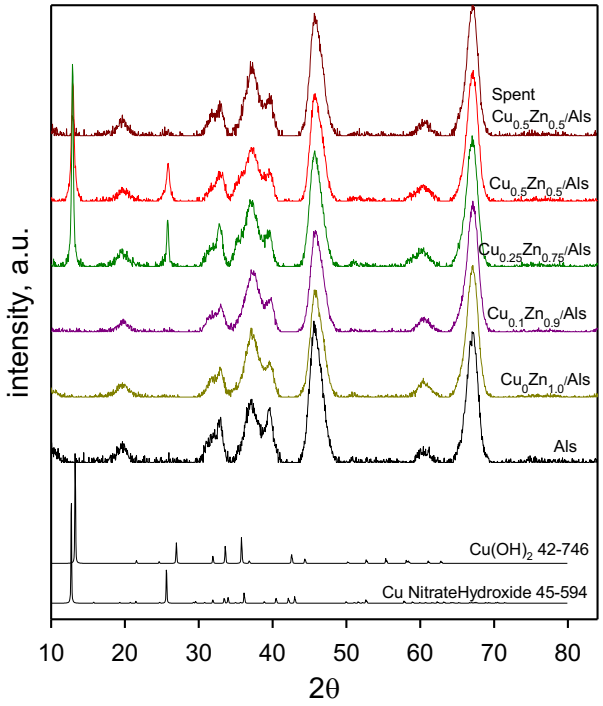

Fig. 3.3. XRD patterns for the raw alumina spheres (Als) and fresh Cu_xZn_{1-x}/Als sorbents. Diffraction spectrum for $Cu_{0.5}Zn_{0.5}$/Als sorbent saturated with H_2S at 3000 ppmv and 30°C, and patterns of $Cu(OH)_2$ and Cu hydroxide nitrate reference compounds, are also shown.

A previous study of Małecka et al. (2015) on the thermal decomposition in air of *d*-metal nitrates supported on alumina, showed that supported copper nitrate started to decompose at ca. 60°C via a multi-step process that was completed for $T \leq 225$°C, whereas its bulk form was slightly more stable and required 250°C to decompose completely. These results contrast ours as it was observed, after the calcination step, the residual presence of copper hydroxy-nitrates on the alumina surface, a feature possibly related to the stabilisation of those solid intermediate species during the drying of sorbents at 120°C. Therefore, tests of TPD of nitrogen oxides (TPD-NO_x) were carried out to verify the residual presence of (hydroxy)nitrates on the functionalised alumina sorbents after calcination. Fig. 3.4

shows the NO_2 and NO concentration profiles for selected alumina-based sorbents under N_2 flux during TPD-NO_x tests.

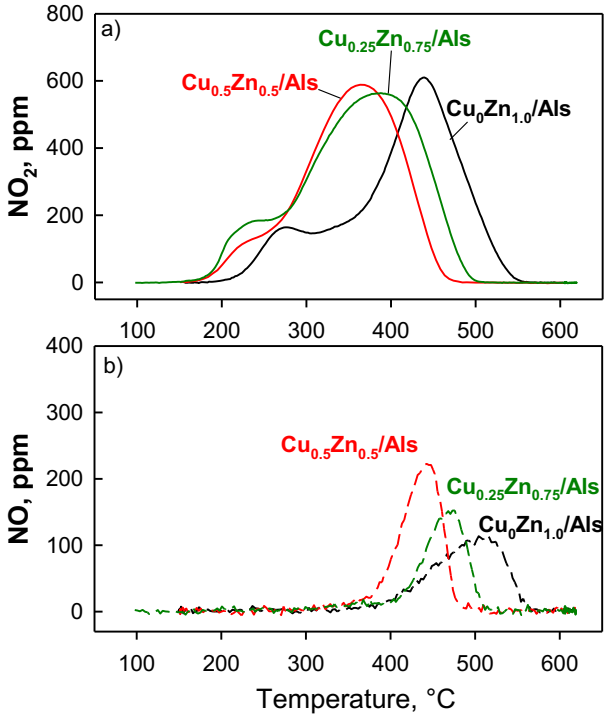

Fig. 3.4. a) NO_2 patterns and b) NO patterns during TPD-NO_x tests for Cu_xZn_{1-x}/Als sorbents after calcination in N_2 at 250°C.

$Cu_0Zn_{1.0}$/Als is characterised by a lower peak centered at 270°C and a second main peak with a maximum at approximately 450°C in the case of the NO_2 desorption pattern. A minor production of NO is also detected (peak at 510°C). The presence of copper in the active phase determines a clear shift of TPD-NO_x profiles towards lower temperatures together with a broadening of the main NO_2 peak, likely ascribable to the overlapping of signals associated with the decomposition of Zn and Cu (hydroxy)nitrates. The experimental observations indicate incomplete decomposition of copper and zinc nitrate precursors under the adopted calcination conditions, and display a significantly higher materials

stability than previously reported, requiring temperatures in excess of 350°C and 450°C, respectively, for them to be fully decomposed.

Fig. 3.5 reports the adsorption breakthrough curves at 3000 ppmv of H_2S and 30°C obtained for Cu_xZn_{1-x}/Als and Als raw sorbents. Values of breakpoint time t_{br} (for which $C_{H_2S}^{out}/C_{H_2S}^{in}$≈0.05) and saturation adsorption capacity ω_s determined from dynamic concentration profiles are summarised in Table 3.2.

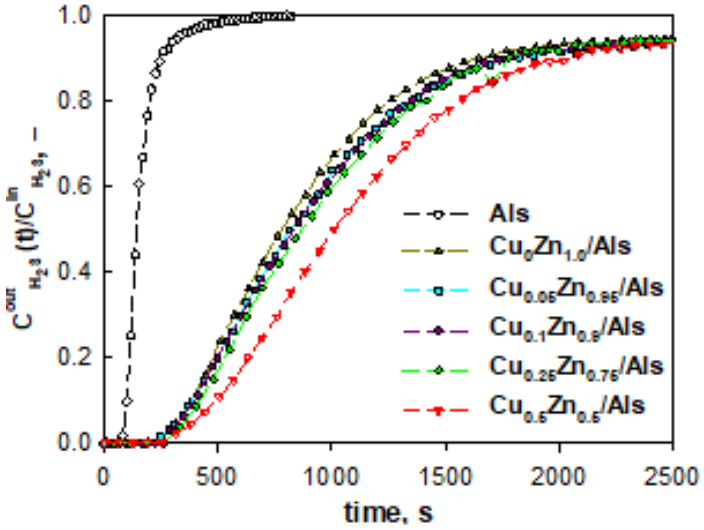

Fig. 3.5. H_2S breakthrough curves for Cu_xZn_{1-x}/Als sorbents and raw alumina. Inlet conditions: $C_{H_2S}^{in}$ =3000 ppmv, T=30°C, P=1 bar.

The results clearly show that the functionalised sorbents are characterised by a significantly higher breakpoint time than the raw alumina, and that the performance improvement is monotonic with the Cu content in the active phase under the investigated compositional range: in fact, the higher the Cu content from $Cu_0Zn_{1.0}$/Als to $Cu_{0.5}Zn_{0.5}$/Als, the lower the position of the breakthrough curves, to indicate a better adsorption performance (*vide etiam* Table 3.2). This result is consistent with similar works in the literature, in which the presence of a second metal in a metal oxide matrix was proved to improve the activity of the single metal oxides (Montes et al., 2013; Elyassi et al., 2014). More in detail, for $Cu_{0.5}Zn_{0.5}$/Als sorbent the adsorption capacity is 9 times greater than that

corresponding to raw alumina, while $Cu_0Zn_{1.0}$/Als exhibits a ω_s value 7.5-folds the one retrieved for Als. The increase in the adsorption capacity along with the copper content, concerning the Cu_xZn_{1-x}/Als sorbents, could be partially ascribable to the formation of Cu hydroxide and hydroxy-nitrate species which are able to determine, with respect a material where only Zn was present (namely, without any Cu), a better reactivity, though these species could be in general less reactive than copper oxides-based species. The occurrence of Cu hydroxide and hydroxy-nitrate species is testified by a comparison of XRD patterns of the $Cu_{0.5}Zn_{0.5}$/Als sorbent before and after adsorption (cf. Fig. 3.3). The effect of the functionalisation can be observed also in terms of breakpoint time, which increases from 65 s for raw alumina to 293 and 362 s, respectively, for the $Cu_0Zn_{1.0}$/Als and $Cu_{0.5}Zn_{0.5}$/Als sorbents. Finally, it should be observed that raw alumina shows a significantly steeper slope of the breakthrough curves with respect to the functionalised sorbents. Hence, it can be hypothesised that the chemical reaction of the pollutant with the active phases and the diffusion of the former in the shell of product (e.g. sulphides) cause a considerable reduction of the rate of the capture process.

TPD tests were carried out in order to study the type of products formed during the capture process and the thermal regenerability of functionalised sorbents. All Cu_xZn_{1-x}/Als sorbents released non-negligible amounts of H_2S, but the total quantity of sulphur desorbed as H_2S compared to SO_2 was much lower (at least one order of magnitude). Consequently, it is confirmed that the capture process involved a minor contribution of physical adsorption (release of H_2S) coupled with reactive adsorption (release of SO_2).

Table 3.2. Adsorption (ads)/desorption (des) performances of the tested samples.

Sorbent	t_{br} [s]	$\omega_{s,ads}$ [mmol g^{-1}]	$\omega_{s,des}^{600°C}$ [mmol g^{-1}]	$\omega_{s,des}^{800°C}$ [mmol g^{-1}]	$\omega_{s,des}^{TPO}$ [mmol g^{-1}]
Als	65	0.09	0.09	0.09	–
$Cu_0Zn_{1.0}$/Als	293	0.68	0.24	0.58	–
$Cu_{0.05}Zn_{0.95}$/Als	296	0.69	0.28	0.58	–
$Cu_{0.1}Zn_{0.9}$/Als	293	0.73	0.25	0.58	–
$Cu_{0.25}Zn_{0.75}$/Als	326	0.74	0.25	0.62	–
$Cu_{0.5}Zn_{0.5}$/Als	362	0.82	0.38	0.74	0.33[a]

[a]TPO test performed adopting 5000 ppmv of O_2 in N_2.

The SO_2 TPD profile obtained for $Cu_{0.5}Zn_{0.5}$/Als is characterised by various decomposition peaks starting from 80°C and occurring in the whole temperature range investigated. The main signal of SO_2 pattern is in the temperature range of 500–800°C, and it can be related to the partial decomposition of copper and zinc sulphates, as suggested by the comparison of reference bulk materials (Fig. 3.6).

The formation of oxidised products of H_2S (e.g. SO_2, copper and zinc sulphates) can be related by the presence of various oxygen sources present in the sorbent, including Cu/Zn (hydro)oxides, metal (hydroxy)nitrates and surface hydroxyl groups of the alumina substrate, and it can occur in absence of molecular oxygen during the reactive capture process and/or the thermal treatment stage. The TPD signal at temperature lower that 500°C can be attributed to the desorption of SO_2 formed in the capture stage or produced during the thermal treatment by oxidation of more reduced S species (such as sulphides or elemental sulphur).

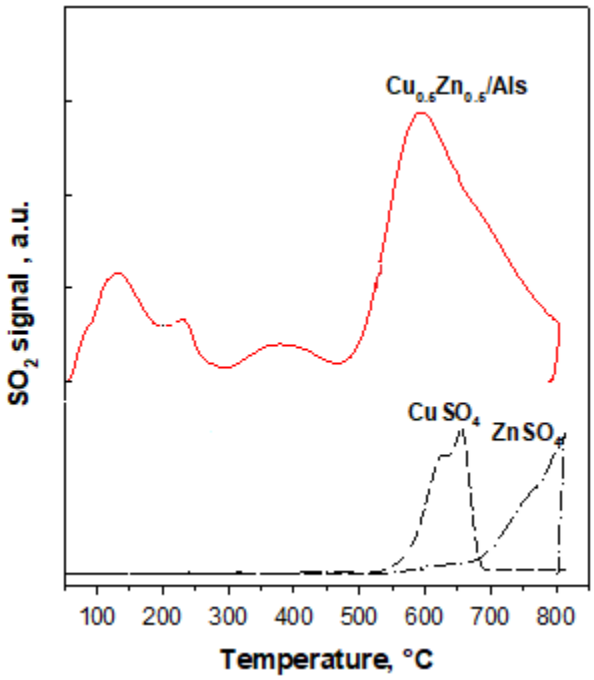

Fig. 3.6. SO_2 release from spent $Cu_{0.5}Zn_{0.5}$/Als previously saturated with H_2S (3000 ppmv in N_2, *T*=30°C, *P*=1 bar) during TPD tests under N_2 flow. SO_2 TPD profiles for reference samples of $CuSO_4$ and $ZnSO_4$ in bulk are also included for comparison purposes.

As an example, Wang et al. (2017) observed the formation of $CuSO_4$ by XPS analyses for spent CuO dispersed onto 3DOM sorbents. Table 3.2 reports the sulphur released during TPD analysis under N_2 flow ($\omega_{s,des}$) obtained by the integration of the corresponding TPD profiles. All the materials released about 80–90% of the adsorbed H_2S after the thermal treatment at 800°C, and $\omega_{s,des}^{800°C}$ generally increases along with the copper content, in good agreement with the easier thermal decomposition of bulk $CuSO_4$ with respect to $ZnSO_4$. It is important to underline that, in order to prevent a significant formation of metal aluminates, the thermal treatment should be limited at 600°C but, in this way, only half of the sulphur content can be removed from the best performing $Cu_{0.5}Zn_{0.5}$/Als sorbent, and even less from Zn-richer materials ($\omega_{s,des}^{600°C}$), once again due to the stability of the corresponding metal sulphates.

Fig. 3.7 shows the results of TPO tests in presence of 5000 ppmv of O_2 in N_2 or in air, and the results of the TPD test carried out on the spent $Cu_{0.5}Zn_{0.5}$/Als sample.

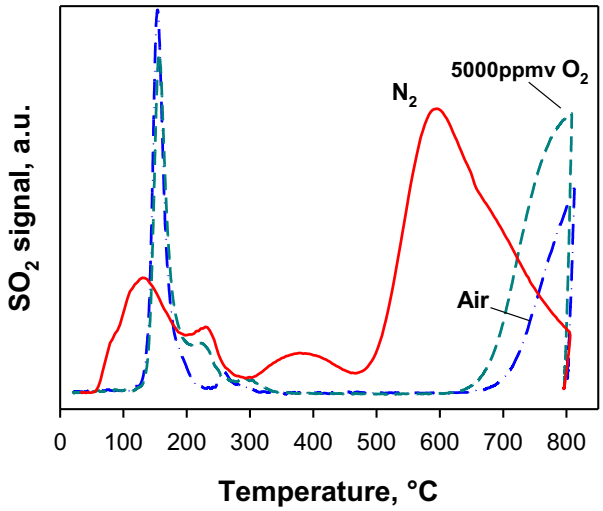

Fig. 3.7. SO_2 release from H_2S-saturated $Cu_{0.5}Zn_{0.5}$/Als during TPD and TPO tests (run under 5000 ppmv of O_2 in N_2 or under air flow).

The results clearly show that the presence of O_2 in the desorbing gas causes a decrease of SO_2 released from the samples and the effect is more pronounced for an increase in the oxygen concentration. The significant differences among the three thermal treatments are evident on the high temperature band ($500<T<800$°C) due to the presence of oxygen that thermally delays the decomposition of sulphates (with an onset temperature shifted towards 700°C), being themselves among the decomposition products (Małecka et al., 2015). Additionally, the formation of more thermally stable products due to the reaction of sulphates with the alumina substrate under oxidising conditions cannot be ruled out. The results are confirmed by the comparison between the values of $\omega_{s,des}^{TPO}$ and $\omega_{s,des}^{800°C}$: the amount of sulphur released is more than halved in the case of TPO tests (Table 3.2). The formation of sulphates and the stabilisation of the active phases is confirmed by DRIFT analysis. In Fig. 3.8, DRIFT spectra of fresh and spent $Cu_0Zn_{1.0}$/Als and $Cu_{0.5}Zn_{0.5}$/Als sorbents, $ZnSO_4$ and $CuSO_4$ are reported.

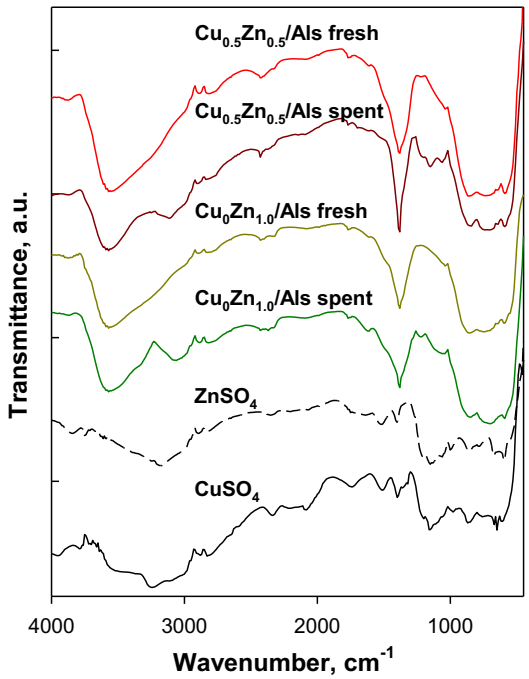

Fig. 3.8. DRIFT spectra of fresh and spent Cu_xZn_{1-x}/Als sorbents and of bulk $CuSO_4$ and $ZnSO_4$ reference compounds.

For the fresh sorbents, it is possible to observe a large band at 3500–3600 cm^{-1}, typical of hydroxyls of hydrated alumina (Al-Abadleh and Grassian, 2003), and a sharp band at 1385 cm^{-1}, assigned to nitrate species (Miller and Wilkins, 1952) and confirming that the calcination temperature (250°C) was not high enough to completely decompose nitrates from precursors salts, in agreement with XRD and TPD-NO_x results. Nevertheless, the nitrate band is also ascribable to aluminium nitrate (Myronyuk et al., 2016) and well matches with the good stability of this compound which turns into aluminium oxide only at T>350°C. In the case of spent sorbents, the nitrate band appears almost unchanged, whereas new signals appear in the 1050–1200 cm^{-1} region, quite strong for the sorbent with 50% Zn substitution for Cu but weak for $Cu_0Zn_{1.0}$/Als, that can be reasonably attributed to the formation of sulphate groups on metals (Miller and Wilkins, 1952) but also on the alumina support (Saur et al. 1986, Kloprogge et al., 2001).

This band is typical of both sulphate reference compounds, and its low intensity in the spectrum of spent $Cu_0Zn_{1.0}$/Als sorbent suggests that the formation of copper sulphate prevails. Nevertheless, some sulphation of alumina surface cannot be ruled out (Kloprogge et al., 2001). For both the spent sorbents, a new band is superimposed to that corresponding to alumina hydroxyls in the region 3000–3700 cm^{-1}, being centred at 3065 cm^{-1} for $Cu_0Zn_{1.0}$/Als and at 3110 cm^{-1} for $Cu_{0.5}Zn_{0.5}$/Als, respectively. Reference $CuSO_4$ and $ZnSO_4$ show bands in the same region: basic copper sulphate monohydrate provides signals at 3300–3400 cm^{-1} (Uzunov et al., 1995), whilst a band centered at 3072 cm^{-1} is attributed to the symmetric stretching mode of water molecule for $ZnSO_4 \cdot 7H2O$ (Saha and Podde, 2011), thus confirming that some zinc sulphate is also formed upon H_2S adsorption. These results generally demonstrate that the copper and zinc sulphate formation occurs directly by oxidation of H_2S during the capture process when alumina is used as support for mixed Cu–Zn active phases.

3.2 Results and discussion for activated carbon sorbents

Table 3.3 lists the main textural properties for virgin and spent raw activated carbon and functionalised sorbents, while in Fig. 3.9 it is shown the PSD of four functionalised sorbents before and after H_2S adsorption tests performed at $C_{H_2S}^{in}$=3000 ppmv and T=30 °C and in the case of adsorption stopped at 90% of saturation at $C_{H_2S}^{in}$=100 ppmv, T=30°C, relative humidity RH=48% and $C_{O_2}^{in}$=2500 ppmv. Textural features of the pristine activated carbon are also included for comparison.

The raw AC shows a BET surface area of 641 $m^2\ g^{-1}$ and it is characterised by the presence of both micro- and mesoporosity. The functionalised samples show a decrease in the surface area down to an average of 550 $m^2\ g^{-1}$. This value could be ascribed to the negligible contribution to the total surface area of the active phase (accounting for ca. 12.7% of the sorbent weight), and the results confirm that the preparation technique allowed obtaining a high dispersion of the metal oxides onto the carbonaceous support. From the analyses of the PSD (Fig 3.9, data collected from 6 Å on), it is possible to observe a different effect of the

active phase composition on the pore texture of the carbonaceous support. In particular, for the sorbents Zn-rich (Zn/AC and $Cu_{0.05}Zn_{0.95}$/AC), it is observed a loss of porosity compared to the raw AC in the region of ultramicropores (<10 Å). Differently, in the case of $Cu_{0.5}Zn_{0.5}$/AC, a micropore size distribution comparable with that for raw AC is observed, whereas a negligible reduction of mesoporosity in the range 26–33 Å was detected. Cu/AC shows a similar PSD in the range of micropores with respect to raw AC, while the deposition of CuO resulted in an evident reduction in the mesopores size range. Consequently, it is possible to suggest that the ZnO and CuO active phases are characterised by a different tendency to be preferentially dispersed onto the surface of micro- and mesopores, respectively.

Table 3.3. Microstructural parameters of fresh and spent samples.

Sorbent	Specific surface area S_{BET} [m^2 g^{-1}]	Total pore volume V_{TOT} [cm^3 g^{-1}]	Micropore volume V_M [cm^3 g^{-1}]
Fresh sorbents			
AC raw	641	0.81	0.23
Zn/AC	558	0.80	0.19
$Cu_{0.05}Zn_{0.95}$/AC	520	0.72	0.18
$Cu_{0.1}Zn_{0.90}$/AC	549	0.76	0.19
$Cu_{0.25}Zn_{0.75}$/AC	555	0.76	0.19
$Cu_{0.5}Zn_{0.5}$/AC	570	0.76	0.20
Cu/AC	559	0.67	0.22
Spent sorbents			
AC raw	604	0.76	0.23
Zn/AC	330	0.54	0.13
$Cu_{0.05}Zn_{0.95}$/AC	327	0.53	0.12
$Cu_{0.5}Zn_{0.5}$/AC	348	0.55	0.13
$Cu_{0.5}Zn_{0.5}$/AC[a]	555	0.76	0.20
$Cu_{0.5}Zn_{0.5}$/AC[b]	441	0.66	0.15
$Cu_{0.5}Zn_{0.5}$/AC[c]	254	0.47	0.10
Cu/AC	426	0.58	0.16
Cu/AC[c]	361	0.55	0.14

[a]After saturation at $C_{H_2S}^{in}$=3000 ppmv, T=30°C.

[b]After adsorption run stopped at ω≈0.3 mmol g^{-1} (inlet conditions $C_{H_2S}^{in}$=100 ppmv, T=30°C).

[c]After adsorption run stopped at 90% of saturation at $C_{H_2S}^{in}$=100 ppmv, T=30°C, RH=48% and $C_{O_2}^{in}$=2500 ppmv.

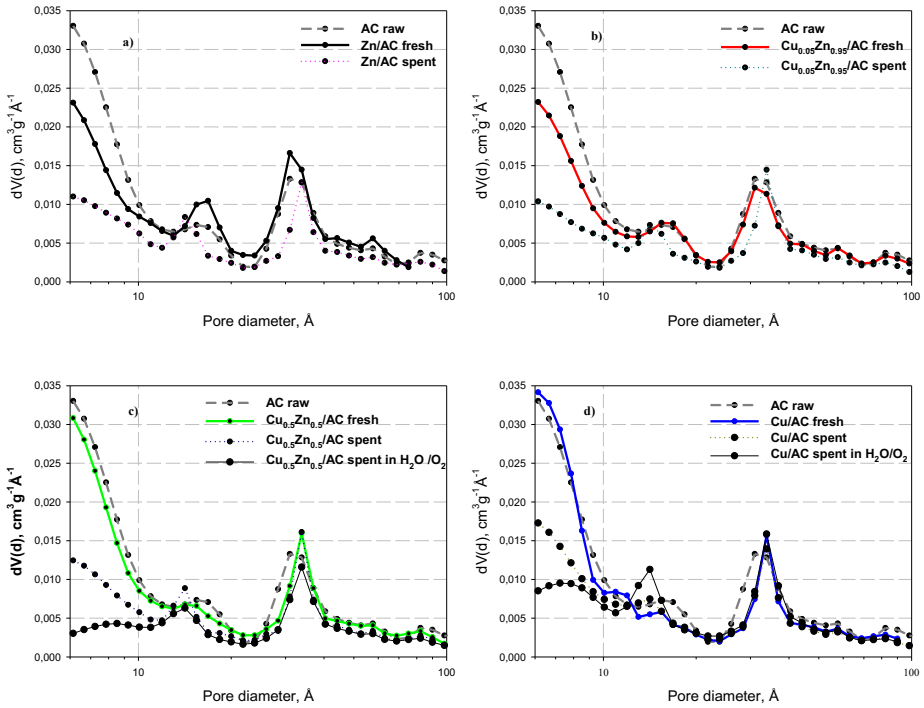

Fig. 3.9. Pore size distributions (PSD) of functionalised sorbents before and after saturation with $C_{H_2S}^{in}$=3000 ppmv in N_2, and after adsorption stopped at 90% of saturation in $C_{H_2S}^{in}$=100 ppmv, *RH*=48% and $C_{O_2}^{in}$=2500 ppmv in N_2, *T*=30°C: a) Zn/AC, b) $Cu_{0.05}Zn_{0.95}$/AC, c) $Cu_{0.5}Zn_{0.5}$/AC, d) Cu/AC. PSD of virgin AC also included for comparison.

In the case of spent samples after adsorption of H_2S at 3000 ppmv in inert flux, all sorbents show a significant reduction of surface area and porosity due to the formation and accumulation of various S-bearing substances. The Zn-rich sorbents display an evident and similar loss of surface area (–40%) due to an occlusion of micropores and a partial occlusion of their smallest mesopores. On the other hand, the spent Cu/AC material retained higher values of S_{BET} (426 m^2 g^{-1}) and V_M due to a larger residual microporosity and to an almost unaffected network of mesopores (Fig. 3.9d). After adsorption of H_2S at 100 ppmv in humid condition (*RH*=48% and $C_{O_2}^{in}$=2500 ppmv), $Cu_{0.5}Zn_{0.5}$/AC and Cu/AC show a higher reduction of surface area with respect to the other saturated sorbents. More

specifically, the BET surface area decreases of 65 and 35% for $Cu_{0.5}Zn_{0.5}$/AC and Cu/AC, respectively, when compared with the BET surface area of the virgin sample. This loss of surface area is mainly due to the occlusion of micropores (cf. V_M in Table 3.3 and Fig. 3.9c-d). Finally, it is obtained the restoring of the textural parameters of $Cu_{0.5}Zn_{0.5}$/AC after spent sample water washing for 5 h. This result indicates that the water-soluble species (sulphates) are the main responsible for the partial occlusion of sample porosity upon the reactive adsorption of H_2S. This is consistent with the much larger ratio of molar volumes for zinc and copper sulphates with respect to their corresponding oxides (average value=3.3), which largely exceeds the corresponding one for zinc and copper sulphides/zinc and copper oxides (average value=1.7) (Green and Perry, 2008).

ICP-MS analysis of metals on the functionalised sorbents confirms the content of Cu+Zn in the range 10.0±0.5% wt., in good agreement with the target loading. Slight variations can be ascribed to the effect of the thermal treatment of the impregnated sorbent as shown in Fig. 3.10, that presents the temporal profiles of evolved gas species CO_2, CO and NO during the initial phase of the calcination step for $Cu_{0.5}Zn_{0.5}$/AC sample. The temperature of the oven was initially set at ca. 100°C before ramping up to 250°C and holding for 3 h. NO emission deriving from decomposition of nitrate species started at temperatures ≥120°C and rapidly increased, and at the same time a significant production of CO_2 (accompanied by some CO) was observed, with a rather sharp peak followed by a long tail. Correspondingly, the temperature inside the reactor showed a rapid increase up to a peak level of ca. 320°C, thus exceeding the preheating level imposed by the external oven (≤250°C). These results clearly indicate that there was a partial combustion of some of the carbon from the support, probably by means of exothermic reactions with the nitrate groups of the precursor salts. This is also testified by the strong transient reduction in the emissions of NO in correspondence to the peak of CO_2.

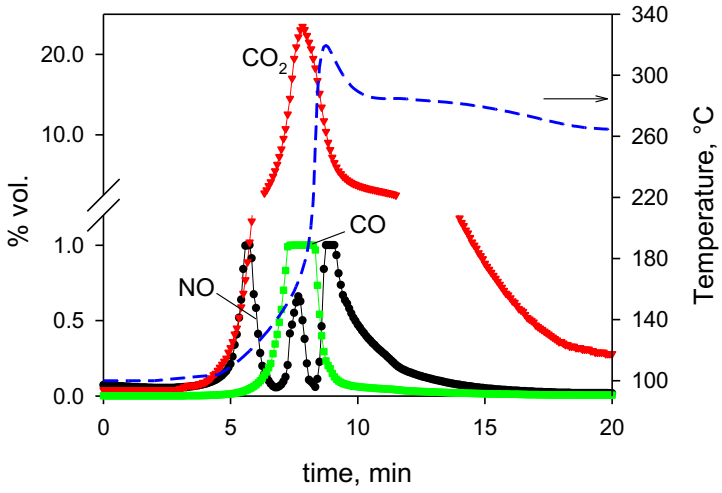

Fig. 3.10. Temporal profiles of CO_2, CO and NO evolved during the initial phase of the heat treatment under N_2 flow used to decompose the metal nitrate precursors impregnated on $Cu_{0.5}Zn_{0.5}$/AC. The blue dashed line represents the temperature in the fixed bed reactor.

TPD-NO_x tests produced flat NO_2 and NO profiles for all the functionalised sorbents after treatment at 250°C under inert atmosphere. Therefore, the decomposition of both Zn and Cu nitrates had been completed at that temperature level, being also favoured by the reaction with the activated carbon support, as previously mentioned. Moreover, ICP-MS analysis shows the presence of impurities due to the content of ashes in the activated carbon, mainly consisting of Si=0.8% wt., Al=0.7% wt., Na=0.6% wt. and Ca=0.5% wt.

Fig. 3.11 shows a typical SEM image of a sectioned granule of $Cu_{0.5}Zn_{0.5}$/AC sorbent together with the corresponding distribution map of Zn and Cu as obtained by EDX analysis. It is possible to observe that the distribution of zinc is homogeneous throughout the sorbent particle, while the distribution of copper is less homogeneous and presents a moderate tendency to accumulate on its outer shell. This result can be related to a lower decomposition temperature of copper nitrate, starting simultaneously to dehydration at around 100°C, with a possible associated transport of copper towards the particle external surface. In

contrast, the decomposition of Zn nitrate occurs at appreciable rates only above 175°C, i.e. when dehydration is over (Małecka et al., 2015).

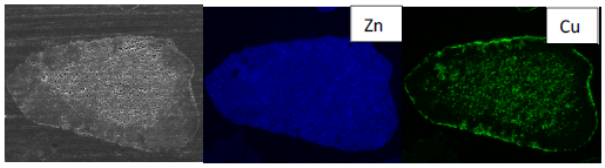

Fig. 3.11. SEM image of a sectioned particle of $Cu_{0.5}Zn_{0.5}$/AC sorbent and corresponding EDX maps in false colours showing the distribution of elements (Zn and Cu) of the active phase.

Fig. 3.12 shows the SEM images of a sectioned granule of saturated $Cu_{0.5}Zn_{0.5}$/AC sorbent, together with the corresponding distribution map of Zn, Cu and S determined by EDX analysis. Sulphur-containing species were homogeneously distributed throughout the sorbent particles along the radial coordinate. Noteworthy, the capture process did not affect the distribution of active elements (Zn, Cu) with respect to the virgin samples (cf. Fig. 3.11). It is important to underline that the high dispersion of the active phases in nano-size form allows the accessibility of H_2S molecules to the entire pore network.

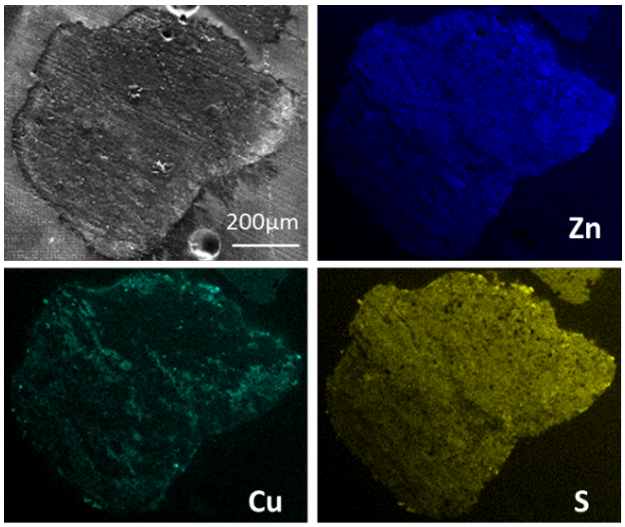

Fig. 3.12. SEM and EDX micrographs for particles (cross-section) of $Cu_{0.5}Zn_{0.5}$/AC spent sorbent (Zn, Cu and S distribution). Adsorption stage performed at $C_{H_2S}^{in}$=3000 ppmv in N_2, T=30°C.

Fig. 3.13 displays the DRIFT spectra for fresh Zn/AC and $Cu_{0.5}Zn_{0.5}$/AC sorbents as well as for the same samples after saturation with H_2S in N_2 at 30°C; the spectrum corresponding to the raw activated carbon support is also shown for comparison. Spectra of fresh and spent samples are very similar, all displaying a weak carbonate band in the 1580–1460 cm^{-1} region. The band in the 1450–1250 cm^{-1} region, present in the spectrum of raw activated carbon, disappeared in the spectra of all the functionalised samples. This band can be assigned to overlapping signals of carboxyl-carbonates and C-H symmetric and asymmetric vibration (Biniak et al., 1997; Tongpoothorn et al., 2011).

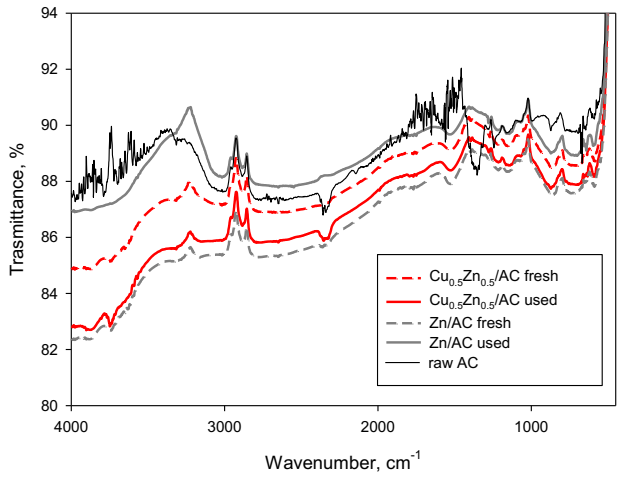

Fig. 3.13. DRIFT spectra for fresh and saturated Zn/AC and $Cu_{0.5}Zn_{0.5}$/AC sorbents compared with that of raw AC (the last showing noise due to its inherent structure).

Its disappearance suggests that those surface functional groups were likely involved in the metal oxides grafting and/or were removed during the thermal treatment performed to decompose the nitrate precursors. In fact, no nitrate bands were found in the spectra of functionalised sorbents, suggesting a complete decomposition of the precursor salts, in agreement with XRD results (*vide infra*). The possible presence of sulphate groups on metals, expected in the 1050–1200 cm^{-1} region (Miller and Wilkins, 1952), was not well detectable due to the occurrence of spectral vibration of activated carbon in the same range of frequency.

Fig. 3.14 show the XRD patterns for the raw Darco AC and the Cu_xZn_{1-x}/AC sorbents, restricted to the 2θ range of 30–60°. All sorbents showed characteristic peaks due to crystalline quartz (Powder Diffraction File, PDF 5-490), a typical impurity in activated carbons deriving from lignite. After the functionalisation, the main peaks of quartz became sharper, indicating an increase in the dimension of the crystallites due to the thermal treatment at 250°C.

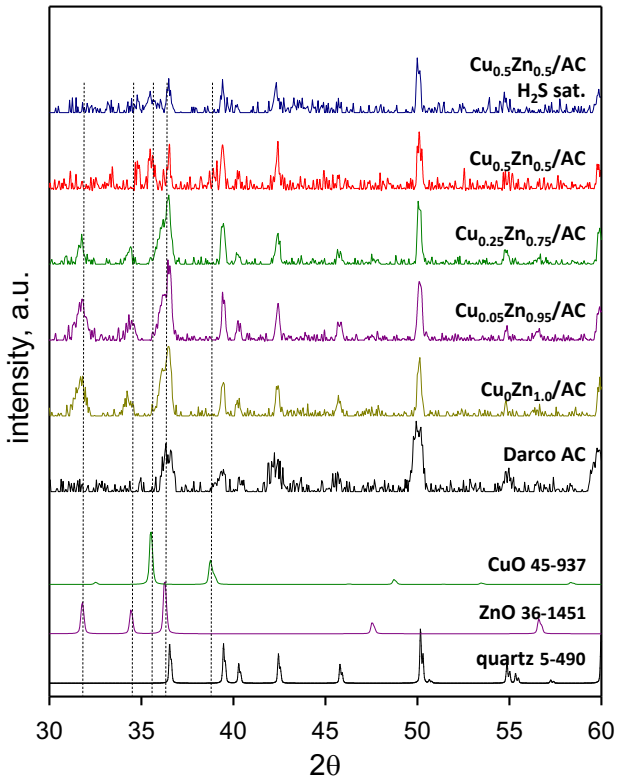

Fig. 3.14. XRD patterns for raw Darco AC (showing noise due to its inherent structure) and fresh Cu_xZn_{1-x}/AC sorbents. The spectrum of $Cu_{0.5}Zn_{0.5}$/AC sorbent saturated with H_2S at 3000 ppmv and 30°C is also shown. Reference patterns for CuO (PDF 45-937), ZnO (PDF 36-1451) and quartz (PDF 5-490) are included for comparison.

A closer inspection of XRD patterns of Cu_xZn_{1-x}/AC sorbents revealed low intensity peaks corresponding to the main reflections of zinc oxide at 2θ=31.8, 34.4 and 36.2° (PDF 36-1451). The intensity of these peaks progressively decreased according to the reduction in the Zn content of the sorbents. In parallel, two small peaks at 2θ=35.5 and 38.8° appeared by increasing the copper content in the active phase above 25%, likely ascribable to the reflection of copper oxide (PDF 45-937). These peaks were slightly more evident in the $Cu_{0.5}Zn_{0.5}$/AC sorbent. The rather small and broad peaks of ZnO and CuO suggest that the typical dimensions of the crystallites are in the order of few nanometers, which is a highly

desirable feature for an effective exploitation of the active phase in the H_2S capture process.

Fig. 3.14 also reports the XRD pattern for the $Cu_{0.5}Zn_{0.5}$/AC sorbent after saturation with H_2S at 3000 ppmv and 30°C: the peaks of ZnO completely disappeared (particularly the one at 2θ=31.8°), while there was a low residual signal in the main zone of CuO (at 2θ=35.5°). Moreover, there was no clear evidence of the formation of new crystalline phases, such as ZnS and CuS or the corresponding metal sulphates. This was confirmed by the DRIFT spectra of spent sorbents (Fig. 3.13), which did not show any new bands compared to those of fresh samples.

Functionalised sorbents and their parent support are firstly tested at a high concentration of H_2S (i.e. 3000 ppmv), and their breakthrough curves are reported in Fig. 3.15. From the breakthrough curves, the dynamic data and the corresponding adsorption capacities were determined according to Eq. (2.1). The results are summarised in Table 3.4. The $\omega_{s,ads}$ values determined by Eq. (2.1) were further checked by elemental analysis of S-content in the spent sorbents (Table 3.4), and the results corresponded to within ±10%.

Cu_xZn_{1-x}/AC sorbents showed a significantly longer breakpoint time t_{br} than their AC support, despite the experimental tests were run with only half of the sorbent mass. In particular, the breakpoint time increased monotonically with the Cu content in the series of mixed oxide sorbents. The outlet H_2S concentration pattern for Darco AC after t_{br} showed a steep slope and a rather short tail, corresponding to a rapid saturation of the sorbent. On the other hand, all the functionalised sorbents showed a slower saturation, testified by less steep profiles and significantly longer tails, which could be ascribed to the arising of many phenomena during H_2S capture (*vide infra*). Zn/AC and Cu/AC samples showed comparable breakpoint times, significantly shorter with respect to figures obtained for sorbents composed by mixed oxides. These results demonstrate that the adsorption capacity did not monotonically increase with copper content and indicate a synergic effect between CuO and ZnO, hence determining a more efficient exploitation of the active phases in the H_2S capture process. In particular,

an equimolar mixture of the oxides represented the optimal composition among those investigated.

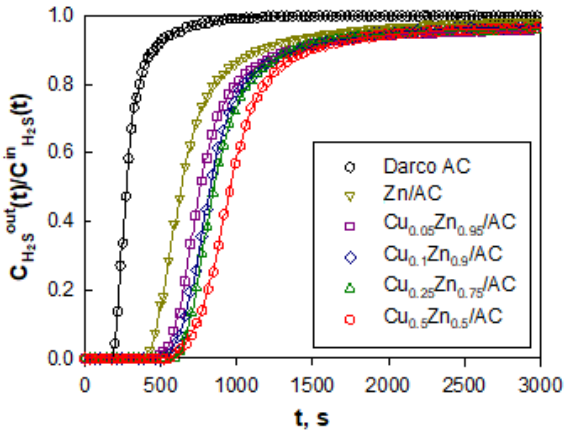

Fig. 3.15. H_2S breakthrough curves for Cu_xZn_{1-x}/AC sorbents (mass: 2.5 g) and the raw Darco AC support (mass: 5 g). Inlet conditions: $C^{in}_{H_2S}$=3000 ppmv, T=30°C, P=1 bar.

Noteworthy, literature studies focusing on Cu-doped ZnO sorbents for H_2S reactive adsorption commonly ascribe the positive role of copper in enhancing the conversion degree of zinc oxide to reduced diffusional limitations in the ZnS product layer with a transition from an outward (for pure ZnO) to inward (for Cu-doped ZnO) growth mechanism (Yang and Tatarchuk, 2010; Bezverkhyy et al., 2012; Elyassi et al., 2014).

Table 3.4. Adsorption performances for AC raw and Cu_xZn_{1-x}/AC sorbents, and S content in spent samples. Sorbent mass: 2.5 g. Inlet conditions: [H_2S]=3000 ppmv in N_2, T=30°C, P=1 bar. For $Cu_{0.5}Zn_{0.5}$/AC, H_2S adsorption tests were also repeated with 40% vol. of either CO_2 or CH_4 in the feed.

Sorbent	t_{br} **[s]**	$\omega_{s,ads}$ **[mmol g^{-1}]**	**S content [% wt.]**	η^b $n_{H2S}/n_{(Cu+Zn)}$ **[–]**	$\omega_{s,des}$ **[mmol g^{-1}]**
AC raw	198[a]	0.20	0.46	–	0.2
Zn/AC	444	0.97	3.40	0.51	0.41
$Cu_{0.05}Zn_{0.95}$/AC	559	1.28	3.66	0.67	0.58
$Cu_{0.1}Zn_{0.9}$/AC	597	1.31	4.00	0.69	0.61
$Cu_{0.25}Zn_{0.75}$/AC	655	1.36	4.03	0.71	0.55
$Cu_{0.5}Zn_{0.5}$/AC	674	1.46	4.69	0.76	0.59
$Cu_{0.5}Zn_{0.5}$/AC[c]	684	1.42	–	0.74	–
$Cu_{0.5}Zn_{0.5}$/AC[d]	503	1.50	–	0.79	–
Cu/AC	429	1.36	–	0.71	0.43

[a]Determined with 5 g sorbent mass.
[b]Calculated subtracting the contribution of the AC support.
[c]Feed containing 40% vol. CH_4.
[d]Feed containing 40% vol. CO_2.

In order to better understand and compare the capture performance, we estimated the active phase utilisation factor, $\eta=n_{H2S}/n_{(Cu+Zn)}$, for functionalised sorbents, corresponding to the molar ratio between the sulphur adsorbed as H_2S and the Cu+Zn content in the sorbent (calculated from ICP elemental analysis). The values of η reported in Table 3.4 were calculated by subtracting the adsorption capacity of the raw support (considering that the weight fraction of the activated carbon in the supported sorbent was ≈0.87, i.e. the complementary to the active phase fraction). The assumption of additive contributions from the substrate and

from the metal oxides to the overall H_2S capture capacity was verified by TPD results (*vide infra*).

The utilisation factor was already above 51% for the sorbent containing only ZnO (i.e. Zn/AC); moreover, even a small amount (5%) of Cu in the active phase formulation enhanced η above 65%. Since the H_2S capture capacity ($\omega_{s,ads}$) progressively increased along with the Cu content, a maximum overall utilisation factor of ca. 76% was estimated for $Cu_{0.5}Zn_{0.5}$/AC.

The significant impact of Cu addition, even at rather low contents, suggested that copper may contrast/reduce the diffusional limitations in the solid state, which are responsible for the low utilisation factors commonly observed in the case of ZnO sorbents (Yang and Tatarchuk, 2010). This is generally attributed to the formation of a compact and thin overlayer (of ZnS) leaving unreacted the underlying core of ZnO (Yang and Tatarchuk, 2010). In fact, it was previously reported that Cu-containing ZnS particles are characterised by a higher mobility of sulphur anions leading to a more rapid exchange with O^{2-} anions due to the presence of sulphur vacancies formed after the charge compensation of Cu^{+} replacing Zn^{2+}, which favours a more rapid growth of ZnS crystallites (Bezverkhyy et al., 2012). Moreover, in our tests we also found evidence for the formation of metal sulphates apart from metal sulphides (*vide infra*), underlying a higher complexity of the surface reactions and of the Cu-doping effect. Finally, the Cu addition could effectively reduce the characteristic dimensions of ZnO crystallites (Baird et al., 1992), thus enhancing their reactivity and utilisation through a higher exposed surface area.

In order to verify the potential competitive adsorption phenomena of CO_2 and CH_4, dedicated H_2S removal tests were performed on $Cu_{0.5}Zn_{0.5}$/AC sorbent with a feed gas also containing 40% vol. of either CO_2 or CH_4 (balance N_2). The corresponding H_2S dynamic adsorption patterns are reported in Fig. 3.16, and compared to the reference case of H_2S in N_2. The characteristic adsorption parameters are collected again in Table 3.4. The presence of CH_4 did not appreciably affected the H_2S adsorption process, as testified by almost overlapped breakthrough profiles and quite similar values of the H_2S saturation adsorption

capacities. On the other hand, the presence of CO_2 determined a shift of the breakthrough profile towards shorter times followed by a longer tail. However, the measured H_2S adsorption capacity at saturation was not significantly altered. These results point to a partial kinetic inhibition effect of the H_2S capture process in the ternary $N_2/CO_2/H_2S$ system, possibly related to the competitive CO_2 adsorption onto active sites present on the carbonaceous surface of $Cu_{0.5}Zn_{0.5}$/AC.

Spent Cu_xZn_{1-x}/AC sorbents, saturated during H_2S capture tests at 3000 ppmv and 30°C, were further subjected to Temperature Programmed Desorption (TPD) tests under N_2 flux up to 620°C, by simultaneously monitoring the evolution of H_2S and SO_2. Interestingly, none of the functionalised sorbents (nor the raw AC) desorbed measurable quantities of H_2S, suggesting a negligible contribution of physical adsorption mechanism under the adopted operating conditions. On the other hand, all the sorbents desorbed significant amounts of SO_2 (Fig. 3.17), confirming that the H_2S reactive capture was coupled with oxidation phenomena.

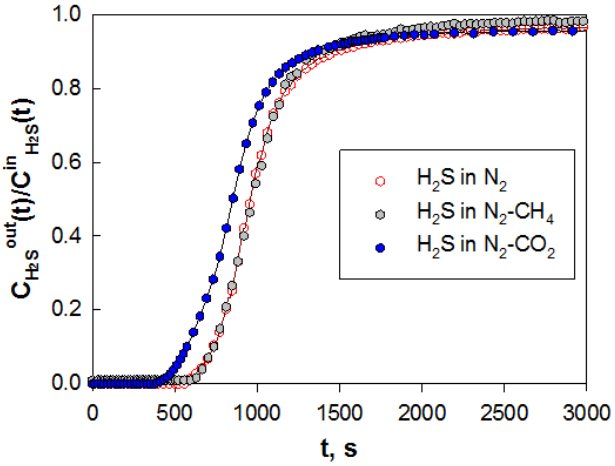

Fig. 3.16. H_2S breakthrough curves for $Cu_{0.5}Zn_{0.5}$/AC sorbent in H_2S/N_2, $H_2S/CO_2/N_2$ and $H_2S/CH_4/N_2$ flux. Inlet conditions: $C_{H_2S}^{in}$=3000 ppmv, $C_{CO_2}^{in}$=40% vol., $C_{CH_4}^{in}$=40% vol., T=30°C, P=1 bar.

In particular, the spent AC showed a single SO_2 peak starting at ca. 170°C and centred at 280°C: this was previously ascribed to the release of SO_2 formed

by oxidation reactions with chemisorbed oxygen or oxygen containing surface groups onto active sites located in small pores of the activated carbon (Bagreev and Bandosz, 2005). The TPD profile for the saturated Zn/AC sorbent showed two main and broad SO_2 emission peaks, respectively centred at ca. 290°C and 500°C. The first, low temperature peak, closely resembled the one observed in the TPD profile of the spent Darco AC. By comparison with the TPD profile of a reference sample prepared by impregnating $ZnSO_4$ on the same activated carbon (reported at the bottom of Fig. 3.17), it was possible to assign the high temperature signal to the decomposition of zinc sulphate. Note that bulk, unsupported $ZnSO_4$ started to decompose releasing SO_2 only at T>700°C (Fig. 3.18), thus revealing a strong interaction effect with the carbon based support that reduced the stability of the sulphate.

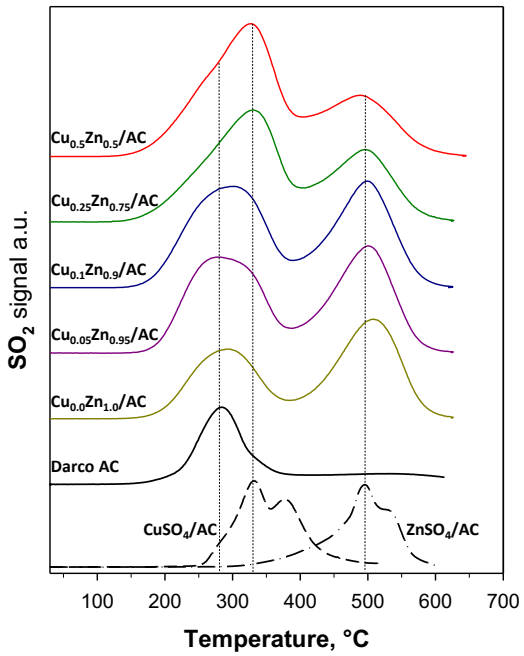

Fig. 3.17. SO_2 release during TPD tests from H_2S-saturated Cu_xZn_{1-x}/AC sorbents and corresponding Darco AC support, as well as from two reference samples of $CuSO_4$ and $ZnSO_4$ impregnated on Darco AC.

The presence of Cu in the active phase determined a new contribution in the TPD profiles of saturated Cu_xZn_{1-x}/AC sorbents, initially as a shoulder centred at ca. 330°C, which progressively became the main signal in the low temperature zone along with increasing Cu content. Also in this case, a close comparison with the TPD profile of a reference sample containing $CuSO_4$ impregnated on the same activated carbon (Fig. 3.18) revealed that the peak at 330°C can be ascribed to the thermal decomposition of copper sulphate in close contact with carbon support, starting at ca. 250°C.

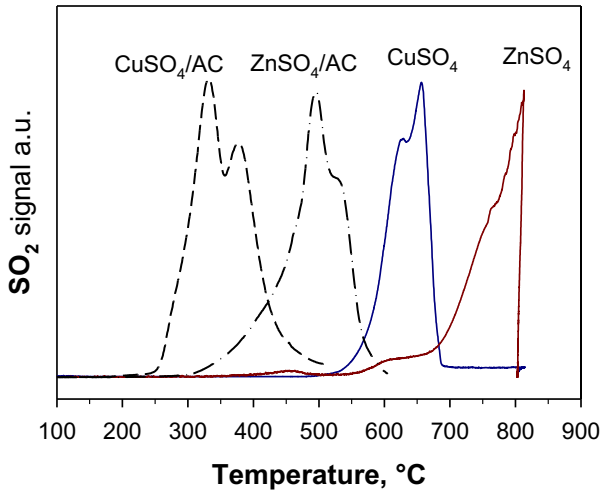

Fig. 3.18. SO_2 signal measured during the TPD experiments performed on bulk and AC supported $ZnSO_4$ and $CuSO_4$ under N_2 flow at a heating rate of 10°C/min.

Note that bulk $CuSO_4$ decomposed releasing SO_2 only at T>550°C (Fig. 3.18). Coherently, along with the reduction of the Zn content in Cu_xZn_{1-x}/AC sorbents, the peak at 500°C, assigned to the decomposition of $ZnSO_4$, was progressively reduced. Qualitative measurements (by ICP-MS and ionic chromatography) confirmed the presence of Zn and Cu sulphates dissolved in solution after contacting spent sorbents with distilled water (*vide infra*).

Noteworthy, most of the literature studies assumed that the reaction of metal oxides (supported or not) with H_2S led to the formation of the corresponding metal sulphides. However, some authors reported experimental evidence for the partial formation of metal sulphates during the H_2S capture process on metal oxides/hydroxides (Florent and Bandosz, 2014). TPD profiles of Cu_xZn_{1-x}/AC sorbents were integrated in order to calculate the total amount of sulphur desorbed as SO_2, and the results are reported in Table 3.4. The (small) amount of H_2S adsorbed on the raw activated carbon was entirely desorbed as SO_2 at T<400°C. On the other hand, spent Cu_xZn_{1-x}/AC sorbents released 40–46% of their initial sulphur content at the end of the TPD test (620°C). The remaining sulphur was likely stored as Zn and Cu sulphides, which are stable species at the investigated

temperature in N_2 atmosphere (Nguyen-Thanh and Bandosz, 2005). However, no direct conclusion could be drawn on the possible presence of elemental sulphur on spent sorbents. All the copper containing sorbents released almost the same amount of SO_2 at $T \leq 620$°C (0.58±0.03 mmol g^{-1}), which was larger than what retrieved for the sample containing only zinc (0.41 mmol g^{-1}). It can be argued that Cu-doping favoured the oxidation of the captured H_2S to form sulphates, whose final quantity was limited by the oxygen availability on the sorbent, since adsorption and desorption tests were conducted under inert atmosphere. It is worth observing that spent sorbents were exposed to air in between adsorption and desorption tests, and therefore the molecular oxygen could have been re-adsorbed on their surface. On the other hand, TPD-NO_x and DRIFT analysis (Fig. 3.13 and 3.14) excluded the residual presence of nitrates (from the corresponding precursors), hence they could not be considered as potential oxygen sources. The progressive substitution of Zn by Cu and the strong interaction with the activated carbon support increased the amount of SO_2 released at relatively low temperatures (i.e. up to 400°C), which is highly desirable in the light of the regenerability of Cu_xZn_{1-x}/AC sorbents by thermal treatments. However, the release of the captured sulphur under inert atmosphere and the restoration of the original active phase appears to be upper limited by the oxygen availability. Therefore, it is foreseen that a more effective regeneration could be achieved by thermally treating spent sorbents in presence of steam and/or under slightly oxidising conditions, in order to enhance the removal of sulphur in metal sulphides or stored as elemental sulphur.

Fig. 3.19 presents the results of XPS analysis conducted on spent $Cu_{0.5}Zn_{0.5}$/AC sorbent in order to identify the main surface species at the end of the reactive process of H_2S adsorption (at 3000 ppmv) and after recovery in air under ambient conditions. It can be observed (Fig. 3.19a) that surface Zn mainly occurred as sulphate with a high intensity $2p_{3/2}$ peak centered at 1022.83 eV, while the Zn $2p_{3/2}$ spectral line with BE=1021.7 eV can be ascribed to a minor surface contribution of ZnS species. Moreover, the Zn $2p_{3/2}$ band peaked at 1025.1 eV is possibly related to compounds formed by reaction of zinc with organic

functionalities of the carbonaceous substrate (such as carboxylates groups) (Wagner et al., 2003). Noteworthy, residual ZnO was not detected from XPS analysis, as expected according to the high degree of conversion of active phase determined from H_2S adsorption tests on $Cu_{0.5}Zn_{0.5}$/AC.

In analogy to Zn, also Cu mainly retained the +2 oxidation state upon reaction with H_2S as demonstrated by the presence of "shake-up" satellite peaks between 940 eV and 945 eV, which are characteristic of CuO and $CuSO_4$ (Fig. 3.19b). The predominant formation of $CuSO_4$ is testified by a main Cu $2p_{3/2}$ line at BE=935.52 eV, in good agreement with the known position for the $CuSO_4$ peak at 935.4 eV. In the BE range between 932.2 eV and 933.6 eV, the spectrum appears to result from the superimposition of the contribution from CuO (933.70 eV) and (at least) a second peak which is difficult to identify since it can be ascribed to several copper species (Krylova and Andrulevičius, 2009; Duan et al., 2016) including CuS (932.2 eV), Cu_2S and Cu_2O (932.5 eV), Cu-Cu (932.63 eV).

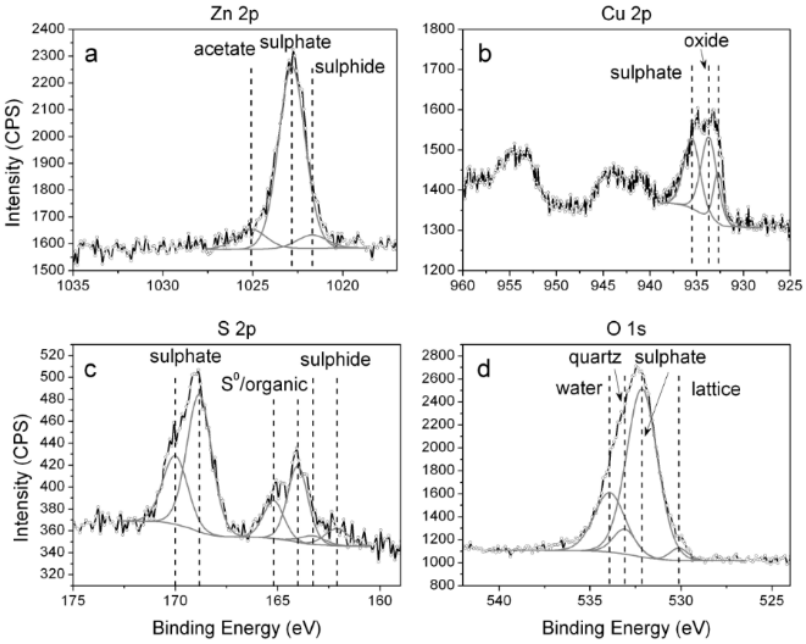

Fig. 3.19. XPS analysis on the saturated $Cu_{0.5}Zn_{0.5}$/AC sorbent ($C_{H_2S}^{in}$=3000 ppmv in N_2, T=30°C) recovered in air, showing the 2p spectral regions of (a) Zn, (b) Cu, (c) S, and the 1s spectral region of O (d).

Noteworthy, according to the recent results by Duan et al. (2016), superficial Cu sulphides possibly formed on CuO/multiwalled carbon nanotubes sensors by reactive adsorption process of H_2S can be effectively re-oxidised during the recovery of spent material in air at room temperature. The deconvolution analysis of peaks in the range 160–172 eV allowed the identification of sulphur-containing compounds (Fig. 3.19c). The predominant form of surface S-species was copper and zinc sulphates with their characteristic S $2p_{3/2}$ and $2p_{1/2}$ lines respectively centered at 168.83 eV and 170.01 eV. A minor presence of Zn sulphide was also identified with S $2p_{3/2}$ and $2p_{1/2}$ lines at 162.11 eV and 163.29 eV, respectively. Interestingly, the S $2p_{3/2}$ and S $2p_{1/2}$ peaks observed at BE=164.02 eV and 165.20 eV are representative of sulphur directly adsorbed on activated carbon as they can be ascribed to the occurrence of some elemental sulphur as well as to organic sulphur compounds, such as thioether (C-

S-C), thiol (C-S-H), thiophene (C_4H_4S) and disulphide groups (Beamson and Briggs, 1992; Wagner et al., 2003). Once formed, these S-species are rather stable upon exposure to air at room temperature (Duan et al., 2016). Eventually, the O 1s signal at 532.15 eV (Fig. 3.19d) confirmed the formation of a considerable amount of metal sulphates from the original metal oxides. Further significant contributions in this spectral region derived from the quartz impurity (533.10 eV) contained in the raw activated carbon and from adsorbed water (533.93 eV). Furthermore, the presence of a minor quantity of lattice oxygen, related to the CuO component, was also identified at BE=530.12 eV (Wagner et al., 2003).

The formation of sulphate species upon H_2S reactive adsorption, detected from XPS analysis, was also confirmed by washing saturated sorbents in water at 60°C. Fig. 3.20 reports the temporal evolution of the amount of sulphate ions released in water after normalisation with respect to the mass of sorbent (ω_{aq}). A sharp increase of dissolved sulphates was observed at the very beginning of the test with each sorbent (up to ca. 0.3 mmol g^{-1}), followed by a slower rise. For Zn/AC and $Cu_{0.05}Zn_{0.95}$/AC, a similar value of ω_{aq}≈0.5 mmol g^{-1} was recorded after about 250 h; in the case of $Cu_{0.5}Zn_{0.5}$/AC, the final value of ω_{aq} increased up to 0.8 mmol g^{-1}, thus mirroring the greater H_2S capture capacity and conversion degree of metal oxides to sulphates (promoted by copper, *vide infra*). The spent Cu/AC sorbent showed faster dynamics of SO_4^{2-} release in the early process stages, and a final value of ω_{aq} as large as 0.9 mmol g^{-1} (still slightly increasing after 300 h).

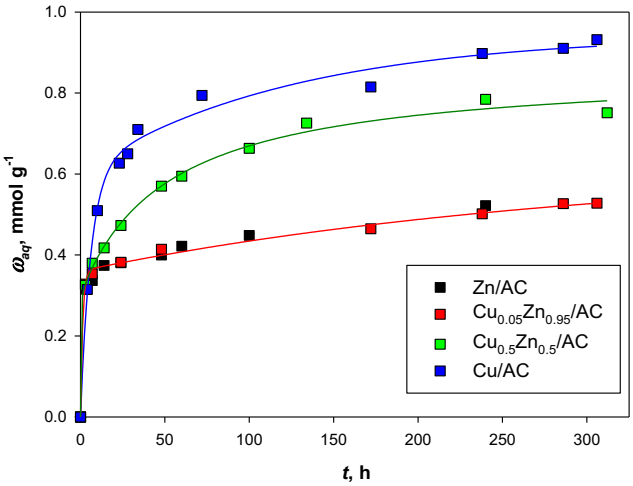

Fig. 3.20. Kinetics of release of sulphate ions in water at 60°C for spent functionalised sorbents ($C^{in}_{H_2S}$=3000 ppmv in N_2, T=30°C).

In this context, the trend of SO_4^{2-} concentration recorded under identical conditions for a mechanical mixture of AC with CuS (results not displayed) suggested the occurrence of a partial oxidation of sulphides (mainly those with copper) to sulphates in aqueous medium. This could explain the slow rise in sulphate release in the case of the exhaust Cu/AC sample. These results pave the way to the development of processes for the recovery of active metal dissolved in water, or the (partial) regeneration of the spent sorbents under operating conditions less energetically intensive with respect to high temperature treatments usually investigated in the pertinent literature (Bagreev et al., 2001).

Dynamic adsorption tests for the various sorbents were repeated employing finer particles in a narrow size range, relatively low concentration of H_2S in the gas feed and very short contact times in an attempt to gain further insights into the kinetics of the capture process and modifications induced by the composition of active phase. Furthermore, other experiments were carried out in order to investigate the effect of O_2, humidity, and the combinate effect of oxygen and humidity for H_2S adsorption. Fig. 3.21 reports breakthrough curves and values for the instantaneous adsorption rate (r defined as the time-derivative of ω, and

plotted against ω), and Table 3.5 the adsorption values for tests carried out at various conditions and T=30°C. For dry condition and in absence of molecular oxygen, raw AC is characterised by low H_2S adsorption capacity ($\omega_{s,ads}$=0.08 mmol g^{-1}). On the other hand, the functionalisation treatment by single, and particularly by composite Zn and Cu oxides, resulted into a significant increase in the adsorption capacity ($\omega_{s,ads}$=0.7–1 mmol g^{-1}), confirming the existence of an optimum of performance for the $Cu_{0.5}Zn_{0.5}$/AC sorbent. As previously suggested, the mechanism of H_2S capture involves chemical reactions with metal oxides in a wide range of compositions of interest for practical applications; thus, all of the functionalised sorbents showed only a moderate decrease of $\omega_{s,ads}$ at an inlet H_2S concentration of 100 ppmv with respect to tests performed at 3000 ppmv. The corresponding lower utilisation factor of active phase was probably due to some kind of kinetic/diffusional limitation. The presence of oxygen in the feed gas involved an increase of $\omega_{s,ads}$ and of adsorption rate, especially for the Cu sorbents; in particular, $\omega_{s,ads}$ increases from 1.00 to 1.28 mmol g^{-1} for $Cu_{0.5}Zn_{0.5}$/AC. The positive role of oxygen may be due to the formation of an oxidising environment on the solid surface, which would orient the sulphur capture toward the formation of more oxidised (e.g., sulphates, sulphur dioxide) rather than more reduced (e.g., sulphides) species. This generally entails larger adsorption capacities.

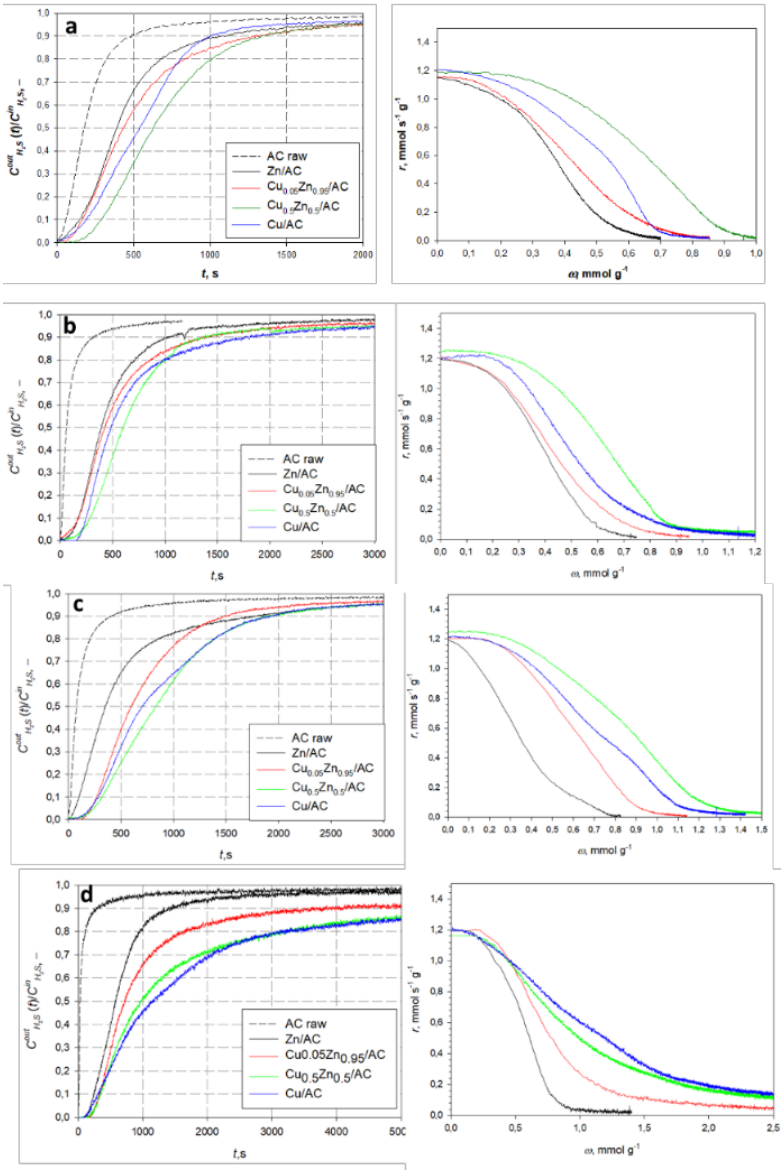

Fig. 3.21. H_2S breakthrough curves (left) and adsorption rates (right) for selected cases: a) $C_{H_2S}^{in}$=100 ppmv in N_2; b) $C_{H_2S}^{in}$=100 ppmv and $C_{O_2}^{in}$=2500 ppmv in N_2; c) $C_{H_2S}^{in}$=100 ppmv and *RH*=48%, d) $C_{H_2S}^{in}$=100 ppmv, $C_{O_2}^{in}$=2500 ppmv and *RH*=48%. Sorbent mass: 20 mg and 80 mg for functionalised and AC raw sorbents, respectively. *T*=30°C.

In the case of the only presence of humidity, a water film is thus formed on the internal surface of AC. It was proposed that the molecules of H_2S were transported and dissolved to produce H^+ and HS^- ions into the water film. Therefore, presence of water has a beneficial effect on the adsorption performance of H_2S on AC and functionalised sorbents (Xiao et al., 2008). Also in this case, the best material is $Cu_{0.5}Zn_{0.5}$/AC that shows an adsorption capacity equal to 1.67 mmol g^{-1}.

In the case of co-presence of humidity and oxygen in the feed gas, the H_2S adsorption capacity is the highest compared with the previous results. This is related to a combined effect of adsorption of oxygen on the surface of AC and formation of the water film on the internal pores of the substrate. It is important to underline that, in this case, Cu/AC is the best adsorbent: it shows an adsorption capacity equal to 4.96 mmol g^{-1}. The presence of copper allows to increase the formation of elemental sulphur and, in the case of co-presence of humidity and oxygen, the main product of reactive adsorption, already underlined in the related literature even if with reference to different adsorbents, is elemental sulphur (Bagreev et al., 2001; Fang et al., 2013; Sitthikhankaew et al., 2014, Zhang et al., 2016).

To complete the analysis, Fig. 3.21 reports the values of the instantaneous adsorption rate r vs. ω which, as expected, progressively decreased after the breakpoint along with the increasing amount of H_2S captured by each sorbent and up to its saturation level. Zn/AC and $Cu_{0.05}Zn_{0.95}$/AC sorbents displayed similar trends, in the case of dry and oxygen conditions, mainly in the early stages of the process, whereas even 5% of Zn substitution by Cu determined higher values for r in particular for ω>0.3 mmol g^{-1}; this eventually enhanced the adsorption capacity and utilisation factor of active phase at saturation.

Table 3.5. Adsorption/desorption performances of AC raw and functionalised sorbents under various operating conditions. Sorbent mass=20 mg and *T*=30°C.

Sorbent	$C_{H_2S}^{in}$ [ppmv]	$C_{O_2}^{in}$ [ppmv]	RH [%]	$\omega_{s,ads}$ [mmol g^{-1}]	$\omega_{s,des}^{TPD}$ [mmol g^{-1}]
AC raw	100	–	–	0.08	0.08
	100	2500	–	0.09	0.09
	100	–	48	0.15	0.15
	100	2500	48	0.34	0.34
Zn/AC	100	–	–	0.73	0.29
	100	2500	–	0.74	0.33
	100	–	48	0.87	0.30
	100	2500	48	0.91[a]	0.40
$Cu_{0.05}Zn_{0.95}$/AC	100	–	–	0.88	0.34
	100	2500	–	0.93	0.39
	100	–	48	0.93	0.30
	100	2500	48	2.20[a]	0.59
$Cu_{0.5}Zn_{0.5}$/AC	100	–	–	1.00	0.39
	100	2500	–	1.28	0.50
	100	–	48	1.67	0.41
	100	2500	48	3.85[a]	0.66
	165	–	–	1.02	0.41
	193	–	–	1.04	0.40
Cu/AC	100	–	–	0.88	0.33
	100	2500	–	1.21	0.51
	100	–	48	1.40	0.28
	100	2500	48	4.96[a]	0.64

[a]Specific adsorption capacity @ $C_{H_2S}^{out}$=0.9$C_{H_2S}^{in}$.

The different behaviour of Zn/AC and $Cu_{0.05}Zn_{0.95}$/AC samples was likely related to a chemical promoting effect of Cu, enhancing the ZnO reactivity with H_2S (Yang and Tatarchuk, 2010; Bezverkhyy et al., 2012; Elyassi et al., 2014). Indeed, it is recalled that both sorbents showed almost identical textural properties due to the low amount of copper substitution, thus intraparticle mass transfer phenomena equally affected the adsorption process. The $Cu_{0.5}Zn_{0.5}$/AC sorbent has the best adsorption rate except in the case of co-presence of humidity and oxygen. Two factors seem to contribute to the performance enhancement with respect to Zn/AC and $Cu_{0.05}Zn_{0.95}$/AC samples: i) the already invoked promoting chemical role of copper on the reactivity of ZnO and ii) the reduced limitations to

intraparticle diffusion linked to a minor alteration of porosity (i.e. occlusion of micropores). This latter effect can be related to the concomitant lower loading of ZnO and to the tendency of zinc and copper to be preferentially located in micropores and mesopores, respectively. The Cu/AC sorbent showed a kinetic pattern in between those for $Cu_{0.05}Zn_{0.95}$/AC and $Cu_{0.5}Zn_{0.5}$/AC in all the studied cases, except for the case of co-presence of humidity and oxygen where Cu/AC is the best sorbent in terms of adsorption capacity and adsorption rate.

Considering the material showing the best performance in dry condition ($Cu_{0.5}Zn_{0.5}$/AC), the investigation was deepened by analysing the effect of $C_{H_2S}^{in}$ (100–193 ppmv) and total flow rate Q of gas stream (20–40 SL h^{-1}). As reported in Table 3.5, the saturation capacity of the sorbent $\omega_{s,ads}$ was not significantly affected by variation of these two operating parameters in the explored ranges.

In order to better evaluate the influence of both $C_{H_2S}^{in}$ and gas flow rate on the H_2S capture dynamics of $Cu_{0.5}Zn_{0.5}$/AC, breakthrough data were processed adopting the Bohart and Adams model (also termed "BA" in the following) for adsorption process in a fixed bed (Bohart and Adams, 1920; Gutiérrez Ortiz et al., 2014), whose integral form is:

$$\ln\left(\frac{C_{H_2S}^{in}}{C_{H_2S}^{out}(t)} - 1\right) = \frac{k_{BA}\omega_{s,ads}\rho_b L(1-\varepsilon)}{1000u\varepsilon} - k_{BA}C_{H_2S}^{in}t \quad (3.1)$$

where L [m] is the length of fixed bed (0.0034 m), ε [–] its void fraction (0.39), u [m s^{-1}] the superficial gas velocity, ρ_b [g L^{-1}] the sorbent bulk density (820 g L^{-1}), k_{BA} [L mol^{-1} s^{-1}] the kinetic parameter of the BA model. It is highlighted that $C_{H_2S}^{in}$ and $C_{H_2S}^{out}(t)$ are here expressed, obviously, in mol L^{-1} and not ppmv. Eq. (3.1) implies that, if k_{BA} is constant and if the BA model is suitable to fit experimental data, the plot of the LHS of Eq. (1) vs. time is represented by a substantially straight line whose intercept and slope allow the determination of $\omega_{s,ads}$ and k_{BA}, respectively. The original BA model assumes that the adsorption rate is governed by a linear driving force and controlled by surface reaction, k_{BA}

being the surface reaction constant. In the present work we keep the original mathematical formulation of the BA model, but the k_{BA} parameter was considered as a global kinetic coefficient embedding the various kinetic resistances. In fact, the complex phenomenology for the investigated gas–solid reactive system should include numerous dynamic steps such as fluid film diffusion, intraparticle diffusion (i.e. H_2S transport within the substrate pore network), solid state diffusion towards the products layers (e.g. sulphates and sulphides) and surface chemical reactions. Additionally, k_{BA} might also vary during the adsorption process due to time-dependent properties of the reacting system including: i) pore volume reduction of the substrate due to the formation of products characterised by molar volumes greater than those of the parent copper and zinc oxides (cf. e.g. Sadegh-Vaziri and Babler, 2017); ii) occurrence of multiple chemical reactions in various steps of the reactive process (*vide infra*); iii) modification of the product layer microstructure.

In order to elucidate the dynamic mechanism governing the adsorption rate in the early process stages (just after the breakpoint), Fig. 3.22a depicts, as an example, the BA plot for H_2S adsorption onto $Cu_{0.5}Zn_{0.5}$/AC at two H_2S inlet concentrations and two total gas flow rates, together with the corresponding fitting according to Eq. (3.1). Please note that the three BA plots are in colour with the legend indicated in Fig. 3.22b, and that the linearised fittings are reported in black.

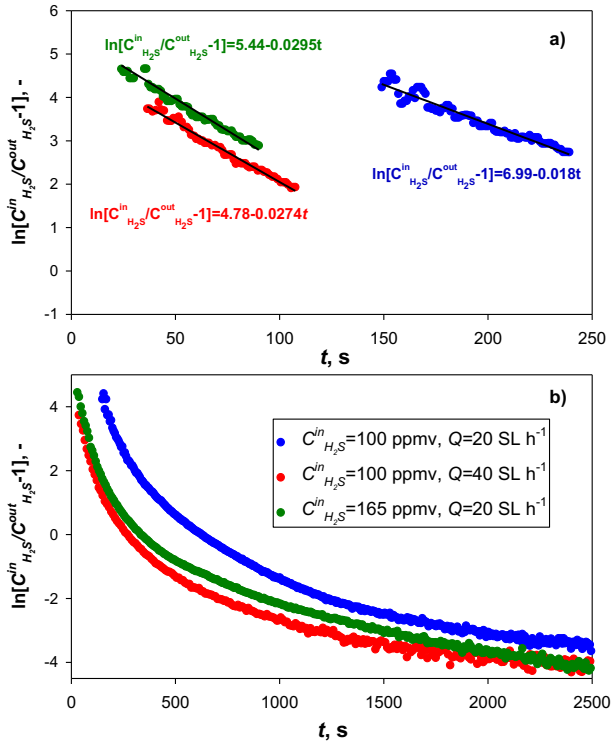

Fig. 3.22. Bohart and Adams plots for H_2S adsorption in a fixed bed of $Cu_{0.5}Zn_{0.5}$/AC (20 mg) at 30°C with different inlet concentrations and total gas flow rates: a) plots for short adsorption times according to Eq. (3.1) and b) plots for the entire time range of the tests.

The value of k_{BA} was substantially independent from the inlet H_2S concentration, with an average estimated value of 4250±150 L mol^{-1} s^{-1} at 20 SL h^{-1}. On the other hand, k_{BA} increased with the flow rate up to 6140 L mol^{-1} s^{-1} at 40 SL h^{-1} and $C_{H_2S}^{in}$=100 ppmv. Therefore, the capture process in the initial phase (until breakpoint and just after it) seems to proceed under a prevalent external mass transfer control. Indeed, the increase of k_{BA} corresponded to the expected increase in the external mass transfer coefficient k_{ext} due to the higher superficial gas velocity u, as $k_{ext} \sim u^{0.6}$ (according to the correlation proposed by Wakao and Funazkri, 1978).

This is a clear indication that the surface chemical reaction (mainly producing $ZnSO_4$ for short process times) was rather fast and that a reacting front initially advanced along the radial particle coordinate in a manner resembling the shrinking core dynamic pattern (Levenspiel, 1999). To confirm this hypothesis, a SEM-EDX analysis was performed on cross-sections of $Cu_{0.5}Zn_{0.5}$/AC particles tested at $C_{H_2S}^{in}$=100 ppmv and 20 SL h^{-1} with the run stopped at ω=0.3 mmol g^{-1} (i.e. approximately at the breakpoint time): results in Fig. 3.23 indicate that sulphur species were predominantly confined in the outer shell of the adsorbent particle (thickness of ca. 10 μm).

The progressive reduction of the adsorption rate after the breakpoint time was mirrored by the decrease of the slope in the BA plot for longer times (*vide* Fig. 3.22b), indicating a strong reduction of the global kinetic parameter (k_{BA}) which could be related to alterations of the support microstructure and to the switch to dominating dynamic mechanisms (e.g. product layer diffusion) other than external fluid film diffusion. The intraparticle diffusion mechanism is obviously ruled, after the breakpoint time, by a partial pore blockage determined by formation in the particle outer shell of large product species (sulphates). In fact, the surface area of $Cu_{0.5}Zn_{0.5}$/AC dropped to ca. 440 m^2 g^{-1} after H_2S reactive adsorption up to t_{br}, a value approximatively 25% lower than the one shown by the pristine functionalised sample (cf. also Table 3.3).

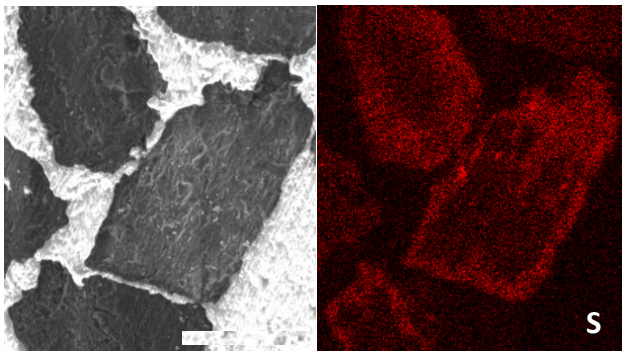

Fig. 3.23. SEM (left) and EDX micrograph of S distribution (right) for multiparticle (cross-section) $Cu_{0.5}Zn_{0.5}$/AC sorbent sample after adsorption test stopped at ω=0.3 mmol g^{-1}. Adsorption stage performed at $C_{H_2S}^{in}$=100 ppmv in N_2, Q=20 SL h^{-1}, T=30°C.

The observed loss in surface area is significantly greater than the one expected on the basis of the weight gain of the sample due to retention of sulphur species (ca. 0.9% wt. at t_{br}). This confirms a reduction of the accessibility to the smallest pores which could, in turn, inhibit the active phase utilisation or remarkably slow down the capture rate.

Fig. 3.24 shows the results of TPD tests carried out on various spent sorbents previously saturated under base conditions ($C_{H_2S}^{in}$=100 ppmv in N_2) and after adsorption of H_2S in presence of humid condition and molecular oxygen (but not re-exposed to ambient air). TPD profiles for materials consisting of $CuSO_4$ and $ZnSO_4$ separately impregnated on AC are reported for reference. The results are expressed as SO_2 signal as a function of desorption temperature; in fact H_2S desorption was negligible, and therefore is not reported.

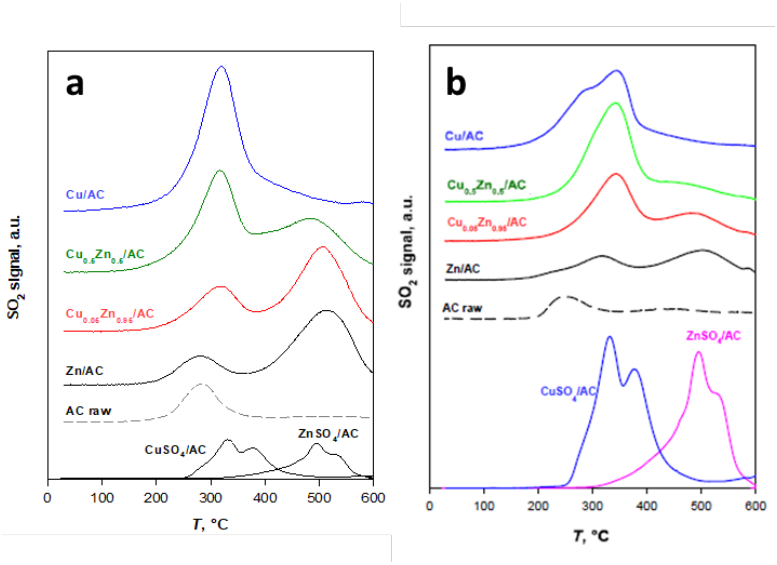

Fig. 3.24. SO_2 release during TPD tests after adsorption **a)** up to saturation at $C_{H_2S}^{in}$=100 ppmv in N_2, Q=20 SL h^{-1}, T=30°C and **b)** up to 90% of saturation at $C_{H_2S}^{in}$=100 ppmv, RH=48% and $C_{O_2}^{in}$=2500 ppmv in N_2, Q=20 SL h^{-1}, T=30°C. TPD profiles for $CuSO_4$ and $ZnSO_4$ separately impregnated on AC are reported for reference.

In the same way as observed for TPD profiles of sorbents saturated at high concentration of H_2S in dry conditions (cf. Fig. 3.18), spent AC raw sample showed a single peak of SO_2 desorption starting at ca. 170°C and centered at 280°C due to desorption of SO_2. For spent Zn/AC, two broad emission peaks were revealed: the first (centered at ca. 290°C) closely resembled the one observed for spent AC; the second (centered at ca. 500°C) can be ascribed to the decomposition of $ZnSO_4$, as evident from the comparison with the TPD profile obtained for the reference $ZnSO_4$/AC material. The progressive substitution of copper for zinc in the mixed active phase of sorbents caused the increase in intensity of the peak centered around 320°C, desorption of $CuSO_4$ (cf. the TPD profile obtained for the reference $CuSO_4$/AC material), and a corresponding reduction of the high temperature peak (i.e., the one related to $ZnSO_4$ decomposition) for mixed functionalised sorbent, which coherently disappeared from the TPD profile of

Cu/AC spent material. For spent samples under wet conditions, spent AC raw and Zn/AC show almost the same emission peak, in terms of emission temperature, with respect to the previous studied case. By increasing the content of copper in the mixed oxide functionalised sorbents, it can be observed that the intensity of the peak at low temperature, sum of the emission of SO_2 and $CuSO_4$, increased. Finally, Cu/AC shows two emissions peaks, one at 280°C, related to SO_2, the second one at 320°C, related to the emission of $CuSO_4$.

The amount of S desorbed from spent materials as SO_2 during TPD tests ($\omega_{s,des}^{TPD}$) is reported in Table 3.6. While 100% of the adsorbed sulphur on AC raw was desorbed ($\omega_{s,des}^{TPD}= \omega_{s,ads}$) in both cases, for functionalised materials it was calculated that $\omega_{s,des}^{TPD}$ accounted for ca. 40% of $\omega_{s,ads}$ in the case of dry condition, whereas the desorbed quantities are 43, 27, 17 and 13% for Zn/AC, $Cu_{0.05}Zn_{0.5}$/AC, $Cu_{0.5}Zn_{0.5}$/AC and Cu/AC in wet conditions, respectively. The remaining fraction of sulphur can be imputed to both Cu and Zn sulphides (known to decompose at temperatures higher than 1000°C in inert environments, Nguyen-Thanh and Bandosz, 2005), and to species not detectable by our TPD procedure ("ghost" species) such as elemental S, which could condense on internal walls of cold pipelines.

TPD investigation was extended to materials previously undergoing adsorption only up to $C_{H_2S}^{out}$=0.02$C_{H_2S}^{in}$, in dry conditions (Fig. 3.25), in order to obtain deeper insights into the type of S-based species early formed during the H_2S capture process, and into the role of copper. The deconvolution of TPD signals was also included for reference.

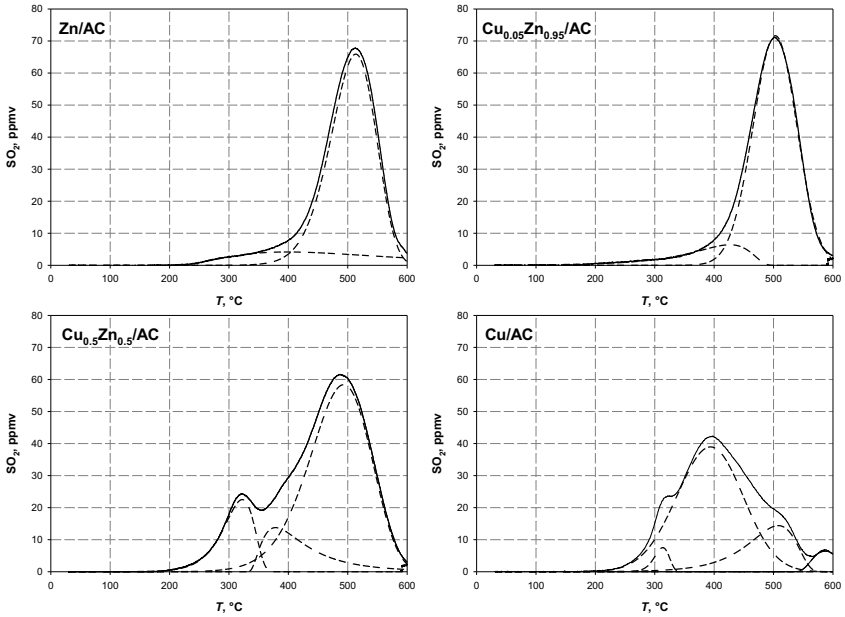

Fig. 3.25. SO_2 release during TPD tests from functionalised sorbents after adsorption up to $C_{H_2S}^{out}/C_{H_2S}^{in}$=0.02 with $C_{H_2S}^{in}$=100 ppmv in N_2, and Q=20 SL h^{-1}, T=30°C. Dashed lines represent deconvolution peaks.

Table 3.6. Adsorption/desorption performances for AC raw and for Cu_xZn_{1-x}/AC sorbents at $C_{H_2S}^{out}$=0.02$C_{H_2S}^{in}$. Sorbent mass: 60 mg. Inlet conditions: $C_{H_2S}^{in}$=100 ppmv in N_2, T=30°C.

Sorbent	**Adsorption capacity $\omega_{s,ads}$ [mmol g^{-1}]**	**$\omega_{s,des}^{TPD}$ [mmol g^{-1}]**
Zn/AC	0.21	0.21
$Cu_{0.05}Zn_{0.95}$/AC	0.22	0.22
$Cu_{0.5}Zn_{0.5}$/AC	0.40	0.27
Cu/AC	0.22	0.15

For Zn/AC, the pattern of SO_2 emission was analogous to what obtained for the saturated sample (cf. Fig. 3.25a), with a main peak at ca. 510°C related to the decomposition of $ZnSO_4$ preceded by a broad peak (of minor intensity) ascribable to the SO_2 contribution deriving from the oxidation of H_2S adsorbed by the parent substrate. The TPD pattern obtained for Cu/AC was rather complex and

it was deconvoluted into four main peaks, differing substantially from what was recorded for the saturated sample (again, cf. Fig. 3.25a). In fact, the lower temperature bands (peaked at around 310°C and 400°C) were assigned to the small contribution of the support and to $CuSO_4$ decomposition. The peaks occurring at higher temperatures (with maximum intensity at 510°C and 590°C) could be imputed to SO_2 deriving from oxidation of S in CuS *via* direct reaction of the latter compound with both $CuSO_4$ and oxygen released from thermal decomposition of $CuSO_4$ (Dunn and Muzenda, 2001; Nafees et al., 2015). Regarding the sorbents with mixed oxides, $Cu_{0.05}Zn_{0.95}$/AC showed the same qualitative features of the Zn/AC sample whereas for $Cu_{0.5}Zn_{0.5}$/AC a third peak became evident (around 400°C), associated with the decomposition of copper sulphate. Further, the deconvolution analysis also provided quantitative indications on the degree of conversion of ZnO to $ZnSO_4$ up to $C_{H_2S}^{out}$=0.02$C_{H_2S}^{in}$. For Zn/AC, $Cu_{0.05}Zn_{0.95}$/AC and $Cu_{0.5}Zn_{0.5}$/AC, conversion values of 10.1%, 10.7% and 21.0% were retrieved, respectively. Therefore, the copper substitution promoted the ZnO conversion to $ZnSO_4$ mainly in the first stages of the capture process (*vide infra*). In this regard, two main factors could be invoked to explain the described pattern: i) a sacrificial role of copper as oxygen donor to accelerate the formation of zinc sulphate; ii) a structural role of copper enabling the formation of smaller-sized ZnO crystallites (phenomenon highlighted e.g. in Baird et al., 1992), with an associated enhanced reactivity. However, an additional contribution of atmospheric humidity and/or oxygen pre-adsorbed onto the sorbent surface to the sulphates formation cannot be ruled out.

Quantitative data concerning adsorbed and desorbed S ($\omega_{s,ads}$ and $\omega_{s,des}^{TPD}$, respectively) for the four sorbents at $C_{H_2S}^{out}$=0.02$C_{H_2S}^{in}$ are correspondingly reported in Table 3.6, from which the following observations can be drawn:

- for Zn/AC and $Cu_{0.05}Zn_{0.95}$/AC (Zn-rich sorbents), $\omega_{s,des}^{TPD}$=$\omega_{s,ads}$. The peaks observed during TPD tests account for the release of all H_2S previously adsorbed, which is mainly oxidised to $ZnSO_4$;

• for $Cu_{0.5}Zn_{0.5}$/AC and Cu/AC ("low-Zn sorbents"), $\omega_{s,des}^{TPD}=0.7\omega_{s,ads}$. The peaks observed during TPD tests only partly account for the release of S previously adsorbed. Apart from Zn and Cu sulphates, "ghost species" such as copper sulphides, elemental S and thiols were formed at significant rates, determining a more effective exploitation of active phases in the case of $Cu_{0.5}Zn_{0.5}$/AC sample.

Moreover, TPD tests performed for $Cu_{0.5}Zn_{0.5}$/AC after various adsorption times (cf. Fig. 3.26) suggest that $ZnSO_4$ formed at a faster rate with respect to $CuSO_4$. In fact, while the main peak associated with $ZnSO_4$ decomposition does not experience substantial modification in the adsorption time range of 8–16 min, the intensity of the $CuSO_4$-deriving peak of SO_2 emission increased. From a quantitative standpoint, the deconvolution analysis (not reported for the sake of brevity) revealed that 8 min capture process ($\omega_{s,ads}$=0.2 mmol g^{-1}) were enough to attain a ZnO conversion to the corresponding sulphate as high as 20%, very close to the asymptotic value retrieved from TPD on saturated sorbent (21%).

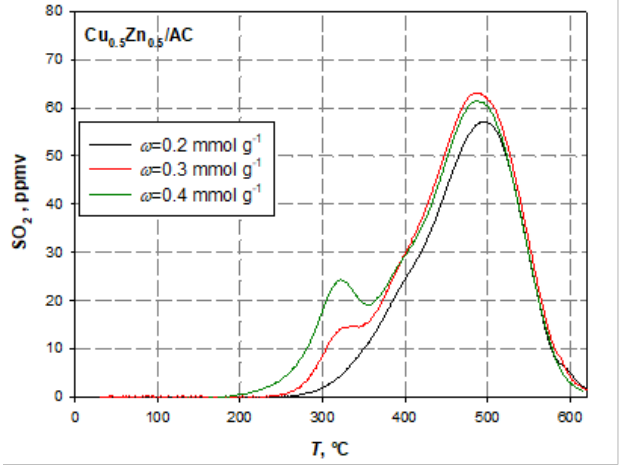

Fig. 3.26. SO_2 release during TPD tests from $Cu_{0.5}Zn_{0.5}$/AC after adsorption carried out at different sulphur loadings (corresponding to different process times) and $C_{H_2S}^{in}$=100 ppmv in N_2, Q=20 SL h^{-1}, T=30°C.

On the contrary, the values of CuO conversion to $CuSO_4$ were 8%, 12% and 21% for capture times of 8 min, 16 min and at saturation, respectively. Altogether the results indicate that, for the equimolar Cu:Zn sorbent, $ZnSO_4$ formed at a faster rate with respect to $CuSO_4$ with copper likely acting as oxygen donor/structural promoter enabling a faster conversion rate and a higher utilisation factor of the ZnO phase. On the other hand, the final degree of conversion for both Zn and Cu oxides to form their sulphates was equivalent and most probably limited by oxygen availability on the sorbent.

Fig. 3.27 shows the results of TPO tests carried out on spent sorbents previously saturated under base conditions. TPO profiles for materials consisting of $CuSO_4$ and $ZnSO_4$ separately impregnated on AC are reported for reference, as well as those for mechanical mixtures of AC with elemental sulphur (S+AC), CuS (CuS+AC) and ZnS (ZnS+AC).

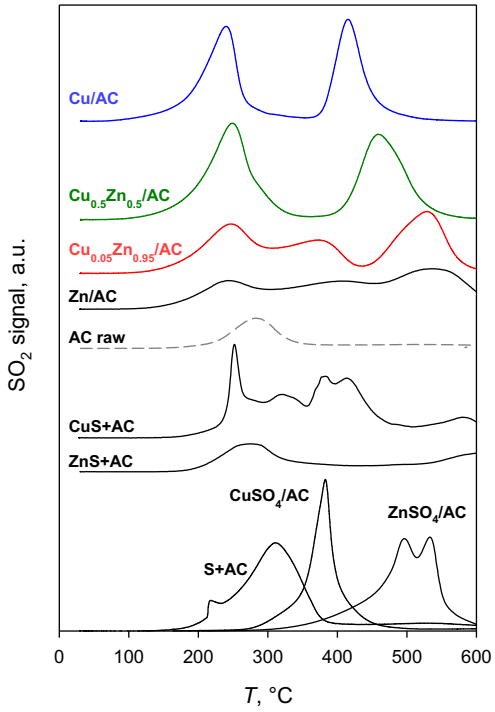

Fig. 3.27. SO_2 release during TPO tests from selected sorbents after adsorption up to saturation with $C^{in}_{H_2S}$=100 ppmv in N_2, Q=20 SL h^{-1}, T=30°C. TPO profiles for $CuSO_4$ and $ZnSO_4$ separately impregnated on AC are reported for reference, as well as those for mechanical mixtures of AC with elemental sulphur, CuS and ZnS.

From a quantitative point of view, the amount of SO_2 evolved during TPO tests corresponded to the amount of H_2S that was previously captured during the adsorption phase ($\omega^{TPO}_{s,des}$= $\omega_{s,ads}$). Therefore, it was confirmed that the only partial recovery of sulphur observed in TPD experiments under inert atmosphere was mainly due to the stability of metal sulphides which, on the other hand, could be oxidised and decomposed during TPO tests. The TPO profile for the saturated Zn/AC sample showed three main SO_2 peaks: the first one, centered at ca. 250°C, could be tentatively assigned to the presence of ZnS by comparison with the

profile retrieved for ZnS+AC mixture; the second peak, at ca. 520°C, was related to the presence of $ZnSO_4$ (see $ZnSO_4$/AC TPO profile). While the formation of $ZnSO_4$ was already commented, TPO tests allowed individuating a TPD ghost species, viz. ZnS. For Zn/AC sample, the presence of a third (intermediate and unresolved) peak was observed at around 400°C. For Cu/AC sample, there were only two main contributions with similar areas: the low temperature peak (at 200°C) could be assigned to the oxidation of some elemental S and CuS, while the high temperature peak (around 410°C) was due to decomposition of $CuSO_4$. The TPO patterns for composite Cu_xZn_{1-x}/AC sorbents were more complex, deriving from the superimposition of peaks related to the presence of copper and zinc sulphates (already observed in TPD) and copper and zinc sulphides (not detectable by TPD), apart from the peak deriving from S and/or SO_2 bound to AC. Nonetheless, it was observed that the prevailing contributions were related to CuS (rather than ZnS) and $ZnSO_4$ (rather than $CuSO_4$). This confirms that, for mixed oxides, Zn prevailingly reacts with H_2S to form $ZnSO_4$, while Cu also forms sulphides and elemental S.

3.3 Comparison between alumina and activated carbon series results

Fig. 3.28 reports a comparison of adsorption capacity of AC and Als both raw and functionalised containing an equimolar Cu–Zn mixture. The figure clearly shows that raw Darco AC has higher adsorption capacities than raw alumina, for any tested H_2S concentration. However, the differences tend to decrease at low H_2S concentrations (i.e. 500–1000 ppmv) and vary in a range of 30–55%. The adsorption capacity at the highest concentration of H_2S (i.e. 3000 ppmv) is approximately 55% higher for Darco AC if compared to alumina.

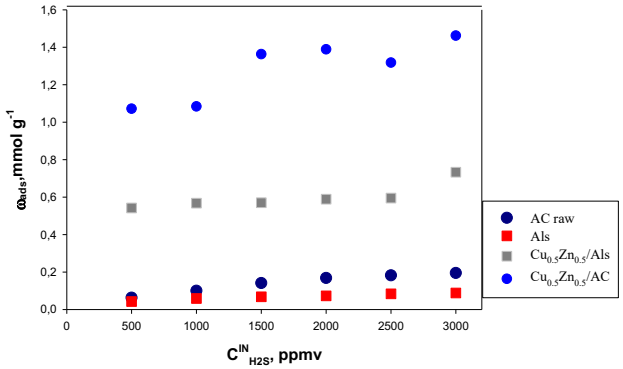

Fig. 3.28. Adsorption isotherm of H_2S on raw alumina and AC, $Cu_{0.5}Zn_{0.5}$/Als and $Cu_{0.5}Zn_{0.5}$/AC. Inlet conditions: $C_{H_2S}^{in}$=3000 ppmv, T=30°C, P=1 bar.

Regarding the comparison of the sorbents containing an equimolar Cu–Zn mixture, Fig. 3.28 witnesses a significantly higher H_2S capture performance in the case of the carbonaceous support, with $\omega_{s,ads}$≈1.8 times larger for $Cu_{0.5}Zn_{0.5}$/AC with respect to $Cu_{0.5}Zn_{0.5}$/Als. The difference of adsorption capacity between the two sorbents is likely linked to: i) the remarkably higher surface area of the carbonaceous support, allowing a greater dispersion of the active phase nanoparticles, also ending up in reduced H_2S diffusion limitations in the capture process (cf. Table 3.1 and Table 3.3); ii) the exhaustive formation of ZnO and CuO on the carbonaceous support which, in contrast, is hindered on the alumina support due to the stabilisation of metal hydroxy-nitrates species as witnessed by the comparison of XRD, DRIFT analyses and TPD-NO_2 tests for the two kind of sorbents.

Comparing the total amount of sulphur released as SO_2 from the sorbent during TPD for the two kind of samples, it is observed that all the alumina sorbents released most of the adsorbed sulphur (between 80–90%) after thermal treatment at 800°C. However, limiting the thermal treatment up to 600°C to prevent a significant formation of metal aluminates, only half of the sulphur content can be removed from the best performing $Cu_{0.5}Zn_{0.5}$/Als sorbent, and even less from Zn-

richer materials ($\omega_{s,des}^{600°C}$), once again due to the stability of the corresponding metal sulphates.

For the same regeneration temperature (600°C), the carbon-based $Cu_{0.5}Zn_{0.5}$/AC sorbent released a significantly higher amount of sulphur. This is due to a strong interaction of the activated carbon support with the metal sulphates formed during the reactive adsorption of H_2S, that reduces the stability of both $CuSO_4$ and $ZnSO_4$ thus lowering their decomposition temperatures by as much as 300°C (Fig. 3.29).

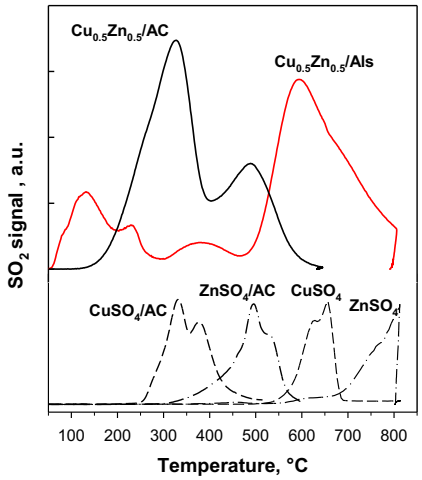

Fig. 3.29. SO_2 release from spent $Cu_{0.5}Zn_{0.5}$/Als and $Cu_{0.5}Zn_{0.5}$/AC sorbents previously saturated with H_2S (3000 ppmv in N_2, T=30°C, P=1 bar) during TPD tests under N_2 flow. SO_2 TPD profiles for reference samples of $CuSO_4$ and $ZnSO_4$ in bulk or supported on activated carbon are also included for comparison purposes (dashed lines).

Finally, in the case of TPO, as expected, it is highlighted that in the case of Cu_xZn_{1-x}/AC sorbents the presence of oxygen during the desorption test produces a complete release of sulphur with an associated combustion of the substrate, whereas in the case of alumina sorbents it is observed a lower amount of sulphur released compared to the value retrieved from the TPD test (cf. Table 3.2).

Chapter 4

Adsorption of HCHO on functionalised materials: results and discussion

A portion of this chapter has appeared in print:

- G. de Falco, M. Barczak, F. Montagnaro, T.J. Bandosz. A new generation of surface active carbon textiles as reactive adsorbents of indoor formaldehyde. ACS Applied Materials & Interfaces 2018, 10, 8066–8076.
- G. de Falco, W. Li, S. Cimino, T.J. Bandosz. Role of sulfur and nitrogen surface groups in adsorption of formaldehyde on nanoporous carbons. Carbon 2018, 138, 283–291 (copyright permission obtained)

4.1 Results and discussion for carbon cloths sorbents

The formaldehyde (HCHO) breakthrough curves measured in the dry conditions on the carbon textiles are collected in Fig. 4.1A. From the breakthrough curves, the dynamic data and corresponding adsorption capacities at saturation were determined and the results are summarised in Table 4.1, in which t_{br} [min] is the breakthrough point time (assumed as the time for which the ratio of the HCHO concentration at the bed outlet relative to that in the feed is 0.05), $\omega_{s,ads}$ [mg g^{-1}] is the HCHO breakthrough capacity and C_{HCHO}^{in} [ppmv] is the inlet concentration of HCHO in the fixed bed reactor. Since in some cases, even after a very long experimental time, the bed saturation was not reached, the HCHO capacity at $\frac{C^{out}}{C^{in}} = 0.95$ was arbitrarily chosen for the performance comparison.

CC and CC-HT revealed similar dynamic behaviours, even though the breakpoint time for CC-HT was longer than that for CC. They both show relatively fast kinetics of the adsorption process and similar saturation capacity ($\omega_{s,ads}$=0.56 and 0.53 mg g^{-1} for CC and CC-HT, respectively). The heat treatment, expected to remove even traces of the residual nylon and/or modify fibers (Florent et al., 2017), did not affect the adsorption capacity. All the chemically modified carbon textiles exhibit better performance as HCHO adsorbents than their unmodified counterparts (CC and CC-HT). Interestingly, the breakthrough curve for CC-P markedly differs from those of the other textiles, which suggests different mechanisms of HCHO adsorption. The saturation capacities $\omega_{s,ads}$ of CC-T, CC-U, CC-P and CC-D are 20, 30, 44 and 170% greater, respectively, than that for CC. The best adsorbent is CC-D, whose t_{br} value equals to 109 min, and the saturation capacity reaches 1.56 mg g^{-1}. CC-P is characterised by the shortest breakpoint time with respect to the others functionalised samples (12 min), but its saturation adsorption capacity is larger than those for CC-U and CC-T.

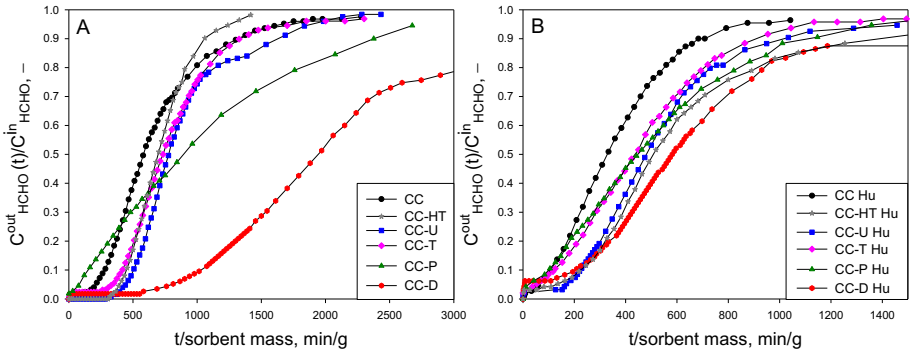

Fig. 4.1. HCHO breakthrough curves measured in dry (A) and moist (B) conditions (the last designed with the symbol "Hu"). Reproduced from de Falco et al., 2018, see article 3) in the Introduction, copyright 2018 American Chemical society obtained.

Table 4.1. Parameters of HCHO adsorption performance of the studied carbon textiles. Reproduced from de Falco et al., 2018, see article 3) in the Introduction, copyright 2018 American Chemical society obtained.

Sorbent	C^{in}_{HCHO} **[ppmv] Dry**	$\omega_{s,ads}$ **[mg g^{-1}] Dry**	t_{br} **[min] Dry**	C^{in}_{HCHO} **[ppmv] Moist**	**Water adsorbed [mg g^{-1}]**	$\omega_{s,ads}$ **[mg g^{-1}] Moist**	t_{br} **[min] Moist**
CC	1.25	0.56	29	1.10	311	0.27	7
CC-HT	1.12	0.53	50	0.95	325	0.34	13
CC-U	1.25	0.73	55	0.94	303	0.33	18
CC-T	1.28	0.68	47	0.95	244	0.29	6
CC-P	1.10	0.80	12	0.96	252	0.34	3
CC-D	1.15	1.56	109	0.95	252	0.53	3

Fig. 4.1B shows the HCHO breakthrough curves measured in the moist conditions (samples are denoted with "Hu") for the modified carbon textiles; the corresponding adsorption capacities and t_{br} values are again listed in Table 1. The presence of moisture on the surface and in the challenge gas markedly decreased the performance of the materials tested as HCHO adsorbents. The effect of water

vapour is visualised in Fig. 4.2. Even though its presence worsens the performance, the extent of the decrease differs. The most pronounced effect was found for the best performing sample CC-D, and the least- for CC-HT. It is likely caused by 1) occupation of HCHO adsorption centres by water vapour molecules during the prehumidification and/or 2) competition between water vapour and HCHO for these centres (Lee et al, 2013). All the functionalised sorbents adsorbed considerable amounts of water (Table 4.1) that can block the micropores which would be otherwise accessible to HCHO, limit the diffusion of the pollutant gas inside the pore structure, in this way decreasing the adsorption capacity. This decrease occurs even though some amount of HCHO is expected to be dissolved in the adsorbed water film. Nevertheless, no direct dependence between the amount of water adsorbed and the decrease in the saturation capacity was found.

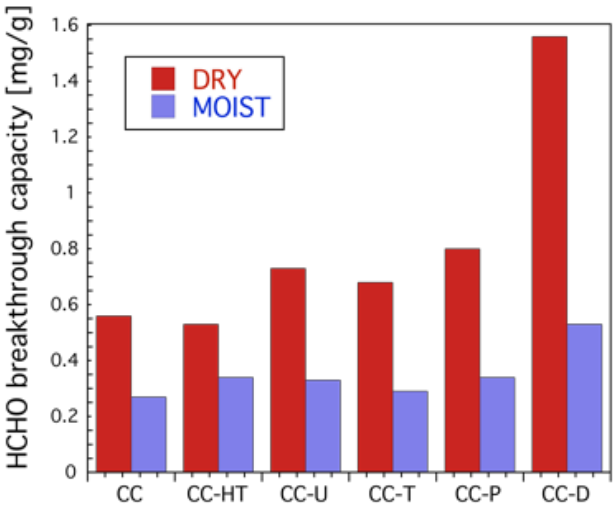

Fig. 4.2. Comparison of HCHO saturation capacity on the tested textiles. Reproduced from de Falco et al., 2018, see article 3) in the Introduction, copyright 2018 American Chemical society obtained.

To understand the adsorption behaviour of the tested materials, their surface features need to be extensively characterised. The measurement of the weight of the textile swatches before and after modification indicates weight losses of 23%,

25%, 29%, 34% and 27% for CC-HT, CC-U, CC-T, CC-P and CC-D, respectively. This highlights the high reactivity of the carbon fibers with the modifiers, especially in the case of CC-P, and since this reactivity might affect the porosity, the parameters of porous structure of the carbon textiles, raw and spent after HCHO adsorption under dry conditions, are collected in Fig. 4.3–4.5. CC is a predominantly microporous material ($\frac{V_M}{V_{tot}}$=88%) of high surface area, 921 m^2 g^{-1}. Heating it at 800°C only slightly decreased the porosity. The surface chemical/thermal treatment had a marked effect on the porosity. After this process, surface and pore volume decreased (Fig. 4.5), likely as a result of the deposition of the active phase/pore blocking. For CC-U, CC-T and CC-D a slight loss of porosity in the micropore region in the range 4–8 Å and 14–20 Å and in the mesopore region of 20–24 Å (Fig. 4.4) are found.

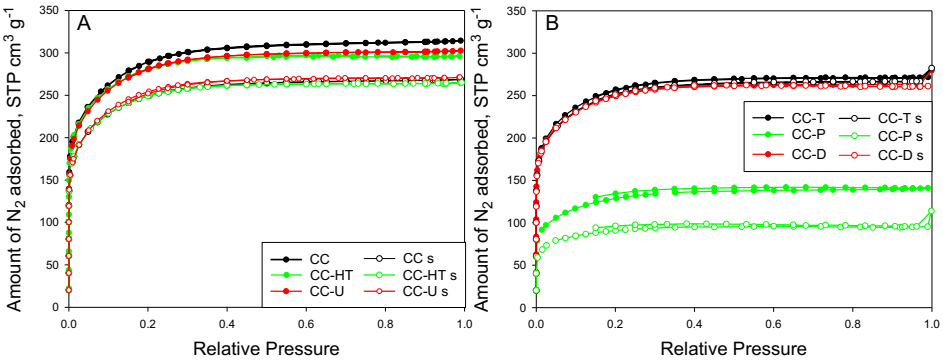

Fig. 4.3. A) Nitrogen adsorption isotherms for CC, CC-HT, CC-U fresh and spent (s) samples; B) Nitrogen adsorption isotherms for CC-T, CC-P, CC-D fresh and spent (s) samples (spent samples are those under dry conditions). Reproduced from de Falco et al., 2018, see article 3) in the Introduction, copyright 2018 American Chemical society obtained.

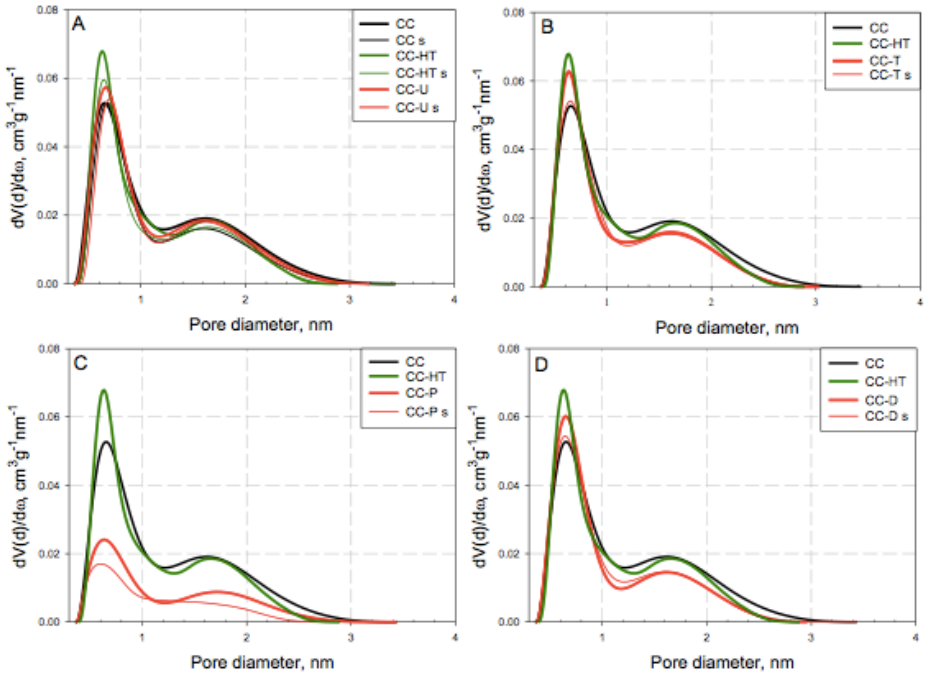

Fig. 4.4 Pore size distributions for the raw and spent (s) textiles under dry conditions: CC-U (A), CC-T (B), CC-P (C) and CC-P (D). In each figure, pore size distributions of CC and CC-HT are also included for comparison (in Fig. A, distributions for spent CC and CC-HT are included as well). Reproduced from de Falco et al., 2018, see article 3) in the Introduction, copyright 2018 American Chemical society obtained.

After HCHO adsorption, all the spent adsorbents, except CC-D, show a decrease in surface area and porosity (Fig. 4.5). Interestingly the porosity of CC-D did not change, in spite of its high adsorption capacity. In analysing this data, we have to take into account that owing to high vacuum and anticipated weak physical adsorption of HCHO in its unchanged form, HCHO is expected to be removed from the pore system before the porosity analysis. Therefore, the observed changes are likely caused by HCHO chemisorption/polymerisation and thus retention on the heteroatom-rich phase on the surface.

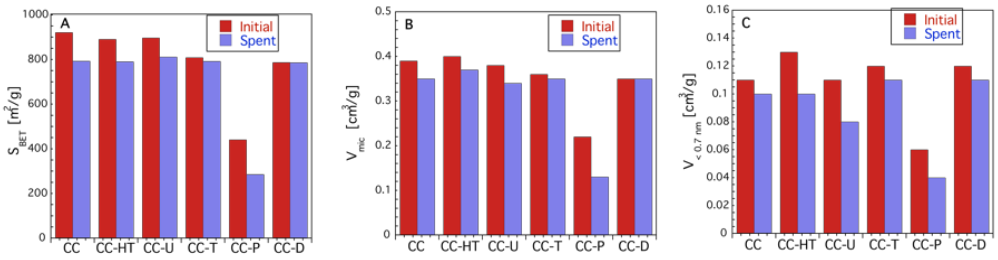

Fig. 4.5. Comparison of the structural parameters for the parent and spent samples in the dry conditions. A- BET surface area; B- micropore volume; C- volume in pores smaller than 0.7 nm. Reproduced from de Falco et al., 2018, see article 3) in the Introduction, copyright 2018 American Chemical society obtained.

This indicates a high dispersion of the active phase. For CC-P, on the other hand, a significant loss of the pore volume in the whole region of pore sizes (Fig. 4.4) is found. This suggests that the large molecule of penicillin G ($C_{16}H_{18}N_2O_4S$) blocks the micropores during the impregnation and its decomposition/carbonisation products remain at their entrances. While trends in the volume of micropores almost exactly follow the trend in the surface area, the most marked differences are seen in the volume of ultramicropores smaller than 0.7 nm. The volume of these pores decreases for CC-D, too. The biggest changes/decrease in porosity was found for CC-P (Fig. 4.4C and 4.5C), which suggests its strong chemical reactivity with HCHO. The high reactivity of the CC-P surface is reflected in the shape of the breakthrough curve, where a very increase in the measured HCHO concentration was recorded (Fig. 4.1). Although no relationship between the extent of the decrease in the volume of ultramicropores and the breakthrough capacity was established, these findings indicate the importance of the pores <0.7 nm for HCHO reactive adsorption.

Based on the above discussion, the surface chemistry is expected to have a marked effect on the amount of HCHO adsorbed on our materials. First, the acid/base character of the samples tested was investigated by potentiometric titration. The proton binding curves and pK_a distributions are presented in Fig. 4.6.

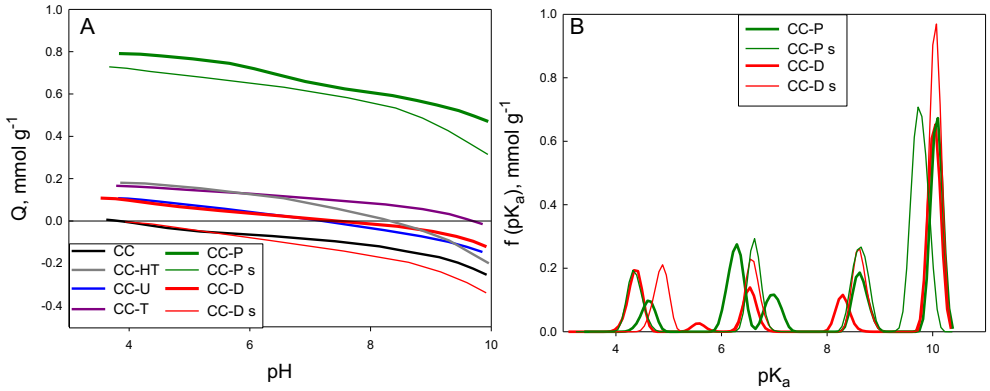

Fig. 4.6. A) Proton binding curves for CC, CC-HT, CC-U, CC-T, CC-P and CC-D; B) comparison of pK_a distributions of the groups present on the surface of CC-P and CC-D. Spent sorbents after adsorption of HCHO at dry conditions are designated with the letter "s". Reproduced from de Falco et al., 2018, see article 3) in the Introduction, copyright 2018 American Chemical society obtained.

Table 4.2 summarises the results and lists the relevance of groups in each category of strength: strongly acidic (3<pK_a<5), close to neutral (5<pK_a<8), and weakly acidic (8<pK_a<11). The treatment of CC, either by heating or impregnation with various precursors followed by heating, led to an increase in the surface pH value from 7.7 to 9.7 for CC-P. Moreover, the total relevance of dissociating groups in our experimental window decreased for all textiles but CC-HT. These results suggest the change in the speciation of the groups and their chemical nature due to the introduction of heteroatom (N and/or S) coming from the modifiers. Indeed, the proton binding curves clearly show a strongly basic character of CC-P and CC-D surfaces (only proton uptake), while the other modified textiles are amphiprotic. The parent CC is rather acidic (proton release) and the heat treatment increases its basic character. Interestingly, some acidification of spent CC-D and CC-P is found after HCHO adsorption. Those are in fact samples on which a gradual increase in the slope of the breakthrough curves

was recorded under dry conditions (Fig. 4.1). This shape suggests some surface reactivity.

Table 4.2. Amount of functional groups in various acidity ranges (in mmol g^{-1}) on the surface of carbons cloths before and after exposure to HCHO. Reproduced from de Falco et al., 2018, see article 3) in the Introduction, copyright 2018 American Chemical society obtained.

Sorbent	**pH[a]**	**Strongly acidic 3<pK_a<5**	**Neutral 5<pK_a<8**	**Weakly acidic 8<pK_a<11**	**All**
CC	7.7	0.08	0.04	0.30	0.42
CC-HT	8.3	0.04	0.08	0.36	0.48
CC-U	8.6	0.04	0.1	0.24	0.35
CC-T	8.6	0.03	0.05	0.19	0.27
CC-P	9.7	0.04	0.13	0.25	0.41
CC-D	8.2	0.07	0.04	0.23	0.34
CC-D s	7.8	0.05	0.10	0.35	0.50
CC-P s	9.3	0.07	0.10	0.42	0.59

[a]In electrolyte solution ($NaNO_3$).

The surfaces of our samples were investigated by thermogravimetric analysis, as well. The TG and DTG curves for the raw and spent adsorbents, measured in helium, are collected in Fig. 4.7. For all the raw samples, the total weight loss ranged between 6–22% (Fig. 4.7A). A 12% weight loss for CC at about 400°C is linked to the removal of a not-peel-off after boiling nylon (Florent et al., 2017). In fact, it could be considered as an intrinsic modifier of CC-HT. The first peak on the DTG curves (Fig. 4.7B) centred at about 80°C likely represents the removal of physically adsorbed water and/or formaldehyde in the case of the spent samples.

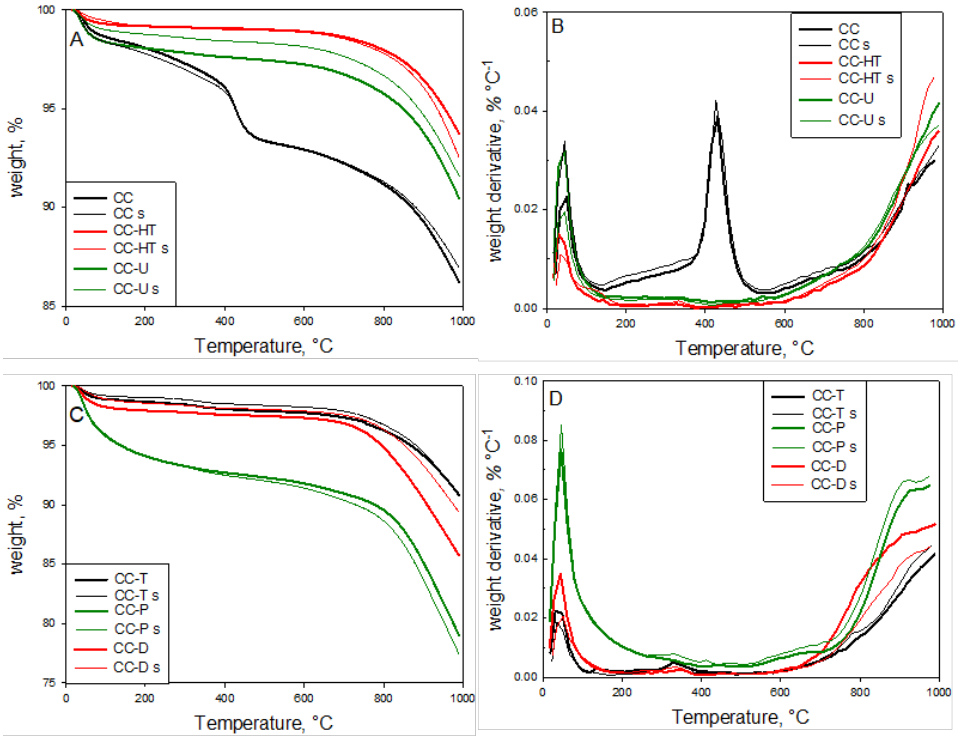

Fig. 4.7. A-B) TG-DTG curves for CC, CC-HT and CC-U fresh and after adsorption of formaldehyde. C-D) TG-DTG curves for CC-T, CC-P and CC-D fresh and spent after adsorption of formaldehyde. Spent samples at dry conditions are designated with the letter "s". Reproduced from de Falco et al., 2018, see article 3) in the Introduction, copyright 2018 American Chemical society obtained.

The results show that all the raw or spent samples, but CC-P, are rather thermally stable up to 800°C (synthesis temperature). In the case of CC-P, a gradual weight loss is observed between 100 and 750°C. The gradual weight loss for raw CC-P implies the highest reactivity of the penicillin-derived phase among all the samples, and this reactivity can affect the mechanism of HCHO retention on this sample. Among all the raw samples, only CC-T shows the groups decomposing between 300 and 400°C and this must be the fingerprint of its modifier, likely related to the sulphur environment. Sulphones formed on the

surface during stabilisation/cooling are expected to decompose in this temperature range (Zhao et al., 2012).

After HCHO adsorption, a new peak between 300 and 400°C appears in the DTG curves for CC-P and CC-D. Moreover, the weight loss pattern at temperatures >800°C is also altered indicating some surface reactivity/deposition of new compounds resulting from the samples' exposure to HCHO. The weight loss between 300 and 400°C might be due to the decomposition of species formed as a result of the surface reactivity of this carbon with HCHO. As discussed above, only for these two samples the surface acidity increased after HCHO exposure. The intensity of these peaks is low but the amounts adsorbed on our samples are generally in the range of a fraction of mg g^{-1} (CC-D is an exception). An unaltered peak representing removal of nylon from CC suggests its chemical inertness in the process of HCHO reactive adsorption.

The MS analysis of the species released from the surface during thermal analysis further confirms the observations based on the weight loss discussed above. In the analysis, we focus on the features of *m*/*z* 18, 28, 29, 30, 44 and 48 thermal profiles. Since they represent H_2O, CO, HCO, HCO/NO, CO_2 and SO, respectively, they were chosen as the most relevant to depict the changes in chemistry upon HCHO adsorption. The detailed results are presented in Fig. 4.8 and 4.9.

Comparison of the trends in *m*/*z* profiles for the parent and exposed samples leads to the following general observations on the effects of HCHO exposure: 1) for *m*/*z* 44, a new peak and an increase in the relative intensity of the signal appears at temperatures less than 200°C, which supports the view of a change in surface chemistry upon HCHO exposure. The most drastic changes in *m*/*z* 44 thermal profiles are seen for CC-P, CC-T and CC-HT; 2) no conclusion on physically adsorbed HCHO can be drawn since *m*/*z* 28 (CO) and *m*/*z* 29 (HCO) have similar patterns. This indicates that these species are released during the low temperature heating of the raw carbons, too, and could also be desorbed from the surface in the time between the breakthrough tests and thermal analysis experiments; 3) sulphur species are involved in HCHO reactive adsorption since their thermal

stability changed as indicated by an increase in the intensity of *m*/*z* 48 for CC-HT and CC-T at T>700°C. The effect is the strongest for CC-T, which in fact shows the highest amount of sulphur on the surface (cf. infra in Table 4.3); 4) for CC-D, there is a visible change in the shape of the thermal profile for *m*/*z* 30 suggesting the marked alteration in the nitrogen environment upon exposure to HCHO. The *m*/*z* 44 (CO_2) pattern for CC-P and its change after HCHO exposure deserves further attention. As discussed above, the change in porosity for this sample after formaldehyde adsorption was the most marked. The explanation is in the high reactivity of this sample's carbon phase with HCHO, which is retained as chemically bound to the surface or in the polymerised form blocking the small pores. Indeed, the comparison of *m*/*z* 44 for all the samples shows the low thermal stability/high reactivity of CC-P (CO_2 is released from various surface environments in the whole temperature range). Exposing this sample to HCHO changes this pattern and less CO_2 is released at low temperature from the most reactive/unstable surface environment characterising CC-P. To further analyse the effects of surface chemistry on the HCHO adsorption on the textiles, XPS analysis was carried out. The surface elemental composition is listed in Table 4.3 and the deconvolution of C 1*s*, O 1*s*, N 1*s* and S 2*p* core energy levels is in Table 4.4. Fig. 4.10 presents examples of deconvolution. The results show that the surface of the textiles markedly changes upon the applied modifications, and all the treated textiles contain more carbon and less oxygen and nitrogen than the parent CC.

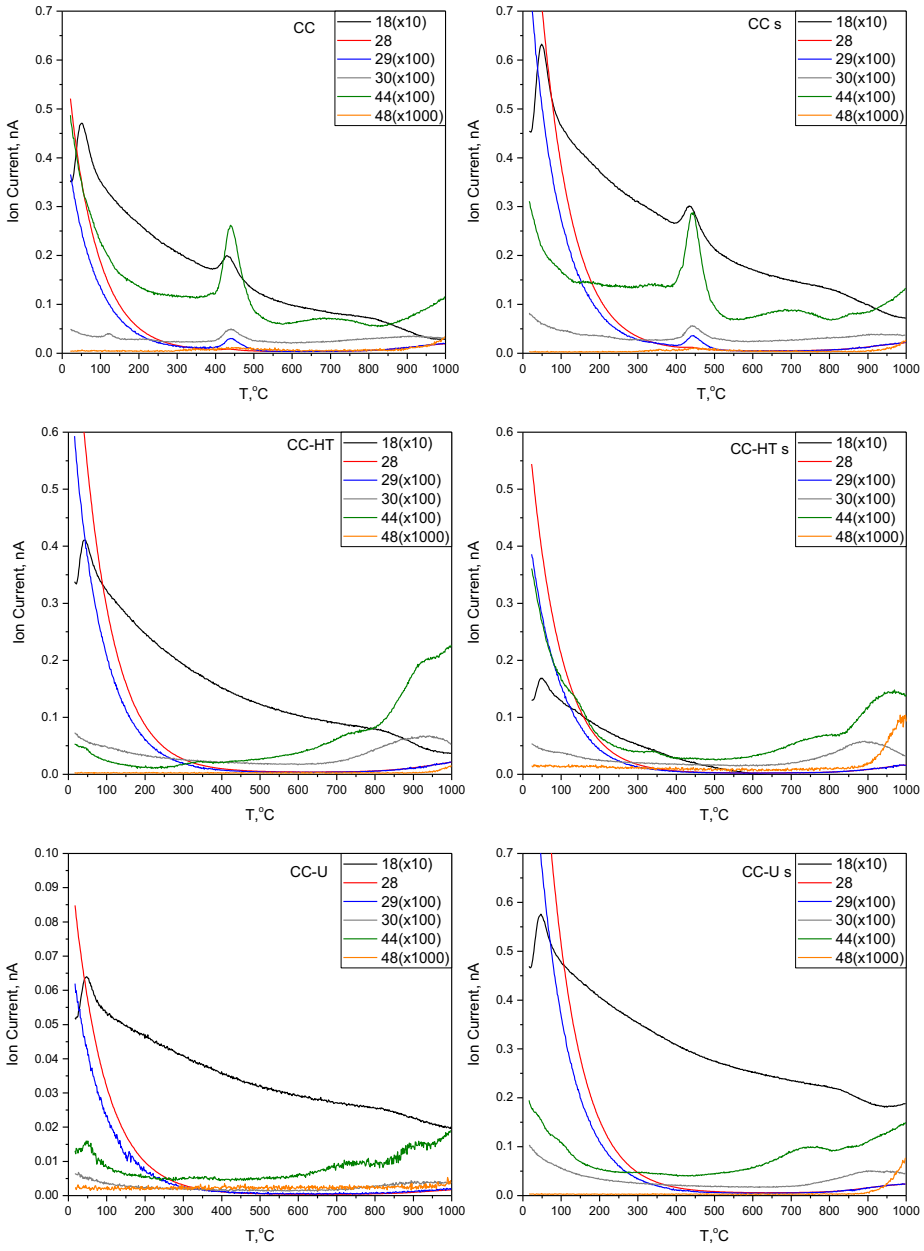

Fig. 4.8. Selected *m/z* thermal profiles for CC, CC-HT and CC-U, raw and spent under dry conditions. Reproduced from de Falco et al., 2018, see article 3) in the Introduction, copyright 2018 American Chemical society obtained.

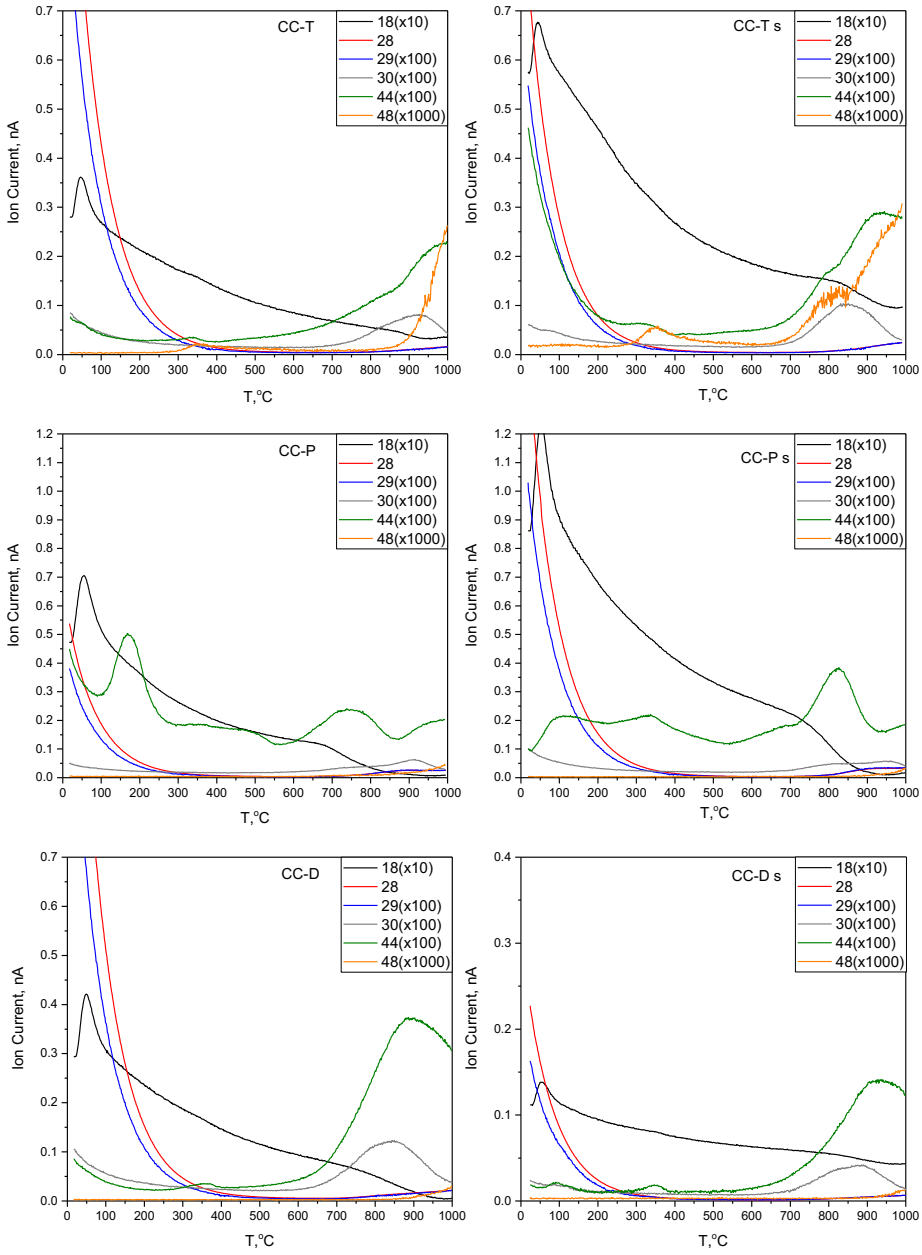

Fig. 4.9. Selected *m/z* thermal profiles for CC-T, CC-P and CC-D, raw and spent ("s") under dry conditions. Reproduced from de Falco et al., 2018, see article 3) in the Introduction, copyright 2018 American Chemical society obtained.

Table 4.3. XPS elemental composition of the surface of the textiles (in % at.). Reproduced from de Falco et al., 2018, see article 3) in the Introduction, copyright 2018 American Chemical society obtained.

Textile	C	O	N	S
CC	78.4	14.1	5.6	1.9
CC-HT	84.3	12.3	3.2	0.2
CC-U	82.5	13.2	3.3	1.1
CC-T	81.2	9.3	4.3	5.1
CC-P	85.1	9.7	3.5	1.7
CC-D	83.5	11.3	4.5	0.7

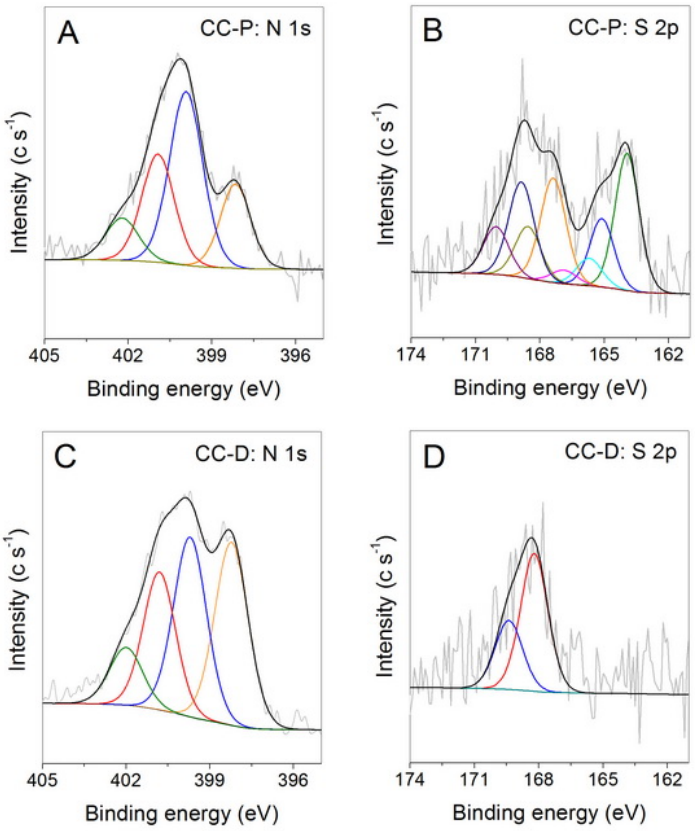

Fig. 4.10. Deconvolution of N 1*s* and S 2*p* core energy levels for A-B) CC-P and C-D) CC-D. Reproduced from de Falco et al., 2018, see article 3) in the Introduction, copyright 2018 American Chemical society obtained.

Table 4.4. Results of the deconvolution of the XPS spectra of C 1*s*, O 1*s*, N 1*s* and S 2*p* (in bold -atomic % of specific elements). Reproduced from de Falco et al., 2018, see article 3) in the Introduction, copyright 2018 American Chemical society obtained.

binding energy [eV]	bond assignment	CC [%]	CC-HT [%]	CC-U [%]	CC-T [%]	CC-P [%]	CC-D [%]
C 1s		**78.4**	**84.3**	**82.5**	**81.2**	**85.1**	**84.1**
284.7	C–C sp^2	67.0	59.2	66.6	69.2	69.2	73.6
286.0–286.2	C–O (phenol, alcohol, ether), C–N (amine, amide	18.9	23.9	18.9	16.8	16.4	16.5
287.2–287.7	C=O (carbonyl, quinone), O=C–N (amide)	6.4	5.8	6.6	6.0	5.9	5.2
288.6–288.9	O=C–O (carboxyl)	4.4	5.7	4.7	4.0	4.6	3.1
291.0	$\pi \rightarrow \pi^*$, π-electrons in aromatic rings	3.3	5.5	3.1	3.9	3.8	1.6
O 1s		**14.1**	**12.3**	**13.2**	**9.3**	**9.7**	**11.4**
530.6–531.2	C=O (aromatic)	29.4	29.3	21.3	22.6	22.2	24.7
531.9–532.3	C=O (aliphatic)	45.4	48.8	58.4	49.0	49.6	57.3
533.1–533.5	C–O	25.2	21.9	20.3	28.4	28.2	18.1
N 1s		**5.6**	**3.2**	**3.3**	**4.3**	**3.5**	**4.5**
398.2–398.4	pyridine	10.6	13.6	15.4	33.9	19.2	33.0
399.7–399.9	pyrrole, amine, amide	56.6	49.7	42.7	34.7	43.7	32.3
400.8–401.1	quaternary nitrogen/ammonium	24.7	28.4	32.3	24.8	26.3	24.2
402.0–402.5	pyridine-N-oxide, C–N^+O–C, NO_x	8.0	8.3	9.7	6.6	10.6	10.5
S $2p_{3/2}$		**1.9**	**0.2**	**1.1**	**5.1**	**1.7**	**0.7**
163.8–163.9	R–S–S– in thiol, bisulfides	14.9	ND		71.0	36.3	
165.7–166.0	R_2–SO		ND		12.4	7.7	
166.8–167.4	SO_3^{2-} (sulfines)	67.6	ND	26.3	6.9	29.3	
168.2–169.0	HSO_3^- (sulfonic acids)	17.5	ND	73.7	9.7	26.7	100.0

Moreover, CC contains a significant amount of sulphur (1.9% at.), as well. Upon the treatments applied, its content decreases for all the samples but for CC-T. To CC-T, sulphur was introduced in the thiourea modifier. The heat treatment of CC almost removes sulphur from its surface and the content of nitrogen significantly decreases.

All the compounds used for the modification of the CC textiles contain nitrogen and, additionally, two of them (penicillin G and thiourea) contain also sulphur. Thus, these heteroatoms are expected to exist on the surface of our textiles in various configurations. The heat treatment decreases the S and N contents and further changes in chemistry should be analysed in comparison with the surface features of CC-HT. After the surface treatment, more nitrogen is incorporated to the carbon surface in the form of pyridines, whose contributions significantly increased (15.4–33.9%) compared to that for the CC or CC-HT samples (10.6% at. and 13.6% at., respectively). These pyridines, along with amines, can participate in coupling reactions (Mannich reaction, see Blicke, 2011) with formaldehyde forming amino-carbonyl compounds. The covalent bond

formation can explain a decrease in the volume of ultramicropores after HCHO adsorption.

The sulphur on the parent CC textile is mainly in the form of sulphines (67.6%) and sulphonic acids (17.5%). Modification with dicyandiamide leads to total oxidation of sulphur to the latter species while, with urea, to sulphines (26.3%) and sulphonic acids/sulphonates (73.7%). The total sulphur content on CC-D and CC-U textiles is much lower than that on CC – so, most likely, sulphur originated from the parent CC textile is covered on the surface by the products of modification. On the other hand, the surface treatment with N- and S-containing penicillin G and thiourea results in either the same S-doping level as on CC (1.7% for CC-P), or its significant increase (5.1% for CC-T). Interestingly, sulphur in the case of CC-P and CC-T textiles is substantially present in the most reduced forms (36.3% for CC-P and 71.0% for CC-T), while in the case of samples treated with dicyandiamide and urea (i.e. reagents not containing sulphur) it is present mainly in the form of sulphines and sulphonic acids.

While the lowest HCHO breakthrough capacities are found for the raw CC sample and for CC-H, the performance of the modified textiles significantly improved. As discussed above on the basis of porosity, the observed differences in the HCHO adsorption must be rather linked to the chemical composition of the textile surfaces. The results indicate that there is no direct relationship between C, O, S and particularly N content on the surface, and the formaldehyde adsorption capacity. The common interpretation of an increase in HCHO adsorption on carbon-based materials discussed in the literature is that the nitrogen content controls the formaldehyde adsorption capacity (Lee et al., 2013). This, however, does not seem to be true in our case. A close look at the particular surface species after deconvolution of N 1*s* and S 2*p* core energy level spectra leads to some interesting observation. The raw CC textile has the majority of its nitrogen in the form of pyrroles, amines and amides (56.6%) – considerable portion of them coming from unremoved nylon traces. This is confirmed by the higher content of oxygen, which nylon is also composed of (McIntyre, 2005). Thus, repulsive interactions between nylon and carbonyl groups of formaldehyde, and those of

nylon (which are always located next to the amide nitrogen), might be partially responsible for the lower HCHO uptake on this textile. Apparently, amides groups of nylon do not advance the HCHO adsorption. Apart from that, the content of pyridinic nitrogen on CC is the lowest among all the samples and this nitrogen, if present on the surface, can participate in the Mannich reaction. The surface pH values collected in Table 4.2 show that the CC cloth is the least basic (pH=7.7) among all textiles tested (pH=8.1–9.7). Some reports in the literature suggest that the HCHO adsorption capacity is strongly related to the density of basic surface functional groups (Carter et al., 2011). Thus, the lower density of those groups in the case of CC sample leads to the smaller HCHO uptake. Even though the basicity of CC-HT increases in comparison with that of CC, CC-HT has much less nitrogen and thus less species available for specific interactions with HCHO, which results in comparable capacities for these two samples.

The CC-D textile exhibits the highest HCHO uptake (1.56 mg g^{-1}). This is likely due to the presence of specific N and S surface species enhancing the interactions with formaldehyde. Indeed, in the case of this sample, the content of pyridinic nitrogen is three times higher than that on CC. These groups increase the basicity of the surface and contribute to the Mannich reaction. Nitrogen in these configurations was also indicated as promoting to the formation of superoxide ions O_2^- (Strelko et al., 2000), which might contribute to the HCHO mineralisation when adsorbed in the ultramicropores. This, and the Mannich reaction, can oppositely affect the porosity evolvement resulting in the unchanged surface area.

The uniqueness of our carbon materials compared to those previously studied is in the presence of S species incorporated to their surface. Thus, the sulphur exclusively as sulphonic acids in CC-D, despite its low content (only 0.7%), can increase the HCHO adsorption by the reaction to form α-hydroxymethanesulphonates (Möller, 2010). The condensation of aromatic sulphonates with formaldehyde is a possible pathway here (Papalos, 1982), too, and the formed product can bring about pore blocking and therefore lead to a decrease in the surface area. CC-T, on the other hand, shows the highest content

of sulphur (5.1%) but only a fraction of it (9.7%) is in the form of sulphonates/sulphonic acid. Thus, despite similar content and distribution of nitrogen as that in CC-D, HCHO adsorption capacity for CC-T is much lower than for CC-D. These two samples are characterised by similar porosity. Additionally, the less polar pyridine N-oxide species are present on the CC-T surface in a smaller quantity than on that of CC-D, and they might contribute to the enhanced adsorption of HCHO on the latter sample. CC-P, even though showing the least developed porous structure when compared to the other textiles, has a considerable amount of sulphur in the form of sulphites/sulphonic acid, which can enhance the HCHO adsorption. Its surface also shows the highest basicity (pH=9.7, Table 4.2) and basic amines can participate in the Mannich reaction. CC-U shows a similar amount of sulphonic acids than that for CC-D, however the content of pyridines and pyridine N-oxides is lower than that for CC-D. This leads to the twice smaller HCHO uptake on CC-U than on CC-D.

To look at the results in a more quantitative way, and as discussed above, CC-D performs better than do CC and CC-HT because of more pyridinic species on its surface. Even though CC-D shows the same absolute amount of pyridines as CC-T does (Table 4.5), it has much more sulphonic acids (0.7% at. on CC-D as oppose to 0.49% at. on CC-T). The HCHO uptake on CC-U is similar as that on CC-T and smaller than that on CC-D, because even though CC-U has a similar absolute content of sulphur as CC-D does (0.82 vs. 0.7%), its content of pyridinic nitrogen is in fact three times smaller (3.3×0.154=0.5%) than that for CC-D.

Table 4.5. Absolute contributions of pyridinic nitrogen and sulphonic sulphur on the surface, and the amount of adsorbed HCHO. Reproduced from de Falco et al., 2018, see article 3) in the Introduction, copyright 2018 American Chemical society obtained.

Sample	Amount of pyridinic nitrogen [%]	Amount of sulphonic sulphur [%]	Amount of adsorbed HCHO [mg g^{-1}]
CC	0.59	0.33	0.56
CC-HT	0.49	0.2	0.53
CC-U	0.51	0.82	0.73
CC-T	1.46	0.49	0.68
CC-P	0.67	0.45	0.80
CC-D	1.48	0.70	1.56

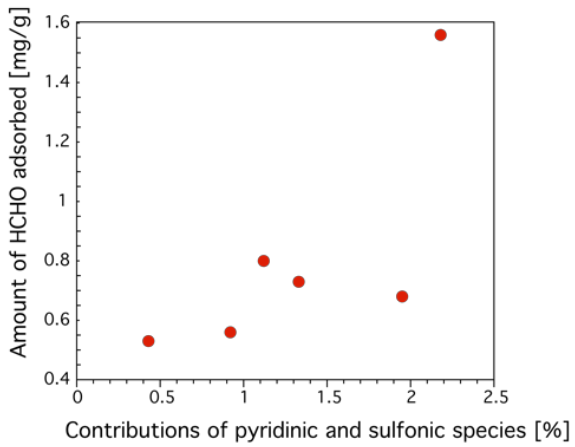

Fig. 4.11. Relationship between the amount of HCHO adsorbed and the sum of the absolute contributions of pyridinic and sulphonic species. Reproduced from de Falco et al., 2018, see article 3) in the Introduction, copyright 2018 American Chemical society obtained.

As seen in Fig. 4.11, the amount of adsorbed HCHO increases with an increase in the absolute amount of sulphonic and pyridinic groups on the surface. However, we do not expect the fully linear behaviour owing to the complexity of the textile surfaces' chemistry and porosity.

The porosity, even though the differences between samples are not substantial, plays a role, as well. The pores close in size to the HCHO molecule attract it with the strongest forces. The order for volume of pores smaller than 0.7 nm (Fig. 4.5C) (CC-P<CC&CC-U<CC-T and CC-D) resembles the one for the breakpoint time reported in Table 4.1 (CC-P<CC<CC-T&CC-U<CC-D). Nevertheless, functional groups that are important for specific interactions/reactive adsorption can only exist at the entrance of ultramicropores or in larger pores, which can accommodate their geometry. Therefore, chemical modifications applied to the textiles increase the utilisation of the carbon fiber surface towards retention of HCHO.

Even though the polar character of the surface can be roughly estimated based on the adsorption of water vapour during prehumidification, and the order in the quantity of water vapour adsorbed indicates that CC-T, CC-D and CC-P are the least hydrophilic ones, this is rather owing to their low oxygen content. These results might be affected by water vapour adsorption kinetics. The most detrimental effect of water vapour preadsorption/competition for HCHO adsorption is found in fact for CC-D and CC-P. There is a high probability that, on the surface of these textiles, water is formed in condensation reactions with involvement of formaldehyde. *In situ* adsorption of this water on the most polar centres or in small pores, where it is formed, can further block the adsorption centres for HCHO.

It should be mentioned here that the exact identification of the groups responsible for the uptake of formaldehyde is not easy as the surface of the textiles is complex and a broad range of O, N and S species is present. Additionally, the differences in the porous structure also affect the interactions of HCHO with the surface. However, it is clearly seen that the content of nitrogen itself cannot be considered as the only factor influencing the adsorption capacity. Its speciation is important. Besides, very polar sulphur groups (particularly sulphonic acids) also play an important role by providing highly active adsorption sites for HCHO adsorption. Since HCHO may behave as both a Lewis acid and a Lewis base, it can potentially interact with both basic (e.g., pyridine, amines pyridine N-oxide)

and acidic (e.g. carboxylic, sulphonic) surface groups. In literature, there is no study on the effect of sulphur on the adsorptive behaviour of carbon materials as formaldehyde removal media, so this is a very first report about the role of sulphur in enhancing the HCHO uptake.

4.2 Results and discussion for activated carbon sorbents

The HCHO breakthrough curves measured at room temperature in dry (A) and wet (B) conditions on the tested carbons are presented in Fig. 4.12. From them, the adsorption parameters were calculated and they are listed in Table 4.6, in which $t_{br,s}$ [min g^{-1}] is here the specific breakthrough time (assumed as the time for which $C_{HCHO}^{out}(t)/C_{HCHO}^{in}$=0.05) divided by the mass of sample used. Table 4.6 lists the specific amount of water adsorbed [g g^{-1}] during the prehumidification step, too.

The HCHO breakthrough curves, in dry condition on the parent BAX and S208, are steep, which indicates fast kinetics of the adsorption process (Fig. 4.12A). Even though S208 is characterised by a shorter breakpoint time than BAX (almost 27% less), ca. 20% more HCHO is adsorbed on that carbon than on BAX. PSC and S208 have similar breakthrough capacities but $t_{br,s}$ of the former is 3 times longer compared to that of S208. The treatment of BAX with thiourea or melamine resulted in a significant increase in both quantitative parameters of HCHO adsorption, compared to those for raw BAX. Thus, the breakthrough point time increased from 44 min g^{-1} to 87 and 215 min g^{-1}, respectively, and the HCHO breakthrough capacities reached values equal to 0.40 and 0.66 mg g^{-1} for BAX-T and BAX-M, respectively.

The presence of moisture on the carbon and in the feed gas decreased $t_{br,s}$ and the adsorption capacities for all samples (Fig. 4.12B, Table 4.6). This is likely caused by the adsorption of water vapour on the active sites of the adsorbents. It occurs as a competitive process during the reactive adsorption, and during the prehumidification process (Lee et al., 2013). Even though the carbons adsorb large quantities of water vapour (Table 4.6), this does not contribute to an increase in the adsorption capacity considering the possibility of HCHO dissolution in a water

film. On the other hand, water molecules likely block the pore entrances and/or occupy the polar centres on which HCHO would be otherwise adsorbed. In particular, the most marked decrease in the amount of adsorbed HCHO is found for S208 and PSC. For both carbons, $\omega_{s,ads}$ decreased of about 38%. $t_{br,s}$ decreased of 28 and 54% for S208 and PSC, respectively. Interestingly, for BAX, BAX-T and BAX-M in the moist conditions, $\omega_{s,ads}$ decreased only of 8, 15 and 14%, and $t_{br,s}$ of 20, 17 and 14%, respectively, which suggests differences in the adsorption mechanisms between the BAX series and the other two carbons tested.

To understand the differences in the performance of the carbons and to identify the surface features relevant to the HCHO retention, the porosity and surface chemistry of our carbons were extensively studied. Nitrogen adsorption isotherms were measured and, from them, the parameters of the pore structure and pore size distributions, PSD, were calculated (Table 4.7 and Fig. 4.13). The porosity of the exhausted samples in dry conditions was evaluated, too.

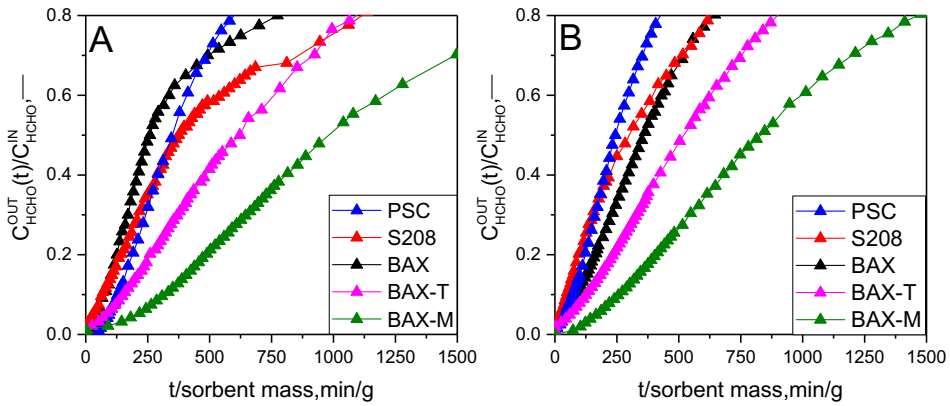

Fig. 4.12. HCHO breakthrough curves measured in dry (A) and moist conditions (B).

Table 4.6. HCHO adsorption parameters in dry and moist conditions.

Sorbent	C^{IN}_{HCHO} [ppmv] Dry	$\omega_{s,ads}$ [mg g^{-1}] Dry	$t_{br,s}$ [min g^{-1}] Dry	C^{IN}_{HCHO} [ppmv] Moist	Water adsorbed [g g^{-1}]	$\omega_{s,ads}$ [mg g^{-1}] Moist	$t_{br,s}$ [min g^{-1}] Moist
PSC	1.22	0.31	96	1.22	0.21	0.20	44

S208	0.94	0.31	32	0.94	0.21	0.19	23
BAX	1.18	0.25	44	0.99	0.61	0.23	35
BAX-T	0.94	0.40	87	1.01	0.58	0.34	72
BAX-M	0.94	0.66	215	1.02	0.64	0.57	185

BAX is a micro/mesoporous carbon ($\frac{V_M}{V_{TOT}}$=55%), with the most developed surface area equal to 2175 m^2 g^{-1}. Its main pore sizes are 0.65, 1.1, 1.9 and 3.6 nm (Fig. 4.13 C-D). After modifications with thiourea and melamine, the porosity changes and the surface area decreased to 1288 and 1588 m^2 g^{-1} for BAX-T and BAX-M AC, respectively.

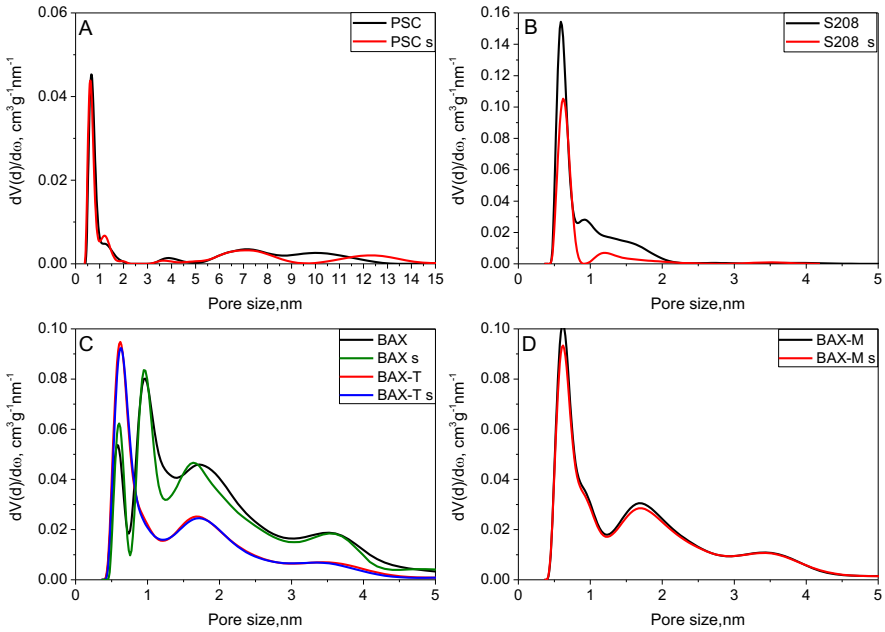

Fig. 4.13. Pore size distributions for raw and spent sorbents in the dry conditions (spent are designated with letter "s"): A) PSC, B) S208 C) BAX and BAX-T, D) BAX-M.

Table 4.7. Parameters of the porous structure calculated from nitrogen adsorption isotherms.

Carbon	S_{BET} [$m^2\ g^{-1}$]	V_{TOT} [$cm^3\ g^{-1}$]	V_M [$cm^3\ g^{-1}$]	$V_{<7Å}$ [$cm^3\ g^{-1}$]	$V_{<10Å}$ [$cm^3\ g^{-1}$]
Raw carbons					
PSC	433	0.40	0.17	0.08	0.14
S208	1042	0.50	0.47	0.24	0.34
BAX	2175	1.32	0.73	0.10	0.26
BAX-T	1288	0.72	0.50	0.17	0.29
BAX-M	1558	0.90	0.58	0.19	0.32
Spent carbons in dry conditions					
PSC	376	0.35	0.16	0.09	0.13
S208	509	0.26	0.25	0.17	0.21
BAX	1979	1.20	0.67	0.08	0.24
BAX-T	1260	0.70	0.49	0.16	0.28
BAX-M	1475	0.86	0.55	0.18	0.30

Interestingly, the volume of ultramicropores <7 Å almost doubled, while those pores in BAX with mean size around 1.1 nm almost disappeared, which might be related to the incorporation of thiourea and melamine onto the carbon matrix and to an increase in the carbonisation level (BAX was synthesised at about 600°C). Even though both modifications resulted in similar trends in the porosity changes, the thiourea treatment decreased the porosity to a slightly greater extent than the melamine's. Among all the tested carbons, PSC has the smallest surface area (1/4 of that of BAX and about 1/2 of that of S208). Its volume of ultramicropores is similar to that of BAX but four times smaller than that of S208. From the point of view of physical adsorption via dispersive forces, these pores are expected to be the most active in HCHO retention. S208 is the most microporous ($\frac{V_M}{V_{TOT}}$=94%) among all the tested carbons.

After HCHO adsorption in dry conditions, the parameters of porous structure decreased. Since the samples were outgassed under high vacuum at 120°C before the measurement, and all the physically adsorbed HCHO was expected to be removed under those conditions, the observed decrease in the

surface area and porosity might be related to either HCHO polymerisation or its reaction with the carbon functional group: as a result of each, some pore could be blocked to N_2 molecules. More specifically, the BET surface area decreased of 9, 51, 13, 2 and 5% for BAX, S208, PSC, BAX-T and BAX-M, respectively. This implies that, for S208 and PSC, the surface chemistry in micropores or at their entrance was most involved in the HCHO reactive adsorption process.

Since the results obtained suggest that the porosity is not the only factor determining the performance of our carbons, their surface chemistry was analysed in detail. First of all, Fig. 4.14 collects the TG and DTG curves measured in helium for the parent and spent samples in dry conditions.

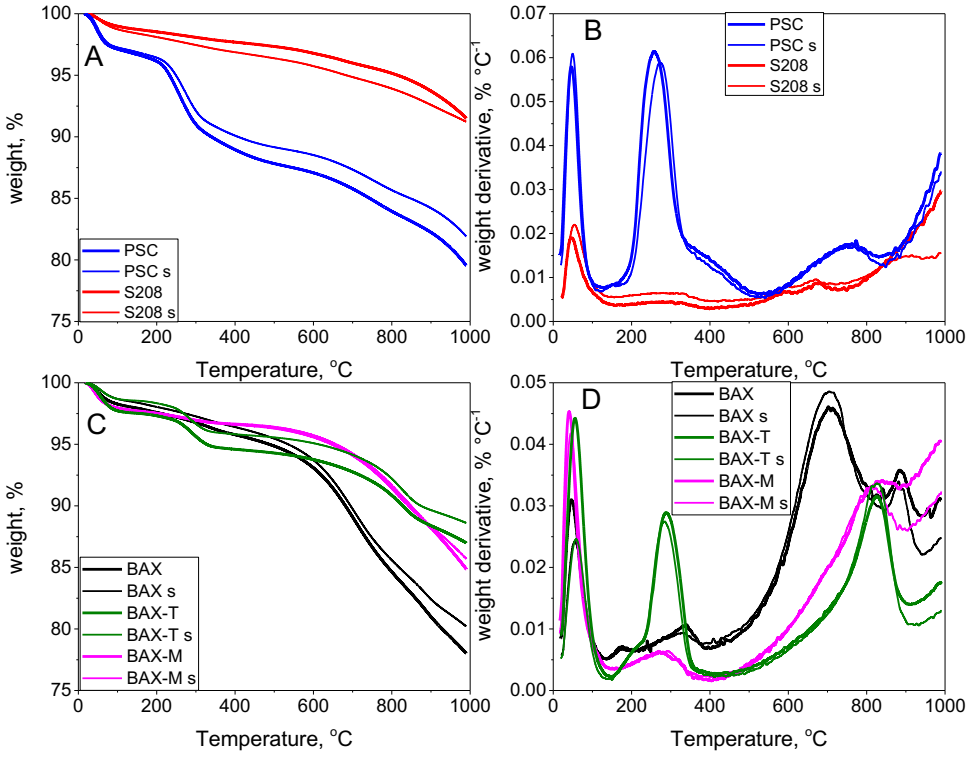

Fig. 4.14. TG (A, C) and DTG curves (B, D) for the parent and spent carbons in dry conditions (spent designated with letter "s"): A-B) PSC and S208, C-D) BAX, BAX-T and BAX-M.

The DTG peaks represent the extent of the weight loss linked to the decomposition of distinct surface species. The total weight loss for all the parent samples was between 7–25% (Fig. 4.14A and C), which is related to the differences in the content of heteroatoms and their chemical environment. The weight loss below 150°C is related to the removal of physically adsorbed water/formaldehyde. The weight loss over 800°C, and for BAX after 600°C, should not be analysed since the samples were originally not exposed to these temperatures. S208 appears as the most thermally stable with weight loss about 7%. Its groups decompose mainly over 500°C and, assuming that oxygen is mainly present on the surface of this commercial carbon, this weight loss represents the removal of phenols (Bandosz and Ania, 2006). BAX is richer in the surface groups than is S208, and its carboxylic acids decompose between 200 and 400°C. In the modification with melamine, these groups were apparently decomposed/consumed. As a result of this process, a marked amount of groups decomposing between 500 and 800°C was incorporated to the surface. The thiourea treatment introduced groups decomposing between 200 and 350°C and at about 800°C. Since they overlap with those on the DTG curves of PSC, which is expected to be rich in sulphur, we link these temperature weight losses mainly to the decomposition of oxidised sulphur species. Apparently, the amount of these species and also their chemical nature is more diverse on the surface of PSC than on that of BAX-T. After exposure to HCHO, no marked change in the weight loss pattern was found, likely owing to the fact that rather small amounts of HCHO were adsorbed and the changes, if any, were below the sensitivity of the method. Nevertheless, a decrease in the weight loss, especially for S and N containing carbons, suggests an improved thermal stability of the surface, likely due to their interactions/reactions with HCHO.

To further study the chemistry of our adsorbents, the thermal decomposition products were analysed by mass spectrometry and relevant *m*/*z* thermal profiles are collected in Fig. 4.15. For the analysis, thermal profiles of *m*/*z* 18, 28, 29, 30, 44 and 48, which represent H_2O, CO, HCO, HCHO/NO, CO_2 and SO, respectively, were chosen owing to their relevance to surface chemistry and

the changes in these features. For BAX-M, *m*/*z* 17 representing NH_3 was selected, as well. The detection of *m*/*z* 48 and its thermal profile for PSC and BAX-T confirm the presence of S on their surface, and some similarities and differences in their chemical nature. Formaldehyde apparently interacted with those species, demonstrated by an increase in the peaks' intensity and changes in their patterns. For S208 after HCHO exposure, the profile for CO (*m*/*z* 28), representing the decomposition of OH groups at high temperature, changed so suggesting the involvement of these groups in HCHO adsorption and/or a release of CO as a result of HCHO retained on the surface. These *m*/*z* values also markedly changed after HCHO adsorption for the BAX series. For BAX-M and S208, also the thermal profiles of *m*/*z* 44, representing CO_2, showed some alteration as a result of carbon surface interactions with HCHO. Generally, the changes are not dramatic owing to, as indicated above, the small amounts of HCHO adsorbed, from which a significant portion is expected to be adsorbed in pores through dispersive interactions.

The surface chemistry of the studied carbons was investigated by potentiometric titration method, too. Fig. 4.16 shows the proton binding curves. The relevance of groups in the category strongly acidic ($3<pK_a<5$), close to neutral ($5<pK_a<8$), and weakly acidic ($8<pK_a<11$) are listed in Table 4.8. An increase in the acidity of the sample modified with thiourea is found, and the one modified with melamine became more basic. Moreover, the functionalisation treatments led to a reduction in the amount of dissociating groups (Table 4.8) due to the introduction of new chemical species (N, S and N/S groups) that modified the surface of BAX. While S208 presents a basic character with the initial pH equal to 8.4, PSC is very acidic (pH=3.3). Additionally, the proton binding curves display the strong acidic character for PSC whereas all the other carbons are amphiprotic.

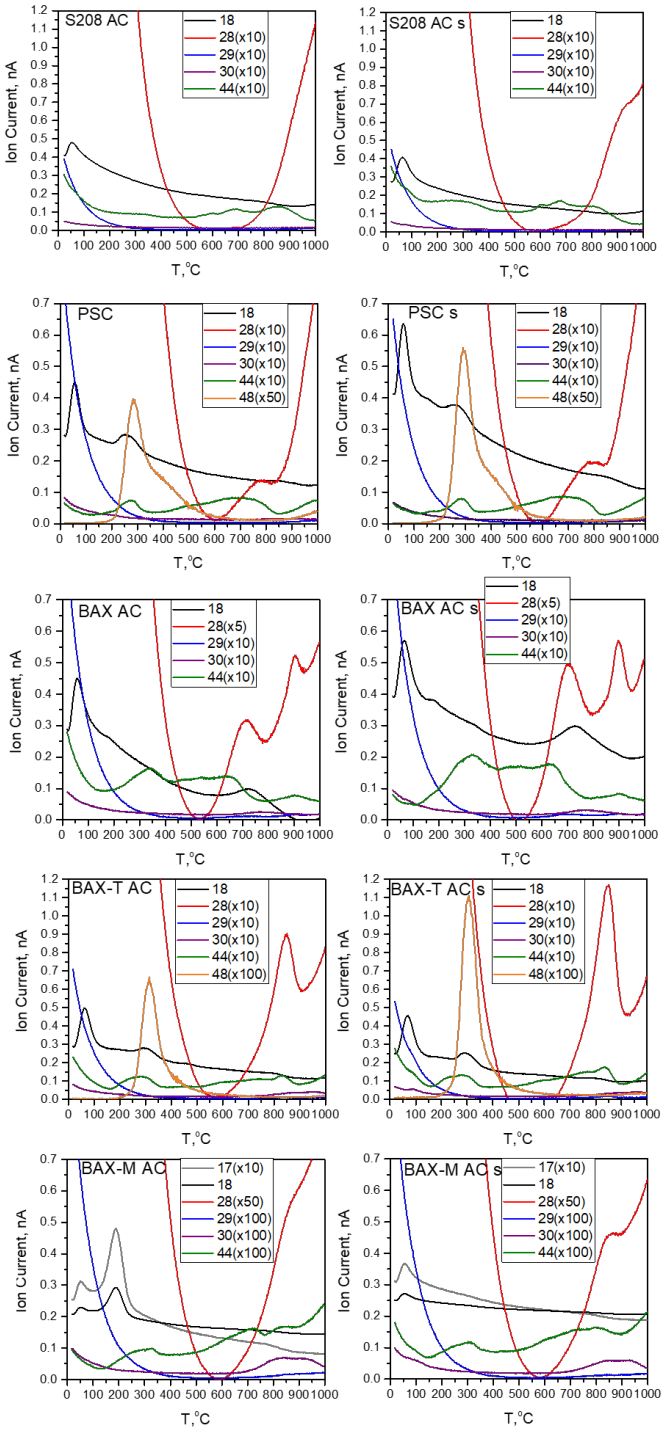

Fig. 4.15. Selected *m*/*z* thermal profiles for S208, PSC and BAX, BAX-T and BAX-M fresh and spent ("s") in dry conditions.

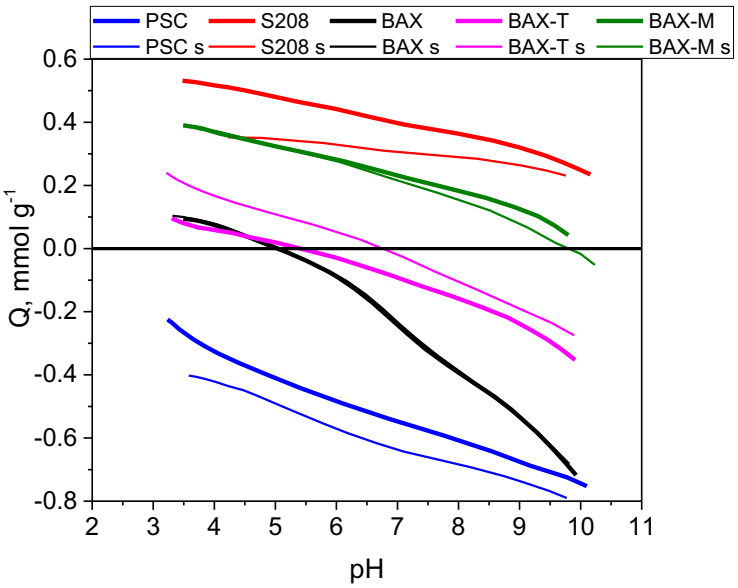

Fig. 4.16. Proton bindings curves for raw and spent (in dry conditions, letter "s") carbons.

Table 4.8. Amount of functional groups (in mmol g^{-1}) in various acidity ranges on the surface of the carbons before and after exposure to HCHO in dry conditions.

Carbon	pH	Strongly acidic $3<pK_a<5$	Neutral $5<pK_a<8$	Weakly acidic $8<pK_a<11$	All
Fresh adsorbent					
PSC	3.3	0.33	0.17	0.24	0.84
S208	8.4	0.10	0.09	0.19	0.39
BAX	5.5	0.10	0.41	0.6	1.11
BAX-T	4.4	0.19	0.16	0.34	0.69
BAX-M	7.3	0.10	0.10	0.29	0.49
Spent adsorbent in dry conditions					
PSC	3.1	0.11	0.18	0.19	0.48
S208	8.4	0.00	0.04	0.09	0.13
BAX	5.1	0.11	0.39	0.47	0.97
BAX-T	4.4	0.26	0.18	0.29	0.73
BAX-M	7.2	0.08	0.10	0.23	0.41

The XPS analysis results on our samples are collected in Table 4.9. BAX-M contains the smallest amount of oxygen and, as expected, the highest content

of nitrogen on the surface. The most chemically heterogeneous is BAX-T, containing the highest amount of oxygen. While on the surface of PSC a marked amount of sulphur is present, S208 appears as the most chemically homogenous, and the potentiometric titration analysis showed that it has the smallest amount of acids on the surface, which dissociate in our experimental window (its average surface pH is 8.4).

The deconvolutions of C 1*s* combined with O 1*s* suggest that, on S208, the majority of oxygen groups is in phenols and, on BAX, carboxylic acids are also present in a marked quantity. Based on the deconvolution of S 2*p*, on PSC and BAX-T, especially on the former, a marked amount of oxygen is in oxidised sulphur species. After thiourea modification, the majority of sulphur is in reduced forms. Even though on the surface of BAX some small amount of nitrogen is present, the treatment with thiourea and melamine, especially the latter, introduced marked amounts of nitrogen that is relatively evenly distributed between pyridines, pyrroles/amines/amides and quaternary nitrogen with a small contribution of pyridine N-oxides. On BAX-T, on the other hand, the majority of nitrogen species is present in pyrroles/amines/amides and pyridine N-oxides. The latter, and a relatively high contribution of sulphonic acids, can explain its average low pH value.

Combining all the textural and chemical characterisation results will help us to explain the differences in the performance between the carbons in terms of amount adsorbed and utilisation degree of their surface, that is directly linked to the surface activity (Fig. 4.17). It is recalled that, in general, the materials based on activated carbons are poorer is sulphur, with respect to carbon cloths (cf. Table 4.4 and Table 4.9). Therefore, for the former, the role of sulphur is less important. The most basic carbon with a marked amount of phenols on the surface is S208. For this carbon, the most pronounced changes in the porosity were found after HCHO adsorption, which was reflected in the significant blocking of its pores (Fig. 4.13, Table 4.7). On the other hand, the changes in the porosity of BAX are much less visible, in spite of more oxygen in phenols.

Table 4.9. Results of the deconvolution of the XPS spectra of C 1*s*, O 1*s*, N 1*s* and S 2*p* (in bold -atomic % of specific elements). For binding energy values, please refer to Table 4.4.

Bond assignment	PSC [%]	S208 [%]	BAX [%]	BAX-T [%]	BAX-M [%]
C 1*s*	**85.1**	**92.6**	**89.2**	**86.1**	**90.4**
C–C sp^2	72.6	83.7	77.9	76.6	68.7
C–O (phenol, alcohol, ether), C–N (amine, amide)	15.4	11.6	12.1	14.0	16.1
C=O (carbonyl, quinone), O=C–N (amide)	5.8	4.7	5.0	5.9	6.7
O=C–O (carboxyl)	3.8	---	3.4	3.5	5.0
π→π*, π-electrons in aromatic rings	2.3	---	1.7	ND	3.4
O 1*s*	**9.8**	**7.4**	**9.1**	**11.6**	**5.2**
C=O	65.2	43.5	44.4	88.5	36.3
C–O	25.1	56.5	55.6	11.5	58.5
Water or chemisorbed O_2, CO_2	9.7	---	ND	ND	5.2
N 1*s*	**0**	**0**	**0.6**	**1.6**	**3.9**
pyridine			41.3	22.4	33.3
pyrrole, amine, amide			36.6	33.1	33.3
quaternary nitrogen/ammonium			ND	18.7	22.3
pyridine N-oxide, $C–N^+O–C$, NO_x			ND	25.8	11.1
$C–N^+O–C$, $Ph–NO_2$, $R–NO_2$, NO_3			22.1	ND	ND
S $2p_{3/2}$	**5.1**	**0**	**0**	**0.6**	**0**
R–S– in thiol, bisulphides, thiophenes	52.4			83.3	
R_2–SO in sulphoxides	14.0			ND	
R–S(O_2) in sulphones	26.3			16.7	
HSO_3^- (sulphonic acids)	7.4			9.7	

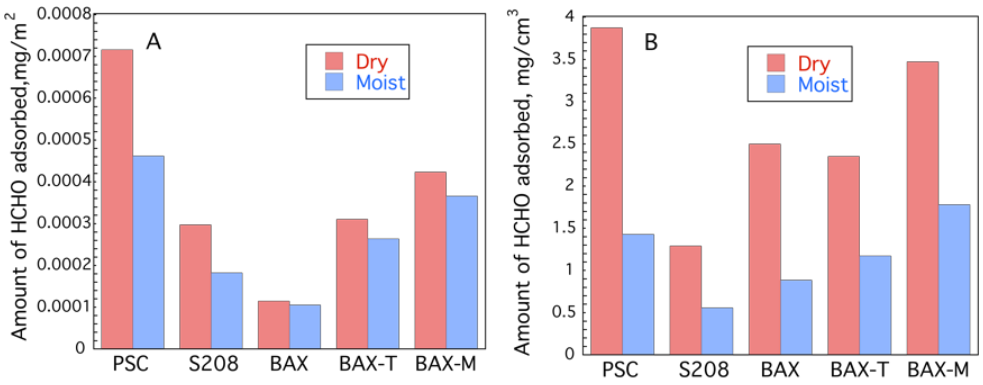

Fig. 4.17. Normalised amounts of HCHO adsorbed per unit surface area (A) and per unit volume of pores smaller than 0.7 nm (B).

Here the differences in the performance might be caused by the differences not only in the volume of small pores promoting HCHO physical adsorption in favour of S208, but also by those in the chemical environment. The basic environment of the S208 carbon likely catalyses the reactions of formaldehyde with phenolic groups in which hydroxybenzyl alcohols are formed and retain on the surface (Sprengling and Freeman, 1950). This reaction can explain the marked decrease in the surface area and the micropore blocking in this carbon after HCHO exposure. This might also explain the higher "utilisation" of this carbon's porosity (Fig. 4.17) compared to that of BAX, and a marked decrease in the relevance of dissociating species after HCHO adsorption.

From the viewpoint of surface utilisation for HCHO adsorption, PSC is the most active, even though its volume of pores in which HCHO could be strongly adsorbed is twice smaller than that in S208. Interestingly, these pores appear almost unchanged after HCHO adsorption, suggesting that a significant part of formaldehyde was physically adsorbed there. Nevertheless, the porosity changes are seen in the disappearance of pores with sizes between 9–11 nm for the exposed samples. HCHO is not expected to be physically adsorbed in these pores, but some bulky sulphonic groups might exist there and react with formaldehyde resulting in hydroxymethanesulphonates (Papalos, 1982). Moreover, this carbon has a significant amount of sulphur in reduced configurations, which might react with

HCHO in condensation reactions (Caesar and Sachanen, 1948) or in reactions analogous to Mannich reactions forming thiomethanols. This results in a decrease in the amount of acids detected on the surface from potentiometric titration experiments.

The explanation of the adsorptive behaviour of BAX- M and BAX-T is more complex. From the viewpoints of surface and pore volume utilisations, BAX-M is second to PSC and it is followed by BAX-T. The modifications significantly improved the performance compared to that of the unmodified counterpart, and the results indicate that the incorporation of N was more beneficial than that of N and S combined. Interestingly, the changes in the porosity after HCHO adsorption are minimal, suggesting that formaldehyde was only physically adsorbed, or the species formed in reactive adsorption were decomposed during outgassing at 120°C and at high vacuum. Changes in the acid-base chemistry are also not visibly marked, especially for the best performing BAX-M. However, in the case of BAX-T, the population of strong acids slightly increased after exposure to HCHO, and the amount of weak acids decreased suggesting some subtle changes. Even though the primary and secondary amines are known to undergo the chemical condensation reaction with formaldehyde and the Mannich reaction is an example here, the chemistry of follow-up reactions and transformations of the formed compounds has been indicated as very complex depending on the nature of amines and their chemical environment (Sprung, 1940). In the case of chemically heterogeneous carbons, even though various techniques can be used to present the complementary views of their surface, the exact description of the surface chemical environment is rather impossible. Therefore, in this discussion we can only present the plausible hypothesis on the role of nitrogen and sulphur surface chemistry along with that of the porosity in enhancing HCHO adsorption on both BAX-M and BAX-T. Since the volume of the pores smaller than 1 nm is very similar in these two carbons, the about 30% better performance of BAX-M must be linked to its nitrogen groups which either chemically (pyridines and amines) or via providing surface polarity (pyridine N-oxides) retain HCHO in larger pores. Supporting for this is the larger total pore

volume of BAX-M than that of BAX-T. These interactions, when occurring in larger pores, might not visibly affect their sizes seen by the very small nitrogen molecule. Moreover, HCHO retained via polar forces, as that through dispersive forces, is expected to be removed during outgassing. The mechanism on BAX-T should be similar that that on BAX-M, however, here the volume of pores with sizes similar to the HCHO molecule is smaller, and the total amount of groups containing heteroatoms is smaller as well. These groups are distributed in the smaller surface of large pores. In a rough evaluation, if one assumes that only chemistry is important, BAX-T has 44% less S+N (% at.) and its HCHO capacity is34 % smaller. Obviously, in this consideration the physical adsorption of formaldehyde in small pores should not be neglected.

Interestingly, on the BAX series the effects of the presence of water on the surface/in the air stream on the amount of HCHO adsorbed per gram of the adsorbent, or that normalised per unit surface area, are the smallest. That insensitivity, compared to that for PSC or S208, might be caused by the adsorption water formed in the condensation reactions in larger pores than on S208 or PSC, which are more microporous than are the BAX series. Even though that water might occupy the polar centres where formaldehyde could be otherwise adsorbed, and thus limit the adsorption of HCHO via specific interactions, the net effect of surface chemistry on the HCHO retention is positive, compared to the performance of the surface without these specific chemical features. When the adsorbed amount is normalised per unit volume of pores smaller than 0.7 nm, the differences between the amounts adsorbed in dry and moist conditions are more or less of 50% for each carbon, which suggests that indeed these pores are very important for HCHO adsorption and their blocking by water during prehumidification can markedly limit the number of adsorption centres.

4.3 Comparison between CC and AC series results

Fig. 4.18 reports the adsorption capacity of the CC series and AC sorbents. It clearly shows that the best adsorbents, among all the samples, is CC-D under dry conditions. Under moist conditions, the performance of BAX-M is

comparable to that for CC-D, possibly due to the almost double specific surface area of the former (cf. Fig. 4.5 and Table 4.7). All the functionalised carbon cloths display better adsorption performance for HCHO capture. Raw CC has a higher adsorption capacity compared to those of commercial activated carbons (approximately, two-fold). The presence of moisture markedly decreased the performance on HCHO adsorption of the materials, due to competitive adsorption of water in the polar centres on which HCHO would be otherwise adsorbed. The difference of adsorption capacity between the two series of sorbents is connected i) to the presence on the surface of polar groups as pyridine, pyridine N-oxide and sulphonic acid groups, detected by XPS analyses (Fig. 4.19), ii) to a higher surface pH of the CC sorbents compared to AC sorbents (cf. Table 4.2 and Table 4.8).

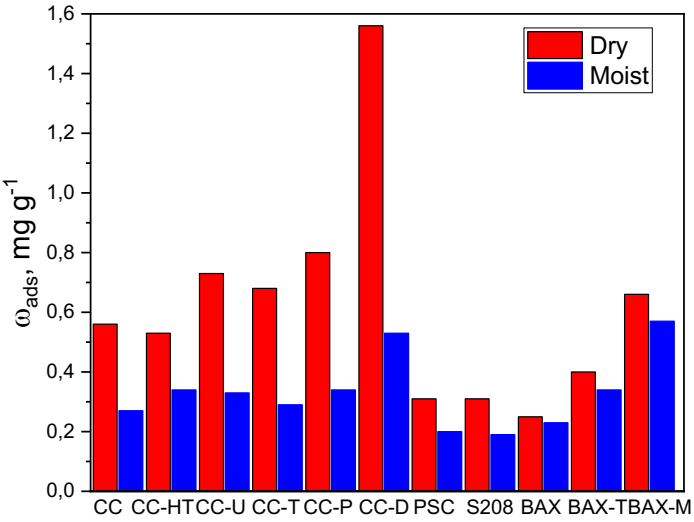

Fig. 4.18. Adsorption capacity in dry and moist conditions for CC and AC series.

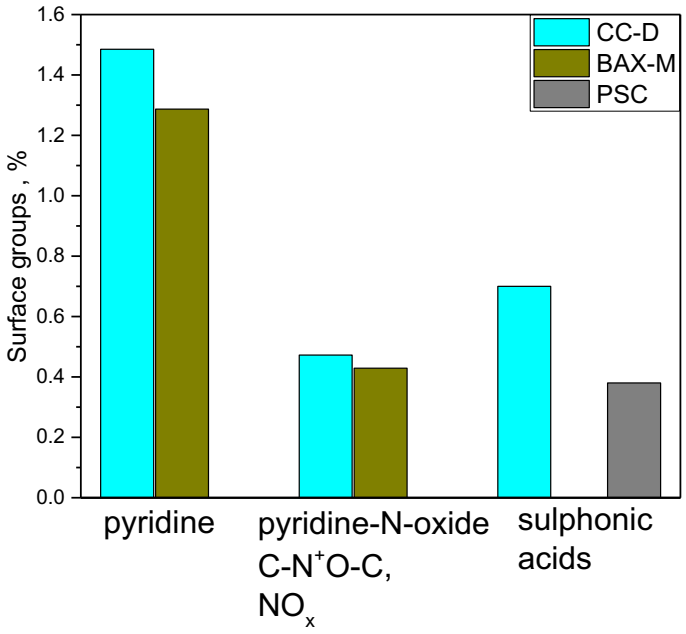

Fig. 4.19. Relevance of pyridine, pyridine N-oxide and sulphonic acids for CC-D, BAX-M and PSC.

Chapter 5

General remarks and conclusions

The present PhD Thesis investigates on new adsorbent materials for: 1) the capture of H_2S from a simulated fuel gas stream, and 2) the capture of HCHO from air.

Concerning H_2S adsorption, sorbents for the deep removal of H_2S from gas streams at room temperature were prepared by dispersing mixed oxides (ZnO–CuO) onto a commercial granulated activated carbon (AC) and γ-alumina spheres at a fixed content of 10% wt. SEM-EDX analyses indicated that the incipient wetness preparation method guaranteed a high dispersion of the active phase, thus largely preserving the textural features of the pristine AC and γ-alumina. A comparison among adsorption performances of AC and alumina sorbents shows that carbonaceous samples have a significantly longer breakpoint time and adsorption capacity at saturation than inorganic materials. This was likely due to the AC remarkably larger surface area, enhancing dispersion of the active phase nanoparticles, but also to the stabilisation of metal hydroxy-nitrates on the surface of the alumina support, which turned out to be less reactive than the corresponding oxides formed on the activated carbon. In this respect, future activity should foresee the preparation of alumina-based materials at higher temperatures, to promote the dissociation of hydroxy-nitrates species. Focusing on AC sorbents, Zn and Cu oxides showed a different tendency to be preferentially dispersed onto the surface of micro and mesopores, respectively.

Compared to the raw activated carbon, all the sorbents functionalised with the pure and composite oxides (ZnO–CuO) displayed a strong improvement of adsorption properties as evaluated by H_2S dynamic capture tests in fixed bed reactors operated at 30°C. In particular, in dry and wet conditions without the presence of O_2, the sorbent with an equimolar amount of Cu and Zn ($Cu_{0.5}Zn_{0.5}$/AC) outperformed both counterparts containing 100% Zn or Cu in terms of saturation S-capacity and sorption kinetics, allowing to discover an evident synergic effect between the two metal oxides. In fact, even a low level of Cu substitution for Zn chemically promoted the degree of ZnO conversion; at higher substitution levels, Cu helped to prevent severe clogging of microporosity that was instead observed upon H_2S adsorption on Zn-rich sorbents. In the case of

the combined effect of oxygen and humidity, Cu/AC becomes the best adsorbent because it allows to increase the formation of elemental sulphur as the main product of reactive adsorption.

XPS analyses and TPD/TPO experiments, performed on dry spent sorbents with various levels of S-saturation, demonstrated that Zn and Cu sulphates were formed with a high rate and at a large extent during the initial phases of the reactive adsorption process. In fact, metal sulphides, commonly recognised in the pertinent literature as the main reaction products from metal oxides, started to be formed with slow overall kinetics after the corresponding sulphates, probably due to the lack of oxygen made available from the sorbent. In particular, in the case of $Cu_{0.5}Zn_{0.5}$/AC material, $ZnSO_4$ formed at a faster rate with respect to $CuSO_4$, and copper oxide likely acted as both oxygen donor and structural promoter. Considering the large increase in the molar volumes of zinc and copper sulphates with respect to their corresponding oxides as well as sulphides, micropores (partially) clogged during adsorption, slowing down the overall capture kinetics due to increased intraparticle diffusion limitations or even inhibiting the direct access to the unreacted active phase.

Concerning HCHO adsorption, sorbents for the removal of formaldehyde from air at room temperature were prepared incorporating S- and N-containing functional groups onto granular activated carbons and carbon cloths. Even though, following the physical adsorption principles, the volume of ultramicropores was expected to govern the adsorbed amount, it has been shown that decorating the surface of the carbon sorbents with sulphur- and nitrogen-containing functional groups, being able to chemically/specifically interact with HCHO, is able to enhance the adsorption capacity. In particular, the HCHO capture is markedly enhanced by the chemical reactivity of formaldehyde with pyridines, amines, and sulphones/sulphonic acids incorporated into the sorbent surfaces. This resulted in a decrease in porosity. Besides, the pyridine N-oxide rich surface also enhanced the polar interaction of formaldehyde with the surface, increasing the adsorptive performance. The comparison of HCHO capture performances between the two kind of carbonaceous sorbents show that the carbon cloths are characterised by a

higher adsorption capacity compared to the granular AC. This is related to a higher surface pH and number of polar groups. The collected results demonstrate that the specifically designed surface modifications of the sorbents can convert them into efficient HCHO removal materials from indoor air.

The two parts of this PhD Thesis have presented results and discussion that also suggest various future research activities. In regard to H_2S adsorption: performing thermal regeneration tests (up to 300°C) using various feed gases compositions with the presence of H_2O or O_2; performing regeneration cycles with the sorbent materials to investigate economic feasibility; synthesising new materials with different substrates having hierarchical structures to prevent micropore clogging. In the case of formaldehyde, adsorption future activities should be focused on: performing regeneration tests on the samples while studying adsorption/desorption cycles; increasing the content of S in the carbonaceous support for better understanding its role in the process; synthesising new adsorbent materials with N and S groups (e.g.: pyridine, pyridine-N-oxide, sulphonic acid) with the intention of increasing formaldehyde adsorption.

Reference

- Adib, F., Bagreev, A., Bandosz, T.J. Analysis of the relationship between H_2S removal capacity and surface properties of unimpregnated activated carbons. **Environmental Science & Technology**, 2000, 34, 686–692.
- Adib, F., Bagreev, A., Bandosz, T.J. Effect of pH and surface chemistry on the mechanism of H_2S removal by activated carbons. **Journal of Colloid and Interface Science**, 1999, 216, 360–369.
- Al-Abadleh, H.A., Grassian, V.H. FT-IR study of water adsorption on aluminum oxide surfaces. **Langmuir**, 2003, 19, 341–347.
- An, H.B., Yu, M.J., Kim, J.M., Jin, M., Jeon, J.K., Park, S.H., Kim, S.S., Park, Y.K. Indoor formaldehyde removal over CMK-3. **Nanoscale Research. Letter**, 2012, 7, 1–6.
- Aslam, Z., Shawabkeh, R.A., Hussein, I.A., Al-Baghli, N., Eic, M. Synthesis of activated carbon from oil fly ash for removal of H_2S from gas stream. **Applied Surface Science**, 2015, 327, 107–115.
- Bagreev, A., Bandosz, T.J. On the mechanism of hydrogen sulfide removal from moist air on catalytic carbonaceous adsorbents. **Industrial & Engineering Chemistry Research**, 2005, 44, 530–538.
- Bagreev, A., Menendez, J.A., Dukhno, I., Tarasenko, Y., Bandosz, T.J. Bituminous coal-based activated carbons modified with nitrogen as adsorbents of hydrogen sulfide. **Carbon**, 2004, 42, 469–476.
- Bagreev, A., Rahman, H., Bandosz, T.J. Study of regeneration of activated carbons used as H_2S adsorbents in water treatment plants. **Advances in Environmental Research**, 2002, 6, 303–311.
- Bagreev, A., Rahman, H., Bandosz, T.J. Thermal regeneration of a spent activated carbon previously used as hydrogen sulfide adsorbent, **Carbon**, 2001, 39, 9, 1319–1326.
- Baird, T., Denny, P.J., Hoyle, R., Mc Monagle, F., Stirling, D., Tweedy, J. Modified zinc oxide absorbents for low-temperature gas desulfurization. **Journal of the Chemical Society**, 1992, 88, 3375–3382.
- Baird, T., Denny, P.J., Hoyle, R., McMonagle, F., Stirling, D., Tweedy, J. Modified zinc oxide absorbents for low-temperature gas desulfurisation. **Journal of the Chemical Society, Faraday Transactions**, 1992, 88, 3375−3382.
- Balichard, K., Nyikeine, C., Bezverkhyy, I. Nanocrystalline $ZnCO_3$-A novel sorbent for low-temperature removal of H_2S. **Journal of Hazardous Materials**, 2014, 264, 79–83.
- Balsamo, M., Di Natale, F., Erto, A., Lancia, A., Montagnaro, F., Santoro, L. Arsenate removal from synthetic wastewater by adsorption onto fly ash. **Desalination**, 2010, 263, 58–63.
- Balsamo, M., Di Natale, F., Erto, A., Lancia, A., Montagnaro, F., Santoro, L. Cadmium adsorption by coal combustion ashes-based sorbents–Relationship between sorbent properties and adsorption capacity. **Journal of Hazardous Materials**, 2011, 187, 371–378.

- Balsamo, M., Di Natale, F., Erto, A., Lancia, A., Montagnaro, F., Santoro, L. Steam- and carbon dioxide-gasification of coal combustion ash for liquid phase cadmium removal by adsorption. **Chemical Engineering Journal**, 2012, 207-208, 66–71.
- Balsamo, M., Di Natale, F., Erto, A., Lancia, A., Montagnaro, F., Santoro, L. Gasification of coal combustion ash for its reuse as adsorbent. **Fuel**, 2013, 106, 147–151.
- Balsamo, M., Erto, A., Lancia, A., Totarella, G., Montagnaro, F., Turco, R. Post-combustion CO_2 capture: on the potentiality of amino acid ionic liquid as modifying agent of mesoporous solids. **Fuel**, 2018, 218, 155–161.
- Balsamo, M., Rodríguez-Reinoso, F., Montagnaro, F., Lancia, A., Erto, A. Highlighting the role of activated carbon particle size on CO_2 capture from model flue gas. **Industrial & Engineering Chemistry Research**, 2013, 52, 12183–12191.
- Balsamo, M., Cimino, S., de Falco, G., Erto, A. Lisi, L. ZnO-CuO supported on activated carbon for H2S removal at room temperature. **Chemical Engineering Journal**, 2016, 304, 399–407
- Bandosz, T.J., Ania, C.O. Activated carbon surfaces in environmental remediation**. Interface Science and Technologies**, 2006, 7, 159–229.
- Bandosz, T.J., Jagiello, J., Contescu, C., Schwarz, J.A. Characterization of the surfaces of activated carbons in terms of their acidity constant distributions. **Carbon**, 1993, 31, 1193–1202.
- Beamson, G., Briggs, D. High Resolution XPS of Organic Polymers - The Scienta ESCA300 Database, Wiley Interscience, 1992.
- Bezverkhyy, I., Skrzypski, J., Safonova, O., Bellat, J.P. Sulfidation mechanism of pure and Cu-doped ZnO nanoparticles at moderate temperature: TEM and in Situ XRD studies. **Journal of Physical Chemistry C**, 2012, 116, 14423–14430.
- Biniak, S., Szymański, G., Siedlewski, J., Świtkowski, A. The characterization of activated carbons with oxygen and nitrogen surface group. **Carbon**, 1997, 35, 1799–1810.
- Blicke, F.F. The Mannich Reaction. Organic Reactions, Wiley Online Library (2011).
- Bohart, G.S., Adams, E.Q. Some aspects of the behavior of charcoal with respect to chlorine. **Journal of the American Chemical Society**, 1920, 42, 523–544.
- Boonamnuayvitaya V., Sae-Ung S., Tanthapanichakoon W. Preparation of activated carbons from coffee residue for the adsorption of formaldehyde. **Separation and Purification Technology**, 2005, 42, 159–168. doi:10.1016/j.seppur.2004.07.007.
- Brasche, S., Bischof, W. Daily time spent indoors in German homes—Baseline data for the assessment of indoor exposure of German

occupants. **International Journal of Hygiene and Environmental Health**, 2005, 208, 247–253.

- Brunauer, S., Emmett, P.H., Teller, E. Adsorption of gases in multimolecular layers. **Journal of the American Chemical Society**, 1938, 60, 309–319.
- Caesar, P.D., Sachanen, A.N. Thiophene-formaldehyde condensation. Industrial & Engineering Chemistry, 1948, 40, 922–928.
- Carter, E.M., Katz, L.E., Speitel, G.E., Ramirez, D. Gas-phase formaldehyde adsorption isotherm studies on activated carbon: Correlations of adsorption capacity to surface functional group density. **Environmental Science & Technology**, 2011, 45, 6498–6503.
- Chen, C., Zhao, B. Review of relationship between indoor and outdoor particles: I/O ratio, infiltration factor and penetration factor. **Atmospheric Environment**, 2011, 45, 275–288.
- Choi, D.-Y., Lee, J.-W., Jang, S.-C., Ahn, B.-S., Choi, D.-K. Adsorption dynamics of hydrogen sulfide in impregnated activated carbon bed. **Adsorption**, 2008, 14, 533–538.
- Cimino, S., Lisi, L., Montagnaro, F., de Falco, G., Balsamo, M., Erto, A. Highlighting the effect of the support during H2S adsorption at low temperature over composite Zn-Cu sorbents. **Fuel**, 2018, 221, 374–379.
- Cosoli, P., Ferrone, M., Pricl, S., Fermeglia, M. Hydrogen sulphide removal from biogas by zeolite adsorption: Part I. GCMC molecular simulations. **Chemical Engineering Journal**, 2008, 145, 86–92.
- Coulson & Richardson's Chemical Engineering, vol. 6 RK Sinnott - Chemical Engineering Design, 2005
- Crittenden, J.C., Berrigan J.K., Hand, D.W. Design of rapid small-scale adsorption tests for a constant diffusivity, **Water Pollution Control Federation**, 1986, 58, 312–319.
- Crittenden, J.C., Weber, W.J. Model for design of multicomponent adsorption systems. **Journal of the Environmental Engineering Division**, 1978, 104, 1175–1195.
- Dhage, P., Samokhvalov, A., Repala, D., Duin, E.C., Bowman, M., Tatarchuk, B.J. Copper-promoted ZnO/SiO_2 regenerable sorbents for the room temperature removal of H_2S from reformate gas streams. **Industrial & Engineering Chemistry Research**, 2010, 49, 8388–8396.
- de Falco, G., Montagnaro, F., Balsamo, M., Erto, A., Deorsola, F.A., Lisi, L., Cimino, S., Synergic effect of Zn and Cu oxides dispersed on activated carbon during reactive adsorption of H_2S at room temperature. Microporous and Mesoporous Materials 2018, 257, 135–146.
- de Falco, G., Barczak, M., Montagnaro, F., Bandosz, T.J, A new generation of surface active carbon textiles as reactive adsorbents of

indoor formaldehyde. **ACS Applied Materials & Interfaces**, 2018, 10, 8066–8076.

- de Falco, G., Li, W., Cimino, S., Bandosz T.J, Role of sulfur and nitrogen surface groups in adsorption of formaldehyde on nanoporous carbons. **Carbon**, 2018, 138, 283–291.
- Do, D.D. Adsorption Analysis: Equilibria and Kinetics (Series on Chemical Engineering vol. 2), Imperial College Press 1998.
- Duan, Y., Pirolli, L., Teplyakov, A.V. Investigation of the H_2S poisoning process for sensing composite material based on carbon nanotubes and metal oxides. **Sensors and Actuators B: Chemical**, 2016, 235, 213–221.
- Dunn, J.G., Muzenda, C. Thermal oxidation of covellite (CuS). **Thermochimica Acta**, 2001, 369, 117–123.
- Elseviers, W.F., Verelst, H. Transition metal oxides for hot gas desulphurisation. **Fuel**, 1999, 78, 601−612.
- Elyassi, B., Al Wahedi, Y., Rajabbeigi, N., Kumar, P., Jeong, J.S., Zhang, X., Kumar, P., Balasubramanian, V.V., Katsiotis, M.S., Mkhoyan, K.A., Boukos, N., Al Hashimi, S., Tsapatsis, M. A high performance adsorbent for hydrogen sulfide removal. **Microporous and Mesoporous Materials**, 2014, 190, 152–155.
- Erto, A., Silvestre-Albero, A., Silvestre-Albero, J., Rodríguez-Reinoso, F., Balsamo, M., Lancia, A., Montagnaro, F. Carbon-supported ionic liquids as innovative adsorbents for CO_2 separation from synthetic flue-gas. **Journal of Colloid and Interface Science**, 2015, 448, 41–50.
- Erzos, A., Olgun, H., Ozdogan, S. Reforming options for hydrogen production from fossil fuels for PEM fuel cells. **Journal of Power Sources**, 2006, 154, 67 –73.
- Fang, H., Zhao, J., Fang, Y., Huang, J. Wang, Y. Selective oxidation of hydrogen sulfide to sulfur over activated carbon-supported metal oxides. **Fuel**, 2013, 108, 143–148.
- Feng, W., Kwon, S., Borguet, E., Vidic, R. Adsorption of hydrogen sulfide onto activated carbon fibers: effect of pore structure and surface chemistry. **Environmental Science & Technology**, 2005, 39, 9744–9749.
- Florent, M., Bandosz, T.J. Effects of surface heterogeneity of cobalt oxyhydroxide/graphite oxide composites on reactive adsorption of hydrogen sulfide. **Microporous and Mesoporous Materials**, 2015, 204, 8–14.
- Florent, M., Giannakoudakis, D.A., Bandosz, T.J. Mustard gas surrogate interactions with modified porous carbon fabrics: effect of oxidative treatment. **Langmui**r, 2017, 33, 11475–11483.
- Fuhrman, H., Mikkelsen, P. S., Ledin, A. Simultaneous removal of As, Cd,Cr, Cu, Ni and Zn from stormwater: Experimental comparison of 11 different sorbents. **Water Research**, 2007,41, 591–602. http://doi.org/10.1016/j.watres.2006.10.024

- Fung, C.C., Yang, P., Zhu, Y.F. Infiltration of Diesel Exhaust in to a Mechanically Ventilated Building. IndoorAir 2014, HongKong.
- Gabriel, D., Deshusses, M.A. Retrofitting existing chemical scrubbers to biotrickling filters for H_2S emission control. **Proceedings of the National Academy of Sciences of the United State of America**, 2003, 100, 6308–6312.
- Green, D.W., Perry, R.H. Perry's Chemical Engineers' Handbook. McGraw Hill (2008).
- Gutiérrez Ortiz, F.J., Aguilera, P.G., Ollero, P. Modeling and simulation of the adsorption of biogas hydrogen sulfide on treated sewage-sludge. **Chemical Engineering Journal**, 2014, 253, 305–315.
- Hauptmann, M., Straif, K., Pesch, B. In Handbuch der Umweltmedizin; Wichmann, H.-E., Schlipkoter, H.-W., Fullgraff, G., Eds.; ECOMED-Verlag: Landsberg, 2006; 3, 1-28.
- Hernandez, S.P., Chiappero, M., Russo, N., Fino, D. A novel ZnO-based adsorbent for biogas purification in H_2 production systems. **Chemical Engineering Journal**, 2011a, 176-177, 272–279.
- Hernandez, S.P., Scarpa, F., Fino, D., Conti, R. Biogas purification for MCFC application. **International Journal of Hydrogen Energy**, 2011b, 36, 8112–8118.
- Huang, C., Chen, C., Chu, S. Effect of moisture on H_2S adsorption by copper impregnated activated carbon. **Journal of Hazardous Materials**, 2006, 136, 866–873.
- Hussain, M., Abbas, N., Fino, D., Russo, N. Novel mesoporous silica supported ZnO adsorbents for the desulphurization of biogas at low temperatures. **Chemical Engineering Journal**, 2012, 188, 222–232.
- Jagiello, J. SAIEUS, version 2.1; 2012, http://www.nldft.com/.
- Jagiello, J. Stable numerical solution of the adsorption integral equation using splines. **Langmuir**, 1994, 10, 2778–2785.
- Jagiello, J., Bandosz, T.J., Schwarz, J.A. Carbon surface characterization in terms of its acidity constant distribution. **Carbon**, 1994, 32, 1026–1028.
- Jagiello, J., Olivier, J.P. 2D-NLDFT adsorption models for carbon slit-shaped pores with surface energetical heterogeneity and geometrical corrugation. **Carbon**, 2013a, 55, 70–80.
- Jagiello, J., Olivier, J.P. Carbon slit pore model incorporating surface energetical heterogeneity and geometrical corrugation. **Adsorption**, 2013b, 19, 777–783.
- Jenkins, P.L., Phillips, T.J., Mulberg, E.J., Hui, S.P. Activity patterns of Californians: Use of and proximity to indoor pollutant sources. **Atmospheric Environment. Part A. General Topics**, 1992, 26, 2141–2148.
- Jiang, D., Su, L., Ma, L., Yao, N., Xu, X., Tang, H., Li, X. Cu-Zn-Al mixed metal oxides derived from hydroxycarbonate precursors for

H_2S removal at low temperature. **Applied Surface Science**, 2010, 256, 3216−3223.

- Kang, S., Bae, J.W., Kim, S., Jun, K. Effect of phosphorus modification on Cu-ZnO-Al_2O_3 for the removal of H_2S. **Energy & Fuels**, 2008, 22, 2580–2584.
- Kloprogge, J.T., Ruan, H., Frost, R.L. Near-infrared spectroscopic study of basic aluminum sulfate and nitrate. **Journal of Material Science**, 2001, 36, 603–607.
- Krylova, V., Andruleviçius, M. Optical, XPS and XRD studies of semiconducting copper sulfide layers on a polyamide film. **International Journal of Photoenergy**, 2009, Article ID 304308.
- Kumagai, S., Sasaki, K., Shimizu, Y., Takeda, K. Formaldehyde and acetaldehyde adsorption properties of heat-treated rice husks. **Separation and Purification Technology**, 2008, 61, 398–403.
- László, K. Characterization and adsorption properties of polymer-based microporous carbons with different surface chemistry. **Microporous and Mesoporous Materials**, 2005, 80, 205–211.
- Lau, L.C., Mohamad Nor, N., Lee, K.T., Mohamed, A.R. Selection of better synthesis route of CeO_2/NaOH/PSAC for hydrogen sulphide removal from biogas. **Journal of Environmental Chemical Engineering**, 2015, 3, 1522–1529.
- Lee, K.J., Miyawaki, J., Shiratori, N., Yoon, S., Jang, J. Toward an effective adsorbent for polar pollutants: formaldehyde adsorption by activated carbon. **Journal of Hazardous Materials**, 2013, 260, 82–88.
- Lee, K.J., Shiratori, N., Lee, G.H., Miyawaki, J., Mochida, I., Yoon, S.-H, Jang, J. Activated carbon nanofiber produced from electrospun polyacrylonitrile nanofiber as a highly efficient formaldehyde adsorbent. **Carbon**, 2010, 48, 4248–4255.
- Leofanti, G., Padovan, M., Tozzola, G., Venturelli B. Surface area and pore texture of catalysts. **Catalysis Today**, 1998, 41, 207–219.
- Levenspiel, O. Chemical reaction engineering. **Industrial & Engineering Chemistry Research**, 1999, 38, 4140–4143.
- Levin, A., Brandon, D. Metastable alumina polymorphs: crystal structures and transition sequences. **Journal of the American Ceramic Society**, 1998, 81, 1995–2012.
- Lew, S., Jothimurugesan, K., Flytzani-Stephanopoulos, M. High-Temperature H2S Removal from Fuel Gases by Regenerable Zinc Oxide-Titanium Dioxide Sorbents. **Industrial and Engineering Chemistry Research**, 1989, 28(5), 535–541.
- Liu, C., Zhang, R., Wei, S., Wang, J., Liu, Y., Li, M., Liu, R. Selective removal of H_2S from biogas using a regenerable hybrid TiO_2/zeolite composite. **Fuel**, 2015, 157, 183–190.
- Liu, G., Huang, Z.-H., Kang, F. Preparation of ZnO/SiO_2 gel composites and their performance of H_2S removal at room temperature. **Journal of Hazardous Materials**, 2012, 215-216, 166–172.

- Mabayoje, O., Seredych, M., Bandosz, T.J. Enhanced adsorption of hydrogen sulfide on mixed zinc/cobalt hydroxides: effect of morphology and an increased number of surface hydroxyl groups. **Journal of Colloid and Interface Science**, 2013, 405, 218–225.
- Małecka, B., Łącz, A., Drożdż, E., Małecki, A. Thermal decomposition of d-metal nitrates supported on alumina. Journal of **Thermal Analysis and Calorimetry**, 2015, 119, 1053–1061.
- Marsh, H., Rodríguez-Reinoso, F. Activated Carbon. Elsevier Science & Technology Books 2006
- McCabe, W.L., Smith, J.C., Harriott, P. Unit Operations of Chemical Engineering. McGraw-Hill 7th edition (2005).
- McIntyre, J.E. Synthetic fibres: nylon, polyester, acrylic, polyolefine. Cambridge: Woodhead (2005).
- Medinsky, M.A., Bond, J.A. Sites and mechanisms for uptake of gases and vapors in the respiratory tract. **Toxicology**, 2001, 160, 165–172.
- Miller, F.A., Wilkins, C.H. Infrared spectra and characteristic frequencies of inorganic ions. **Analytical Chemistry**, 1952, 24, 1253–1294.
- Möller, D. Chemistry of the Climate System. Walter de Gruyter (2010).
- Montagnaro, F., Santoro, L. Reuse of coal combustion ashes as dyes and heavy metal adsorbents: effect of sieving and demineralization on waste properties and adsorption capacity. **Chemical Engineering Journal**, 2009, 150, 174–180.
- Montagnaro, F., Silvestre-Albero, A., Silvestre-Albero, J., Rodríguez-Reinoso, F., Erto, A., Lancia, A., Balsamo, M. Post-combustion CO_2 adsorption on activated carbons with different textural properties. **Microporous and Mesoporous Materials**, 2015, 209, 157–164.
- Montes, D., Tocuyo, E., González, E., Rodriguez, D., Solano, R., Atencio, R., Ramos, M.A., Moronta, A. Reactive H_2S chemisorption on mesoporous silica molecular sieve-supported CuO or ZnO. **Microporous and Mesoporous Materials**, 2013, 168, 111–120.
- Mureddu, M., Ferino, I., Rombi, E., Cutrufello, M.G., Deiana, P., Ardu, A., Musinu, A., Piccaluga, G., Cannas, C. ZnO/SBA-15 composites for mid-temperature removal of H_2S: Synthesis, performance and regeneration studies. **Fuel**, 2012, 102, 691–700.
- Myronyuk, I.F., Mandzyuk, V.I., Sachko, V.M., Gun'ko, V.M. Structural and morphological features of disperse alumina synthesized using aluminum nitrate nonahydrate. **Nanoscale Research Letter**, 2016, 11, 153.
- Nafees, M., Ikram, M., Ali, S. Thermal behavior and decomposition of copper sulfide nanomaterial synthesized by aqueous sol

method. **Digest Journal of Nanomaterials and Biostructures**, 2015, 10, 635–641.

- Neveux, L., Chiche, D., Bazer-Bachi, D., Favergeon, L., Pijolat, M. New insight on the ZnO sulfidation reaction: evidences for an outward growth process of the ZnS phase. **Chemical Engineering Journal**, 2012, 181-182, 508−515.
- Nguyen-Thanh, D., Bandosz, T.J. Activated carbons with metal containing bentonite binders as adsorbents of hydrogen sulfide. **Carbon**, 2005, 43, 359–367.
- Nguyen-Thanh, D., Bandosz, T.J. Activated carbons with metal containing bentonite binders as adsorbents of hydrogen sulphide. **Carbon**, 2005, 43, 359–367.
- Novochinskii, I.I., Song, C., Ma, X., Liu, X., Shore, L., Lampert, J., Farrauto, R.J. Low-temperature H_2S removal from steam-containing gas mixtures with ZnO for fuel cell application. 2. Wash-coated monolith. **Energy**, 2004, 81, 584–589.
- O'Neill, P. Environmental Chemistry, Chapman and Hall, London, 1993.
- Ozekmekci, M., Salkic, G., Fellah, M.F. Use of zeolites for the removal of H_2S: A mini-review. **Fuel Processing Technology**, 2015, 139, 49–60.
- Paglia, G. Determination of the structure of γ-$Al2O_3$ using empirical and first principles calculations combined with supporting experiments, DSc. Academic Dissertation, 2004 Curtin University of Technology.
- Papalos, J.G. Condensation products of aromatic sulphonic acids with formaldehyde. Europen Patent Application 0073606 A, 1982.
- Pourzolfaghar, H., Ismail, MHS. Study of H_2S removal efficiency of virgin zeolite in POME biogas desulfurization at ambient temperature and pressure. Developments in Sustainable Chemical and Bioprocess Technology**,** Springer, Boston, 2014
- Rahmani, A., Mousavi, H.Z., Fazli, M. Effect of nanostructure alumina onadsorption of heavy metals. **Desalination**, 2010 253, 94–100.
- Rengga, W.D.P., Chafidz, A., Sudibandriyo, M., Nasikin, M., Abasaeed, A.E. Silver nano-particles deposited on bamboo-based activated carbon for removal of formaldehyde. **Journal of Environmental Chemistry Engineering**, 2017, 5, 1657–1665.
- Rengga, W.D.P., Sudibandriyo, M., Nasikin, M. Adsorption of low-concentration formaldehyde from air by silver and copper nano-particles attached on bamboo-based activated carbon. **International Journal of Chemical Engineering and Applications**, 2013, 4, 332–336.
- Reuss, G., Disteldorf, W., Gamer, A.O., Hilt, A. Ullmann's Encyclopedia of Industrial Chemistry; WILEY-VCH: Weinheim, 2002.

- Rong, H., Ryu, Z., Zheng, J., Zhang, Y. Effect of oxidation of rayon based activated carbon fibers on the adsorption behavior for formaldehyde. **Carbon**, 2002, 40, 2291–2300.
- Rong, H., Ryu, Z., Zheng, J., Zhang, Y. Influence of heat treatment of rayon-based activated carbon fibers on the adsorption of formaldehyde. **Journal of Colloid and Interface Science**, 2003, 261, 207–212.
- Rosso, I., Galletti, C., Bizzi, M., Saracco, G., Specchia, V. Zinc oxide sorbents for the removal of hydrogen sulfide from syngas. **Industrial & Engineering Chemistry Research**, 2003, 42, 1688–1697.
- Ruthven, M.D. Principles of Adsorption and Adsorption Process. John Wiley & Sons, New York, 1984.
- Sadegh-Vaziri, R., Babler, M.U. Numerical investigation of the outward growth of ZnS in the removal of H2S in a packed bed of ZnO. **Chemical Engineering Science**, 2017, 158, 328–339.
- Saha, J.K., Podde, J. Crystallization of zinc sulphate single crystals and its structural, thermal and optical characterization**. Journal of Bangladesh Academy Science**, 2011, 35, 203–210.
- Samanta, A., Zhao, A., Shimizu, G.K.H., Sarkar, P., Gupta, R. Post-combustion CO_2 capture using solid sorbents: A review. **Industrial & Engineering Chemistry Research**, 2012, 51, 1438–1463.
- Samokhvalov, A., Tatarchuk, B.J. Characterization of active sites, determination of mechanisms of H_2S, COS and CS_2 sorption and regeneration of ZnO low-temperature sorbents: past, current and perspectives. **Physical Chemistry Chemical Physics**, 2011, 13, 3197–3209.
- Santamouris, M. Energy and Climate in the Urban Built Environment, James & James, London, 2001.
- Sasaoka, E., Hirano, S., Kasaoka, S., Sakata, Y.Characterization of Reaction between Zinc Oxide and Hydrogen Sulfide. **Energy & Fuels**, 1994, 8, 1100–1105.
- Saur, O., Bensitel, M., Mohammed Saad, A.B., Lavalley, J.C., Tripp C.P., Morrow B.A. The structure and stability of sulfated alumina and titania. **Journal of Catalysis**, 1986, 99, 104–110.
- Sayari, A., Belmabkhout, Y., Serna-Guerrero, R. Flue gas treatment via CO_2 adsorption. **Chemical Engineering Journal**, 2011, 171, 760–774.
- Shin, S.K., Song, J.H. Modeling and simulations of the removal of formaldehyde using silver nano-particles attached to granular activated carbon. **Journal of Hazardous Materials**, 2011, 194, 385–392.
- Sitthikhankaew, R., Chadwick, D., Assabumrungrat, S., Laosiripojana, N. Effects of humidity, O2, and CO2 on H2S adsorption onto upgraded and KOH impregnated activated carbons. **Fuel Processing Technology**, 2014, 124, 249–257.

- Sjostorm, S., Krutka, H., Starns, T., Campbell T. Pilot test results of post-combustion CO_2 capture using solid sorbents. **Energy Procedia**, 2011, 4, 1584–1592.
- Skrzypski, J., Bezverkhyy, I., Heintz, O., Bellat, J.-P. Low temperature H_2S removal with metal-doped nanostructure ZnO sorbents: study of the origin of enhanced reactivity in Cu-containing materials. **Industrial & Engineering Chemistry Research**, 2011, 50, 5714−5722.
- Song, Y., Qiao, W., Yoon, S.-H, Mochida, I., Guo, Q., Liu, L. Removal of formaldehyde at low concentration using various activated carbon fibers. **Journal of Applied Polymer Science**, 2007, 106, 2151–2157.
- Sprengling GR., Freeman J.H. The Reaction of Phenol with Formaldehyde, **Journal of American Chemical Society**. 1950; 72, 1982–1985.
- Sprung, M.M. A summary of the reactions of aldehydes with amines. **Chemical Reviews**, 1940, 26, 297–338.
- Strelko, V.V., Kuts, V.S., Thrower, P.A. On the mechanism of possible influence of heteroatoms of nitrogen, boron and phosphorus in a carbon matrix on the catalytic activity of carbons in electron transfer reactions. **Carbon**, 2000, 38, 1499–503.
- Sun, Q., Li, H., Yan, J., Liu, L., Yu, Z., Yu, X. Selection of appropriate biogas upgrading technology-a review of biogas cleaning, upgrading and utilisation. **Renewable and Sustainable Energy Reviews,** 2015, 51, 521–532.
- Sun, Y., Walspurger, S., Tessonnier, J.-P., Louis, B., Sommer, J. Highly dispersed iron oxide nanoclusters supported on ordered mesoporous SBA-15: A very active catalyst for Friedel–Crafts alkylations. **Applied Catalysis A: General**, 2006, 300, 1–7.
- Suresh, S., Bandosz, T.J. Removal of formaldehyde on carbon-based materials: A review of the recent approaches and findings. **Carbon**, 2018, 137, 207–221.
- Tajizadegan, H., Rashidzadeh, M., Jafari, M., Ebrahimi-Kahrizsangi, R. Novel $ZnO–Al_2O_3$ composite particles as sorbent for low temperature H_2S removal. **Chinese Chemical Letters**, 2013, 24, 167–169. http://doi.org/10.1016/j.cclet.2013.01.027
- Tanada, S., Kawasaki, N., Nakamura, T., Araki, M. Isomura, M. Removal of formaldehyde by activated carbons containing amino groups. **Journal of Colloid and Interface Science**,1999, 214, 106–108.
- Tongpoothorn, W., Sriuttha, M., Homchan, P., Chanthai, S., Ruangviriyachai, C. Preparation of activated carbon derived from Jatropha curcas fruit shell by simple thermo-chemical activation and characterization of their physico-chemical properties. **Chemical Engineering Research and Design**, 2011, 89, 335–340.
- Tsai, J. Removal of H_2S from exhaust gas by use of alkaline activated carbon. **Adsorption**, 2001, 7, 357–366.

- Uzunov, I., Klissurski, D., Teocharov, L. Thermal decomposition of basic copper sulphate monohydrate. **Journal of Thermal Analysis**, 1995, 44, 685–696.
- Wagner, C.D., Naumkin, A.V., Kraut-Vass, A., Allison, J.W., Powell, C.J., Rumble, J.R.Jr. NIST Standard Reference Database 20, Version 3.4 (web version) (http:/srdata.nist.gov/xps/), 2003.
- Wagner, C.D., Naumkin, A.V., Kraut-Vass, A., Allison, J.W., Powell, C.J., Rumble, J.R. NIST standard reference database 20, version 3.4 (Web version 2003)
- Wakao, N., Funazkri, T. Effect of fluid dispersion coefficients on particle-to-fluid mass transfer coefficients in packed beds. Correlation of Sherwood number. **Chemical Engineering Science**, 1978, 33, 1375–1384.
- Wang, J., Wang, L., Fan, H., Wang, H., Hu, Y., Wang, Z. Highly porous copper oxide sorbent for H2S capture at ambient temperature. **Fuel**, 2017, 209, 329–338.
- Wang, X., Ma, X., Xu, X., Sun, L., Song, C. Mesoporous-molecular-sieve-supported polymer sorbents for removing H_2S from hydrogen gas streams. **Topics in Catalysis**, 2008a, 49, 108–117.
- Wang, X., Sun, T., Yang, J., Zhao, L., Jia, J. Low-temperature H_2S removal from gas streams with SBA-15 supported ZnO nanoparticles. **Chemical Engineering Journal**, 2008b, 142, 48–55.
- Wen, Q., Li, C., Cai, Z., Zhang, W., Gao, H., Chen, L., Zeng, G., Shu, X., Zhao, Y. Study on activated carbon derived from sewage sludge for adsorption of gaseous formaldehyde. **Bioresource Technology**, 2011, 102, 942–947.
- Westmoreland, P.R., Harrison, D.P. Evaluation of candidate solids for high-temperature desulfurization of low-Btu gases. **Environmental Science & Technology**, 1976, 10, 659−661.
- Whaby, A., Ramos-Fernandez, J.M., Martínez-Escandell, M., Sepulveda-Escribano, A., Silvestre Albero, J., Rodríguez-Reinoso F. High-surface-area carbon molecular sieves for selective CO_2 adsorption. **ChemSusChem**, 2010, 3, 974–981.
- World Health Organization, WHO Guidelines for Indoor Air Quality: Selected Pollutants, WHO Regional Office of Europe, 2010.
- Xiao, Y., Wang, S., Wu, D., Yuan, Q. Experimental and simulation study of hydrogen sulfide adsorption on impregnated activated carbon under anaerobic conditions. **Journal of Hazardous Materials**, 2008, 153, 1193–1200.
- Yan, R., Liang, D. T., Tsen, L., Tay, J. H. Kinetics and mechanisms of H_2S adsorption by alkaline activated carbon. **Environmental Science and Technology**, 2002, 36,4460–4466. http://doi.org/10.1021/es0205840

- Yan, R., Liang, D.T., Tsen, L., Tay, J.H. Kinetics and mechanisms of H_2S adsorption by alkaline activated carbon. **Environmental Science & Technology**, 2002, 36, 4460–4466.
- Yang, H., Lu, Y., Tatarchuk, BJ.Glass fiber entrapped sorbent for reformates desulfurization for logistic PEM fuel cell power systems. **Journal of Power Sources**, 2007, 174, 302–311. http://doi.org/10.1016/j.jpowsour.2007.08.031
- Yang, H., Tatarchuk, B. Novel-doped zinc oxide sorbents for low temperature regenerable desulfurization application, **AIChE Journal,** 2010, 56, 2898–2904
- Yaşyerli, S., Ar, İ., Doğu, G., Doğu, T. Removal of hydrogen sulfide by clinoptilolite in a fixed bed adsorber. **Chemical Engineering and Processing: Process Intensification**, 2002, 41, 785–792.
- Zhang, L., Steinmaus, C., Eastmond, D.A., Xin, X.K., Smith, M.T. Formaldehyde exposure and leukemia: a new meta-analysis and potential mechanisms. **Mutation Research**, 2009, 681, 150–168.
- Zhang, Z., Wang, J., Li, W., Wang, M., Qiao, W., Long, D., Ling, L. Millimeter-sized mesoporous carbon spheres for highly efficient catalytic oxidation of hydrogen sulfide at room temperature. **Carbon**, 2016, 96, 608–615.
- Zhao, X., Zhang, Q., Chen, C-M., Zhang, B., Reiche, S., Wang, A., Zhang, T., Schlogl, R., Su, D.S. Aromatic sulfide, sulfoxide, and sulfone mediated mesoporous carbon monolith for use in supercapacitor. **Nano Energy**, 2012, 1, 624–630.

Appendix – PhD Course Activity Summary

Candidate: Giacomo de Falco **Tutor:** Prof. Fabio Montagnaro

1) **Attended Courses (6 minimum, 8 hours each):**

- *Production of Native and Mutant Recombinant Proteins* (Prof. Angela Duilio, 2016).
- *Advanced Mass Spectrometry* (Prof. Piero Pucci, 2016).
- *Glycoscience* (Prof. Michelangelo Parrilli, Dott. Emiliano Bedini, 2016).
- *Chemical Reactors for Solid–Gas Processes Aimed at Energy Production* (Prof. Fabio Montagnaro, 2016).
- *Techniques of Solid-Liquid Extraction Used in the Preparation of Samples for Chemical Analysis and Production of Extracts for Industrial Uses* (Prof. Daniele Naviglio, March 2016).
- *Persistent organic pollutants (POPs)* (Dr. Anna Andolfi, 2018).

2) **Attended Seminars:**

Title	Speaker	Date	Place
Multimodel approaches for preclinical molecular imaging	Dr. Minichetti	05/02/2016	DSC-UniNa
Dalle Piante alle Microalghe	Prof. Filippone	26/10/2016	DSC-UniNa
Supramolecular Chemistry of Chiral Calixarenes	Prof. Mauro Mocerino	13/01/2017	DSC-UniNa
Modified Nucleotides and oligonucleotides for Biomedical Applications	Prof. Daniela Montesarchio	18/01/2017	DSC-UniNa
Oxy-combustion of coal/biomass in the framework of CO2 capture and storage (bio-CCS)	Dr. Luis Diez	06/04/2017	DSC-UniNa
Calorimetria a scansione differenziale	Dr. Luciana Lisi	03/06/2017	IRC-CNR
The collapse of complex societies	Dr. Luca Iandoli	20/06/2018	DIE UniNa
Smart City in a smart world	Dr. G. Feruzzi	22/06/2018	DIE UniNa
Environmental Impact and risk	Prof. Sluser	27/06/2018	DICMaPI Unina

DSC-UniNa = Dept. of Chemical Sciences – University of Naples Federico II

DIE-Unina = Dept. Industrial Engineering – University of Naples Federico II

IRC-CNR = Institute for research on combustion

DICMaPI Unina = Department of Chemical, Materials and Production Engineering

3) Attended Integration Exams (for candidates not graduated in Chemical Science):

Title	Professor	Date
Chimica dei sistemi di coordinazione	Prof. Aldo Vitagliano	14/09/2017
Chimica Fisica 2	Prof. Michele Pavone	19/07/2018

4) Visiting periods in Institutions different from the University of Naples Federico II:

Host Institution	Country	Start Date	End Date
City College of New York	USA	21/09/2017	21/02/2018

5) Publications:

- M. Balsamo, S. Cimino, G. de Falco, A. Erto, L. Lisi. ZnO-CuO supported on activated carbon for H_2S removal at room temperature. **Chemical Engineering Journal** 2016, 304, 399–407.
- M. Balsamo, S. Cimino, G. de Falco, A. Erto, L. Lisi. Synergic effect of mixed ZnO and CuO nanoparticles supported on activated carbon for H_2S adsorption at room temperature. **Advance Science Letter** 2017, 6, 5879–5882
- Cimino, L. Lisi, G. de Falco, F. Montagnaro, M. Balsamo, A. Erto. Highlighting the effect of the support during H_2S adsorption at low temperature over composite Zn-Cu sorbents. **Fuel** 2018, 221, 374–379.
- G. de Falco, M. Barczak, F. Montagnaro, T.J. Bandosz. A new generation of surface active carbon textiles as reactive adsorbents of indoor formaldehyde. **ACS Applied Materials & Interfaces** 2018, 10, 8066–8076.
- G. de Falco, F. Montagnaro, M. Balsamo, A. Erto, F.A. Deorsola, L. Lisi, S. Cimino. Synergic effect of Zn and Cu oxides dispersed on activated carbon during reactive adsorption of H_2S at room

temperature. **Microporous and Mesoporous Materials** 2018, 257, 135–146.

- G. de Falco, W. Li, S. Cimino, T.J. Bandosz. Role of sulfur and nitrogen surface groups in adsorption of formaldehyde on nanoporous carbons. **Carbon** 2018, 138, 283–291.

6) Attended congresses/workshops/summer schools:

- *Bioeconomy in the Circular Economy*, University of Naples (I), January 2016.
- *39th Meeting Italian Section Combustion Institute.,* Naples, July 2016.
- *VI International Workshop on Oxide-based Materials,* Naples, September 2016.
- *Gli orizzonti 2020 dell'Ingegneria Chimica*, Anacapri, September 2016.
- *National School of Gricu,* Anacapri, September 2016.
- *Tenth Mediterranean Combustion Symposium,* Naples, September 2016.
- *Joint Meeting of the German and Italian Sections of the Combustion Institute 41st Meeting on Combustion,* Sorrento, May 2018
- *25th International Conference on Chemical Reaction Engineering,* Firenze, May 2018

Appendix B

Scientific articles published by the candidate

Chemical Engineering Journal 304 (2016) 399–407

Contents lists available at ScienceDirect

Chemical Engineering Journal

journal homepage: www.elsevier.com/locate/cej

ZnO-CuO supported on activated carbon for H_2S removal at room temperature

M. Balsamo [a], S. Cimino [b,*], G. de Falco [b], A. Erto [a], L. Lisi [b]

[a] Università degli Studi di Napoli Federico II, Dipartimento di Ingegneria Chimica dei Materiali e della Produzione Industriale, P.le Tecchio, 80, 80125 Napoli, Italy
[b] Istituto Ricerche sulla Combustione IRC – CNR, P.le Tecchio, 80, 80125 Napoli, Italy

HIGHLIGHTS

- ZnO-CuO dispersion on activated carbon enhances H_2S adsorption capacity.
- Effect of Cu:Zn ratio investigated at fixed total metal loading in the sorbent.
- H_2S dynamic adsorption tests run at 30 °C in N_2 followed by TPD of H_2S and SO_2.
- Cu addition improves adsorption capacity and active phase utilization factor.
- Reactive H_2S adsorption forms both metal sulphates and sulphides.

GRAPHICAL ABSTRACT

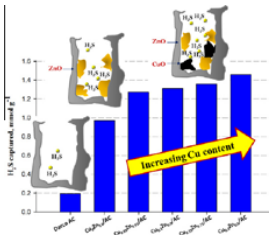

ARTICLE INFO

Article history:
Received 6 April 2016
Received in revised form 13 June 2016
Accepted 15 June 2016
Available online 16 June 2016

Keywords:
Reactive adsorption
Mixed metal oxides
Sulphur poisoning
Sorbent
Gas cleaning

ABSTRACT

Sorbents for low temperature reactive adsorption of H_2S were prepared by dispersing mixed Zn and Cu oxides onto a commercial activated carbon at fixed total metal loading and Cu:Zn atomic ratios from 0:1 to 1:1. Fresh and spent sorbents were characterized by means of ICP-MS, SEM-EDX, XRD, BET and pore size distribution, DRIFT and sulphur elemental analysis. H_2S (50–3000 ppmv in N_2) removal tests were run under dynamic conditions at 30 °C. Due to the high dispersion of the metal oxide phase and its favorable interaction with the carbonaceous support, the functionalized sorbents showed a strongly enhanced adsorption capacity with respect to the raw activated carbon, under dry conditions. Furthermore, the utilization factor of the active phase (moles of S captured per mole of Cu + Zn) increased along with the Cu content up to 76%, thus demonstrating a clear promoting effect of Cu-insertion on the reactivity of ZnO, already at low Cu concentration. Temperature Programmed Desorption (TPD) of H_2S and SO_2 from saturated sorbents showed that H_2S adsorption was coupled with oxidation phenomena leading to the formation of metal sulphates apart from metal sulphides and/or elemental sulphur, testifying the complexity of the surface reactions.

1. Introduction

Gas cleaning and, particularly, efficient removal of H_2S from reformate fuel gas streams and biogas remains one of the big challenges for the profitable development of clean and sustainable technologies valorizing low grade feedstocks and biomasses. Apart from being hazardous to health, corrosive to equipment, and pollutant to environment, H_2S is a strong poison for catalytic systems for fuel processing units and fuel cell electrodes, therefore its maximum tolerated concentration is generally below 1 ppmv [1–2].

* Corresponding author.
E-mail address: stefano.cimino@cnr.it (S. Cimino).

http://dx.doi.org/10.1016/j.cej.2016.06.085
1385-8947/

Currently, adsorbents mainly based on Zn, Fe and Cu metal oxides, hydroxides, and carbonates, are widely studied for the purification of gas streams and used to protect catalysts in ammonia, methanol, and hydrogen plants [2–8]. In fact, the formation of the corresponding metal sulphides according to the general reaction $H_2S + MeO \rightarrow MeS + H_2O$ is thermodynamically favored already at low temperature. Nevertheless, their use is generally limited to T > 250 °C, due to kinetic limitations, which can lead to rather low utilization factors [2,3,6–10].

Therefore, current research efforts are devoted to develop high performance sorbents capable to work at low temperature (down to room temperature): a promising approach is to disperse nanosized active metal oxides onto highly porous supports, such as zeolites, mesoporous silicas and activated carbons, or in composites with graphite oxides [7,8,11–16].

Inorganic supports offer the possible advantage of being (partially) regenerable via thermal (oxidative) treatments [8,10,17]. In particular, promising results were reported for the functionalization of mesoporous silicas with a combination of ZnO-CuO, which determined significant synergic effects in terms of H_2S adsorption capacity [7,8,17]. High surface area Zn-Cu-Al mixed oxides prepared from hydroxycarbonate precursors also showed remarkable H_2S removal capacity at low temperature, assigned to the smaller mean size of metal oxide crystallites, and to a faster sulphidation rate of CuO compared to ZnO, due to an easier rearrangement of anions (HS^-, S^{2-}, O^{2-}) in lattice upon sulphidation reaction [18].

Alternatively, activated carbons, particularly those impregnated with basic groups such as NaOH and KOH [19,20] or transition metal oxides [11,13,16,21,22] can be used for H_2S desulphurization. Their H_2S capture capacities are controlled by morphology (i.e. high surface area and micro/meso pore volume), but, above all, by the surface chemistry, which can also promote an adsorption–catalytic oxidation mechanism for H_2S (leading to elemental S, SO_2, sulphates, sulphuric acid, apart from metal sulphides) in the presence of even small amounts of oxygen and high moisture contents [20,21,23,24]. In particular, some recent literature reports suggest that effective low temperature adsorbents capable to simultaneously remove H_2S and other pollutants from reformate streams can be obtained by dispersing Zn or Cu oxides onto activated carbon supports [11,13,22].

However, to the best of our knowledge, the possible synergic effects deriving from doping, or partially substituting, ZnO with CuO have not been systematically explored when those active phases are dispersed onto activated carbons. In fact, the sulphidation mechanism of mixed metal oxides is still debated, whereas the identification of the species formed during H_2S reactive adsorption in the presence of an active support such as an activated carbon is of paramount importance to design novel highly performing sorbents [9,10].

In this work, we set out to investigate the low temperature H_2S capture mechanism and removal performance of a series of highly dispersed ZnO-CuO sorbents, which were prepared via impregnation of the active phase onto a commercial activated carbon support (Darco, by Norit). In particular, we explored systematically the effect of the Cu:Zn atomic ratio from 0:1 to 1:1 while keeping the total metal loading on the sorbents fixed at 10% wt. Fresh and spent sorbents, as well as the raw activated carbon support, were fully characterized by means of ICP-MS, SEM-EDX, XRD, BET and pore size distribution, DRIFT, and sulphur elemental analysis. H_2S removal tests were carried out under dynamic conditions at 30 °C in the concentration range 50–3000 ppmv diluted in N_2, and eventually in the presence of 40% vol. of either CH_4 or CO_2. Finally, a Temperature Programmed Desorption (TPD) procedure was set up to follow the release of H_2S and SO_2 from saturated sorbents in order to elucidate the mechanism and the type of compounds formed during the H_2S reactive adsorption on the ZnO-CuO active phases, under dry conditions and in the absence of molecular oxygen.

2. Materials and methods

2.1. Sorbent preparation

ZnO and CuO mixed oxides were dispersed onto a commercial, general purpose, acid-washed activated carbon deriving from lignite (Darco granulated AC 20–40 mesh, by Norit) with particle size distribution in the range 0.42–0.85 mm, which was used without any further pretreatment. In particular, five different sorbents were prepared by incipient wetness impregnation with aqueous solutions of $Zn(NO_3)_2{\cdot}6H_2O$ and $Cu(NO_3)_2{\cdot}5/2H_2O$ (Sigma Aldrich) followed by drying at 100 °C and thermal treatment in N_2 flow for 3 h at 250 °C. The nominal metal loading (Zn + Cu) in functionalized sorbents was set to 10% wt, whereas the Cu:Zn atomic ratio was varied. The sorbents were labelled as Cu_xZn_{1-x}/AC, in which x represented the atomic fraction of Cu with respect to (Zn + Cu), and was set to 0, 0.05, 0.10, 0.25 and 0.50.

2.2. Sorbent characterization

The actual content of metals in the sorbents was determined by inductively coupled plasma spectrometry using an Agilent 7500 ICP-MS instrument, after microwave-assisted digestion of samples in nitric/hydrochloric acid solution. The total sulphur content in spent sorbents was determined with a LECO SC 144-DR analyzer.

Scanning electron microscopy (SEM) was carried out on sections of sorbent grains with a FEI Inspect instrument equipped with an energy dispersive X-ray (EDX) probe.

The textural properties of the sorbents were determined by N_2 adsorption at −196 °C with a Quantachrome Autosorb 1-C, after degassing for 4 h at 150 °C. In particular, the Brunauer–Emmett–Teller (BET) method was adopted for the calculation of the specific surface area, while pore size distribution was evaluated by means of Barrett-Joyner-Halenda (BJH) desorption method for mesopores and Dubinin-Astakhov (DA) method for micropores.

X-ray powder diffraction analysis (XRD) was performed with a Bruker D2 Phaser diffractometer operated at diffraction angles ranging between 10 and 80° 2θ with a scan rate of 0.02° 2θ s^{-1}.

Diffuse Reflectance Infrared Fourier Transform Spectroscopy (DRIFT) experiments were performed on a Perkin Elmer Spectrum GX spectrometer equipped with a liquid-N_2 cooled MCT detector with a spectral resolution of 4 cm^{-1}, averaging each spectrum over 50 scans. The sorbent samples were diluted in KBr (2%) and about 0.1 g of finely grounded powder was placed in the DRIFT cell equipped with a ZnSe window and connected to gas lines. Spectra were collected at 40 °C rationing against pure KBr, following a pretreatment at 120 °C for 40 min under flowing Ar.

2.3. H_2S adsorption tests

H_2S dynamic adsorption tests were carried out at T = 30 °C and total P = 1 atm in a lab-scale experimental apparatus based on a fixed-bed reactor, already described in Balsamo et al. [25]. 2.5 g of sorbent (5 g in the case of raw AC, due to its lower adsorption capacity) were loaded in a fixed-bed column (d_{in} = 20 mm) made up of Pyrex glass, whose temperature was regulated by means of cylindrical shell band heaters. The feed H_2S concentration was regulated in the range 500–3000 ppmv (in N_2) using two independent mass flow controllers (El Flow Bronkhorst 201-CV); the inlet flow rate was set constant to 90 SL h^{-1}. Some adsorption tests were run under identical conditions but substituting part of N_2 flow with

either CO_2 or CH_4 in order to realize an inlet concentration of 40% vol. Further experiments at inlet H_2S concentrations $\leqslant$200 ppmv were run in the apparatus set-up for TPD analysis (Section 2.4).

H_2S concentration measurements were performed by a continuous GAS 3240 R BIOGAS analyzer (GEIT Europe), equipped with an electrochemical selective sensor for H_2S operating in the range of 0–10,000 ppmv with accuracy better than 3% of span. Data acquisition and elaboration were performed by interfacing the analyzer with a PC unit by means of the SCADA monitoring software.

H_2S adsorption capacity at saturation, ω_s [mmol g^{-1}], was determined through a material balance on H_2S over the adsorption column, leading to the following expression:

$$\omega_s = \frac{Q^t C^{in}_{H_2S} \rho_{H_2S}}{m M_{H_2S}} \int_0^{t^*} \left(1 - \frac{C^{out}_{H_2S}(t)}{C^{in}_{H_2S}}\right) dt \quad (1)$$

where Q^t [L s^{-1}] is the total gas flow rate, $C^{in}_{H_2S}$ [–] is the H_2S volumetric fraction in the gas feed, $C^{out}_{H_2S}$ [–] is the H_2S volumetric fraction at the bed outlet, ρ_{H_2S} is H_2S density (1370 mg L^{-1} at 30 °C and 1 bar) while M_{H_2S} [mg $mmol^{-1}$] is its molecular weight; m [g] is the sorbent dose and t^* [s] represents the time required to reach 99% recovery of the initial inlet concentration of H_2S. The resolution of Eq. (1) for all the investigated inlet H_2S concentrations allowed determining the adsorption isotherm, under the verified assumption of constant total flow during the test.

2.4. Temperature Programmed Desorption (TPD) tests

Temperature Programmed Desorption (TPD) tests were carried out in a lab-scale plant schematically represented in Fig. 1, in order to investigate the residual presence of nitrates on the synthesized sorbents (TPD-NO_x), and to provide insights into H_2S adsorption/desorption mechanisms while evaluating the thermal regenerability of the sorbents.

A weighted amount of sorbent (20–100 mg) was loaded in a quartz reactor with annular section (d_{in} = 6 mm, d_{out} = 10 mm) placed in a vertical tubular furnace, as already described elsewhere [26]. The temperature was measured by a K-type thermocouple placed inside the inner section of the reactor with its tip in correspondence of the sorbent bed ("Tc" in Fig. 1). The desorbing gas (99.999% N_2) flow rate was set at 20 SL h^{-1} using a mass flow controller. During a typical TPD test, the temperature was ramped at 10 °C min^{-1} up to a maximum of 620 °C, so to minimize any volatilization/thermal degradation of the carbon-based species from the support. Gas analysis was performed by means of two continuous analyzers with cross sensitivity corrections: i) an Emerson X-Stream XEGP with independent measures for NO (NDIR) and NO_2 (UV); ii) an ABB Optima Advance Limas 11 UV, for the simultaneous measurement of H_2S (0–300 ppmv) and SO_2 (0–100 ppmv) with accuracy better than 1% of span.

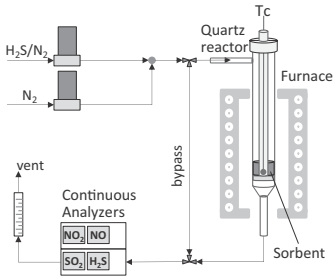

Fig. 1. Schematic representation of the experimental equipment used for TPD tests and for dynamic adsorption measurements at inlet concentration of $H_2S \leqslant$ 200 ppmv.

The same experimental set-up was employed for dynamic adsorption tests at 30 °C with inlet H_2S concentrations $\leqslant$200 ppmv. The simultaneous measurement of both H_2S and SO_2 also allowed to control and to exclude the possible release of SO_2 from the sorbents during the H_2S adsorption phase.

3. Results and discussion

3.1. Sorbent characterization

ICP-MS analysis of metals in the functionalized sorbents revealed a content of Cu + Zn in the range 10.0 ± 0.5% wt, with a mean value equal to 10.2% wt, in good agreement with the target loading. Slight variations can be ascribed to the effect of the thermal treatment of the impregnated sorbent, during which a partial combustion of the carbon support was observed, as testified by the evolution of some CO_2 (Fig. S1 in Supplementary material), most probably formed by means of the exothermic reaction with the nitrate groups of the precursor salts. The Cu:Zn ratio in each sorbent corresponded to the nominal value, thus confirming a good control and repeatability of the preparation procedure. Moreover, the ICP-MS analysis confirmed the presence of impurities due to the content of ashes in the activated carbon, mainly consisting of Si = 0.8% wt, Al = 0.7% wt, Na = 0.6% wt and Ca = 0.5% wt.

Fig. 2 shows a typical SEM image of a sectioned granule of $Cu_{0.5}Zn_{0.5}$/AC sorbent together with the corresponding distribution map of Zn and Cu as obtained by EDX analysis; similar results were obtained for all the other sorbents prepared. It can be observed that Zn was quite uniformly distributed throughout the sorbent particle, whereas Cu presented a moderate tendency to accumulate on its outer shell, although it was detected at all positions across the section. This effect might be related to the lower decomposition temperature of Cu nitrate, starting simultaneously to dehydration at around 100 °C, with a possible associated transport of copper towards the particle external surface. In contrast, the decomposition of Zn nitrate occurs at appreciable rates only above 175 °C when dehydration is over [27]. EDX analysis also indicated the presence of residual Cl (ca. 0.2% wt) probably deriving from the acid wash treatment of the activated carbon support.

TPD-NO_x tests produced flat NO_2 and NO profiles for all the functionalized sorbents after treatment at 250 °C under inert atmosphere. Therefore, the decomposition of both Zn and Cu nitrates had been completed at that temperature level [27], being also favored by the reaction with the activated carbon support, as previously mentioned. DRIFT spectra of the functionalized sorbents (Fig. S2 in Supplementary material) further confirmed the absence of nitrate bands. Moreover, only weak bands related to carbonate-species were detected, thus suggesting the predominant formation of the target metal oxides.

The textural properties of the raw activated carbon and Cu_xZn_{1-x}/AC sorbents are collected in Table 1, while in Fig. 3 the pore size distribution (PSD) of two of the functionalized sorbents (taken as example) are compared with the parent support. The commercial Darco AC support showed a BET surface area of 641 $m^2 g^{-1}$ and it was characterized by the presence of both micro- and mesoporosity, with characteristic mean pore sizes estimated equal to 14.4 and 35 Å, respectively (Table 1). Cu_xZn_{1-x}/AC sorbents showed a decrease in their specific surface area down to an average of 550 $m^2 g^{-1}$. Such a value closely agrees with what expected for a negligible contribution to the total surface area deriving from the mixed oxide active phase (accounting for ca. 12.7% of the sorbent weight). In fact, the PSD calculated for Cu_xZn_{1-x}/AC sorbents (Fig. 3) was almost identical to that of the

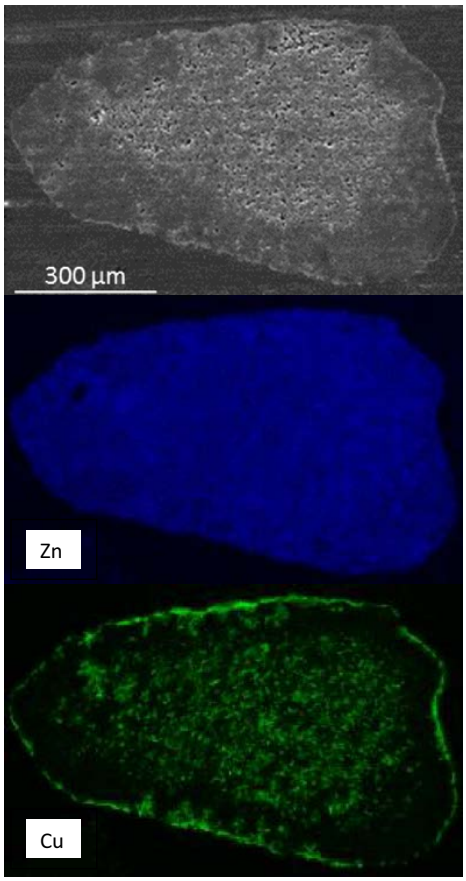

Fig. 2. SEM image of a sectioned particle of $Cu_{0.5}Zn_{0.5}$/AC sorbent and corresponding EDX maps in false colors showing the distribution of the elements (Zn and Cu) of the active phase.

Table 1
BET surface area, total porosity, micropore volume, and average sizes of micro- and meso-pores for the raw Darco AC support and the Cu_xZn_{1-x}/AC sorbents treated in N_2 at 250 °C.

Sorbent	BET surface area $m^2\,g^{-1}$	Total porosity $cm^3\,g^{-1}$	Micropore volume $cm^3\,g^{-1}$	Average pore sizes Å
Darco AC	641	0.81	0.23	14.4; 35
$Cu_0Zn_{1.0}$/AC	558	0.80	0.19	14.8; 36
$Cu_{0.05}Zn_{0.95}$/AC	520	0.72	0.18	14.8; 35
$Cu_{0.1}Zn_{0.9}$/AC	549	0.76	0.19	14.6; 36
$Cu_{0.25}Zn_{0.75}$/AC	555	0.78	0.19	14.6; 36
$Cu_{0.5}Zn_{0.5}$/AC	570	0.76	0.20	14.6; 36

parent support, regardless of the specific Cu:Zn ratio, indicating that the active phase was highly dispersed and no significant occlusion or collapse/widening of the pores occurred during the impregnation step and the following thermal treatment. The small loss of total porosity for Cu_xZn_{1-x}/AC sorbents was mainly due to a reduction of the micropore volume of the parent support (Table 1),

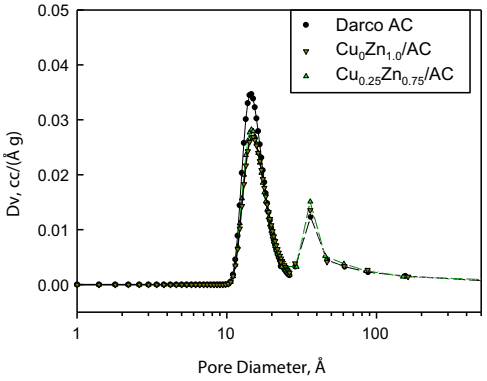

Fig. 3. Pore size distribution for Darco AC, $Cu_0Zn_{1.0}$/AC and $Cu_{0.25}Zn_{0.75}$/AC sorbents.

thus suggesting that metal oxides nanoparticles were dispersed on the surface of micropores of the activated carbon.

Fig. 4 presents the XRD patterns for the raw Darco AC and the Cu_xZn_{1-x}/AC sorbents, restricted to the 2θ range of 30–60°. All of the sorbents showed characteristic peaks due to crystalline quartz (Powder Diffraction File, PDF 5-490), a typical impurity in activated carbons deriving from lignite. After the functionalization, the main peaks of quartz became sharper, indicating an increase in the dimension of the crystallites due to the thermal treatment at 250 °C.

A closer inspection of XRD patterns of Cu_xZn_{1-x}/AC sorbents revealed low intensity peaks corresponding to the main reflections of zinc oxide at 2θ = 31.8, 34.4 and 36.2° (PDF 36-1451). The intensity of those peaks decreased progressively according to the reduction in the Zn content of the sorbents. In parallel, two small peaks

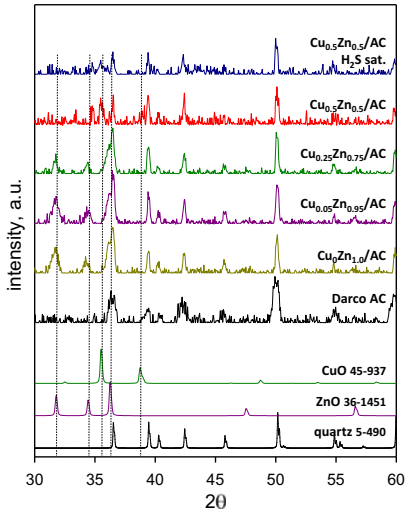

Fig. 4. XRD patterns for raw Darco AC and fresh Cu_xZn_{1-x}/AC sorbents. The spectrum of $Cu_{0.5}Zn_{0.5}$/AC sorbent saturated with H_2S at 3000 ppmv and 30 °C is also shown. Reference patterns for CuO (PDF 45-937), ZnO (PDF 36-1451), and quartz (PDF 5-490) are included for comparison.

at 2θ = 35.5 and 38.8° appeared by increasing the copper content in the active phase above 25%, likely ascribable to the reflection of copper oxide (PDF 45-937). Those peaks were slightly more evident in the $Cu_{0.5}Zn_{0.5}$/AC sorbent. The rather small and broad peaks of ZnO and CuO suggest that the typical dimensions of the crystallites are in the order of few nanometers, which is a highly desirable feature for an effective exploitation of the active phase in the H_2S capture process.

Fig. 4 also reports the XRD pattern of the $Cu_{0.5}Zn_{0.5}$/AC sorbent after saturation with H_2S at 3000 ppmv and 30 °C: the peaks of ZnO completely disappeared (particularly the one at 2θ = 31.8°), while there was a low residual signal in the main zone of CuO (at 2θ = 35.5°). Moreover, there was no clear evidence of the formation of new crystalline phases, such as ZnS and CuS or the corresponding metal sulphates. This was confirmed by the DRIFT spectra of spent sorbents (Fig. S2 Supplementary material), which did not show any new bands compared to those of fresh samples.

3.2. H_2S adsorption tests

Cu_xZn_{1-x}/AC sorbents and their parent support were tested at a fixed inlet concentration of H_2S (i.e. 3000 ppmv) and their breakthrough curves are reported in Fig. 5. From the breakthrough curves, the dynamic data and the corresponding adsorption capacities were determined (according to Eq. (1)). The results are summarized in Table 2, in which t_{br} [s] is the breakpoint time (assumed as the time for which the ratio of H_2S concentration at the bed outlet relative to that in the feed is 0.05), t^* [s] is the saturation time, ω_{br} [mmol g^{-1}] is the adsorption capacity at breakpoint, ω_s [mmol g^{-1}] is the saturation adsorption capacity. The ω_s values determined by Eq. (1) were further checked by elemental analysis of S-content in the spent sorbents (Table 2), and the results corresponded to within ±10%. Moreover, the experiments performed at inlet H_2S content ⩽200 ppmv with a high sensitivity SO_2 analyzer allowed excluding the evolution of SO_2 during the capture process, thus confirming the correctness of the material balance for sulphur (Eq. (1)).

Cu_xZn_{1-x}/AC sorbents showed a significantly longer breakpoint time t_{br} than Darco AC support, despite the experimental tests were run with only half of the sorbent mass. In particular, the breakpoint time increased monotonically with the Cu content in the series Cu_xZn_{1-x}/AC. The outlet H_2S concentration pattern for Darco AC after t_{br} showed a steep slope and a rather short tail, corresponding to a rapid saturation of the sorbent. On the other hand,

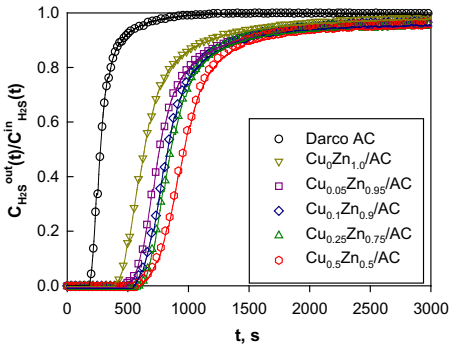

Fig. 5. H_2S breakthrough curves for Cu_xZn_{1-x}/AC sorbents (mass: 2.5 g) and raw Darco AC support (mass: 5 g). Inlet conditions: [H_2S] = 3000 ppmv, T = 30 °C, P = 1 bar.

Table 2
Adsorption performances of Darco AC and Cu_xZn_{1-x}/AC sorbents and S content in spent samples. Sorbent mass: 2.5 g. Inlet conditions: [H_2S] = 3000 ppmv in N_2, T = 30 °C, P = 1 bar. For $Cu_{0.5}Zn_{0.5}$/AC, H_2S adsorption tests were also repeated with 40% vol. of either CO_2 or CH_4 in the feed.

Sorbent	t_{br}	t^*	ω_{br}	ω_s	S content	η[b] $n_{H_2S}/n_{(Cu+Zn)}$
	s	s	mmol g^{-1}	mmol g^{-1}	% wt	–
Darco AC	198[a]	846[a]	0.12	0.20	0.46	–
$Cu_0Zn_{1.0}$/AC	444	2964	0.56	0.97	3.40	0.51
$Cu_{0.05}Zn_{0.95}$/AC	559	5545	0.71	1.28	3.66	0.67
$Cu_{0.1}Zn_{0.9}$/AC	597	5556	0.75	1.31	4.00	0.69
$Cu_{0.25}Zn_{0.75}$/AC	655	5668	0.83	1.36	4.03	0.71
$Cu_{0.5}Zn_{0.5}$/AC	674	5921	0.85	1.46	4.69	0.76
$Cu_{0.5}Zn_{0.5}$/AC[c]	684	5085	0.85	1.42	–	0.74
$Cu_{0.5}Zn_{0.5}$/AC[d]	503	7173	0.59	1.50	–	0.79

[a] Determined with 5 g sorbent mass.
[b] Calculated subtracting the contribution of the AC support.
[c] Feed containing 40% vol. CH_4.
[d] Feed containing 40% vol. CO_2.

Cu_xZn_{1-x}/AC sorbents showed a slower saturation, testified by less steep profiles and significantly longer tails, which could be ascribed to the arising of different phenomena during H_2S capture (*vide infra*). Interestingly, the increase in the Cu content in the active phase determined shorter tails in the adsorption patterns, likely due to faster adsorption rates of CuO.

Following the same ranking shown in terms of breakpoint time, also the H_2S adsorption capacity increased along with the Cu content. The saturation capacity ω_s of $Cu_0Zn_{1.0}$/AC and $Cu_{0.5}Zn_{0.5}$/AC was as much as 5 and 7.5 times larger than that of the corresponding raw Darco AC. This is possibly due to faster sulphidation/sulphation rates of CuO with respect to ZnO, as reported by Jiang et al. [18], who tested unsupported mixed CuO-ZnO sorbents.

In order to better understand and compare the capture performance, we estimated the active phase utilization factor $\eta = n_{H_2S}/n_{(Cu+Zn)}$ for Cu_xZn_{1-x}/AC sorbents, corresponding to the molar ratio between the sulphur adsorbed as H_2S and the Cu + Zn content in the sorbent (from ICP elemental analysis). The values of η reported in Table 2 were calculated by subtracting the adsorption capacity of the raw support (considering that the weight fraction of the activated carbon in the supported sorbent was ≈0.87, i.e. the complementary to the active phase fraction). The assumption of additive contributions from the substrate and from the metal oxides to the overall H_2S capture capacity was verified by TPD results (*vide infra*).

The utilization factor was already above 51% for the sorbent containing only ZnO (i.e. $Cu_0Zn_{1.0}$/AC); moreover, even a small amount (5%) of Cu in the active phase formulation enhanced η above 65%. Since the H_2S capture capacity (ω_s) progressively increased along with the Cu content, a maximum overall utilization factor of ca. 76% was estimated for $Cu_{0.5}Zn_{0.5}$/AC.

Table 3 compares ω_s and η values obtained for $Cu_0Zn_{1.0}$/AC and $Cu_{0.5}Zn_{0.5}$/AC sorbents with figures retrieved from the literature for supported Zn, Cu and Cu-Zn oxide active phases, as well as for two commercial ZnO-based sorbents, and two commercial impregnated activated carbons specifically developed for H_2S adsorption. The comparison was strictly limited to analogous experimental conditions (room temperature, dry feed, possibly without molecular oxygen) in order to derive the unique contribution of the active phase to the H_2S adsorption capacity, thus excluding the possible adsorption catalytic–oxidation mechanisms promoted by the presence of moisture and oxygen in the treated gas.

Commercial unsupported ZnO sorbents are characterized by rather low utilization factors of the active phase (9% in the best reported case) [17], confirming that a large fraction of the oxide remains unconverted due to significant solid state diffusion

Table 3
A performance summary for H_2S adsorption at room temperature under dry conditions over state-of-the-art sorbents based on bulk and supported zinc and copper oxides, and two commercial impregnated activated carbons.

Active phase	Support	Loading % wt	S_{BET} $m^2\ g^{-1}$	ω_s mg g^{-1}	η $n_{H_2S}/n_{(Metal)}$ –	T °C	Inlet H_2S ppmv	Refs.
ZnO BASF	Unsupported	90		19	0.05	20	10,000 in H_2	[17]
ZnO SudChemie	Unsupported	90		32	0.09	"	"	[17]
ZnO	MCM41	10	584	10	0.17	25	200 in N_2	[28]
ZnO	KIT 6	10	387	11	0.19	"	"	[28]
ZnO	SBA-15-S	10	280	14	0.24	"	"	[28]
ZnO	SBA-15-F	10	460	21	0.35	"	"	[28]
ZnO	SiO_2 MSU-1	20	18	15[a]	0.17	25	50,000 in CH_4	[6]
CuO	SiO_2 MSU-1	20	323	19[a]	0.18	"	"	[6]
ZnO	SiO_2	17	250	19	0.28	20	8000 in H_2	[7]
$Cu_{0.05}Zn_{0.95}O$	SiO_2	17	250	36	0.53	"	"	[7]
ZnO	SiO_2	15	460	32	0.54	20	10,000 in H_2	[17]
$Cu_{0.05}Zn_{0.95}$ O	SiO_2	15	450	43	0.73	"	"	[17]
$Cu_{0.2}Zn_{0.8}$ O	SiO_2	15	450	45	0.76	"	"	[17]
$Cu_{0.2}Zn_{0.8}$ O	SiO_2	21		78	0.94	"	"	[17]
ZnO (+KI)	AC ROZ3 Norit	10	851	29	0.34	28	200 in N_2	[13]
ZnO	AC Darco Norit	12	558	33	0.51	30	3000 in N_2	[this work]
$Cu_{0.5}Zn_{0.5}O$	AC Darco Norit	12	570	50	0.76	30	3000 in N_2	[this work]
Cu-Cr	AC RGM1 Norit		1599	27		30	200 in N_2	[22]
KOH	AC RBAA1 Norit		817	20		"	"	[22]

[a] Breakthrough capacity calculated at H_2S_{out} = 10,000 ppmv.

limitations of reactant species across the outer reacted layer (*vide infra*). On the other hand, Hussain et al. [28] demonstrated that the dispersion of ZnO onto large surface area mesoporous silica supports (i.e. MCM41, KIT 6 or SBA-15) allows a better exploitation of the active phase, with η reaching a value of 0.35. Montes et al. [6] reported that CuO or ZnO showed quite similar H_2S capture capacities when supported at 20% wt over the same SiO_2 MSU-1. Doping of zinc oxide with a different metal (in particular copper) was found to induce synergic effects and to increase the conversion degree of ZnO during H_2S capture process at low temperature [7,17]. In particular, Dhage et al. [17] derived utilization factors as high as 0.76 and 0.94 for mixed $Cu_{0.2}Zn_{0.8}O$ supported onto a high surface area silica, indicating a clear improvement with respect to non-doped ZnO on the same support (η = 0.54). Those values correspond well to our results of utilization factors obtained with similar oxides dispersed onto the Darco activated carbon. However, $Cu_{0.5}Zn_{0.5}$/AC sorbent outperformed SiO_2-supported counterparts (at similar loadings) in terms of ω_s due to the contribution to H_2S capture coming from the activated carbon itself. Table 3 also witnesses the higher conversion degree of the mixed metal phases attained for $Cu_{0.5}Zn_{0.5}$/AC (η = 0.76) with respect to the value reported [13] for a Norit ROZ3 activated carbon loaded with ZnO at 10% wt (η = 0.34, as derived by subtracting the contribution of the KI impregnated support). Furthermore, ω_s for $Cu_{0.5}Zn_{0.5}$/AC sorbent exceeded by as much as 1.9 and 2.5 times the corresponding values for two commercial activated carbons, respectively RGM1 loaded with Cu-Cr, and RBAA1 impregnated with KOH [22].

Finally, it was reported that the presence of humidity did not affect H_2S capture performance of $Cu_xZn_{1-x}O$ composite oxide when supported onto SiO_2 [17]. On the other hand, carbon-based sorbents determine significant sulphur removal mainly under moist conditions [7]. In turn, this suggests a greater potential applicability of activated carbons functionalized with mixed CuO-ZnO for high H_2S uptake from multicomponent streams, such as biogas, thanks to the synergistic contributions of the active phase and the carbonaceous support.

The significant impact of Cu addition, even at rather low contents, suggested that copper may contrast/reduce the diffusional limitations in the solid state, which are responsible for the low utilization factors commonly observed in the case of ZnO sorbents [7]. This is generally attributed to the formation of a compact and thin overlayer (of ZnS) leaving the underlying core of ZnO unreacted [7]. In fact, it was previously reported that Cu-containing ZnS particles possess a higher mobility of sulphur anions leading to a more rapid exchange with O^{2-} anions due to the presence of sulphur vacancies formed after the charge compensation of Cu^{1+} replacing Zn^{2+}, which favors a more rapid growth of ZnS crystallites [29]. Moreover, in our tests we also found evidence for the formation of metal sulphates apart from metal sulphides (*vide infra* 3.3), underlying a higher complexity of the surface reactions and of the Cu-doping effect. Finally, Cu addition could effectively reduce the characteristic dimensions of ZnO crystallites [30], thus enhancing their reactivity and utilization through a higher exposed surface area.

Considering its highest H_2S adsorption capacity, the $Cu_{0.5}Zn_{0.5}$/AC sorbent was selected for further dynamic tests at several inlet concentration levels in the range 50–3000 ppmv: Fig. 6 presents the results in terms of the H_2S saturation capacities measured at 30 °C and 1 bar, in comparison with the results obtained on the raw Darco AC. Across the entire investigated range of concentrations, $Cu_{0.5}Zn_{0.5}$/AC showed a much larger H_2S adsorption capacity than the raw AC support. For both sorbents ω_s increased slightly with the H_2S partial pressure, and an almost asymptotic value was reached at the highest tested concentrations. For $Cu_{0.5}Zn_{0.5}$/AC, an adsorption capacity of ca. 1 mmol g^{-1} was already achieved in correspondence of rather low H_2S concentrations (50–200 ppmv), indicating that the H_2S capture mechanism involves chemical reactions with the composite metal oxides [31] in a relatively wide range of compositions of interest for practical applications.

In order to verify the potential competitive adsorption phenomena of CO_2 and CH_4, dedicated H_2S removal tests were performed on $Cu_{0.5}Zn_{0.5}$/AC sorbent with a feed gas also containing 40% vol. of either CO_2 or CH_4 (balance N_2). The corresponding H_2S dynamic adsorption patterns are reported in Fig. 7, and compared to the reference case of H_2S in N_2. The characteristic adsorption parameters are collected in Table 2. The presence of CH_4 did not appreciably affect the H_2S adsorption process, as testified by almost overlapped breakthrough profiles and quite similar values of the H_2S saturation adsorption capacities. On the other hand, the presence of CO_2 determined a shift of the breakthrough profile towards shorter times followed by a longer tail (cf. also t_{br} and t^* values in Table 2). However, the measured H_2S adsorption capacity at saturation was not significantly altered. These results point to a partial kinetic

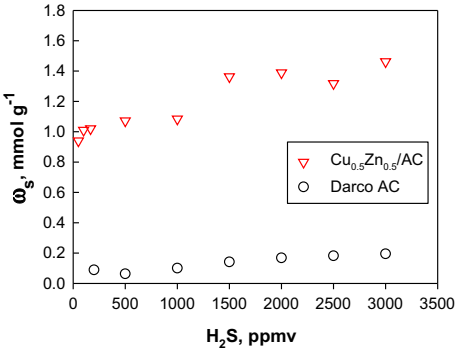

Fig. 6. H_2S adsorption isotherms on Darco AC and $Cu_{0.5}Zn_{0.5}$/AC sorbent. T = 30 °C, P = 1 bar.

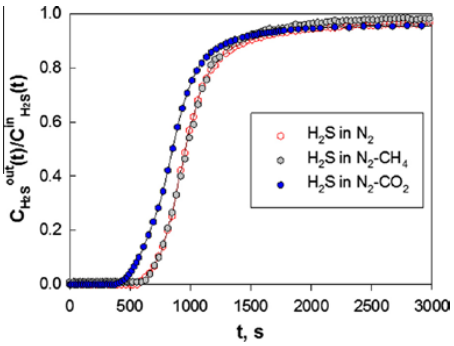

Fig. 7. H_2S breakthrough curves for $Cu_{0.5}Zn_{0.5}$/AC sorbent in H_2S/N_2, $H_2S/CO_2/N_2$ and $H_2S/CH_4/N_2$ flux. Inlet conditions: $[H_2S]$ = 3000 ppmv, $[CO_2]$ = 40% vol., $[CH_4]$ = 40% vol., T = 30 °C, P = 1 bar.

inhibition effect of the H_2S capture process in the ternary $N_2/CO_2/H_2S$ system, possibly related to the competitive CO_2 adsorption onto active sites on the carbonaceous surface of $Cu_{0.5}Zn_{0.5}$/AC.

3.3. TPD tests

Spent Cu_xZn_{1-x}/AC sorbents, saturated during H_2S capture tests at 3000 ppmv and 30 °C, were further subjected to Temperature Programmed Desorption (TPD) tests under N_2 flux up to 620 °C, by monitoring simultaneously the evolution of H_2S and SO_2. The tests aimed at acquiring insights on the type of compounds formed during H_2S adsorption while assessing the thermal regenerability of the Cu_xZn_{1-x}/AC sorbents (after being exposed to air at room temperature).

Interestingly, none of the Cu_xZn_{1-x}/AC sorbents (nor the raw AC) desorbed measurable quantities of H_2S, suggesting a negligible contribution of physical adsorption mechanism under the adopted operating conditions. On the other hand, all sorbents desorbed significant amounts of SO_2 (Fig. 8), confirming that the H_2S reactive capture was coupled with oxidation phenomena.

In particular, the spent Darco AC support showed a single SO_2 peak starting at ca. 170 °C and centred at 280 °C: this was previously ascribed to the release of SO_2 formed by oxidation reactions with chemisorbed oxygen or oxygen containing surface groups

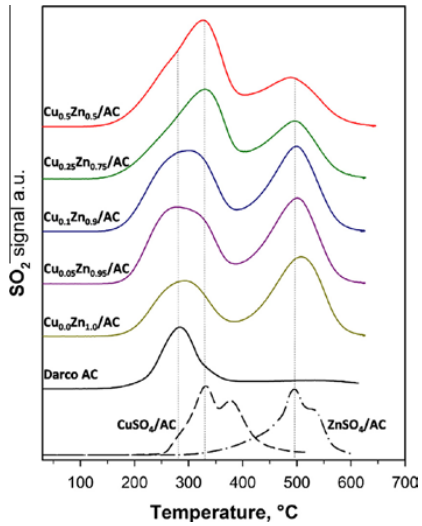

Fig. 8. SO_2 release during TPD tests from H_2S-saturated Cu_xZn_{1-x}/AC sorbents and corresponding Darco AC support, as well as from two reference samples of $CuSO_4$ and $ZnSO_4$ impregnated on Darco AC.

onto active sites located in small pores of the activated carbon [20,23,24,32].

The TPD profile for the saturated $Cu_0Zn_{1.0}$/AC sorbent showed two main and broad SO_2 emission peaks, respectively centred at ca. 290 °C and 500 °C. The first, low temperature peak closely resembled the one observed in the TPD profile of the spent Darco AC. By comparison with the TPD profile of a reference sample prepared by impregnating $ZnSO_4$ on the same activated carbon (reported at the bottom of Fig. 8), it was possible to assign the high temperature signal to the decomposition of zinc sulphate. Note that bulk, unsupported $ZnSO_4$ started to decompose releasing SO_2 only at T > 700 °C (Fig. S3 Supplementary material), thus revealing a strong interaction effect with the carbon based support that reduced the stability of the sulphate [33,34].

The presence of Cu in the active phase determined a new contribution in the TPD profiles of saturated Cu_xZn_{1-x}/AC sorbents, initially as a shoulder centred at ca. 330 °C, which progressively became the main signal in the low temperature zone along with increasing Cu content. Also in this case, a close comparison with the TPD profile of a reference sample containing $CuSO_4$ impregnated on the same activated carbon (Fig. 8) revealed that the peak at 330 °C can be ascribed to the thermal decomposition of copper sulphate in close contact with carbon support, starting at ca. 250 °C. Note that bulk $CuSO_4$ decomposed releasing SO_2 only at T > 550 °C (Fig. S3 Supplementary material). Coherently, along with the reduction of the Zn content in Cu_xZn_{1-x}/AC sorbents, the peak at 500 °C, assigned to the decomposition of $ZnSO_4$, progressively decreased.

Qualitative measurements (by ICP-MS and Ionic Chromatography, not reported) confirmed the presence of Zn and Cu sulphates dissolved in solution after contacting spent sorbents with distilled water.

Noteworthy, most of the literature studies assumed that the reaction of metal oxides (supported or not) with H_2S led to the formation of the corresponding metal sulphides. However, some authors reported experimental evidence for the partial formation

of metal sulphates during the H_2S capture process on metal oxides/hydroxides [14,20,23,35,36]. For example, Florent and Bandosz [36] detected the formation of $CoSO_4$ (apart from sulphur and cobalt sulphide), by FTIR and TG/MS measurements, after H_2S adsorption onto cobalt oxyhydroxide/graphite oxide composites under moist and dry conditions. Formation of metal sulphates together with elemental sulphur was also reported by Zhang et al. [35] investigating the use of mesoporous carbon spheres impregnated with MgO for the catalytic oxidation of H_2S at room temperature. The authors ascribed sulphate formation (detected by means of XPS analysis) to the oxidation of H_2S to the acidic SO_3 species, the latter being able to neutralize the basic MgO.

In general, the identification of the actual phases produced along the H_2S conversion process is of paramount importance to design optimal regeneration strategies of the exhausted sorbent. To this aim, TPD profiles of Cu_xZn_{1-x}/AC sorbents were integrated in order to calculate the total amount of sulphur desorbed as SO_2, up to two different temperature levels (i.e. 400 and 620 °C). The results are reported in Table 4, together with a direct comparison with the corresponding H_2S adsorption capacity at saturation. The (small) amount of H_2S adsorbed on the raw activated carbon was entirely desorbed as SO_2 at T < 400 °C. On the other hand, spent Cu_xZn_{1-x}/AC sorbents released 40–46% of their initial sulphur content at the end of the TPD (620 °C), whereas this figure dropped to only 18–27% when considering temperatures up to 400 °C.

In particular, the amount of SO_2 released by Cu_0 $Zn_{1.0}$/AC at temperature ⩽400 °C closely corresponded to the amount of SO_2 desorbed by the raw activated carbon (Table 4). The latter finding corroborates the hypothesis according to which the support determined a similar contribution to H_2S capture capacity also when partly covered by the metal oxides of the active phase (Section 3.2).

The remaining sulphur was likely stored as Zn and Cu sulphides, which are stable species at the investigated temperature in N_2 atmosphere [21]. However, no direct conclusion could be drawn on the eventual presence of elemental sulphur on spent sorbents.

All copper containing sorbents released almost the same amount of SO_2 at T ⩽ 620 °C (0.58 ± 0.03 mmol g^{-1}), which was larger than what retrieved for the sample containing only zinc (0.41 mmol g^{-1}). It can be argued that Cu-doping favored the oxidation of the captured H_2S to form sulphates, whose final quantity was limited by the oxygen availability on the sorbent, since adsorption and desorption tests were conducted under an inert atmosphere. It is worth observing that spent sorbents were exposed to air in between adsorption and desorption tests, and therefore molecular oxygen could have been re-adsorbed on their surface. On the other hand, TPD-NO_x, and DRIFT analysis (Supplementary material) excluded the residual presence of nitrates (from the corresponding precursors), hence they could not be considered as potential oxygen sources.

It also follows that the surplus of H_2S captured by samples with progressively higher Cu contents had to be stored as metal sulphides or elemental sulphur.

Table 4
Specific amount of sulphur desorbed as SO_2 from spent Cu_xZn_{1-x}/AC sorbents during TPD tests in N_2 up to two different temperature levels (i.e. 400 and 620 °C).

Sorbent	ω_s	Desorbed SO_2 up to 400 °C		Desorbed SO_2 up to 620 °C	
	mmol g^{-1}	mmol g^{-1}	% of ω_s	mmol g^{-1}	% of ω_s
Darco AC	0.20	0.20	100	–	–
Cu_0 $Zn_{1.0}$/AC	0.97	0.18	18.1	0.41	42.1
$Cu_{0.05}$ $Zn_{0.95}$/AC	1.28	0.30	23.5	0.58	45.4
$Cu_{0.1}ZnO_{0.9}$/AC	1.31	0.33	25.0	0.61	46.3
$Cu_{0.25}$ $Zn_{0.75}$/AC	1.36	0.34	25.0	0.55	40.6
$Cu_{0.5}Zn_{0.5}$/AC	1.46	0.39	26.7	0.59	40.3

The progressive substitution of Zn by Cu and the strong interaction with the activated carbon support increased the amount of SO_2 released at relatively low temperatures (i.e. up to 400 °C), which is highly desirable in the light of the regenerability of Cu_xZn_{1-x}/AC sorbents by thermal treatments. However, the release of the captured sulphur under inert atmosphere and the restoration of the original active phase appears to be upper limited by oxygen availability. Therefore, it is foreseen that a more effective regeneration could be achieved by thermally treating spent sorbents in the presence of steam [16] and/or slightly oxidizing conditions, in order to enhance the removal of sulphur in metal sulphides or stored as elemental sulphur.

4. Conclusions

Novel sorbents for H_2S removal were prepared by finely dispersing mixed ZnO and CuO onto a commercial activated carbon at fixed total metal loading (10% wt) and Cu:Zn atomic ratios ranging from 0:1 to 1:1. Their H_2S removal performance and capture mechanism were investigated at low temperature under dry conditions.

The pore size distribution of the activated carbon support was hardly affected due to the high dispersion of the metal oxides that, on contrary, strongly enhanced the original adsorption capacity of the raw activated carbon. The partial substitution of ZnO for CuO induced a progressive increase in the H_2S sorption capacity, which was poorly affected by the inlet H_2S concentration in the range 50–3000 ppmv, as well as by the presence of CH_4 or CO_2 in the gas mixture. The beneficial effect of Cu, even at low loadings, was likely related to a reduction of diffusional limitations in the lattice of the composite active phase and through the reacted overlayer, which is a known issue for ZnO-based sorbents at low temperature.

At the maximum copper content explored, $Cu_{0.5}Zn_{0.5}$/AC sorbent provided an utilization factor of the active metal oxides as high as 0.76, excluding the contribution deriving from the activated carbon itself. This is comparable to the best literature results for analogue composite Zn-Cu oxides dispersed on high surface area SiO_2 supports and tested under similar operating conditions. Further improvements of H_2S capture capacity are expected only for those sorbents with an active phase dispersed on activated carbon if operating with humid and/or oxygen-containing feeds. Indeed (impregnated) activated carbons have the peculiar property to induce catalytic oxidation effects and store oxidized sulphur species in their pores.

In view of the current results, an optimization strategy for the class of Cu_xZn_{1-x}/AC sorbents should investigate higher active phase loadings and relative copper contents, as well as the use of alternative activated carbons supports.

The reactive adsorption mechanism was investigated through Temperature Programmed Desorption of H_2S and SO_2 from the saturated sorbents. A negligible release of H_2S was coupled to a large emission of SO_2 accounting for 40–45% of the total sulphur captured by Cu_xZn_{1-x}/AC sorbents. Direct comparison with TPD profiles of reference samples suggested that formation of both Zn and Cu sulphates occurred during the H_2S reactive adsorption. The remaining amount of sulphur was likely stored as stable metal sulphides or elemental sulphur, underlying the complexity of the surface reactions.

The strong interaction of the active phase with the carbon support reduced significantly the stability and the decomposition temperature of metal sulphates formed during reactive adsorption. Moreover, the substitution of Zn for Cu, increased the fraction of sulphates that can be decomposed at lower temperature (<400 °C). This is highly desirable in view of an easy regenerability of spent sorbents with restoration of the active phase.

Acknowledgments

This work was supported by the Italian Ministry for Economic Development (MISE) within the framework of Industria 2015 Efficienza Energetica project #EE01_00050.

Appendix A. Supplementary data

Supplementary data associated with this article can be found, in the online version, at http://dx.doi.org/10.1016/j.cej.2016.06.085.

References

[1] S. Rasi, J. Läntelä, J. Rintala, Trace compounds affecting biogas energy utilisation – a review, Energy Convers. Manage. 52 (12) (2011) 3369–3375.
[2] I. Rosso, C. Galletti, M. Bizzi, G. Saracco, V. Specchia, Zinc oxide sorbents for the removal of hydrogen sulfide from syngas, Ind. Eng. Chem. Res. 42 (8) (2003) 1688–1697.
[3] H.F. Garces, H.M. Galindo, L.J. Garces, J. Hunt, A. Morey, S.L. Suib, Low temperature H_2S dry-desulfurization with zinc-oxide, Microporous Mesoporous Mater. 127 (2010) 190–197.
[4] K. Balichard, C. Nyikeine, I. Bezverkhvy, Nanocrystalline $ZnCO_3$ – a novel sorbent for low temperature removal of H_2S, J. Hazard. Mater. 264 (2014) 79–83.
[5] S. Kang, J.W. Bae, S. Kim, K. Jun, Effect of phosphorus modification on Cu–ZnO–Al_2O_3 for the removal of H_2S, Energy Fuels 22 (6) (2008) 2580–2584.
[6] D. Montes, E. Tocuyo, E. González, D. Rodríguez, R. Solano, R. Atencio, A. Moronta, Reactive H_2S chemisorption on mesoporous silica molecular sieve-supported CuO or ZnO, Microporous Mesoporous Mater. 168 (2013) 111–120.
[7] H. Yang, B. Tatarchuk, Novel-doped zinc oxide sorbents for low temperature regenerable desulfurization applications, AIChE J. 56 (2010) 2898–2904.
[8] B. Elyassi, Y. Al Wahedi, N. Rajabbeigi, P. Kumar, J.S. Jeong, X. Zhang, P. Kumar, V.V. Balasubramanian, M.S. Katsiotis, K.A. Mkhoyan, N. Boukos, S. Al Hashimi, M. Tsapatsis, High-performance adsorbent for hydrogen sulfide removal, Microporous Mesoporous Mater. 190 (2014) 152–155.
[9] T. Yamamoto, M. Tayakout-Fayolle, C. Geantet, Gas-phase removal of hydrogen sulfide using iron oxyhydroxide at low temperature: measurement of breakthrough curve and modeling of sulfidation mechanism, Chem. Eng. J. 262 (2015) 702–709.
[10] V. Girard, A. Baudot, D. Chiche, D. Bazer-Bachi, C. Bounie, C. Geantet, Rational selection of single oxide sorbents for syngas desulfurization regenerable at reduced temperature: thermochemical calculations and experimental study, Fuel 128 (2014) 220–230.
[11] C. Huang, C. Chen, S. Chu, Effect of moisture on H_2S adsorption by copper impregnated activated carbon, J. Hazard. Mater. 136 (3) (2006) 866–873.
[12] X. Wang, T. Sun, J. Yang, L. Zhao, J. Jia, Low-temperature H_2S removal from gas streams with SBA-15 supported ZnO nanoparticles, Chem. Eng. J. 142 (2008) 48–55.
[13] S.P. Hernández, M. Chiappero, N. Russo, D. Fino, A novel ZnO-based adsorbent for biogas purification in H_2 production systems, Chem. Eng. J. 176–177 (2011) 272–279.
[14] J.A. Arcibar-Orozco, R. Wallace, J.K. Mitchell, T.J. Bandosz, Role of surface chemistry and morphology in the reactive adsorption of H_2S on iron (hydr) oxide/graphite oxide composites, Langmuir 31 (9) (2015) 2730–2742.
[15] M. Florent, T. Bandosz, Effects of surface heterogeneity of cobalt oxyhydroxide/graphite oxide composites on reactive adsorption of hydrogen sulfide, Microporous Mesoporous Mater. 204 (2015) 8–14.
[16] Y. Feng, J. Dou, A. Tahmasebi, J. Xu, X. Li, J. Yu, R. Yin, Regeneration of Fe–Zn–Cu sorbents supported on activated lignite char for the desulfurization of coke oven gas, Energy Fuels 29 (11) (2015) 7124–7134.
[17] P. Dhage, A. Samokhvalov, D. Repala, C.E. Duin, M. Bowman, B.J. Tatarchuk, Copper-promoted ZnO/SiO_2 regenerable sorbents for the room temperature removal of H_2S from reformate gas streams, Ind. Eng. Chem. Res. 49 (18) (2010) 8388–8396.
[18] D. Jiang, L. Su, L. Ma, N. Yao, X. Xu, H. Tang, X. Li, Cu–Zn–Al mixed metal oxides derived from hydroxycarbonate precursors for H_2S removal at low temperature, Appl. Surf. Sci. 256 (2010) 3216–3223.
[19] R. Yan, D.T. Liang, L. Tsen, J.H. Tay, Kinetics and mechanisms of H_2S adsorption by alkaline activated carbon, Environ. Sci. Technol. 36 (20) (2002) 4460–4466.
[20] R. Yan, T. Chin, Y.L. Ng, H. Duan, D.T. Liang, J.H. Tay, Influence of surface properties on the mechanism of H_2S removal by alkaline activated carbons, Environ. Sci. Technol. 38 (2004) 316–323.
[21] D. Nguyen-Thanh, T.J. Bandosz, Activated carbons with metal containing bentonite binders as adsorbents of hydrogen sulphide, Carbon 43 (2) (2005) 359–367.
[22] E. Sisani, G. Cinti, G. Discepoli, D. Penchini, U. Desideri, F. Marmottini, Adsorptive removal of H_2S in biogas conditions for high temperature fuel cell systems, Int. J. Hydrogen Energy 39 (36) (2014) 21753–21766.
[23] A. Bagreev, T.J. Bandosz, On the mechanism of hydrogen sulfide removal from moist air on catalytic carbonaceous adsorbents, Ind. Eng. Chem. Res. 44 (3) (2005) 530–538.
[24] W. Feng, S. Kwon, E. Borguet, R. Vidic, Adsorption of hydrogen sulfide onto activated carbon fibers: effect of pore structure and surface chemistry, Environ. Sci. Technol. 39 (24) (2005) 9744–9749.
[25] M. Balsamo, F. Rodriguez-Reinoso, F. Montagnaro, A. Lancia, A. Erto, Highlighting the role of activated carbon particle size on CO_2 capture from model flue-gas, Ind. Eng. Chem. Res. 52 (2013) 12183–12191.
[26] S. Cimino, L. Lisi, M. Tortorelli, Low temperature SCR on supported MnO_x catalysts for marine exhaust gas cleaning: effect of KCl poisoning, Chem. Eng. J. 283 (2016) 223–230.
[27] B. Małecka, A. Łącz, E. Drożdż, A. Małecki, Thermal decomposition of d-metal nitrates supported on alumina, J. Therm. Anal. Calorim. 119 (2) (2015) 1053–1061.
[28] M. Hussain, N. Abbas, D. Fino, N. Russo, Novel mesoporous silica supported ZnO adsorbents for the desulphurization of biogas at low temperatures, Chem. Eng. J. 188 (2012) 222–232.
[29] I. Bezverkhyy, J. Skrzypski, O. Safonova, J.P. Bella, Sulfidation mechanism of pure and Cu-doped ZnO nanoparticles at moderate temperature: TEM and in Situ XRD studies, J. Phys. Chem. C. 116 (27) (2012) 14423–14430.
[30] T. Baird, P.J. Denny, R. Hoyle, F. Mc Monagle, D. Stirling, J. Tweedy, Modified zinc oxide absorbents for low-temperature gas desulfurization, J. Chem. Soc. Faraday Trans. 88 (22) (1992) 3375–3382.
[31] A. Bagreev, S. Katikaneni, S. Parab, T.J. Bandosz, Desulfurization of digester gas: prediction of activated carbon bed performance at low concentrations of hydrogen sulfide, Catal. Today 99 (3–4) (2005) 329–337.
[32] J. Guo, Y. Luo, A. Chong Lua, R. Chi, Y. Chen, X. Bao, S. Xiang, Adsorption of hydrogen sulphide (H_2S) by activated carbons derived from oil-palm shell, Carbon 45 (2007) 330–336.
[33] R. Narayan, A. Tabatabaie-Raissi, M.J. Antal, Study of zinc sulfate decomposition at low heating rates, Ind. Eng. Chem. Res. 27 (1988) 1050–1058.
[34] B.S. Boyanov, DTA and TGA study of MeSO4 (Me=Fe Co, Ni) dissociation in the presence of coke, J. Min. Metall. Sect. B 38 (1–2) (2002) 103–116.
[35] Z. Zhang, J. Wang, W. Li, M. Wang, W. Qiao, D. Long, L. Ling, Millimeter-sized mesoporous carbon spheres for highly efficient catalytic oxidation of hydrogen sulfide at room temperature, Carbon 96 (2016) 608–615.
[36] M. Florent, T. Bandosz, Effects of surface heterogeneity of cobalt oxyhydroxide/graphite oxide composites on reactive adsorption of hydrogen sulphide, Microporous Mesoporous Mater. 204 (2015) 8–14.

II

Microporous and Mesoporous Materials 257 (2018) 135–146

Contents lists available at ScienceDirect

Microporous and Mesoporous Materials

journal homepage: www.elsevier.com/locate/micromeso

Synergic effect of Zn and Cu oxides dispersed on activated carbon during reactive adsorption of H_2S at room temperature

Giacomo de Falco [a, b], Fabio Montagnaro [b], Marco Balsamo [c, *], Alessandro Erto [c], Fabio Alessandro Deorsola [d], Luciana Lisi [a], Stefano Cimino [a]

[a] Istituto di Ricerche sulla Combustione, Consiglio Nazionale delle Ricerche, Piazzale Vincenzo Tecchio 80, 80125 Napoli, Italy
[b] Dipartimento di Scienze Chimiche, Università degli Studi di Napoli Federico II, Complesso Universitario di Monte Sant'Angelo, 80126 Napoli, Italy
[c] Dipartimento di Ingegneria Chimica, dei Materiali e della Produzione Industriale, Università degli Studi di Napoli Federico II, Piazzale Vincenzo Tecchio 80, 80125 Napoli, Italy
[d] Dipartimento Scienza Applicata e Tecnologia, Politecnico di Torino, Corso Duca degli Abruzzi 24, 10129 Torino, Italy

ARTICLE INFO

Article history:
Received 6 July 2017
Received in revised form
31 July 2017
Accepted 14 August 2017
Available online 17 August 2017

Keywords:
Reactive adsorption
Mixed metal oxides
Activated carbon
Sulphur poisoning
Gas cleaning

ABSTRACT

The origin of the synergic effect of zinc and copper oxides (ZnO-CuO) supported onto activated carbon on the removal of hydrogen sulphide (H_2S) from gaseous streams at low temperature is investigated in this work. Sorbents with a fixed total metal content and variable Zn:Cu ratios were prepared by impregnation of a commercial activated carbon. H_2S (100–3000 ppmv in N_2) removal tests were run under dynamic conditions at 30 °C and compared through analysis of their breakthrough curves, adsorption rates and values of adsorption capacity. Fresh and spent sorbents were characterized by BET and pore size distribution *via* N_2-adsorption, SEM-EDX and XPS. TPD/TPO experiments from partially and completely saturated sorbents allowed the speciation of adsorbed sulphur species, testifying the complexity of the surface reactions which strongly depended on the Zn:Cu ratio, on the interactions of metal oxides with activated carbon and on the textural properties of the sorbent.

1. Introduction

Hydrogen sulphide (H_2S) is a toxic compound found in a variety of fuel resources such as crude petroleum, natural gas and biogas [1]. A few ppm of H_2S can corrode pipelines [2], poison catalysts used in fuel cells [3] and emission of sulfur compounds can contribute to the production of acid rains [4]. As an example Bao et al. [5] studied the effect of the concentration of H_2S on the poisoning of a fuel cell based on solid oxides, concluding that even 1 ppmv of H_2S causes an immediate performance loss. Adsorption is one of the most suitable methods for the removal of H_2S from a gas stream, as it allows a deep purification (down to H_2S concentration less than 1 ppmv) and a cost effective approach. However, highly performing adsorbent materials are required to obtain a deep purification particularly at low (i.e. room) temperature [6,7]. Currently, research efforts are mainly devoted to sorbents based on metal oxides, hydroxides and carbonates supported onto a matrix of high superficial area such as zeolites, mesoporous silicas, activated carbons and graphene/graphite oxides [8,9]. In particular activated carbons (AC) are extensively used as support for the removal of H_2S as their properties, such as surface area and surface chemistry, play an important role [10–12].

The identification of the compounds produced upon the adsorption process of H_2S is of paramount importance to select optimal chemical formulations and textural properties of sorbents and to set-up potential regeneration strategies for exhausted materials. Many literature studies focused on the formation of metal sulphides as a product of the reaction between metal oxides (supported or not) and H_2S [13,14]. Hernández et al. [15] employed two different commercial AC supporting 10% wt. of ZnO to evaluate the adsorption capacity in presence of a stream containing 200 ppmv of H_2S in N_2 at 28 °C. They detected, by means of X-ray photoelectron spectroscopy (XPS) analysis, the sole formation of ZnS. Huang et al. [16] studied the behaviour of $Cu(OH)_2$ supported on AC assuming the sole formation of CuS after adsorption tests in presence of a stream containing 270 ppmv of H_2S in He and with relative humidity of 40–80%. The assumption of the formation of metal sulphides, though relevant, should be integrated by other considerations, taking into account that the process of H_2S adsorption might likely involve the formation of a complex variety

* Corresponding author.
E-mail address: marco.balsamo@unina.it (M. Balsamo).

http://dx.doi.org/10.1016/j.micromeso.2017.08.025
1387-1811/

of compounds such as elemental sulphur, sulphur dioxide, sulphuric acid, metal sulphates. In particular, some authors reported experimental evidence of partial formation of metal sulphates during the H_2S capture on metal oxides/hydroxides [17–19]. Zhang et al. [20] highlighted the formation of metal sulphates together with elemental sulphur using spheres of mesoporous carbon impregnated with MgO for catalytic oxidation of H_2S at room temperature. Those authors ascribed the sulphate formation (detected by means of XPS analysis) to the oxidation of H_2S to acidic SO_3 species, the latter being able to neutralise basic MgO. Mabayoje et al. [21] found the formation of copper sulphate, by thermogravimetric measurement, after H_2S adsorption onto copper (hydr) oxychlorides supported on graphene/graphite oxide. In this case, the formation of sulphate is the result of the ability of copper to activate oxygen, and the oxidised graphene can contribute to this process as well [21].

Following this path, in our recent work [22] we inferred the formation of both Zn and Cu sulphates by temperature programmed desorption (TPD) tests upon reactive adsorption of H_2S on mixed oxides (ZnO–CuO) supported on commercial activated carbon. Moreover, we found that the partial substitution of CuO for ZnO within a given range, at fixed total loading of metal (10% wt.), induced a progressive increase in the sorption capacity of H_2S. The highest adsorption capacity was observed for the sorbent having Cu:Zn molar ratio equal to one. The present paper extends and complements the previous investigation with respect to the promoting role of copper in mixed ZnO–CuO supported systems on the H_2S removal mechanism, focusing on the interrelationships among properties of functionalized activated carbon, operating conditions and process outcomes. Moreover, a significant effort was made in order to identify the adsorbed sulphur species produced during capture process, so to shed light on the complexity of the surface reactions.

H_2S removal experiments (100–3000 ppmv in N_2) under dynamic conditions at room temperature were complemented by BET and pore size distribution analysis, SEM-EDX and XPS analysis for the characterisation of fresh and spent sorbents. Additionally, a TPD/TPO experimental protocol was established for the speciation analysis of sulphur species formed at different stages during the reactive adsorption process depending on the specific formulation of the active phase.

2. Materials and methods

2.1. Adsorbents

Hybrid adsorbents based on ZnO–CuO highly dispersed onto a commercial activated carbon (Darco G40, Norit) were produced by incipient wetness impregnation using aqueous solutions of metal nitrates, and finally heat treated at 250 °C under inert flow. More details on the preparation procedure were already reported elsewhere [22]. The nominal loading of metals (Zn + Cu) in functionalized sorbents was set to 10% wt., whereas the relative content of Zn and Cu was varied, including formulations with only Zn or only Cu. Sorbents with mixed oxides were labelled as Cu_xZn_{1-x}/AC, where x represents the molar fraction of Cu with respect to (Zn + Cu). Sorbent containing only Zn or only Cu were termed as Zn/AC or Cu/AC, respectively.

2.2. Adsorbent characterization

SEM-EDX analysis was carried out on cross-sections of sorbent particles using a FEI Inspect instrument. The textural properties of the sorbents were determined by N_2 adsorption at −196 °C with a Quantachrome Autosorb 1-C instrument. In particular, the Brunauer–Emmett–Teller (BET) method was adopted for the calculation of the specific surface area (S_{BET}), while the micropore volume (V_M) and the total pore volume (V_{TOT}) were respectively computed by means of the Dubinin–Astakov and Gurvitsch's rule applied to the N_2 amount adsorbed at $P/P_0 = 0.99$. Finally, the pore size distribution (PSD) was evaluated *via* the Quenched Solid Density Functional Theory.

XPS analysis was carried out on a XPS PHI 5000 Versa probe apparatus, using a band-pass energy of 187.85 eV, a 45° take off angle and a 100.0 μm diameter X-ray spot size for survey spectra. High-resolution XP-spectra were recorded in the following conditions: pass energy of 20 eV, resolution of 1.1 eV, and step of 0.2 eV. Sample charging effects were eliminated by correcting the line shift of the C 1s signal from its binding energy value of 284.6 eV. XP-spectra were analysed by means of a commercial software (CasaXPS, version 2.3.16), by applying mixed Gaussian–Lorentzian (70–30%) profiles. Assignation of XPS signals was based on the NIST compilation of spectral data [23], unless otherwise stated.

The amount of sulphur released from spent materials in aqueous phase as sulphate ions (ω_{aq}) was evaluated by contacting 0.05 g of each sorbent, previously saturated with H_2S at 3000 ppmv, with 0.1 L of distilled water at 60 °C. The supernatant solution was analysed for times ranging from 3 to 480 h by means of a 883 Basic IC Plus ionic chromatograph (Metrohm).

2.3. H_2S adsorption tests

Dynamic adsorption tests of H_2S were carried out at atmospheric pressure and $T = 30$ °C, in a lab-scale experimental apparatus based on a fixed bed reactor with annular section made of quartz, already described elsewhere [24,25]. A weighted amount of sorbent (20 mg for functionalized materials, if not otherwise reported; 80 mg for raw AC) with a particle size range of 125–200 μm was mixed with quartz to obtain a total mass of the bed of 200 mg. The temperature was measured by a K-type thermocouple placed inside the inner section of the reactor with its tip at the middle of the sorbent bed. The inlet concentration of H_2S ($C^{in}_{H_2S}$) was varied in the range 100–193 ppmv (100 ppmv as base-case) by mixing two streams of high purity N_2 and H_2S in N_2 regulated by independent mass flow controllers. The inlet flow rate of gas was varied in the range 20–40 SL h^{-1}, corresponding to contact times as low as 3.4–6.8 ms as referred to the volume of functionalized sorbent. Gas analysis was performed with a continuous analyser (ABB Optima Advance Limas 11 UV) with cross sensitivity correction for the simultaneous measurement of H_2S and SO_2, with accuracy better than 1% of span (200 ppmv).

In addition, some specific H_2S adsorption tests at higher concentration were carried out to complement the investigation published in Balsamo et al. [22]. These tests were performed in a fixed bed column (see Ref. [22] for a detailed description of the lab-scale apparatus) under the following experimental conditions: 2.5 g sorbent (particle size 420–850 μm), temperature $T = 30$ °C, pressure $P = 1$ atm, $C^{in}_{H_2S} = 3000$ ppmv in N_2, total gas flow rate $Q = 90$ SL h^{-1} (verified as constant).

The specific adsorption capacity of H_2S at saturation, ω_{ads} [mmol g^{-1}], was determined through a material balance over the adsorption column (saturation is referred to conditions under which the outlet H_2S concentration ($C^{out}_{H_2S}$) equals 99% $C^{in}_{H_2S}$):

$$\omega_{ads} = \int_0^{t^*} r(t)\,\mathrm{d}t = \int_0^{t^*} \frac{Q\, y^{in}_{H_2S}\, \rho_{H_2S}}{m\, M_{H_2S}} \left(1 - \frac{y^{out}_{H_2S}(t)}{y^{in}_{H_2S}}\right) \mathrm{d}t \qquad (1)$$

where $r(t)$ [mmol s^{-1} g^{-1}] is the instantaneous adsorption rate, $y^{in}_{H_2S}$ and $y^{out}_{H_2S}$ are the volumetric fractions of H_2S in gas inlet and outlet, respectively, ρ_{H_2S} is H_2S density [g L^{-1}], M_{H_2S} [g $mmol^{-1}$] its molecular weight, m [g] the sorbent dose and t^* [s] the saturation time.

Some adsorption tests were stopped at different times before saturation (corresponding to different levels of H_2S capture) in order to investigate the nature of sulphur species progressively formed during the process.

2.4. TPD/TPO tests

Temperature programmed desorption and temperature programmed oxidation (TPD/TPO) tests were carried out in the same lab-scale plant described in section 2.3. TPD tests provided insights into sulphur adsorption/reaction and desorption mechanisms while also evaluating the thermal regenerability of the sorbents. In a typical TPD test, the adsorbents (just after the adsorption test, without being exposed to air) were treated under a flow of 20 SL h^{-1} of high purity nitrogen (99.999%) and heated at 10 °C min^{-1} up to a maximum of 620 °C so to minimize any volatilisation/thermal degradation of the carbon-based species from the support. In a typical TPO test, the adsorbent material (just after the adsorption test) was heated under O_2/N_2 flux (5000 ppmv of O_2, 20 SL h^{-1}) at 10 °C min^{-1} up to a maximum of 620 °C. During TPD/TPO tests, the specific amount of desorbed sulphur-based species (termed ω^{TPD}_{des} and ω^{TPO}_{des} for TPD and TPO tests, respectively) was evaluated in a similar way as in Eq. (1) by integrating the temporal profiles of $H_2S + SO_2$.

3. Results and discussion

3.1. H_2S adsorption tests at high concentration

Table 1 compares the performance of H_2S capture of Cu_xZn_{1-x}/AC sorbents previously reported in Balsamo et al. [22] with the results obtained for the sorbent containing only copper oxide as active phase (Cu/AC), in terms of breakpoint time t_{br} (assumed as the time for which $y^{out}_{H_2S}(t)/y^{in}_{H_2S} = 0.05$) and ω_{ads}, for tests carried out at $C^{in}_{H_2S} = 3000$ ppmv and $T = 30$ °C. The saturation adsorption capacity of Cu/AC was approximately 7% lower than the value retrieved for the best-performing sample ($Cu_{0.5}Zn_{0.5}$/AC), while higher than that observed for $Cu_{0.05}Zn_{0.95}$/AC, Zn/AC and obviously AC raw. However, Zn/AC and Cu/AC samples showed comparable breakpoint times that were significantly shorter with respect to figures obtained for sorbents composed by mixed oxides. These results demonstrate that the adsorption capacity did not monotonically increase with copper content and indicate a synergic effect between CuO and ZnO, hence determining a more efficient exploitation of the active phases in the H_2S capture process. In particular, an equimolar mixture of the oxides represented the optimal composition among those investigated. Noteworthy, literature studies focusing on Cu-doped ZnO sorbents for H_2S reactive adsorption commonly ascribe the positive role of copper in enhancing the conversion degree of zinc oxide to reduced diffusional limitations in the ZnS product layer with a transition from an outward (for pure ZnO) to inward (for Cu-doped ZnO) growth mechanism [7,26,27]. However, the presence of multiple reaction products (such as sulphates or sulphur) besides sulphides, experimentally determined for the systems under investigation (*vide infra*), suggests a more complex promoting role of copper for mixed oxide sorbents in the process of H_2S capture.

Fig. 1 presents the results of XPS analysis conducted on spent $Cu_{0.5}Zn_{0.5}$/AC sorbent in order to identify the main surface species at the end of the reactive process of H_2S adsorption (at 3000 ppmv) and after recovery in air under ambient conditions. It can be observed (Fig. 1a) that surface Zn mainly occurred as sulphate with a high intensity $2p_{3/2}$ peak centered at 1022.83 eV, while the Zn $2p_{3/2}$ spectral line with BE = 1021.7 eV can be ascribed to a minor surface contribution of ZnS species. Moreover, the Zn $2p_{3/2}$ band peaked at 1025.1 eV is possibly related to compounds formed by reaction of zinc with organic functionalities of the carbonaceous substrate (such as carboxylates groups) [28]. Noteworthy, residual ZnO was not detected from XPS analysis, as expected according to the high degree of conversion of active phase determined from H_2S adsorption tests on $Cu_{0.5}Zn_{0.5}$/AC. In analogy to Zn, also Cu mainly retained the +2 oxidation state upon reaction with H_2S as demonstrated by the presence of "shake-up" satellite peaks between 940 eV and 945 eV, which are characteristic of CuO and $CuSO_4$ (Fig. 1b). The predominant formation of $CuSO_4$ is testified by a main Cu $2p_{3/2}$ line at BE = 935.52 eV, in good agreement with the known position for the $CuSO_4$ peak at 935.4 eV. In the BE range between 932.2 eV and 933.6 eV, the spectrum appears to result from the superimposition of the contribution from CuO (933.70 eV) and (at least) a second peak which is difficult to identify since it can be ascribed to several copper species [29,30] including CuS (932.2 eV), Cu_2S and Cu_2O (932.5 eV), Cu-Cu (932.63 eV). Noteworthy, according to the recent results by Duan et al. [30], superficial Cu sulphides possibly formed on CuO/multiwalled carbon nanotubes sensors by reactive adsorption process of H_2S can be effectively re-oxidised during the recovery of spent material in air at room temperature. The deconvolution analysis of peaks in the range 160–172 eV allowed the identification of sulphur-containing compounds (Fig. 1c). The predominant form of surface S-species was copper and zinc sulfates with their characteristic S $2p_{3/2}$ and $2p_{1/2}$ lines respectively centered at 168.83 eV and 170.01 eV. A minor presence of Zn sulphide was also identified with S $2p_{3/2}$ and $2p_{1/2}$ lines at 162.11 eV and 163.29 eV respectively. Interestingly, the S $2p_{3/2}$ and S $2p_{1/2}$ peaks observed at BE = 164.02 eV and 165.20 eV are representative of sulphur directly adsorbed on activated carbon as they can be ascribed to the occurrence of some elemental sulphur [20] as well as to organic sulphur compounds, such as sulphide (C-S-C), thiol (C-S-H), thiophene (C_4S-H) and

Table 1
H_2S adsorption and desorption performances of AC raw and functionalized sorbents. Experimental conditions for adsorption tests: sorbent mass = 2.5 g, $C^{in}_{H_2S} = 3000$ ppmv in N_2, $T = 30$ °C. Experimental conditions for TPO tests: sorbent mass = 20 mg, temperature range = 30–620 °C.

Sorbent	Breakpoint time t_{br} [s]	Adsorption capacity ω_{ads} [mmol g^{-1}][a]	SO_2 released during TPO ω^{TPO}_{des} [mmol g^{-1}]
AC raw	198[b]	0.20	0.20
Zn/AC	444	0.97	0.97
$Cu_{0.05}Zn_{0.95}$/AC	559	1.28	1.28
$Cu_{0.5}Zn_{0.5}$/AC	674	1.46	1.46
Cu/AC	429	1.36	1.36

[a] Specific adsorption capacity @ $C^{out}_{H_2S} = 0.99\ C^{in}_{H_2S}$.
[b] Determined with 5 g sorbent mass.

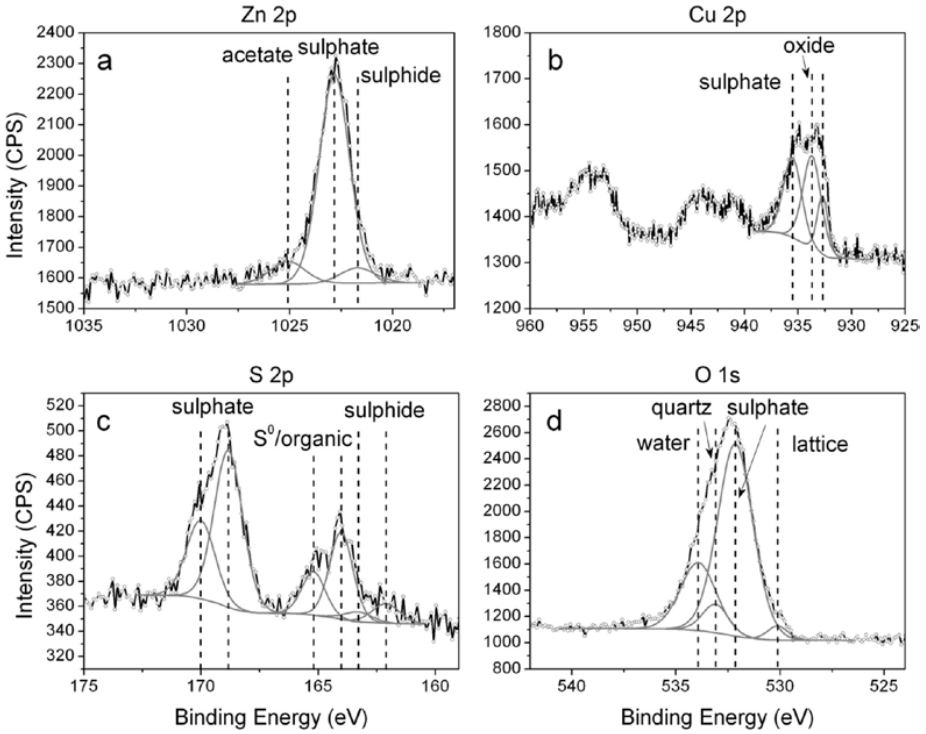

Fig. 1. XPS analysis on the saturated $Cu_{0.5}Zn_{0.5}$/AC sorbent ($C^{in}_{H_2S}$ = 3000 ppmv in N_2, T = 30 °C) recovered in air, showing the 2p spectral regions of (a) Zn, (b) Cu, (c) S, and the 1s spectral region of O (d).

disulphide (C-S-S-C) [20,28,31]. Once formed, those S-species are rather stable upon exposure to air at room temperature [30]. Eventually, the O 1s signal at 532.15 eV (Fig. 1d) confirmed the formation of a considerable amount of metal sulphates from the original metal oxides. Further significant contributions in this spectral region derived from the quartz impurity (533.10 eV) contained in the raw activated carbon [22] and from adsorbed water (533.93 eV). Furthermore, the presence of a minor quantity of lattice oxygen, related to the CuO component, was also identified at BE = 530.12 eV [28].

The formation of sulphate species upon H_2S reactive adsorption, detected from XPS analysis, was also confirmed by washing saturated sorbents in water at 60 °C. Fig. 2 reports the temporal evolution of the amount of sulphate ions released in water after normalization with respect to the mass of sorbent (ω_{aq}). A sharp increase of dissolved sulphates was observed at the very beginning of the test with each sorbent (up to ca. 0.3 mmol g^{-1}), followed by a slower rise. For Zn/AC and $Cu_{0.05}Zn_{0.95}$/AC a similar value of $\omega_{aq} \approx$ 0.5 mmol g^{-1} was recorded after about 250 h; in the case of $Cu_{0.5}Zn_{0.5}$/AC the final value of ω_{aq} increased up to 0.8 mmol g^{-1}, thus mirroring the greater H_2S capture capacity and conversion degree of metal oxides to sulphates (promoted by copper, *vide infra*). The spent Cu/AC sorbent showed faster dynamics of SO_4^{2-} release in the early process stages and a final value of ω_{aq} as large as 0.9 mmol g^{-1} (still slightly increasing after 300 h). In this context, the trend of SO_4^{2-} concentration recorded under identical

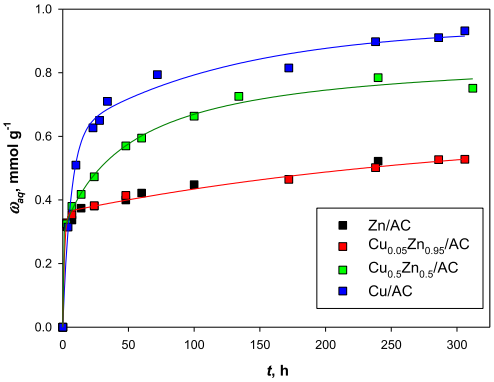

Fig. 2. Kinetics of release of sulphate ions in water at 60 °C for spent functionalized sorbents ($C^{in}_{H_2S}$ = 3000 ppmv in N_2, T = 30 °C).

conditions for a mechanical mixture of AC with CuS (results not displayed for the sake of clarity) suggested the occurrence of a partial oxidation of sulphides (mainly those with copper) to sulphates in aqueous medium. This experimental evidence could

explain the slow rise in sulphate release in the case of the exhaust Cu/AC sample. These results pave the way to the development of processes for the recovery of active metal dissolved in water, or the (partial) regeneration of the spent sorbents under operating conditions less energetically intensive with respect to high temperature treatments usually investigated in the pertinent literature [32].

Fig. 3 shows SEM images of a sectioned granule of saturated $Cu_{0.5}Zn_{0.5}$/AC sorbent, together with the corresponding distribution map of Zn, Cu and S determined by EDX analysis. Sulphur-containing species were homogeneously distributed throughout sorbent particles along the radial coordinate. Noteworthy, the capture process did not affect the distribution of active elements (Zn, Cu) with respect to the virgin samples (cf. also [22]). It can be argued that the high dispersion of active phases in nano-sized form guaranteed accessibility of H_2S molecules to the entire pore network and enabled to reach a remarkably high overall degree of conversion (76%, [22]) of the metal oxides in $Cu_{0.5}Zn_{0.5}$/AC sorbent at saturation.

Table 2 and Fig. 4 report, respectively, the main microstructural parameters and the PSD determined for Cu_xZn_{1-x}/AC, Zn/AC and Cu/AC sorbents before and after H_2S adsorption tests performed at $C^{in}_{H_2S} = 3000$ ppmv and $T = 30$ °C. Textural features of the pristine activated carbon are also included for comparison. Results for fresh sorbents confirm that the preparation technique allowed obtaining a high dispersion of the metal oxides onto the support thus largely preserving the pore size distribution of the raw AC. However, a systematic effect of the active phase composition on the pore texture can be pointed out. In particular, Zn/AC and $Cu_{0.05}Zn_{0.95}$/AC sorbents (i.e. those Zn-rich samples) displayed a loss of porosity with respect to the AC substrate in the region of micropores smaller than 10 Å. On the other hand, $Cu_{0.5}Zn_{0.5}$/AC sorbent showed a micropore size distribution rather similar to the one retrieved for raw AC, whereas a minor reduction of mesoporosity in the size range 26–33 Å was detected. The PSD of Cu/AC and AC raw overlapped in the micropore size range, but the deposition of CuO resulted in a more evident reduction of mesoporosity with respect to $Cu_{0.5}Zn_{0.5}$ sample. These observations were also confirmed by the greater V_M values determined for $Cu_{0.5}Zn_{0.5}$/AC and Cu/AC samples. Therefore, it can be argued that ZnO and CuO phases showed a different tendency to be preferentially dispersed onto the surface of micro and mesopores, respectively.

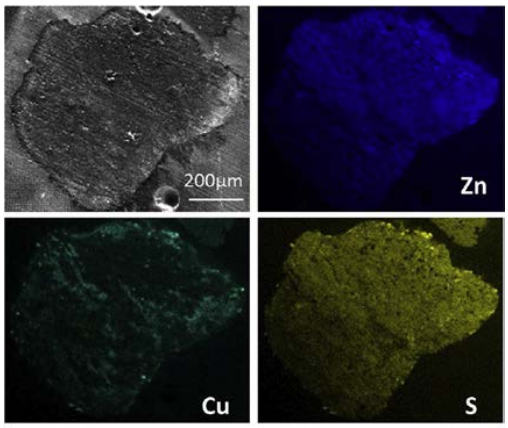

Fig. 3. SEM and EDX micrographs for particles (cross-section) of $Cu_{0.5}Zn_{0.5}$/AC spent sorbent (Zn, Cu and S distribution). Adsorption stage performed at $C^{in}_{H_2S} = 3000$ ppmv in N_2, $T = 30$ °C.

After saturation with H_2S, all of the spent sorbents experienced a significant reduction of surface area and porosity due to the formation and accumulation of different S-bearing compounds. More specifically, among saturated sorbents, the Zn-containing materials displayed an evident and similar loss of BET surface area (−40%) down to ca. 330 $m^2\ g^{-1}$ which occurred almost independently from the amount of sulphur captured (3–4.7% wt. from Table 1) and was mainly due to occlusion of micropores. Furthermore, Zn-rich sorbents also showed signs of partial occlusion of their smallest mesopores (Fig. 4a–c). On the other hand, the spent Cu/AC material retained higher values of S_{BET} (426 $m^2\ g^{-1}$) and V_M due to a larger residual microporosity and to an almost unaffected network of mesopores (Fig. 4d). Interesting observations can be drawn when comparing the textural parameters determined for $Cu_{0.5}Zn_{0.5}$/AC raw and after the removal of those easily soluble sulphate species by water washing for ca. 5 h (Table 2). The textural properties of the pristine sorbent were completely restored, thus indicating that sulphate species were the main responsible for the partial occlusion of sample porosity upon the reactive adsorption of H_2S. This is consistent with the much larger ratio of molar volumes for zinc and copper sulphates with respect to their corresponding oxides (average value = 3.3), which largely exceeds the corresponding one for zinc and copper sulphides/zinc and copper oxides (average value = 1.7) [33].

3.2. H_2S adsorption tests at short contact time and low concentration

Dynamic adsorption tests for the different sorbents were repeated employing finer particles in a narrow size range, relatively low concentration of H_2S in the gas feed and very short contact times in an attempt to gain further insights into the kinetics of the capture process and modifications induced by the composition of active phase. Fig. 5 reports breakthrough curves and values for the instantaneous adsorption rate for tests carried out at $C^{in}_{H_2S} = 100$ ppmv and $T = 30$ °C. The corresponding values of t_{br} and ω_{ads} are listed in Table 3. In agreement with the results at higher inlet partial pressures of H_2S [22], the raw AC is characterised by low H_2S adsorption capacity ($\omega_{ads} = 0.08$ mmol g^{-1}). On the other hand, the functionalisation treatment by single, and particularly by composite Zn and Cu oxides, resulted into a significant increase in both the quantitative parameters of adsorption (t_{br} = 83–225 s; ω_{ads} = 0.7–1 mmol g^{-1}), confirming the existence of a clear optimum of performance for the $Cu_{0.5}Zn_{0.5}$/AC sorbent (i.e. with equimolar Cu and Zn content). As previously suggested, the mechanism of H_2S capture involves chemical reactions with metal oxides [32] in a wide range of compositions of interest for practical applications [22]; thus, all of the functionalized sorbents showed only a moderate decrease of ω_{ads} at an inlet H_2S concentration of 100 ppmv with respect to tests performed at 3000 ppmv. The corresponding lower utilization factor of active phase was probably due to some kind of kinetic/diffusional limitations.

To complete the analysis, Fig. 5b reports the values of the instantaneous adsorption rate r vs. ω which, as expected, progressively decreased after the breakpoint along with the increasing amount of H_2S captured by each sorbent and up to its saturation level. Zn/AC and $Cu_{0.05}Zn_{0.95}$/AC sorbents displayed similar trends of the capture rates mainly in the early stages of the process, whereas even 5% of Zn substitution by Cu determined higher values for r in particular for $\omega > 0.3$ mmol g^{-1} and eventually enhanced the adsorption capacity and utilization factor of active phase at saturation [22]. The different behavior of Zn/AC and $Cu_{0.05}Zn_{0.95}$/AC samples was likely related to a chemical promoting effect of Cu

Table 2
Microstructural parameters of fresh, spent and water treated spent samples.

Sorbent	Specific surface area S_{BET} [$m^2\ g^{-1}$]	Total pore volume V_{TOT} [$cm^3\ g^{-1}$]	Micropore volume V_M [$cm^3\ g^{-1}$]
Fresh sorbents			
AC raw	641	0.81	0.23
Zn/AC	558	0.80	0.19
$Cu_{0.05}Zn_{0.95}$/AC	520	0.72	0.18
$Cu_{0.5}Zn_{0.5}$/AC	570	0.76	0.20
Cu/AC	559	0.67	0.22
Spent sorbents			
AC raw[a]	604	0.76	0.23
Zn/AC[a]	330	0.54	0.13
$Cu_{0.05}Zn_{0.95}$/AC[a]	327	0.53	0.12
$Cu_{0.5}Zn_{0.5}$/AC[a]	348	0.55	0.13
$Cu_{0.5}Zn_{0.5}$/AC[b]	555	0.76	0.20
$Cu_{0.5}Zn_{0.5}$/AC[c]	441	0.66	0.15
Cu/AC[a]	426	0.58	0.16

[a] After saturation at $C^{in}_{H_2S} = 3000$ ppmv, $T = 30$ °C.
[b] After test of sulphate ions released from spent sorbent performed in distilled water at 60 °C for 5 h.
[c] After adsorption run stopped at $\omega \approx 0.3$ mmol g^{-1} (inlet conditions $C^{in}_{H_2S} = 100$ ppmv, $T = 30$ °C).

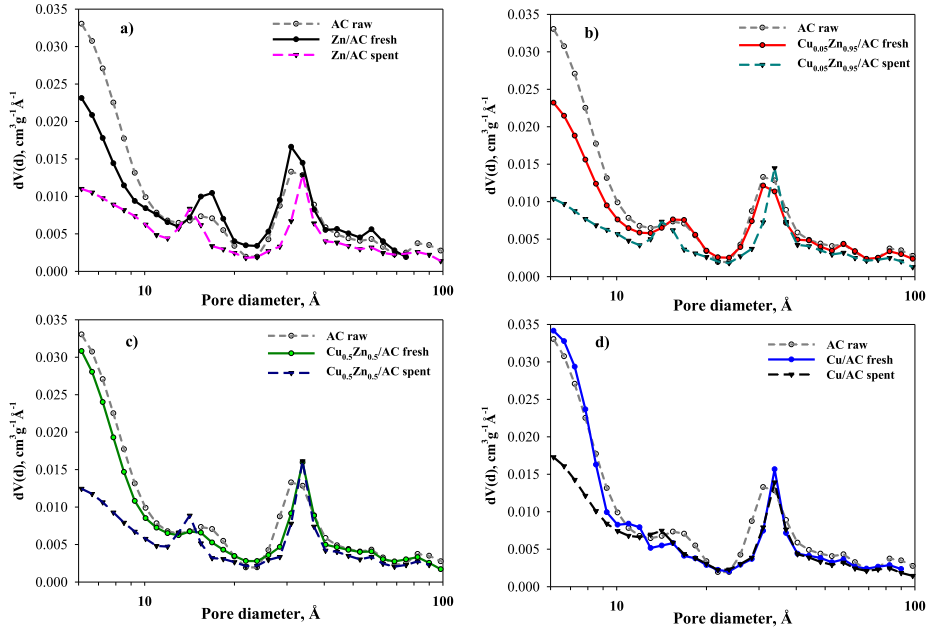

Fig. 4. Pore size distributions of functionalized sorbents before and after saturation with $C^{in}_{H_2S} = 3000$ ppmv in N_2, $T = 30$ °C: a) Zn/AC, b) $Cu_{0.05}Zn_{0.95}$/AC, c) $Cu_{0.5}Zn_{0.5}$/AC, d) Cu/AC. PSD of virgin AC also included for comparison.

enhancing ZnO reactivity with H_2S [7,26,27]. Indeed, it is recalled that both sorbents showed almost identical textural properties due to the low amount of copper substitution, thus intraparticle mass transfer phenomena equally affected the adsorption process. $Cu_{0.5}Zn_{0.5}$/AC sorbent was capable to keep the adsorption rate equal to the molar feeding rate of H_2S up to $\omega \approx 0.3$ mmol g^{-1}, a value significantly higher than those determined for Zn/AC (at $\approx$0.11 mmol g^{-1}) and $Cu_{0.05}Zn_{0.95}$/AC (at $\approx$0.15 mmol g^{-1}). Moreover, as already discussed, the highest value of the adsorption capacity at saturation was attained for $Cu_{0.5}Zn_{0.5}$/AC sample. In this case, two factors seem to contribute to the performance enhancement with respect to Zn/AC and $Cu_{0.05}Zn_{0.95}$/AC samples: i) the already invoked promoting chemical role of copper on the reactivity of ZnO and ii) the reduced limitations to intraparticle diffusion linked to a minor alteration of porosity (i.e. occlusion of micropores). This latter effect can be related to the concomitant lower loading of ZnO and to the tendency of zinc and copper to be preferentially located in micropores and mesopores, respectively

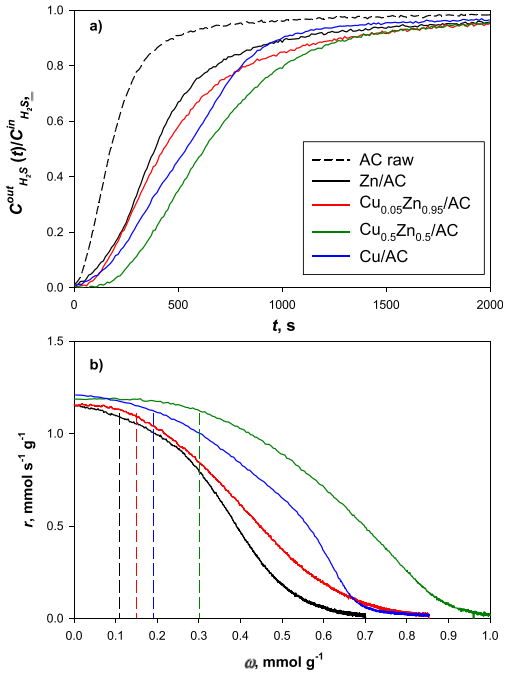

Fig. 5. a) H_2S breakthrough curves and b) adsorption rates for selected sorbents. Sorbent mass: 20 mg and 80 mg for functionalized and AC raw sorbents, respectively. $C^{in}_{H_2S}$ = 100 ppmv in N_2, Q = 20 SL h^{-1}, T = 30 °C. Dashed lines in panel b) indicate the quantity of H_2S captured up to the breakpoint.

(cf. § 3.1). Cu/AC sorbent showed a kinetic pattern in between those of $Cu_{0.05}Zn_{0.95}$/AC and $Cu_{0.5}Zn_{0.5}$/AC: the overall capture rate was constantly higher than for $Cu_{0.05}Zn_{0.95}$/AC but it decreased very sharply for $\omega > 0.5$ mmol g^{-1}, so that the adsorption capacity at saturation was comparable with the one retrieved for $Cu_{0.05}Zn_{0.95}$/AC sorbent. The aforementioned analysis highlights, once again, the important synergic role of mixed copper and zinc oxides in enhancing both adsorption capacity of H_2S and capture rate.

Considering the material showing the best performance ($Cu_{0.5}Zn_{0.5}$/AC), the investigation was deepened by analysing the effect of $C^{in}_{H_2S}$ (100–193 ppmv) and total flow rate of gas stream (20–40 SL h^{-1}). As reported in Table 3, the saturation capacity of the sorbent ω_{ads} was not significantly affected by variation of those two operating parameters in the explored ranges.

In order to better evaluate the influence of both $C^{in}_{H_2S}$ and gas flow rate on the H_2S capture dynamics of $Cu_{0.5}Zn_{0.5}$/AC, breakthrough data were processed adopting the Bohart and Adams model (termed BA in the following) for adsorption process in a fixed bed [34,35], whose integral form is:

$$\ln\left(\frac{C^{in}_{H_2S}}{C^{out}_{H_2S}(t)} - 1\right) = \frac{k_{BA}\omega_{ads}\rho_b L(1-\varepsilon)}{1000u\varepsilon} - k_{BA}C^{in}_{H_2S}t \qquad (2)$$

where L [m] is the length of fixed bed (0.0034 m), ε [–] its void fraction (0.39), u [m s^{-1}] the superficial gas velocity, ρ_b [g L^{-1}] the sorbent bulk density (820 g L^{-1}), k_{BA} [L mol^{-1} s^{-1}] the kinetic parameter of the BA model. It is highlighted that $C^{in}_{H_2S}$ and $C^{out}_{H_2S}(t)$ are here expressed in mol L^{-1}. Equation (2) implies that, if k_{BA} is constant and if the BA model is suitable to fit experimental data, the plot of LHS vs. time is represented by a substantially straight line whose slope and intercept allow the determination of ω_{ads} and k_{BA}, respectively. The original BA model assumes that the adsorption rate is governed by a linear driving force and controlled by surface reaction, k_{BA} being the surface reaction constant. In the present work we keep the original mathematical formulation of the BA model, but the k_{BA} parameter can be considered as a global kinetic coefficient embedding the different kinetic resistances. In fact, the complex phenomenology for the investigated gas–solid reactive system should include numerous dynamic steps such as fluid film diffusion, intraparticle diffusion (i.e. H_2S transport within the substrate pore network), solid state diffusion towards the products layers (e.g. sulphates and sulphides) and surface chemical reactions. Additionally, k_{BA} might also vary during the adsorption process due to time-dependent properties of the reacting system including: i) pore volume reduction of the substrate due to the formation of products characterised by molar volumes greater than those of the parent copper and zinc oxides (cf. e.g. Ref. [36]); ii) occurrence of multiple chemical reactions in different steps of the reactive process (*vide* § 3.3); iii) modification of the product layer microstructure.

In order to elucidate the dynamic mechanism governing the adsorption rate in the early process stages (just after the breakpoint) Fig. 6a depicts, as an example, the BA plot for H_2S adsorption onto $Cu_{0.5}Zn_{0.5}$/AC at two H_2S inlet concentrations and two total gas flow rates, together with the corresponding fitting according to Eq. (2). The value of k_{BA} was substantially independent from the inlet H_2S concentration, with an average estimated value of 4250 ± 150 L mol^{-1} s^{-1} at 20 SL h^{-1}. On the other hand, k_{BA} increased with the flow rate up to 6140 L mol^{-1} s^{-1} at 40 SL h^{-1} and

Table 3
Adsorption/desorption performances of AC raw and functionalized sorbents under different operating conditions. Sorbent mass = 20 mg and T = 30 °C.

Sorbent	$C^{in}_{H_2S}$ [ppmv]	Breakpoint time t_{br} [s]	Adsorption capacity ω_{ads} [mmol g^{-1}][a]	SO_2 released during TPD ω^{TPD}_{des} [mmol g^{-1}]
AC raw	100	35[b]	0.08	0.08
Zn/AC	100	83	0.73	0.29
$Cu_{0.05}Zn_{0.95}$/AC	100	120	0.88	0.34
$Cu_{0.5}Zn_{0.5}$/AC	100	225	1.00	0.39
	165	95	1.02	0.41
	193	80	1.04	0.40
Cu/AC	100	121	0.88	0.33

[a] Specific adsorption capacity @ $C^{out}_{H_2S} = 0.99\ C^{in}_{H_2S}$.
[b] Determined with 80 mg sorbent mass.

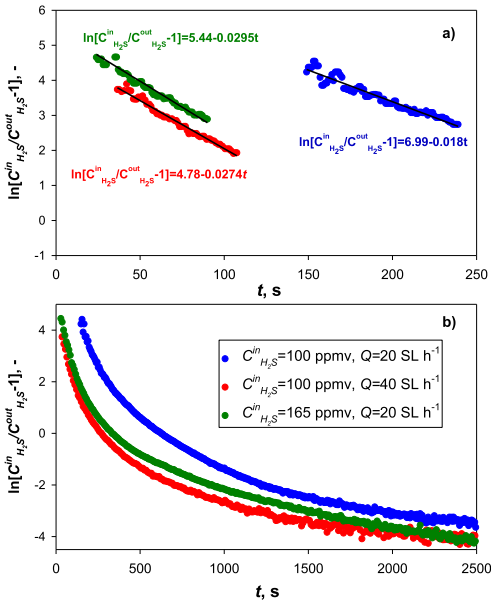

Fig. 6. Bohart and Adams plots for H_2S adsorption in a fixed bed of $Cu_{0.5}Zn_{0.5}$/AC (20 mg) at 30 °C with different inlet concentrations and total gas flow rates: a) linear plots for short adsorption times according to Eq. (2) and b) plots for the entire time range of the tests.

$C^{in}_{H_2S} = 100$ ppmv. Therefore, the capture process in the initial phase (until breakpoint and just after it) seems to proceed under a prevalent external mass transfer control. Indeed, the increase of k_{BA} corresponded to the expected increase in the external mass transfer coefficient k_{ext} due to the higher superficial gas velocity u, as $k_{ext} \sim u^{0.6}$ (according to Wakao and Funazkri correlation [37]). This is a clear indication that the surface chemical reaction (mainly producing $ZnSO_4$ for short process times, *vide* § 3.3) was rather fast and that a reacting front initially advanced along the radial particle coordinate in a manner resembling the shrinking core dynamic pattern [38]. To confirm this hypothesis, a SEM-EDX analysis was performed on cross-sections of $Cu_{0.5}Zn_{0.5}$/AC particles tested at $C^{in}_{H_2S} = 100$ ppmv and 20 SL h^{-1} with the run stopped at $\omega = 0.3$ mmol g^{-1} (i.e. approximately at the breakpoint time): results in Fig. 7 indicate that sulphur species were predominantly confined in the outer shell of the adsorbent particle (thickness of ca. 10 μm).

The progressive reduction of the adsorption rate after the breakpoint time was mirrored by the decrease of the slope in the BA plot for longer times (*vide* Fig. 6b), indicating a strong reduction of the global kinetic parameter (k_{BA}) which could be related to alterations of the support microstructure and to the switch to different dominating dynamic mechanisms (e.g. product layer diffusion) other than external fluid film diffusion. The intraparticle diffusion mechanism is obviously affected after the breakpoint time due to a partial pore blockage determined by formation in the particle outer shell of large product species (sulphates, *vide* § 3.3). In fact the surface area of $Cu_{0.5}Zn_{0.5}$/AC dropped to ca. 440 m^2 g^{-1} after H_2S reactive adsorption up to t_{br}, a value approximatively 25% lower than the pristine functionalized sample (cf. also Table 2). The

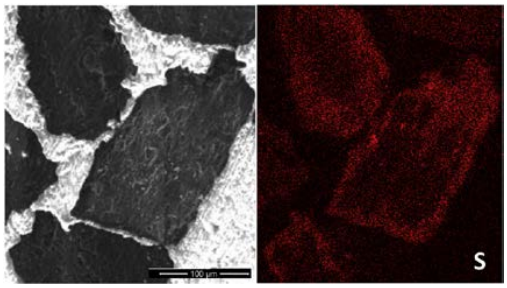

Fig. 7. SEM (left) and EDX micrograph of S distribution (right) for multiparticle (cross-section) $Cu_{0.5}Zn_{0.5}$/AC sorbent after adsorption test stopped at $\omega = 0.3$ mmol g^{-1}. Adsorption stage performed at $C^{in}_{H_2S} = 100$ ppmv in N_2, $Q = 20$ SL h^{-1}, $T = 30$ °C.

observed loss in surface area is significantly greater than the one expected on the basis of the weight gain of the sample due to retention of sulphur species (ca. 0.9% wt. at t_{br}). This confirms a reduction of the accessibility to the smallest pores which could, in turn, inhibit active phase utilization or remarkably slow down the capture rate.

3.3. TPD tests

TPD tests onto spent sorbents were carried out to investigate the nature of the species formed on the solid material upon H_2S adsorption and to simultaneously evaluate their potential regenerability by thermal treatments. Fig. 8 shows the results of TPD tests carried out on different spent sorbents previously saturated under base conditions (but not re-exposed to ambient air). TPD profiles for materials consisting of $CuSO_4$ and $ZnSO_4$ separately impregnated on AC are reported for reference. The results are expressed as SO_2 signal as a function of desorption temperature; in fact, H_2S desorption was negligible, and therefore is not reported. The spent activated carbon (AC raw) showed a single peak of SO_2 desorption starting at ca. 170 °C and centered at 280 °C. This peak was previously ascribed [22] to the release of SO_2 formed by oxidation reactions occurring in small pores between (adsorbed) short chains of elemental S and chemisorbed oxygen or oxygen-containing surface groups. It is recalled that the presence of oxygen on AC surface can be due to both activated carbon nature and unavoidable preweathering during the different stages of treatment. For spent Zn/AC, two broad emission peaks were revealed: the first (centered at ca. 290 °C) closely resembled the one observed for spent AC; the second (centered at ca. 500 °C) can be ascribed to the decomposition of $ZnSO_4$, as evident from the comparison with the TPD profile obtained for the reference $ZnSO_4$/AC material. For spent $Cu_{0.05}Zn_{0.95}$/AC, the first SO_2 peak centered at 310 °C can be seen as the sum of contributions deriving from: i) SO_2 adsorbed onto AC; ii) $CuSO_4$ decomposition (cf. the TPD profile obtained for the reference $CuSO_4$/AC material). The second SO_2 peak was clearly related to the decomposition of $ZnSO_4$, as previously observed. The progressive substitution of copper for zinc in the mixed active phase of sorbents caused the increase in intensity of the peak centered around 320 °C and a corresponding reduction of the high temperature peak (i.e., the one related to $ZnSO_4$ decomposition), which coherently disappeared from the TPD profile of Cu/AC spent material.

The amount of S desorbed from spent materials as SO_2 during TPD tests (ω^{TPD}_{des}) is reported in Table 3. While 100% of the adsorbed sulphur on AC raw was desorbed ($\omega^{TPD}_{des} = \omega_{ads}$), for functionalized materials it was calculated that ω^{TPD}_{des} accounted for ca. 40% of ω_{ads}.

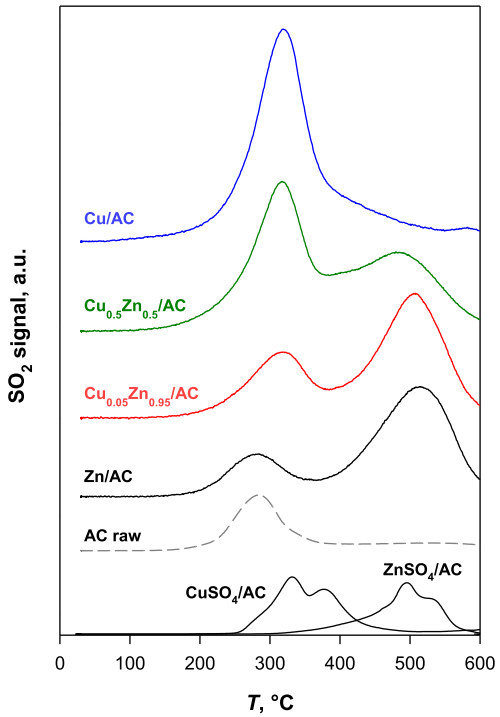

Fig. 8. SO_2 release during TPD tests after adsorption up to saturation at $C^{in}_{H_2S}$ = 100 ppmv in N_2, Q = 20 SL h^{-1}, T = 30 °C. TPD profiles for $CuSO_4$ and $ZnSO_4$ separately impregnated on AC are reported for reference.

Slightly greater values were retrieved for spent sorbents that were recovered in air before the TPD test, confirming that a partial oxidation of some surface S-species (especially Cu sulphides) can occur at room temperature [30], as already inferred from XPS measurements. The remaining fraction of sulphur can be imputed to both Cu and Zn sulphides (known to decompose at temperatures higher than 1000 °C in inert environments [39]), and to species not detectable by our TPD procedure ("ghost" species) such as elemental S, which could condense on internal walls of cold pipelines.

TPD investigation was extended to materials previously undergoing adsorption only up to $C^{out}_{H_2S} = 0.02\ C^{in}_{H_2S}$ (Fig. 9) in order to obtain deeper insights into the type of S-based species early formed during the H_2S capture process and into the role of copper. The deconvolution of TPD signals was also included for reference. For Zn/AC, the pattern of SO_2 emission was analogous to what obtained for the saturated sample (cf. Fig. 8), with a main peak at ca. 510 °C related to the decomposition of $ZnSO_4$ preceded by a broad peak (of minor intensity) ascribable to the SO_2 contribution deriving from the oxidation of H_2S adsorbed by the parent substrate. The TPD pattern obtained for Cu/AC was rather complex and it was deconvoluted into four main peaks, differing substantially from what was recorded for the saturated sample (again, cf. Fig. 8). In fact, the lower temperature bands (peaked at around 310 °C and 400 °C) were assigned to the small contribution of the support and to $CuSO_4$ decomposition. The peaks occurring at higher temperatures (with maximum intensity at 510 °C and 590 °C) could be imputed to SO_2 deriving from oxidation of S in CuS *via* direct reaction of the latter compound with both $CuSO_4$ and with oxygen released from thermal decomposition of $CuSO_4$ [40,41]. Regarding the sorbents with mixed oxides, $Cu_{0.05}Zn_{0.95}$/AC showed the same qualitative features of the Zn/AC sample whereas for $Cu_{0.5}Zn_{0.5}$/AC a third peak became evident (around 400 °C) associated with the decomposition of copper sulphate. Further, the deconvolution analysis also provided quantitative indications on the degree of conversion of ZnO to $ZnSO_4$ up to $C^{out}_{H_2S} = 0.02\ C^{in}_{H_2S}$. For Zn/AC, $Cu_{0.05}Zn_{0.95}$/AC and $Cu_{0.5}Zn_{0.5}$/AC, conversion values of 10.1%, 10.7% and 21.0% were retrieved. Therefore, copper substitution promoted the ZnO conversion to $ZnSO_4$ mainly in the first stages of the capture process (*vide infra*). In this regard, two main factors could be invoked to explain the described pattern: i) a sacrificial role of copper as oxygen donor to accelerate formation of zinc sulphate; ii) a structural role of copper enabling the formation of smaller-sized ZnO crystallites (phenomenon highlighted e.g. in Ref. [42]), with an associated enhanced reactivity. However, an additional contribution of atmospheric humidity and/or oxygen pre-adsorbed onto the sorbent surface to the sulphates formation cannot be ruled out.

Quantitative data concerning adsorbed and desorbed S (ω_{ads} and ω^{TPD}_{des}, respectively) for the four sorbents at $C^{out}_{H_2S} = 0.02\ C^{in}_{H_2S}$ are correspondingly reported in Table 4, from which the following observations can be drawn:

- for Zn/AC and $Cu_{0.05}Zn_{0.95}$/AC (Zn-rich sorbents), $\omega^{TPD}_{des} = \omega_{ads}$. The peaks observed during TPD tests account for the release of all H_2S previously adsorbed, which is mainly oxidised to $ZnSO_4$;
- for $Cu_{0.5}Zn_{0.5}$/AC and Cu/AC ("low-Zn sorbents"), $\omega^{TPD}_{des} = 0.7\ \omega_{ads}$. The peaks observed during TPD tests only partly account for the release of S previously adsorbed. Apart from Zn and Cu sulphates, "ghost species" such as copper sulphides, elemental S and thiols were formed at significant rates, determining a more effective exploitation of active phases in the case of $Cu_{0.5}Zn_{0.5}$/AC sample.

Moreover, TPD tests performed for $Cu_{0.5}Zn_{0.5}$/AC after different adsorption times (cf. Fig. 10) suggest that $ZnSO_4$ formed at a faster rate with respect to $CuSO_4$. In fact, while the main peak associated with $ZnSO_4$ decomposition does not experience substantial modification in the adsorption time range of 8–16 min, the intensity of the $CuSO_4$-deriving peak of SO_2 emission increased. From a quantitative standpoint the deconvolution analysis (not reported for the sake of brevity) revealed that 8 min capture process (ω_{ads} = 0.2 mmol g^{-1}) were enough to attain a ZnO conversion to the corresponding sulphate as high as 20%, very close to the asymptotic value retrieved from TPD on saturated sorbent (21%). On the contrary, the values of CuO conversion to $CuSO_4$ were 8%, 12% and 21% for capture times of 8 min, 16 min and at saturation, respectively. Altogether results indicate that for the equimolar Cu:Zn sorbent, $ZnSO_4$ formed at a faster rate with respect to $CuSO_4$ with copper likely acting as oxygen donor/structural promoter enabling a faster conversion rate and a higher utilization factor of the ZnO phase. On the other hand, the final degree of conversion of both Zn and Cu oxides to form their sulphates was equivalent and most probably limited by oxygen availability on the sorbent.

3.4. TPO tests

Fig. 11 shows the results of TPO tests carried out on different spent sorbents previously saturated under base conditions. TPO profiles for materials consisting of $CuSO_4$ and $ZnSO_4$ separately impregnated on AC are reported for reference, as well as those for mechanical mixtures of AC with elemental sulphur (S + AC), CuS

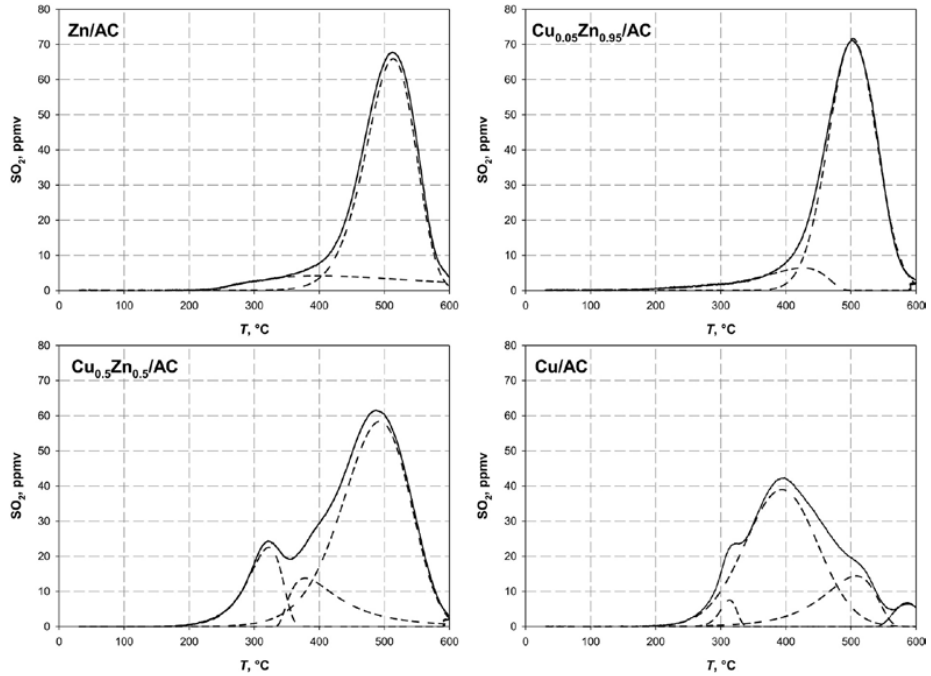

Fig. 9. SO_2 release during TPD tests from functionalized sorbents after adsorption up to $C^{out}_{H_2S}/C^{in}_{H_2S} = 0.02$ with $C^{in}_{H_2S} = 100$ ppmv in N_2, $Q = 20$ SL h^{-1}, $T = 30$ °C. Dashed lines represent deconvolution peaks.

Table 4
Adsorption/desorption performances of AC raw and Cu_xZn_{1-x}/AC sorbents at $C^{out}_{H_2S} = 0.02\ C^{in}_{H_2S}$. Sorbent mass: 60 mg. Inlet conditions: $C^{in}_{H_2S} = 100$ ppmv in N_2, $T = 30$ °C.

Sorbent	Adsorption capacity ω_{ads} [mmol g^{-1}]	SO_2 released during TPD ω^{TPD}_{des} [mmol g^{-1}]
Zn/AC	0.21	0.21
$Cu_{0.05}Zn_{0.95}$/AC	0.22	0.22
$Cu_{0.5}Zn_{0.5}$/AC	0.40	0.27
Cu/AC	0.22	0.15

(CuS + AC) and ZnS (ZnS + AC). From a quantitative point of view, the amount of SO_2 evolved during TPO tests corresponded to the amount of H_2S that was previously captured during the adsorption phase ($\omega^{TPO}_{des} = \omega_{ads}$, cf. Table 1). Therefore, it was confirmed that the partial recovery of sulphur observed in TPD experiments under inert atmosphere was mainly due to the stability of metal sulphides which, on the other hand, could be oxidized and decomposed during TPO tests. The TPO profile for the saturated Zn/AC sample showed three main SO_2 peaks: the first one, centered at ca. 250 °C, could be tentatively assigned to the presence of ZnS by comparison with the profile retrieved for ZnS + AC mixture; the second peak at ca. 520 °C was related to the presence of $ZnSO_4$ (see $ZnSO_4$/AC TPO profile). While the formation of $ZnSO_4$ was already commented in Fig. 9 (TPD tests), TPO tests allowed individuating a TPD ghost species, viz. ZnS. For Zn/AC sample, the presence of a third (intermediate and unresolved) peak was observed at around 400 °C. For Cu/AC sample, there were only two main contributions with similar

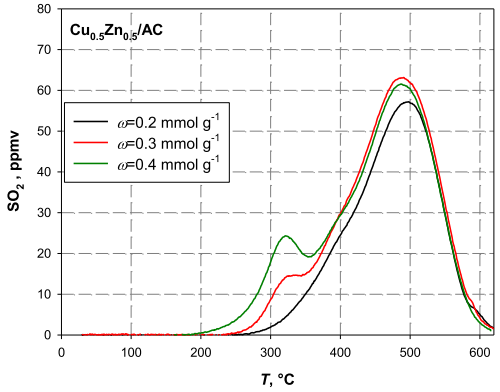

Fig. 10. SO_2 release during TPD tests from $Cu_{0.5}Zn_{0.5}$/AC after adsorption carried out at different sulphur loadings (corresponding to different process times) and $C^{in}_{H_2S} = 100$ ppmv in N_2, $Q = 20$ SL h^{-1}, $T = 30$ °C.

areas: the low temperature peak (at 200 °C) could be assigned to the oxidation of some elemental S and CuS, while the high temperature peak (around 410 °C) was due to decomposition of $CuSO_4$. The TPO patterns for composite Cu_xZn_{1-x}/AC sorbents were more complex, deriving from the superimposition of peaks related to the

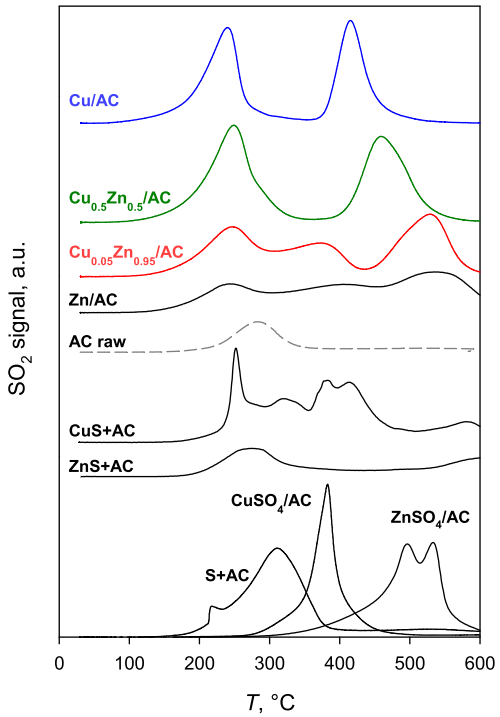

Fig. 11. SO_2 release during TPO tests from selected sorbents after adsorption up to saturation with $C^{in}_{H_2S} = 100$ ppmv in N_2, $Q = 20$ SL h^{-1}, $T = 30$ °C. TPO profiles for $CuSO_4$ and $ZnSO_4$ separately impregnated on AC are reported for reference, as well as those for mechanical mixtures of AC with elemental sulphur, CuS and ZnS.

presence of copper and zinc sulphates (already observed in TPD, see Fig. 9) and copper and zinc sulphides (not detectable by TPD), apart from the peak deriving from S and/or SO_2 bound to AC. Nonetheless, it was observed that the prevailing contributions were related to CuS (rather than ZnS) and $ZnSO_4$ (rather than $CuSO_4$). This confirms that, for mixed oxides, Zn prevailingly reacts with H_2S to form $ZnSO_4$ while Cu also forms sulphides and elemental S.

4. Conclusions

Sorbents for the deep removal of H_2S from gas streams at room temperature were prepared by dispersing mixed oxides (ZnO–CuO) onto a commercial granulated activated carbon at fixed 10% wt. total metal loading and Cu:Zn molar ratio varying in the range from 0:1 to 1:0. Pore size distribution and SEM-EDX analyses indicated that the incipient wetness preparation method guaranteed a high dispersion of the active phase largely preserving the textural features of the pristine AC. Nevertheless, Zn and Cu oxides showed a different tendency to be preferentially dispersed onto the surface of micro and mesopores, respectively.

Compared to the raw activated carbon, all of the sorbents functionalized with the pure and composite oxides (ZnO–CuO) displayed a strong improvement of adsorption properties as evaluated by H_2S (100–3000 ppmv in N_2) dynamic capture tests in fixed bed flow reactors operated at 30 °C and various contact times. In particular the sorbent with an equimolar amount of Cu and Zn ($Cu_{0.5}Zn_{0.5}$/AC) outperformed both counterparts containing 100% Zn or Cu in terms of saturation S-capacity and sorption kinetics, discovering an evident synergic effect between the two metal oxides. In fact, even a low level of Cu substitution for Zn chemically promoted the degree of ZnO conversion; at higher substitution levels, Cu helped to prevent severe clogging of microporosity that was observed upon H_2S adsorption on Zn-rich sorbents.

Notably, XPS analysis and TPD/TPO experiments performed on used sorbents with different levels of S-saturation demonstrated that Zn and Cu sulphates were formed with a high rate and at a large extent during the initial phases of the reactive adsorption process. In fact, metal sulphides, commonly recognized in the pertinent literature as the main reaction products from metal oxide, started to be formed with slow overall kinetics after the corresponding sulphates, probably due to the lack of oxygen available from the sorbent. In particular, in the case of $Cu_{0.5}Zn_{0.5}$/AC material, $ZnSO_4$ formed at a faster rate with respect to $CuSO_4$, and copper oxide likely acted as both oxygen donor and structural promoter.

Considering the large increase in the molar volumes of zinc and copper sulphates with respect to their corresponding oxides as well as sulphides, micropores (partially) clogged during adsorption, slowing down the overall capture kinetics due to increased intraparticle diffusion limitations or even inhibiting direct access to the unreacted active phase.

Nevertheless, it was found that metal sulphates formed by reactive adsorption of H_2S could be easily removed from partially or totally saturated Cu_xZn_{1-x}/AC sorbents by washing them in water, which also restored the initial textural features (BET surface area and pore size distribution) of fresh material. The formation of sulphates was also favourable for an easier regenerability of spent sorbents by thermal treatments under inert atmosphere. $CuSO_4$ and $ZnSO_4$ on AC could be decomposed respectively at relatively low temperatures of ca. 300 °C and 500 °C, leading to partial restoration of oxide active phase.

Acknowledgments

Mr. Luciano Cortese and Mr. Fernando Stanzione (IRC-CNR) are gratefully acknowledged for their help in carrying out SEM-EDX and Ion Chromatography characterisations.

References

[1] D. Stirling, The Sulfur Problem: Cleaning up Industrial Feedstocks, Royal Society of Chemistry, Cambridge, 2000.
[2] S. Nam, K.B. Hur, N.H. Lee, Environ. Eng. Res. 16 (2011) 159–164.
[3] S. Rasi, J. Läntelä, J. Rintala, Energy Convers. Manag. 52 (2011) 3369–3375.
[4] P. O'Neill, Environmental Chemistry, second ed., Chapman and Hall, London, 1993.
[5] J.E. Bao, G.N. Krishnan, P. Jayaweera, K.H. Lau, A. Sanjurjo, J. Power Sources 193 (2009) 617–624.
[6] D. Montes, E. Tocuyo, E. González, D. Rodríguez, R. Solano, R. Atencio, A. Moronta, Micropor. Mesopor. Mater 168 (2013) 111–120.
[7] H. Yang, B. Tatarchuk, AIChE J. 56 (2010) 2898–2904.
[8] N. Abatzoglou, S. Boivin, Biofuel. Bioprod. Bior. 3 (2009) 42–71.
[9] L. Sigot, G. Ducom, P. Germain, Chem. Eng. J. 287 (2016) 47–53.
[10] F. Adib, A. Bagreev, T.J. Bandosz, Environ. Sci. Technol. 34 (2000) 686–692.
[11] T.J. Bandosz, J. Colloid Interf. Sci. 246 (2002) 1–20.
[12] W. Feng, S. Kwon, E. Borguet, R. Vidic, Environ. Sci. Technol. 39 (2005) 9744–9749.
[13] A. Bagreev, T.J. Bandosz, Fuel 228 (2004) 150–156.
[14] C.L. Carnes, K.J. Klabunde, Chem. Mater 14 (2002) 1806–1811.
[15] S.P. Hernández, M. Chiappero, N. Russo, D. Fino, Chem. Eng. J. 176–177 (2011) 272–279.
[16] C. Huang, C.H. Chen, S.M. Chu, J. Hazard. Mater B136 (2006) 866–873.
[17] J.A. Arcibar-Orozco, R. Wallace, J.K. Mitchell, T.J. Bandosz, Langmuir 31 (2015) 2730–2742.
[18] R. Yan, T. Chin, Y.L. Ng, H. Duan, D.T. Liang, J.H. Tay, Environ. Sci. Technol. 38 (2004) 316–323.
[19] M. Florent, T.J. Bandosz, Micropor. Mesopor. Mater 204 (2015) 8–14.

[20] Z. Zhang, J. Wang, W. Li, M. Wang, W. Qiao, D. Long, L. Ling, Carbon 96 (2016) 608–615.
[21] O. Mabayoje, M. Seredych, T.J. Bandosz, ACS Appl. Mater. Inter 4 (2012) 3316–3324.
[22] M. Balsamo, S. Cimino, G. de Falco, A. Erto, L. Lisi, Chem. Eng. J. 304 (2016) 399–407.
[23] NIST X-ray photoelectron spectroscopy database. https://srdata.nist.gov/xps/Default.aspx, 2012. (Accessed 31 July 2017).
[24] S. Cimino, L. Lisi, M. Tortorelli, Chem. Eng. J. 283 (2016) 223–230.
[25] M. Balsamo, F. Rodriguez-Reinoso, F. Montagnaro, A. Lancia, A. Erto, Ind. Eng. Chem. Res. 52 (2013) 12183–12191.
[26] B. Elyassi, Y. Al Wahedi, N. Rajabbeigi, P. Kumar, J.S. Jeong, X. Zhang, P. Kumar, V.V. Balasubramanian, M.S. Katsiotis, K.A. Mkhoyan, N. Boukos, S. Al Hashimi, M. Tsapatsis, Micropor. Mesopor. Mater 190 (2014) 152–155.
[27] I. Bezverkhyy, J. Skrzypski, O. Safonova, J.P. Bella, J. Phys. Chem. C 116 (2012) 14423–14430.
[28] C.D. Wagner, A.V. Naumkin, A. Kraut-Vass, J.W. Allison, C.J. Powell, J.R. Rumble Jr., NIST standard reference database 20, version 3.4 (Web version). http:/srdata.nist.gov/xps/, 2003.
[29] V. Krylova, M. Andrulevičius, Int. J. Photoenergy 2009 (2009) 304308.
[30] Y. Duan, L. Pirolli, A.V. Teplyakov, Sens. Actuator B235 (2016) 213–221.
[31] G. Beamson, D. Briggs, High Resolution XPS of Organic Polymers - The Scienta ESCA300 Database, Wiley Interscience, 1992.
[32] A. Bagreev, H. Rahman, T.J. Bandosz, Carbon 39 (2001) 1319–1326.
[33] D.W. Green, R.H. Perry, Perry's Chemical Engineers' Handbook, McGraw Hill, New York, 2008.
[34] G.S. Bohart, E.Q. Adams, J. Am. Chem. Soc. 42 (1920) 523–544.
[35] F.J. Gutiérrez Ortiz, P.G. Aguilera, P. Ollero, Chem. Eng. J. 253 (2014) 272–279.
[36] R. Sadegh-Vaziri, M.U. Babler, Chem. Eng. Sci. 158 (2017) 328–339.
[37] N. Wakao, T. Funazkri, Chem. Eng. Sci. 33 (1978) 1375–1384.
[38] O. Levenspiel, Chemical Reaction Engineering, third ed., Wiley, 1999.
[39] D. Nguyen-Thanh, T.J. Bandosz, Carbon 43 (2005) 359–367.
[40] M. Nafees, M. Ikram, S. Ali, Dig. J. Nanomater. Bios. 10 (2015) 635–641.
[41] J.G. Dunn, C. Muzenda, Thermochim. Acta 369 (2001) 117–123.
[42] T. Baird, P.J. Denny, R. Hoyle, F. Mc Monagle, D. Stirling, J. Tweedy, J. Chem. Soc. Faraday Trans. 88 (1992) 3375–3382.

ACS APPLIED MATERIALS & INTERFACES

Research Article

Cite This: ACS Appl. Mater. Interfaces 2018, 10, 8066−8076

www.acsami.org

A New Generation of Surface Active Carbon Textiles As Reactive Adsorbents of Indoor Formaldehyde

Giacomo de Falco,[†,‡,§] Mariusz Barczak,[†,∥] Fabio Montagnaro,[§] and Teresa J. Bandosz*[,†]

[†]Department of Chemistry and Biochemistry, The City College of New York, 160 Convent Avenue, New York, New York 10031, United States

[‡]Institute of Research on Combustion, National Research Council, IRC−CNR, Piazzale Vincenzo Tecchio 80, 80125 Napoli, Italy

[§]Department of Chemical Sciences, University of Naples Federico II, Complesso Universitario di Monte Sant'Angelo, 80126 Napoli, Italy

[∥]Faculty of Chemistry, Maria Curie-Sklodowska University, Maria Curie-Sklodowska Sq. 3, 20-031 Lublin, Poland

Supporting Information

ABSTRACT: Highly porous carbon textiles were modified by impregnation with urea, thiourea, dicyandiamide, or penicillin G, followed by heat treatment at 800 °C. This resulted in an incorporation of nitrogen or nitrogen and sulfur heteroatoms in various configurations to the carbon surface. The volume of pores and, especially, ultramicropores was also affected to various extents. The modified textiles were then used as adsorbents of formaldehyde (1 ppmv) in dynamic conditions. The modifications applied significantly improved the adsorptive performance. For the majority of samples, formaldehyde adsorption resulted in a decrease in the volume of ultramicropores. The enhancement in the adsorption was linked not only to the physical adsorption of formaldehyde in small pores but also to its reactivity with sulfonic groups and amines present on the surface. Water on the surface and in challenge gas decreased the adsorptive performance owing to the competition with formaldehyde for polar centers. The results collected show that the S- and N-modified textiles can work as efficient media for indoor formaldehyde removal.

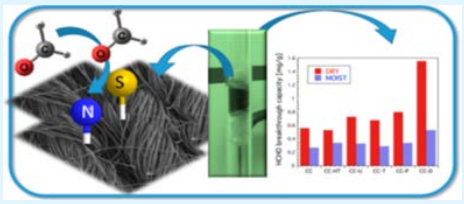

KEYWORDS: *formaldehyde adsorption, carbon textiles, nanopores, surface chemistry, reactivity, S- and N-doped carbon surface*

1. INTRODUCTION

Formaldehyde, HCHO, is one of the most common toxic pollutants found in indoor air. At ambient conditions, it is a flammable and colorless gas of a pungent distinct odor. Its boiling point is −19 °C. The HCHO molecule is polar with a dipole moment of 1.85 D and pK_a of 13.27. Even though small amounts of formaldehyde are produced naturally by plants, animal, and humans, its main source is anthropogenic. US Consumer Products Safety Report of 1997 lists its either indoor or outdoor concentration at the level of 0.03 ppm.[1] It is introduced to the atmosphere through a combustion process, industrial production or as a component of the resins used in furniture and building materials. Its most common sources are pressed woods and particle boards.[1−5] On the basis of its toxicity, formaldehyde is classified as a known human carcinogen.[1]

There are only few reports addressing adsorption of formaldehyde on activated carbons, AC.[6−12] Since various concentrations and experimental conditions were used, the results obtained are rather difficult to compare. Owing to weak adsorption forces and polar character of HCHO, carbons with small pores and hydrophilic surface are desired. However, the latter causes that formaldehyde has to compete with water for adsorption sites.

To increase the formaldehyde adsorption on carbons, modifications with amides have been explored.[9−12] Tanada et al. measured formaldehyde adsorption isotherms from its water solutions onto untreated and treated AC.[9] The carbon used was oxidized with the concentrated sulfuric acid/nitric acid for 24 h, and then reduced with iron powder and washed with HCl for 30 and 60 min. The authors claimed that in this way amines were introduced to the surface. At 35 mg L^{-1} as the initial formaldehyde concentration and at 15 °C, the adsorption capacity increased from 0.4 mg g^{-1} for the initial sample to 0.8 mg g^{-1} for the modified samples, respectively. At 25 °C a 2-fold increase in the capacity was measured. An enhancement in the performance was linked to the specific interactions between formaldehyde and the surface basic groups/amines of AC and to the importance of the chemisorption process.

The kinetics of formaldehyde adsorption (2.3 ppm) at 45% relative humidity and at 30 °C on microporous ACs prepared

Received: December 23, 2017
Accepted: February 20, 2018
Published: February 20, 2018

DOI: 10.1021/acsami.7b19519
ACS Appl. Mater. Interfaces 2018, 10, 8066−8076

from poly(ethylene terephthalate) and polyacrylonitrile (PAN) were investigated by Laszlo.[10] The oxygen content was less than 10% and PAN derived carbon had 5.3% nitrogen on the surface. The latter sample was found as having the highest formaldehyde uptake per unit surface area. It was concluded that the high oxygen content yielded a greater affinity toward water, as did the presence of nitrogen functionalities in the PAN derived samples. Similar effects of an amine modification were also found by An et al.[11] and Ma et al.[12] In the latter work, ACs with pore sizes between 2 and 4 nm were modified with hexamethylene diamine (HMDA) and used to remove 2.2 ppm of formaldehyde from air. The volume of pores decreased with an increase in the HMDA loading. The HMDA modification significantly improved the HCHO adsorption. On the best performing sample, 3.80 mg g^{-1} was adsorbed which was much higher than the amount adsorbed on the unmodified sample (0.08 mg g^{-1}).

An et al. activated mesoporous carbons with H_2SO_4 or NH_3 and used the samples for the adsorption of low-concentration formaldehyde (1 ppm).[11] Interestingly, the adsorption on the acid modified sample was similar to that on the parent one despite its smaller specific surface area. This trend was linked to an increase in the number of surface oxygen groups. Ammonia modified samples showed the highest formaldehyde adsorption efficiency (>70%) owing to the presence of nitrogen groups and an increase in the surface area. Besides amination, another way to increase the AC capacity for formaldehyde removal was its modification with organosilanes and organosiloxanes.[13,14] Other active species, which were deposited on activated carbons to increase their performance as formaldehyde adsorbents, were metal nanoparticles such as silver or copper nanoparticles.[15−17]

Parallel with the study of formaldehyde adsorption on activated carbons, the performance of activated carbon fibers, ACFs, was explored. Rong et al.[18] used rayon-based ACFs for formaldehyde + water adsorption from a vapor phase in dynamic conditions. Their fibers were air-oxidized between 350−450 °C for various periods of time (1−3 h) and the maximum formaldehyde adsorption at not specified concentration was 583.4 mL g^{-1} on the sample oxidized at 420 °C for 1 h. A competitive adsorption between formaldehyde and water vapor was pointed out. Rong et al. also studied the effect of different heat treatment conditions of rayon-based ACFs on the adsorption of formaldehyde from a vapor phase.[19] The adsorption capacity for formaldehyde reached its maximum of 631 mL g^{-1} on a sample heated at 450 °C for 0.5 h. An enhancement in the HCHO adsorption was linked to the presence of acidic carboxylic groups, dipole−dipole interactions, hydrogen bonding and the extent of the surface area and porosity.

Song et al. investigated adsorption of low concentration formaldehyde on various ACFs, such as pitch-based, rayon-based, and PAN-based.[20] The initial formaldehyde concentration was 20 ppm. The samples differed markedly in surface areas and pore volumes. The measured adsorption capacities were between 0.01 to 0.478 mmol g^{-1}. Since all PAN-based ACFs showed higher formaldehyde adsorption capacity and longer breakthrough time than did pitch-based or rayon-based ACFs, it was concluded that abundant nitrogen-containing groups in the PAN derived fibers, and especially pyrrolic, pyridonic pyridinic, and quaternary groups, promoted the adsorption of formaldehyde. In humid condition, however, the HCHO adsorption capability of the PAN-based ACFs dropped drastically because of a competitive adsorption of HCHO and water.

Lee et al. studied HCHO adsorption on conventional pitch-based ACF and PAN-based ACF at 11 ppm of the formaldehyde concentration.[21] The breakthrough time on the latter fibers was 10.5 h, while on the former was 5.5 h. The amounts of formaldehyde adsorbed at dry and humid conditions on the best performing samples were 5.0×10^{-5} and 2.2×10^{-5} mol g^{-1}, respectively.

On the basis of published results and on our experience on the catalytic properties of metal-free nanoporous carbons, high surface area, and elastic carbon textiles of a new generation were modified and tested as HCHO adsorbents. Even though the initial textiles contain some sulfur and nitrogen, which must originate from the fiber source, the swatches were further thermally treated with nitrogen- or sulfur-containing precursors. Those compounds were chosen to introduce more variety of surface groups which might not only attract formaldehyde via physical adsorption forces but also might contribute to its decomposition/reaction.[22] As an initial concentration, about 1 ppm of HCHO in dry air was chosen. Our objective is to investigate in details the effects of surface heterogeneity, chemical, and textural, on the formaldehyde retention on the highly porous carbon textiles. The indoor adsorbents in the form of fabrics are more advantageous than are granules or powders of activated carbons.

2. MATERIALS AND METHODS

2.1. Adsorbents. Carbon textile was received from the U.S. Army Natick Soldier Research, Development & Engineering Center. It is composed of an inner porous carbon layer and outer nylon layer. To remove the outer nylon layer, a swatch was placed in boiling water for 30 min. The remaining inert carbon layer is referred to as CC. The functionalized CC were obtained by immersing the CC swatches in 40 mL of an aqueous solution containing 1 g of four different precursors, dicyandiamide (D), penicillin G (P), thiourea (T), or urea (U), with mass ratio of CC:precursor (1:2) for 72 h. Then the textile swatches were dried overnight at 80 °C and heated in a horizontal furnace at 800 °C (20 °C min^{-1}) for 40 min in N_2 flow (180 mL min^{-1}). The obtained samples are referred to as CC-D, CC-P, CC-T, and CC-U, where last letter represents the modifier. A CC swatch, without functionalization process, was thermally treated at 800 °C in the same operation conditions as the modified samples. It is referred to as CC-HT. This sample is used as a heat treated standard to evaluate the extent of changes in surface chemistry caused by the chemical modifications. At this stage we were not able to find textiles of similar textural properties but lacking any heteroatoms, which would help us to evaluate effects of S and N in a more direct way. The spent samples exposed to HCHO under the dry conditions are referred to with letter "s".

2.2. Adsorbent Characterization. The surface area and the porosity of the adsorbents were determined from N_2 adsorption isotherms measured on an ASAP 2020 (Micromeritics). All the samples were degassed at 120 °C to a constant vacuum (10^{-4} Torr). The specific surface area was determined by the BET method. The total pore volume, V_{tot}, was calculated from the last point of the isotherms based on the volume of nitrogen adsorbed. The micropore volume, V_{μ}, and pore size distribution were calculated using nonlinear density functional theory, 2D-NLDFT, which assumes the heterogeneity of the pore sizes.[23−25]

Potentiometric titration of samples tested was performed on an 888 Titrando automatic titrator (Metrohm). A mass of 0.1 g of carbon textiles was placed in a vessel and dispersed in $NaNO_3$ 0.1 M solution. The solution was maintained at a constant stirring overnight. The pH was recorded and adjusted to about 3.2 by adding HCl 0.1 M and the suspension was titrated with NaOH (0.1 M) up to pH ≈ 10. The proton binding curves, Q,[26] were derived from the titration data. The

DOI: 10.1021/acsami.7b19519
ACS Appl. Mater. Interfaces 2018, 10, 8066−8076

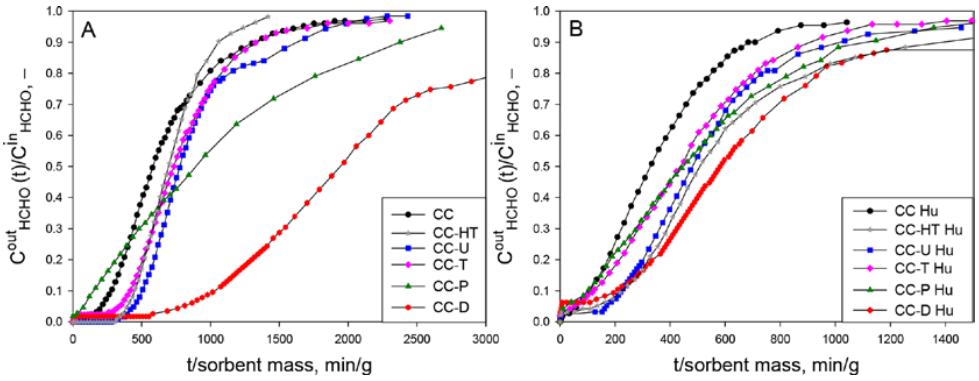

Figure 1. HCHO breakthrough curves measured in dry (A) and moist (B) conditions (designed with the symbol Hu).

Table 1. Parameters of the HCHO Adsorption Performance of the Carbon Textiles Studied

sorbent	C^{in}_{HCHO} [ppmv] dry	ω_{ads} [mg g^{-1}] dry	t_{br} [min] dry	C^{in}_{HCHO} [ppmv] moist	water adsorbed [mg g^{-1}]	ω_{ads} [mg g^{-1}] moist	t_{br} [min] moist
CC	1.25	0.56	29	1.10	311	0.27	7
CC-HT	1.12	0.53	50	0.95	325	0.34	13
CC-U	1.25	0.73	55	0.94	303	0.33	18
CC-T	1.28	0.68	47	0.95	244	0.29	6
CC-P	1.10	0.80	12	0.96	252	0.34	3
CC-D	1.15	1.56	109	0.95	252	0.53	3

pK_a distributions,[27] f(pK_a), of the surface acidic groups were calculated by finding a stable solution of the Fredholm integral equation that relates Q to f(pK_a). For this, SAIEUS procedure was used.[28]

Thermogravimetric (TG) and differential TG (DTG) curves were measured on a SDT Q600 apparatus (TA Instruments). The samples were heated up to 1000 °C at a rate of 10 °C min^{-1} in helium flow (100 mL min^{-1}). The m/z thermal profiles of the exhausted gases/vapors, with an emphasis on m/z 18 (H_2O), 28 (CO) and 44 (CO_2), were collected using a mass spectrometer (MS, Omnistar GSD 320, Pfeiffer Vacuum).

X-ray photoelectron spectroscopy (XPS) spectra were obtained by using a Multi-Chamber Analytical System (Prevac) with monochromatic 450 W Al K-alpha X-ray radiation source (1486.6 eV) (Gammadata Scienta). The vacuum in the analysis chamber was 8 × 10^{-9} Pa. The binding energy (BE) scale was referenced against C 1s = 284.7 eV line. Deconvolutions of the spectra were done using MultiPak software.

2.3. HCHO Dynamic Adsorption Test. Adsorption of HCHO at dynamic conditions was carried out at ambient pressure and T = 25 °C. A glass column of an internal diameter 9 mm was filled with approximately 0.130 g of carbon textiles cut in little pieces. The bed height was 2.7 cm. Formaldehyde was generated by a calibrated formaldehyde permeation tube (Metronics, Inc.) using a Dynacalibrator (Model 150, Metronics, Inc.) operated at 80 °C with 100 mL min^{-1} nitrogen as a carrier gas. The outlet flow from the generator, before reaching the testing column, was mixed with 400 mL min^{-1} of air, dry (passing through $CaSO_4$ to totally remove any humidity) or moist of 70% humidity (passing through a water bed). The inlet flow rate of a challenge gas was set to 500 mL min^{-1}, the inlet concentration of formaldehyde (C^{in}_{HCHO}) was set to approximately 1 ppmv. Before running experiments in the moist conditions, the adsorbent bed was prehumidified for 1 h with moist air (500 mL min^{-1}). The samples after exposure to moist air were weighted and the weight difference represents the amount of water adsorbed.

Gas analysis was performed with a continuous analyzer equipped with an electrochemical sensor (RM 16 Interscan Corporation) with accuracy of 2% of the reading value (working range of analyzer 0–2 ppmv of formaldehyde). The measurement on each textile was repeated twice and the difference in the results is less than 12% (Figures 1 and 1S and Tables 1S and 2S).

The specific adsorption capacity of HCHO at saturation, ω_{ads} [mg g^{-1}], was determined through the integration of the area above the breakthrough curve using the flow rate, concentration of HCHO, time, and mass of the adsorbent material.

3. RESULTS AND DISCUSSION

The formaldehyde (HCHO) breakthrough curves measured in the dry conditions on the carbon textiles are collected in Figure 1A, and Figure 1S. From the breakthrough curves, the dynamic data and corresponding adsorption capacities at saturation were determined and the results are summarized in Table 1, in which t_{br} [min] is the breakthrough point time (assumed as the time for which the ratio of the HCHO concentration at the bed outlet relative to that in the feed is 0.05), ω_{ads} [mg g^{-1}] is the HCHO breakthrough capacity and C^{in}_{HCHO} [ppmv] is the inlet concentration of HCHO in the fixed bed reactor. Since in some cases, even after a very long experimental time, the bed saturation was not reached, the HCHO capacity at C^{in}_{HCHO} = 0.95 was arbitrarily chosen for the performance comparison.

CC and CC-HT revealed similar dynamic behaviors, even though the breakpoint time for CC-HT is longer than that for CC. They show relatively fast kinetics of the adsorption process and similar saturation capacity (ω_{ads} = 0.56 and 0.53 mg g^{-1} for CC and CC-HT, respectively). The heat treatment, which was expected to remove even traces of the residual nylon or modify fibers,[29] did not affect the adsorption capacity. All chemically modified carbon textiles exhibit better performance as HCHO adsorbents than their unmodified counterparts (CC and CC-HT). Interestingly the breakthrough curve of CC-P differs markedly from those of the other textiles, which suggests

DOI: 10.1021/acsami.7b19519
ACS Appl. Mater. Interfaces 2018, 10, 8066–8076

different mechanisms of HCHO adsorption. The saturation capacities ω_{sds} of CC-T, CC-U, CC-P, and CC-D are 20%, 30%, 44%, and 170% greater, respectively, than that for CC. The best adsorbent is CC-D whose t_{br} value equals to 109 min, and the saturation capacity reaches 1.56 mg g^{-1}. CC-P is characterized by the shortest breakpoint time with respect to the others functionalized samples (12 min) but its saturation adsorption capacity is bigger than those of CC-U and CC-T.

Figure 1B shows the HCHO breakthrough curves measured in the moist conditions (samples are denoted with "Hu") for the modified carbon textiles; the corresponding adsorption capacities and t_{br} values are listed in Tables 1 and 2S. As seen, the presence of moisture on the surface and in the challenge gas markedly decreased the performance of the materials tested as HCHO adsorbents. The effect of water is visualized in Figure 2.

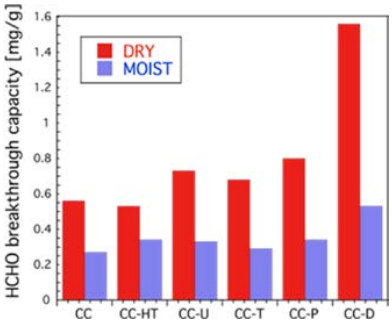

Figure 2. Comparison of HCHO saturation capacity on the textiles tested.

Even though its presence worsens the performance, the extent of the decrease differs. Thus, the most pronounced effect was found for the best performing sample CC-D, and the least was found for CC-HT. It is likely caused by (1) occupation of HCHO adsorption centers by water during the prehumidification or (2) competition between water and HCHO for these centers.[13,30,31] All functionalized sorbents adsorbed considerable amounts of water (Table 1) that can block the micropores which would be otherwise accessible to HCHO, limit the diffusion of the pollutant gas inside the pore structure, and in this way decreasing the adsorption capacity. This decrease occurs even though some amount of HCHO is expected to be dissolved in the adsorbed water film. Nevertheless, no direct dependence between the amount of water adsorbed and the decrease in the saturation capacity was found.

To understand the adsorption behavior of the materials tested, their surface features need to be extensively characterized. The measurement of the weight of the textile swatches before and after modifications indicates weight losses of 23%, 25%, 29%, 34%, and 27% for CC-HT, CC-U, CC-T, CC-P, and CC-D, respectively. This indicates the high reactivity of the carbon fibers with the modifiers, especially in the case of CC-P, and since this reactivity might affect the porosity, the parameters of porous structure of the carbon textiles, initial and spent in HCHO adsorption under dry conditions, are collected in Figures 3–5 and Table 3S of the Supporting Information. CC is a predominantly microporous material ($\frac{V_\mu}{V_{tot}}$=88%) of a high surface area of 921 m^2 g^{-1}. Heating it at 800 °C only slightly decreased the porosity. On the other hand, the surface chemical/thermal treatment had a marked effect on the porosity. After this process, the surface and pore volume decreased (Figure 5), likely as a result of the deposition of the active phase/pore blocking. In particular, for CC-U, CC-T, and CC-D a slight loss of porosity in the micropore region in the range 4–8 Å and 14–20 Å and in the mesopore region of 20–24 Å (Figure 4) are found. This indicates a high dispersion of the active phase. For CC-P, on the other hand, a significant loss of the pore volume in a whole region of pore sizes (Figure 4) is found. This suggests that the large molecule of penicillin G ($C_{16}H_{18}N_2O_4S$) blocks micropores during the impregnation and its thermal reactivity/decomposition/carbonization products remain at their entrances.

After the HCHO adsorption, all spent adsorbents, except CC-D, show a decrease in the surface area and porosity (Figure 5). Interestingly the porosity of CC-D did not change, in spite of its high adsorption capacity. In analyzing this data, we have to take into account that owing to high vacuum and anticipated

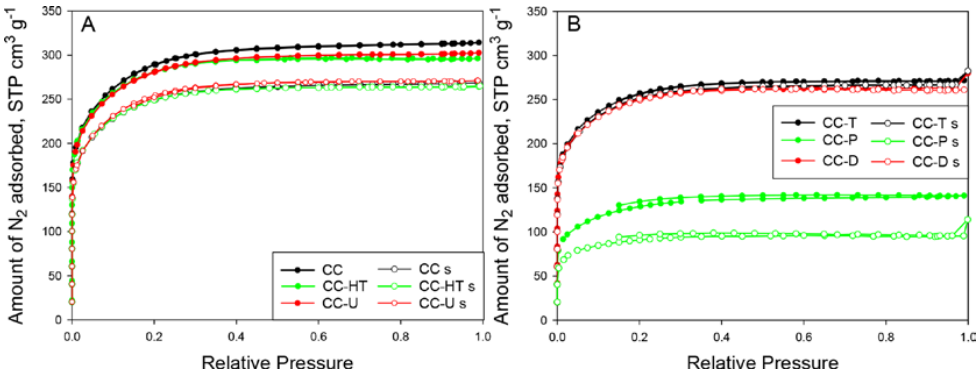

Figure 3. (A) Nitrogen adsorption isotherms for CC, CC-HT, CC-U fresh and spent (s) samples. (B) Nitrogen adsorption isotherms for CC-T, CC-P, CC-D fresh and spent (s) samples (spent samples are those under dry conditions).

DOI: 10.1021/acsami.7b19519
ACS Appl. Mater. Interfaces 2018, 10, 8066–8076

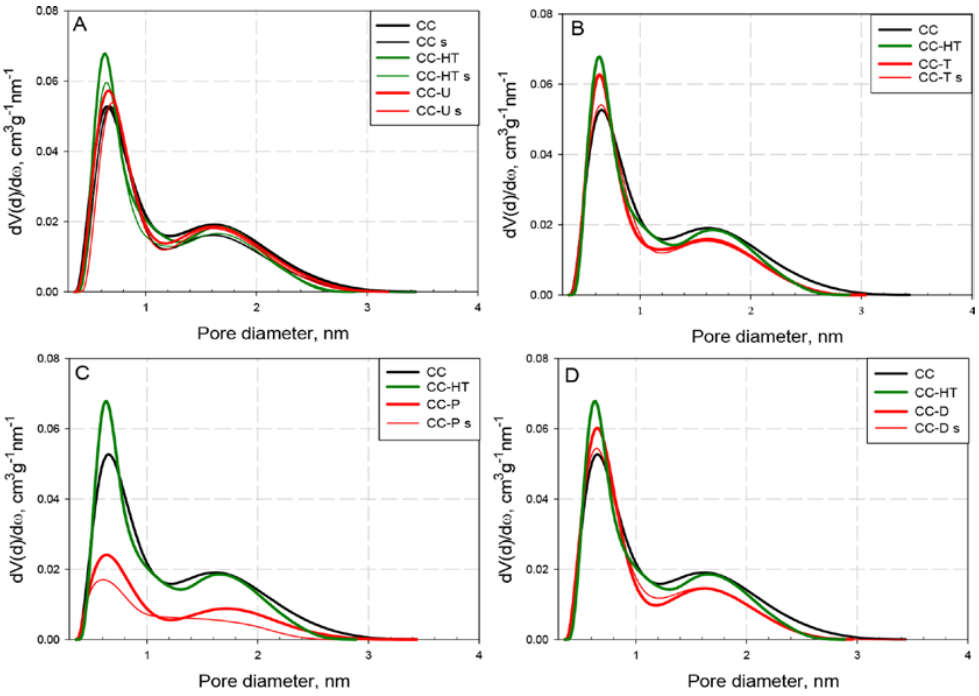

Figure 4. Pore size distributions for the initial and spent (s) textiles under dry conditions: CC-U (A), CC-T (B), CC-P (C), and CC-P (D). In each figure, pore size distributions of CC and CC-HT are also included for comparison (in panel A, distributions for spent CC and CC-HT are included).

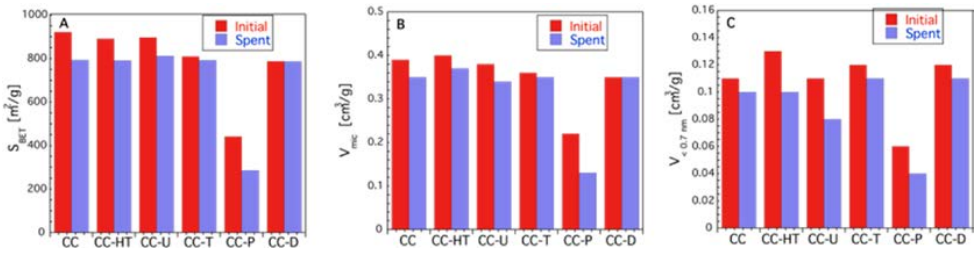

Figure 5. Comparison of the structural parameters for the initial and spent samples in the dry conditions: A, BET surface area; B, micropore volume; C, volume in pores smaller than 0.7 nm.

weak physical adsorption of HCHO in its unchanged form, it is expected to be removed from the pore system before the porosity analysis. Therefore, the changes observed are likely caused by its chemisorption/polymerization and thus retention on the heteroatom-rich phase on the surface.

While trends in the volume of micropores almost exactly follow the trend in the surface area, the most marked differences are seen in the volume of ultramicropores smaller than 0.7 nm. The volume of these pores also decreases for CC-D. The biggest changes/decrease in porosity was found for CC-P (Figures 4 and 5C), which suggests its strong chemical reactivity with HCHO. The high reactivity of CC-P surface is reflected in the shape of the breakthrough curve where a very increase in the measured HCHO concentration was recorded (Figure 1).

Although no relationship between the extent of the decrease in the volume of ultramicropores and the breakthrough capacity was established, these findings indicate the importance of the pores <0.7 nm for HCHO reactive adsorption.

Based on the above discussion, the surface chemistry is expected to have a marked effect on the amount of HCHO adsorbed on our materials. First the acid/base character of the samples tested was investigated by the potentiometric titration. The proton binding curves and pK_a distributions are presented

DOI: 10.1021/acsami.7b19519
ACS Appl. Mater. Interfaces 2018, 10, 8066−8076

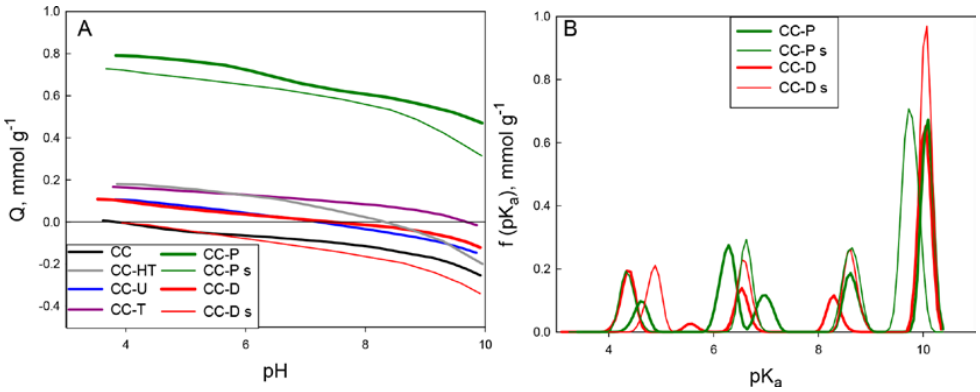

Figure 6. (A) Proton binding curves for CC, CC-HT, CC-U, CC-T, CC-P, and CC-D. (B) Comparison of pK_a distributions of the groups present on the surface of CC-P and CC-D. Spent sorbents after adsorption of HCHO at dry conditions are designated with letter "s".

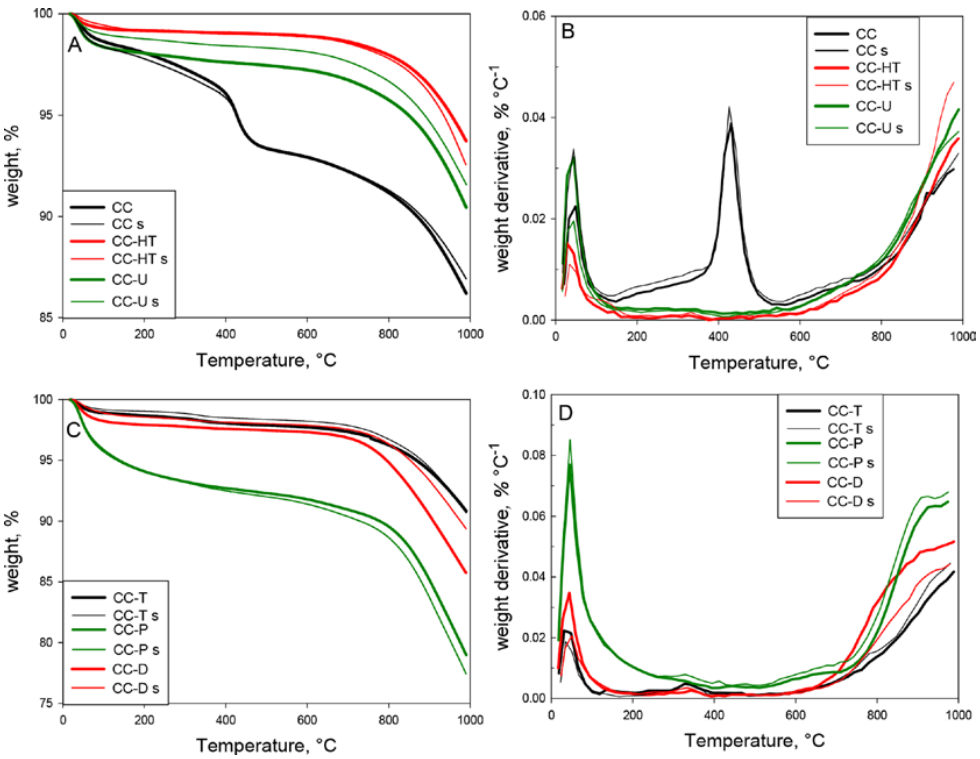

Figure 7. (A, B) TG-DTG curves for CC, CC-HT, and CC-U fresh and after adsorption of formaldehyde. (C, D) TG-DTG curves for CC-T, CC-P, and CC-D fresh and spent after adsorption of formaldehyde. Spent samples at dry conditions are designated with letter "s".

in Figure 6. Table 4S summarizes the results and lists the numbers of groups in each category of strength: strongly acidic (3 < pK_a < 5), close to neutral (5 < pK_a < 8), and weakly acidic (8 < pK_a < 11). The treatment of CC, either by heating or

DOI: 10.1021/acsami.7b19519
ACS Appl. Mater. Interfaces 2018, 10, 8066−8076

impregnation with various precursors followed by heating, led to an increase in the surface pH value from 7.7 to 9.7 for CC-P. Moreover, the total number of dissociating groups in our experimental window decreased for all textiles but CC-HT. These results suggest the change in the speciation of the groups and their chemical nature due to the introduction of heteroatom from the modifiers (N or S). Indeed, the proton binding curves clearly show strongly basic character of CC-P and CC-D surfaces (only a proton uptake) while other modified textiles are amphiprotic. The initial CC is rather acidic (proton release) and heat treatment increases its basic character. Interestingly, some acidification of spent CC-D and CC-P is found after HCHO adsorption. Those are in fact samples on which a gradual increase in the slope of the breakthrough curves was recorded under dry conditions (Figures 1 and S1). This shape suggests some surface reactivity.

The surfaces of our samples were also investigated by thermogravimetric analysis. The TG and DTG curves for the initial and spent adsorbents, measured in helium, are collected in Figure 7. For all initial samples the total weight loss ranged between 6−22% (Figure 7A). 12% weight loss for CC at about 400 °C is linked to the removal of a not-peel-off after boiling nylon.[29] In fact, it could be considered as an intrinsic modifier of CC-HT. The first peak on the DTG curves (Figure 7B) centered at about 80 °C likely represents the removal of physically adsorbed water and/or formaldehyde in the case of the spent samples. The results show that all initial or spent samples but CC-P are rather thermally stable up to 800 °C (synthesis temperature). In the case of CC-P a gradual weight loss is observed between 100 and 750 °C. The gradual weight loss for the initial CC-P implies the highest reactivity of the penicillin-derived phase among all samples and this reactivity can affect the mechanism of HCHO retention on this sample. From all initial samples only CC-T shows the groups decomposing between 300 and 400 °C and it must be the fingerprint of its modifier, likely related to the sulfur environment. Sulfones formed on the surface during stabilization/cooling are expected to decompose at this temperature range.[32]

After HCHO adsorption a new peak between 300 and 400 °C appears on the DTG curves for CC-P and CC-D. Moreover, the weight loss pattern at temperatures >800 °C is also altered indicating some surface reactivity/deposition of new compounds resulting from the samples' exposure to HCHO. The weight loss between 300 and 400 °C might be due to the decomposition of species formed as a result of this carbon surface reactivity with HCHO. As discussed above, only for these two samples the surface acidity increased after HCHO exposure. The intensity of those peaks is low but the amounts adsorbed on our samples are generally in the range of a fraction of mg g^{-1} (CC-D is an exception). An unaltered peak representing removal of nylon from CC suggests its chemical inertness in the process of HCHO reactive adsorption.

The MS analysis of the species released from the surface during thermal analysis further confirms the observations based on the weight loss discussed above. In the analysis, we focus on the features of m/z 18, 28, 29, 30, 44, and 48 thermal profiles. Since they represent H_2O, CO, HCO, HCO/NO, CO_2, and SO, respectively, they were chosen as the most relevant to depict the changes in chemistry upon HCHO adsorption. The detailed results are presented in Figures 2S and 3S. Comparison of the trends in m/z profiles for the initial and exposed samples leads to the following general observations on the effects of HCHO exposure: (1) on m/z 44 the new peak and an increase in the relative intensity of the signal appears at temperatures less than 200 °C, which supports the change in surface chemistry upon HCHO exposure. The most drastic changes in m/z 44 thermal profiles are seen for CC-P, CC-T, and CC-HT; (2) no conclusion on the physically adsorbed HCHO can be drawn since m/z 28 (CO) and m/z 29 (HCO) have similar patterns. This indicates that these species are also released during the low temperature heating of the initial carbons and could also be desorbed from the surface between the breakthrough tests and thermal analysis experiments; (3) sulfur species are involved in HCHO reactive adsorption since their thermal stability changed as indicated by an increase in the intensity of m/z 48 CC-HT and CC-T at $T > 700$ °C. The effect is the strongest for CC-T, which in fact has the highest amount of sulfur on the surface (Table 2); (4) for CC-D there is a visible change in the shape of its thermal profile for m/z 30 suggesting the marked alteration in the nitrogen environment upon exposure to HCHO.

Table 2. XPS Elemental Composition of the Surface of the Textiles (in at. %)

textile	C (%)	O (%)	N (%)	S (%)
CC	78.4	14.1	5.6	1.9
CC-HT	84.3	12.3	3.2	0.2
CC-U	82.5	13.2	3.3	1.1
CC-T	81.2	9.3	4.3	5.1
CC-P	85.1	9.7	3.5	1.7
CC-D	83.5	11.3	4.5	0.7

The m/z 44 (CO_2) pattern for CC-P and its change after HCHO exposure deserves further attention. As discussed above, the change in porosity of this sample after the formaldehyde adsorption was the most marked. The explanation is in the high reactivity of this sample's carbon phase with HCHO, which retains as chemically bound to the surface or in the polymerized form blocking the small pores. Indeed, the comparison of m/z 44 for all samples shows the low thermal stability/high reactivity of CC-P (CO_2 is released from various surface environments in the whole temperature range). Exposing this sample to HCHO changes this pattern and less CO_2 is released at low temperature from the most reactive/unstable surface environment of CC-P.

To further analyze the effects of surface chemistry on the HCHO adsorption on the textiles, XPS analysis was carried out. The surface elemental composition is listed in Table 2, and the deconvolution of C 1s, O 1s, N 1s, and S 2p core energy levels is in Table 3. Figure 8 presents the examples of the deconvolution and all deconvolution results are included in Figures S4−S9. The results show that the surface of the textiles is markedly changed upon the applied modifications and all treated textiles contain more carbon and less oxygen and nitrogen than the initial CC. Moreover, CC also contains a significant amount of sulfur (1.9 at. %). Upon the treatments applied, its content decreases for all samples but for CC-T. To CC-T sulfur was introduced in the thiourea modifier. The heat treatment of CC almost removes sulfur from its surface and the content of nitrogen significantly decreases.

All the compounds used for the modification of the CC textiles contain nitrogen and additionally two of them (penicillin G and thiourea) contain also sulfur. Thus, these heteroatoms are expected to exist on the surface of our textiles

DOI: 10.1021/acsami.7b19519
ACS Appl. Mater. Interfaces 2018, 10, 8066−8076

Table 3. Results of the Deconvolution of the XPS Spectra of C 1s, O 1s, N 1s, and S 2p[a]

binding energy [eV]	bond assignment	CC [%]	CC-HT [%]	CC-U [%]	CC-T [%]	CC-P [%]	CC-D [%]
C 1s		**78.4**	**84.3**	**82.5**	**81.2**	**85.1**	**84.1**
284.7	C−C sp^2	67.0	59.2	66.6	69.2	69.2	73.6
286.0−286.2	C−O (phenol, alcohol, ether), C−N (amine, amide	18.9	23.9	18.9	16.8	16.4	16.5
287.2−287.7	C═O (carbonyl, quinone), O═C−N (amide)	6.4	5.8	6.6	6.0	5.9	5.2
288.6−288.9	O═C−O (carboxyl)	4.4	5.7	4.7	4.0	4.6	3.1
291.0	$\pi \rightarrow \pi^*$, π-electrons in aromatic rings	3.3	5.5	3.1	3.9	3.8	1.6
O 1s		**14.1**	**12.3**	**13.2**	**9.3**	**9.7**	**11.4**
530.6−531.2	C═O (aromatic)	29.4	29.3	21.3	22.6	22.2	24.7
531.9−532.3	C═O (aliphatic)	45.4	48.8	58.4	49.0	49.6	57.3
533.1−533.5	C−O	25.2	21.9	20.3	28.4	28.2	18.1
N 1s		**5.6**	**3.2**	**3.3**	**4.3**	**3.5**	**4.5**
398.2−398.4	pyridine	10.6	13.6	15.4	33.9	19.2	33.0
399.7−399.9	pyrrole, amine, amide	56.6	49.7	42.7	34.7	43.7	32.3
400.8−401.1	quaternary nitrogen/ammonium	24.7	28.4	32.3	24.8	26.3	24.2
402.0−402.5	pyridine-N-oxide, C−N^+O−C, NO_x	8.0	8.3	9.7	6.6	10.6	10.5
S $2p_{3/2}$		**1.9**	**0.2**	**1.1**	**5.1**	**1.7**	**0.7**
163.8−163.9	R−S−S− in thiol, bisulfides	14.9	ND		71.0	36.3	
165.7−166.0	R_2−SO		ND		12.4	7.7	
166.8−167.4	SO_3^{2-} (sulfines)	67.6	ND	26.3	6.9	29.3	
168.2−169.0	HSO_3^- (sulfonic acids)	17.5	ND	73.7	9.7	26.7	100.0

[a]In bold, atomic % of specific elements. CC, deconvoluted C 1s, O 1s, N 1s, and S 2p signals.

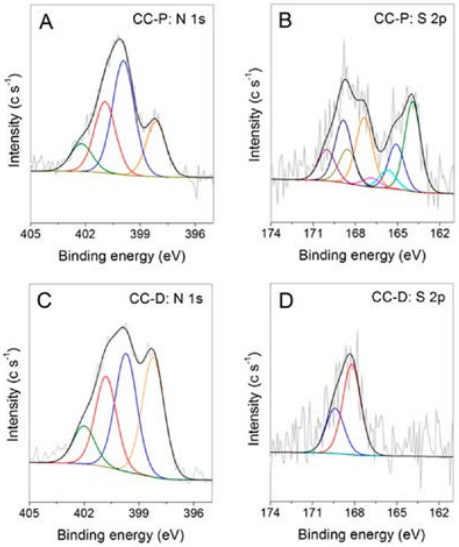

Figure 8. Deconvolution of N 1s and S 2p core energy levels for (A, B) CC-P and (C, D) CC-D.

in various configurations. The heat treatment decreases the S and N contents and further changes in chemistry should be analyzed in comparison with the surface feature of CC-HT. After the surface treatment, more nitrogen is incorporated to the carbon surface in the form of pyridines, whose contributions significantly increased (15.4−33.9%) compared to that of the CC or CC-HT samples (10.6 at. % and 13.6 at. %, respectively). Those pyridines, along with amines, can participate in coupling reactions (Mannich reaction[33]) with formaldehyde forming amino-carbonyl compounds. This covalent bond formation can explain a decrease in the volume of ultramicropores after HCHO adsorption.

The sulfur on the initial CC textile is mainly in the form of sulfines (67.6%) and sulfonic acids (17.5%). Modification with Dicyandiamide leads to total oxidation of sulfur to the latter species while with urea to the sulfines (26.3%) and sulfonic acids/sulfonates (73.7%). The total sulfur content on the CC-D and CC-U textiles is much lower than that on CC, so most likely sulfur originated from the initial CC textile is covered on the surface by the products of modifications. On the other hand, the surface treatment with N- and S-containing penicillin G and thiourea results in either the same S-doping level as on CC (1.7% for CC-P) or its significant increase (5.1% for CC-T). Interestingly, sulfur in the case of CC-P and CC-T textiles is mostly present in the most reduced forms (36.3% for CC-P and 71.0% for CC-T), while in the case of samples treated with dicyandiamide and urea (i.e., reagents not containing sulfur) it is present mainly in the form of sulfines and sulfonic acids.

While the lowest HCHO breakthrough capacities are found for the initial CC sample and for CC-H, the performance of the modified textiles significantly improved. As discussed above based on the porosity, the observed differences in the HCHO adsorption must be rather linked to the chemical composition of the textile surfaces. The results indicate that there is no direct relationship between the carbon, oxygen, sulfur and particularly nitrogen content on the surface and the formaldehyde adsorption capacity. The common interpretation of an increase in HCHO adsorption on carbon-based materials discussed in the literature is that nitrogen content controls the formaldehyde adsorption capacity.[31,34] This is, however, not true in our case. A close look at the particular surface species after deconvolution of N 1s and S 2p core energy level spectra leads to some interesting observations. The initial CC textile has a majority of its nitrogen in the form of pyrroles, amines, and amides (56.6%)—considerable portion of them coming from unremoved nylon traces. This is confirmed by the higher content of oxygen, which nylon is also composed of.[35] Thus,

DOI: 10.1021/acsami.7b19519
ACS Appl. Mater. Interfaces 2018, 10, 8066−8076

repulsive interactions between nylon and carbonyl groups of formaldehyde and those of nylon (which are always located next to the amide nitrogen) might be partially responsible for the lower HCHO uptake on this textile. Apparently, amides groups of nylon do not advance HCHO adsorption. Apart from that, the content of pyridinic nitrogen on CC is lowest among all the samples and that nitrogen, if present on the surface, can participate in Mannich reaction. The surface pH values collected in Table 4S show that the CC cloth is the least basic (pH = 7.7) among all textiles tested (pH = 8.1−9.7). Some reports in the literature suggest that the HCHO adsorption capacity is strongly related to the density of basic surface functional groups.[8,20] Thus, the lower density of those groups in the case of CC sample leads to the smaller HCHO uptake. Even though the basicity of CC-HT increases in comparison with that of CC, it has much less nitrogen and thus less species available for specific interactions with HCHO, which results in the comparable capacities of these two samples.

The CC-D textile exhibits the highest HCHO uptake (1.56 mg g^{-1}). This is likely due to the presence of specific nitrogen and sulfur surface species enhancing the interactions with formaldehyde. Indeed, in the case of this sample, the content of pyridinic nitrogen is three times higher than that on CC. These groups increase the basicity of the surface and contribute to Mannich reaction. Nitrogen in these configurations was also indicated as promoting to the formation of superoxide ions O_2^-,[36,37] which might contribute to the HCHO mineralization when adsorbed in the ultramicropores. This and the Mannich reaction can affect oppositely the porosity evolvement resulting in the apparently unchanged surface area.

The uniqueness of our carbon materials compared to those studied previously is in the presence of sulfur species incorporated to their surface. Thus, that sulfur exclusively in sulfonic acids in CC-D, despite its low content (only 0.7%) can increase HCHO adsorption by the reaction to form α-hydroxymethanesulfonates.[38] The condensation of aromatic sulfonates with formaldehyde is also a possible pathway here[39,40] and formed product can result in the pore blocking and therefore lead to a decrease in the surface area. CC-T, on the other hand, has the highest content of sulfur (5.1%) but only a fraction of it (9.7%) is in the form of sulfonates/sulfonic acid. Thus, despite similar content and distribution of nitrogen as that in CC-D, its HCHO adsorption capacity is much lower than on CC-D. These two samples have similar porosities. Additionally, the less polar pyridine-N-oxide species are present on the CC-T surface in a smaller quantity than on that of CC-D, and they might contribute to the enhanced adsorption of HCHO on the latter sample. CC-P, even though it has a least developed porous structure when compared to other textiles tested, it has a considerable amount of sulfur in the form of sulfites/sulfonic acid, which can enhance the HCHO adsorption. Its surface shows also the highest basicity (pH = 9.7, Table 2S) and basic amines can participate in Mannich reaction. CC-U has a similar amount of sulfonic acids to that on CC-D, however the content of pyridines and pyridine-N-oxides is lower than that on CC-D. This leads to the twice smaller HCHO uptake on CC-U than that on CC-D.

To look at the results in a more quantitative way, and as discussed above, CC-D performs better than does CC and CC-HT because of more pyridinic species on its surface. Even though it has the same absolute amount of pyridines as has CC-T (Table 5S), it has much more sulfonic acids (0.7 at. % on CC-D as oppose to 0.49% on CC-T). The HCHO uptake on CC-U is similar as that on CC-T and smaller than on CC-D because even though CC-U has a similar absolute content of sulfur as has CC-D (0.82 vs 0.7%) its content of pyridinic nitrogen is in fact three times smaller (3.3 × 0.154 = 0.5%) than that on CC-D.

As seen in Figure 9, the amount of HCHO adsorbed increases with an increase in the absolute amount of sulfonic and pyridinic groups on the surface. We do not expect the fully linear behavior owing to the complexity of the textile surfaces' chemistry and porosity.

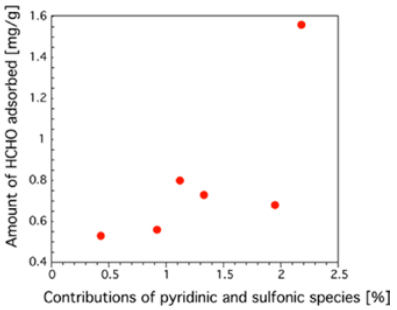

Figure 9. Relationship between the amount of HCHO adsorbed and the sum of the absolute contributions of pyridinic and sulfonic species.

The porosity, even though the differences between samples are not substantial, plays also a role. The pores close in size to HCHO molecule attract it with the strongest forces. The order in the volume of pores smaller than 0.7 nm (Figure 5C) (CC-P < CC and CC-U < CC-T and CC-D) resembles the one of the breakpoint time reported in Table 1 (CC-P < CC < CC-T and CC-U < CC-D). Nevertheless, functional groups that are important for specific interactions/reactive adsorption can only exist at the entrance of ultramicropores or in larger pores, which can accommodate their geometry. Therefore, chemical modifications applied to the textiles increase the utilization of the carbon fiber surface toward retention of HCHO.

Even though the polar character of the surface can be roughly estimated based on the adsorption of water during prehumidification, and the order in the quantity of water adsorbed indicates that CC-T, CC-D, and CC-P are least hydrophilic ones, this is rather owing to their low oxygen content. These results might be affected by water adsorption kinetics. The most detrimental effect of water preadsorption/competition on the HCHO adsorption is found in fact for CC-D and CC-P. There is a high probability that, on the surface of these textiles, water is formed in condensation reactions with involvement of formaldehyde. Adsorption of that water in situ on the most polar centers or in small pores, where it is formed, can further block the adsorption centers for HCHO.

It should be mentioned here, that the exact identification of the groups responsible for the uptake of formaldehyde is not easy as the surface of textiles is complex and a broad range of O, N and S species is present. Additionally, the differences in the porous structure also affect the interactions of HCHO with the surface. However, it is clearly seen that the content of nitrogen itself cannot be considered as an only factor influencing the adsorption capacities. Its speciation is important. Besides, very polar sulfur groups (particularly sulfonic acids) also play an

DOI: 10.1021/acsami.7b19519
ACS Appl. Mater. Interfaces 2018, 10, 8066−8076

important role by providing highly active adsorption sites for the HCHO adsorption. Since HCHO may behave as both a Lewis acid and a Lewis base, it can potentially interact with both basic (e.g., pyridine, amines pyridine-N-oxide) and acidic (e.g., carboxylic, sulfonic) surface groups. In the literature, there is no study on the effect of sulfur on the adsorptive behavior of carbon materials as formaldehyde removal media so this is a very first report about the role of sulfur in enhancing the HCHO uptake.

4. CONCLUSIONS

The results presented in this paper show that modification of highly porous carbon textiles with S and N containing functional groups significantly enhances their adsorption capacity for removal of low concentration of formaldehyde at ambient conditions. The modified textiles have a high volume of ultramicropores, which promotes physical adsorption of formaldehyde. That process is markedly enhanced by the chemical reactivity of formaldehyde with pyridines, amines, and sulfones/sulfonic acids incorporated to the textiles' surfaces. This resulted in a decrease in the porosity. Besides, the pyridine N-oxide rich surface also enhanced polar interaction of formaldehyde with the fibers' surface, increasing the adsorptive performance. The effect of the improvement in HCHO adsorption on the carbon surface is a novelty of this work, apart from the analysis of the performance of porous carbon textiles of a new generation. The collected results demonstrate that the specifically designed surface modifications of carbon textiles can convert them into efficient HCHO removal media from indoor air.

■ ASSOCIATED CONTENT

Supporting Information

The Supporting Information is available free of charge on the ACS Publications website at DOI: 10.1021/acsami.7b19519.

Repeated breakthrough curves, breakthrough capacity, % difference in the calculated breakthrough capacity, the details on integration procedure, the m/z thermal profiles, the parameters of porous structure, the numbers of functional groups in various acidity ranges and the samples' pH values, the deconvolutions of XPS spectra, and the absolute contributions of pyridinic and sulfonic groups on the surfaces of the textiles tested (PDF)

■ AUTHOR INFORMATION

Corresponding Author

*E-mail: tbandosz@ccny.cuny.edu.

ORCID

Fabio Montagnaro: 0000-0002-6377-3989

Teresa J. Bandosz: 0000-0003-2673-3782

Notes

The authors declare no competing financial interest.

■ ACKNOWLEDGMENTS

M.B. thanks the Polish-American Fulbright Commission for supporting his research at City College of New York. The support of the PhD Course in Chemical Sciences (University of Naples, Italy) and of the Short Term Mobility Program of IRC−CNR (CUP B53C17001430005) for the stay of G.d.F. at City College of New York is gratefully acknowledged as well.

■ REFERENCES

(1) NIH. Formaldehyde and Cancer Risk. https://www.cancer.gov/about-cancer/causes-prevention/risk/substances/formaldehyde/formaldehyde-fact-sheet (accessed Feb. 14, 2018).

(2) Agency for Toxic Substances and Disease Registry. Public health statement for formaldehyde. https://www.atsdr.cdc.gov/PHS/PHS.asp?id=218&tid=39.

(3) Chung, P. R.; Tzeng, C.-T.; Ke, M.-T.; Lee, C.-Y. Formaldehyde gas sensors: A review. *Sensors* **2013**, *13*, 4468−4484.

(4) USA Consumer Products Safety Commission. An update on formaldehyde. https://www.cpsc.gov/PageFiles/121919/AN%20UPDATE%20ON%20FORMALDEHYDE%20final%200113.pdf.

(5) CDC. What you should know about formaldehyde. https://www.cdc.gov/nceh/drywall/docs/whatyoushouldknowaboutformaldehyde.pdf.

(6) Shiraishi, F.; Yamaguchi, S.; Ohbuchi, Y. A rapid treatment of formaldehyde in a highly tight room using a photocatalytic reactor combined with a continuous adsorption and desorption apparatus. *Chem. Eng. Sci.* **2003**, *58*, 929−934.

(7) Boonamnuayvitaya, V.; Sae-ung, S.; Tanthapanichakoon, W. Preparation of activated carbons from coffee residue for the adsorption of formaldehyde. *Sep. Purif. Technol.* **2005**, *42*, 159−168.

(8) Carter, E. M.; Katz, L. E.; Speitel, G. E.; Ramirez, D. Gas-phase formaldehyde adsorption isotherm studies on activated carbon: correlations of adsorption capacity to surface functional group density. *Environ. Sci. Technol.* **2011**, *45*, 6498−6503.

(9) Tanada, S.; Kawasaki, N.; Nakamura, T.; Araki, M.; Isomura, M. Removal of formaldehyde by activated carbons containing amino groups. *J. Colloid Interface Sci.* **1999**, *214*, 106−108.

(10) Laszlo, K. Characterization and adsorption properties of polymer-based microporous carbons with different surface chemistry. *Microporous Mesoporous Mater.* **2005**, *80*, 205−211.

(11) An, H. B.; Yu, M. J.; Kim, J. M.; Jin, M.; Jeon, J. K.; Park, S. H.; Kim, S. S.; Park, Y. K. Indoor formaldehyde removal over CMK-3. *Nanoscale Res. Lett.* **2012**, *7*, 7.

(12) Ma, C.; Li, X.; Zhu, T. Removal of low-concentration formaldehyde in air by adsorption on activated carbon modified by hexamethylene diamine. *Carbon* **2011**, *49*, 2873−2877.

(13) Li, J.; et al. Effect of Relative Humidity on Adsorption of Formaldehyde on Modified Activated Carbons. *Chin. J. Chem. Eng.* **2008**, *16*, 871−875.

(14) Matsuo, Y.; Nishino, Y.; Fukutsuka, T.; Sugie, Y. Removal of formaldehyde from gas phase by silylated graphite oxide containing amino groups. *Carbon* **2008**, *46*, 1162−1163.

(15) Shin, S. K.; Song, J. H. Modeling and simulations of the removal of formaldehyde using silver nano-particles attached to granular activated carbon. *J. Hazard. Mater.* **2011**, *194*, 385−392.

(16) Rengga, W. D. P.; Sudibandriyo, M.; Nasikin, M. Adsorption of low-concentration formaldehyde from air by silver and copper nano-particles attached on bamboo-based activated carbon. *Int. J. Chem. Eng. Appl.* **2013**, *4*, 332−336.

(17) Rengga, W. D. P.; Chafidz, A.; Sudibandriyo, M.; Abasaeed, A. E.; et al. Silver Nano-particles Deposited on Bamboo-based Activated Carbon for Removal of Formaldehyde. *J. Environ. Chem. Eng.* **2017**, *5*, 1657−1665.

(18) Rong, H.; Ryu, Z.; Zheng, J.; Zhang, Y. Effect of oxidation of rayon based activated carbon fibers on the adsorption behavior for formaldehyde. *Carbon* **2002**, *40*, 2291−2300.

(19) Rong, H.; Ryu, Z.; Zheng, J.; Zhang, Y. Influence of heat treatment of rayon-based activated carbon fibers on the adsorption of formaldehyde. *J. Colloid Interface Sci.* **2003**, *261*, 207−212.

(20) Song, Y.; Qiao, W.; Yoon, S.-H.; Mochida, I.; Guo, Q.; Liu, L. Removal of formaldehyde at low concentration using various activated carbon fibers. *J. Appl. Polym. Sci.* **2007**, *106*, 2151−2157.

(21) Lee, K. J.; Shiratori, N.; Lee, G. H.; Miyawaki, J.; Mochida, I.; Yoon, S.-H.; Jang, J. Activated carbon nanofiber produced from electrospun polyacrylonitrile nanofiber as a highly efficient formaldehyde adsorbent. *Carbon* **2010**, *48*, 4248−4255.

DOI: 10.1021/acsami.7b19519
ACS Appl. Mater. Interfaces 2018, 10, 8066−8076

(22) Seredych, M.; Łoś, S.; Giannakoudakis, D. A.; Rodríguez-Castellón, E.; Bandosz, T. J. Photoactivity of g-C_3N_4/S-doped porous carbon composite: synergistic effect of composite formation. *ChemSusChem* **2016**, *9*, 795−799.
(23) Jagiello, J.; Olivier, J. P. 2D-NLDFT Adsorption Models for Carbon Slit-Shaped Pores with Surface Energetical Heterogeneity and Geometrical Corrugation. *Carbon* **2013**, *55*, 70−80.
(24) Jagiello, J.; Olivier, J. P. Carbon Slit Pore Model Incorporating Surface Energetical Heterogeneity and Geometrical Corrugation. *Adsorption* **2013**, *19* (2), 777−783.
(25) Jagiello, J. *SAIEUS*, version 2.1; Micromeritics Instrument Corp.: Norcross, GA, 2012; http://www.nldft.com/.
(26) Bandosz, T. J.; Jagiello, J.; Contescu, C.; Schwarz, J. A. Characterization of the Surfaces of Activated Carbons in Terms of Their Acidity Constant Distributions. *Carbon* **1993**, *31* (7), 1193−1202.
(27) Jagiello, J. Stable numerical solution of the adsorption integral equation using splines. *Langmuir* **1994**, *10*, 2778−2785.
(28) Jagiello, J.; Bandosz, T. J.; Schwarz, J. A. Carbon Surface Characterization in Terms of Its Acidity Constant Distribution. *Carbon* **1994**, *32* (5), 1026−1028.
(29) Florent, M.; Giannakoudakis, D. A.; Bandosz, T. J. Mustard Gas Surrogate Interactions with Modified Porous Carbon Fabrics: Effect of Oxidative Treatment. *Langmuir* **2017**, *33*, 11475−11483.
(30) Pei, J.; Zhang, J. S. On the performance and mechanisms of formaldehyde removal by chemi-sorbents. *Chem. Eng. J.* **2011**, *167*, 59−66.
(31) Lee, K. J.; Miyawaki, J.; Shiratori, N.; Yoon, S.; Jang, J. Toward an effective adsorbent for polar pollutants: Formaldehyde adsorption by activated carbon. *J. Hazard. Mater.* **2013**, *260*, 82−88.
(32) Zhao, X.; Zhang, Q.; Chen, C.-M.; Zhang, B.; Reiche, S.; Wang, A.; Zhang, T.; Schlogl, R.; Su, D. S. Aromatic sulfide, sulfoxide, and sulfone mediated mesoporous carbon monolith for use in super-capacitor. *Nano Energy* **2012**, *1*, 624−630.
(33) Blicke, F. F. *The Mannich Reaction. Organic Reactions*; Wiley Online Library, 2011.
(34) Matsuo, Y.; Nishino, Y.; Fukutsuka, T.; Sugie, Y. Removal of formaldehyde from gas phase by silylated graphite oxide containing amino groups. *Carbon* **2008**, *46*, 1162−1163.
(35) McIntyre, J. E. *Synthetic Fibres: Nylon, Polyester, Acrylic, Polyolefin*, 1st ed.; Woodhead: Cambridge, 2005.
(36) Stöhr, B.; Boehm, H. P.; Schlögl, R. Enhancement of the catalytic activity of activated carbons in oxidation reactions by thermal treatment with ammonia or hydrogen cyanide and observation of a superoxide species as a possible intermediate. *Carbon* **1991**, *29*, 707−720.
(37) Strelko, V. V.; Kuts, V. S.; Thrower, P. A. On the mechanism of possible influence of heteroatoms of nitrogen, boron and phosphorus in a carbon matrix on the catalytic activity of carbons in electron transfer reactions. *Carbon* **2000**, *38*, 1499−503.
(38) Möller, D. *Chemistry of the Climate System*; Walter de Gruyter: Berlin, 2010.
(39) Papalos, J. G. Condensation products of aromatic sulphonlc acids with formaldehyde. European Patent Application 0073606 A, 1982.
(40) Law, R. E., Sulfonated aromatic-formaldehyde condensation products. US patent 3954677 A, 1976.

DOI: 10.1021/acsami.7b19519
ACS Appl. Mater. Interfaces 2018, 10, 8066−8076

IV

Fuel 221 (2018) 374–379

Contents lists available at ScienceDirect

Fuel

journal homepage: www.elsevier.com/locate/fuel

Full Length Article

Highlighting the effect of the support during H_2S adsorption at low temperature over composite Zn-Cu sorbents

S. Cimino[a,*], L. Lisi[a], G. de Falco[a,b], F. Montagnaro[b], M. Balsamo[c], A. Erto[c]

[a] Istituto di Ricerche sulla Combustione, Consiglio Nazionale delle Ricerche, Piazzale Vincenzo Tecchio 80, 80125 Napoli, Italy
[b] Dipartimento di Scienze Chimiche, Università degli Studi di Napoli Federico II, Complesso Universitario di Monte Sant'Angelo, 80126 Napoli, Italy
[c] Dipartimento di Ingegneria Chimica, dei Materiali e della Produzione Industriale, Università degli Studi di Napoli Federico II, Piazzale Vincenzo Tecchio 80, 80125 Napoli, Italy

ARTICLE INFO

Keywords:
Purification
Reactive adsorption
Gas cleaning
Supported mixed oxides
Hydrogen sulphide

ABSTRACT

Reactive adsorption of hydrogen sulphide (H_2S) from gaseous streams at room temperature with mixed Zn and Cu active phase supported onto γ-alumina is dealt in this manuscript. Sorbents with a fixed total metal content and variable Cu:Zn ratios were prepared by impregnation of commercial γ-alumina spheres in order to investigate the role of the support and the possible synergic effect between the two metals on the adsorption mechanism and performance. H_2S (500–3000 ppmv in N_2) removal tests were run under dynamic conditions at 30 °C. Experimental techniques such as BET and pore size distribution by N_2-adsorption, SEM-EDX, XRD and DRIFT analysis were coupled for the characterization of fresh and spent sorbents. TPD/TPO experiments on saturated sorbents were performed to assess their regenerability and allowed the speciation of adsorbed sulphur species, testifying the complexity of the surface reactions and the effect of the support.

1. Introduction

The removal of H_2S from a fuel gas stream (crude petroleum, natural gas and biogas) represents a crucial stage in the industrial practice because the gas can corrode pipelines and poison catalysts used in fuel cells, even at a few ppm levels [1,2]. Many purification technologies have been proposed to remove H_2S, including chemical absorption into basic solutions (e.g. NaOH), membrane separation, biological filtration and adsorption [3–5]. Among them, adsorption is very attractive due to its potentially high removal efficiency/operating flexibility and generally low maintenance costs. The adoption of reactive nano-sized active phases (such as metal oxides, hydroxides, carbonates) dispersed onto highly porous substrates allows to attain H_2S capture performances typically higher than their unsupported form also at relatively low temperatures [5–10]. In particular, different porous supports such as activated carbons, mesoporous silicas (e.g., SBA-15, MCM-41) and three-dimensionally ordered macroporous structure (3DOM) have been employed to disperse ZnO and CuO or mixtures thereof for the selective removal of hydrogen sulphide from different gaseous streams [5,9–13]. Contextually, we have recently investigated the application of mixed Zn and Cu oxides supported onto a commercial activated carbon (at Cu:Zn molar ratios varying from 0:1 to 1:0) for H_2S reactive adsorption [9,10]. The beneficial role of Cu, even at low loadings, in determining a better utilization of the active phases has been ascribed to a reduction of the diffusional limitations in the lattice of the composite active phase and through the reacted overlayer. Moreover, the strong interaction of the composite oxides with the activated carbon support improved metal dispersion and significantly reduced the stability and the decomposition temperature of metal sulphates formed during reactive adsorption.

However, inorganic supports offer the advantage of high thermal stability and they are potentially regenerable after the sulphation stage via thermal treatments, usually carried out under oxygen/air streams [5,11]. Elyassi et al. observed that a sequence of oxidation (in a 5/95% O_2/N_2 mixture @ 400 °C) followed by reduction (in a 10/90% H_2/He mixture @ 400 °C to reduce $CuSO_4$ species) of a spent Cu-ZnO-SBA-15 sorbent was effective in fully restoring the H_2S capture capacity of the adsorbent [5]. On the other hand, the feasibility of a regeneration process for an exhaust sorbent is not trivial and might depend on different factors including the nature of the substrate/sulphation products, their chemical interactions and possible sintering phenomena of the active phase induced by the high temperature treatment. For instance, Wang et al. observed that the H_2S capture capacity at ambient temperature of CuO-SiO_2 3DOM sorbents was significantly reduced when performing the regeneration stage at 650 °C in air [13], due to the aggregation of CuO upon exposure to high temperature. Consequently, the analysis of the sorbent regenerability has to be verified case by case.

* Corresponding author.
E-mail address: stefano.cimino@cnr.it (S. Cimino).

https://doi.org/10.1016/j.fuel.2018.02.109
Received 19 December 2017; Received in revised form 5 February 2018; Accepted 15 February 2018
Available online 24 February 2018
0016-2361/

Following the path drawn in our previous papers, in which a carbonaceous support was employed for the dispersion of Zn/Cu mixed phases [9,10], this contribution aims at elucidating the role of a different support such as mesoporous γ-alumina spheres for the same active species for the H_2S capture process. H_2S adsorption tests onto the alumina both raw and functionalized with 8% wt. total metal content and various Cu:Zn proportions were carried out at room temperature under dynamic conditions in a lab-scale fixed-bed adsorption column. A thorough sorbent characterization was carried out by SEM, XRD and N_2 adsorption at −196 °C analyses. Finally, DRIFT analysis and temperature programmed desorption (TPD) or oxidation (TPO) tests were performed to shed light on the type of compounds formed upon the H_2S reactive adsorption process and to assess the sorbent regenerability.

2. Materials and method

The porous substrate adopted for the deposition of Zn- and Cu-based active phase was a commercial γ-Al_2O_3 (SASOL PURALOX 1-160, spheres with 1 mm diameter, $Al_2O_3 \geq 98\%$ wt.). The functionalization procedure included an impregnation step of alumina spheres (12.5 g) at ambient conditions with an aqueous solution (10 mL, 1.72 mol L^{-1}) of metal nitrates precursors ($Zn(NO_3)_2{\cdot}6H_2O$ and $Cu(NO_3)_2{\cdot}2.5H_2O$, Aldrich, respectively with purity of 99.3% and 98.6% wt.). Thereafter, the sorbents were dried at 120 °C in air and eventually calcined for 2 h at 250 °C, in analogy to our previous work in which the same precursors dispersed onto an activated carbon support were used [9]. In this case, the low calcination temperature allowed preventing the undesired formation of superficial metal aluminates [14 and refs. therein]. The nominal metal loading (Zn + Cu) was set at 8% wt., whereas the Cu:Zn atomic ratio was varied in the range 0:1–1:1. The sorbents were labelled as Cu_xZn_{1-x}/Als, with x representing the atomic fraction of Cu with respect to the total metal content.

The actual metal loading on the sorbents was verified by ICP-MS using an Agilent 7500 instrument. Scanning electron microscopy (SEM) was carried out with a FEI Inspect instrument equipped with an EDX probe. The textural properties of the sorbents were determined by N_2 adsorption at −196 °C from P/P_0 10^{-5} using a Quantachrome Autosorb 1-C (BET method for specific surface area, Barrett-Joyner-Halenda (BJH) method applied to the desorption branch for pore size distribution, PSD). XRD analysis was performed with a Bruker D2 Phaser diffractometer operated at diffraction angles ranging between 10° and 90°2θ with a scan rate of 0.02° s^{-1}.

H_2S dynamic adsorption tests at initial pollutant concentration ranging from 500 to 3000 ppmv in N_2 (90 SL h^{-1}) were carried out at 30 °C in a fixed-bed reactor using 5.0 g of either raw alumina spheres or functionalized sorbents. The dynamic evolution of H_2S concentration was measured by a continuous GAS 3240 R BIOGAS gas analyzer (GEIT Europe). H_2S adsorption capacity at saturation, ω_s [mmol g^{-1}], was determined through a material balance on H_2S over the adsorption column, leading to the following expression:

$$\omega_s = \frac{Q^t C^{in}_{H_2S} \rho_{H_2S}}{m M_{H_2S}} \int_0^{t^*} \left(1 - \frac{C^{out}_{H_2S}(t)}{C^{in}_{H_2S}}\right) \mathrm{d}t \quad (1)$$

where Q^t [L s^{-1}] is the total gas flow rate, $C^{in}_{H_2S}$ [−] is the H_2S volumetric fraction in the gas feed, $C^{out}_{H_2S}$ [−] is the H_2S volumetric fraction at the bed outlet, ρ_{H_2S} [mg L^{-1}] is the H_2S density (at 30 °C and 1 bar) while M_{H_2S} [mg $mmol^{-1}$] is its molecular weight; m [g] is the sorbent dose and t^* [s] represents the saturation time for which $C^{out}_{H_2S}/C^{in}_{H_2S} \approx 0.99$.

Temperature Programmed Desorption (TPD) tests were carried out in a lab-scale rig [9], in order to analyze the residual presence of nitrates on the calcined sorbents (TPD-NO_x) and to shed light on the species formed upon the sulphidation process, while evaluating the thermal regenerability of the spent sorbents. Temperature Programmed Oxidation (TPO) tests were also performed on spent sorbents in order to further explore their thermal regenerability. To this end, a known sorbent amount (20–150 mg) was heated at 10 °C min^{-1} up to 800 °C (620 °C for TPD-NO_x tests) under a N_2 flow (30 SL h^{-1}); TPO tests were performed under a flow of air or O_2 (5000 ppmv) in N_2. Gas analysis was performed by means of two continuous analyzers with cross sensitivity corrections: i) an ABB Optima Advance Limas 11 UV for NO and NO_2; ii) an ABB Optima Advance Limas 11 UV for the simultaneous measurement of H_2S (0–300 ppmv) and SO_2 (0–100 ppmv) concentrations.

DRIFT experiments were performed on a Perkin Elmer Spectrum GX spectrometer equipped with a liquid-N_2 cooled MCT detector with a spectral resolution of 4 cm^{-1} averaging each spectrum over 50 scans. Samples were diluted in KBr (2%) and about 100 mg finely grounded powder was placed in the DRIFT cell equipped with a ZnSe window and connected to gas lines. Samples were pre-treated for 40 min at 120 °C under Ar flow and then cooled down to 40 °C.

3. Results and discussion

The elemental analysis performed on functionalized sorbents showed that the total metal content (Cu + Zn) was in the range 8.2 ± 0.15% wt., in line with the target loading. SEM-EDX analysis carried out on the sorbent containing an equimolar Cu:Zn ratio (Fig. 1) highlighted a homogeneous distribution of both the elements across the section of the spherical alumina particles.

BET surface area values obtained for the tested sorbents are listed in Table 1. Results indicate that the deposition of the active phases determines a nearly 10% reduction of the surface area for functionalized sorbents with respect to the bare substrate, whereas BET values for Cu_xZn_{1-x}/Als sorbents (157 ± 1 m^2 g^{-1}) are not influenced by the Cu:Zn ratio.

Fig. 2 shows the PSD for both raw alumina and $Cu_{0.5}Zn_{0.5}$/Als sorbents. Data highlight that the functionalization treatment does not affect the PSD of the parent support and induces a minor reduction of its pore volume, thus confirming a homogenous dispersion of the active phases onto the mesoporous alumina.

Fig. 3 depicts the XRD patterns of the raw and functionalized alumina sorbents together with the diffraction spectrum of the $Cu_{0.5}Zn_{0.5}$/Als sample after saturation with H_2S at 3000 ppmv and 30 °C.

The support spheres show the typical diffraction peaks of γ-alumina. The XRD patterns for $Cu_0Zn_{1.0}$/Als and $Cu_{0.1}Zn_{0.9}$/Als are equivalent to the one of the parent substrate, probably due to the low content of the active phases associated to a high dispersion and/or poor crystallinity.

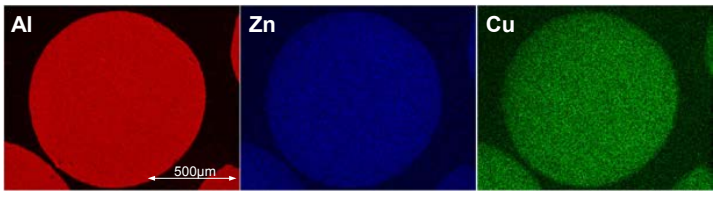

Fig. 1. SEM-EDX maps in false colours showing the distribution of the elements (Al, Zn and Cu) across the section of a spherical particle of $Cu_{0.5}Zn_{0.5}$/Als sorbent.

Table 1
BET surface area and adsorption/desorption performances of the tested sorbents. Inlet conditions: T = 30 °C, P = 1 bar.

Sorbent	BET surface area [$m^2\,g^{-1}$]	t_{br} [s]	ω_s [mmol g^{-1}]	$\omega_{des}^{600\,°C}$ [mmol g^{-1}]	$\omega_{des}^{800\,°C}$ [mmol g^{-1}]	ω_{des}^{TPO} [mmol g^{-1}]
Als	174	65	0.09	0.09	0.09	–
$Cu_0Zn_{1.0}$/Als	156	293	0.68	0.24	0.58	–
$Cu_{0.05}Zn_{0.95}$/Als	156	296	0.69	0.28	0.58	–
$Cu_{0.1}Zn_{0.9}$/Als	157	293	0.73	0.25	0.58	–
$Cu_{0.25}Zn_{0.75}$/Als	157	326	0.74	0.25	0.62	–
$Cu_{0.5}Zn_{0.5}$/Als	157	362	0.82	0.38	0.74	0.33[a]
Darco AC*	641	198	0.20	0.20	–	–
$Cu_{0.5}Zn_{0.5}$/AC*	570	674	1.46	0.59	–	1.46[a]

* After Balsamo et al. [9].
[a] TPO test performed adopting 5000 ppmv of O_2 in N_2.

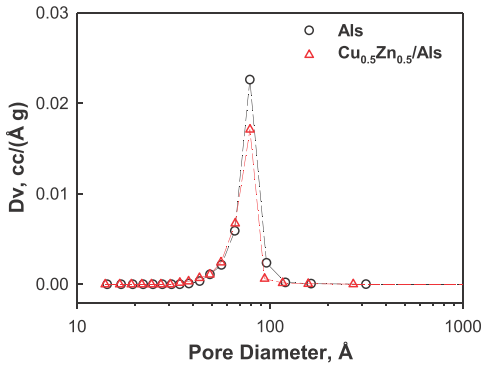

Fig. 2. BJH pore size distribution for the raw alumina spheres (Als) and $Cu_{0.5}Zn_{0.5}$/Als sorbent.

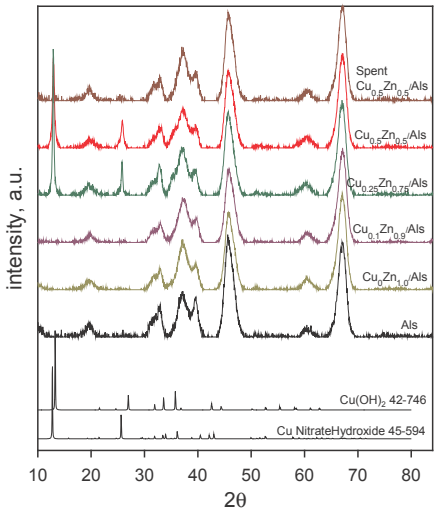

Fig. 3. XRD patterns of the raw alumina spheres (Als) and fresh Cu_xZn_{1-x}/Als sorbents. Diffraction spectrum of $Cu_{0.5}Zn_{0.5}$/Als sorbent saturated with H_2S at 3000 ppmv and 30 °C and patterns of $Cu(OH)_2$ and Cu nitrate-hydroxide reference compounds are also shown.

An increase in the copper content determines the occurrence of two new peaks at 2θ = 12.9° and 25.7° ascribable to the formation of $Cu_2(OH)_3NO_3$ (ICDD: 45-594) and to a minor contribution of $Cu(OH)_2$ (ICDD: 42-746). Note that the presence of Zn hydroxynitrate (ICDD: 70-1361) is also possible, having a spectrum quite similar to the corresponding Cu phase. For the spent $Cu_{0.5}Zn_{0.5}$/Als sorbent, the Cu-related peaks disappear due to the reaction with H_2S during adsorption though there is no clear evidence of the formation of new crystalline phases, such as ZnS and CuS nor $ZnSO_4$ and $CuSO_4$.

These results contrast with previous thermogravimetric studies on the thermal decomposition in air of d-metal nitrates supported on alumina [15], showing that (supported) copper nitrate started to decompose at ca. 60 °C via a multi-step process that was completed for $T \leq 225$ °C, whereas its bulk form was slightly more stable and required 250 °C to decompose completely. The residual presence of copper hydroxynitrates on the alumina surface after calcination at 250 °C could be possibly related to the stabilization of those solid intermediate species during the drying of sorbents at 120 °C. Moreover, the absence of specific XRD diffraction peaks cannot exclude the occurrence of analogue amorphous Zn hydroxynitrates, which, on the contrary, should be favored considering the slightly higher decomposition temperature recorded for Zn nitrate supported on alumina (250–300 °C) if compared to Cu nitrate [15].

Therefore, TPD of nitrogen oxides (TPD-NO_x) was carried out in order to verify the residual presence of (hydroxy)nitrates on the

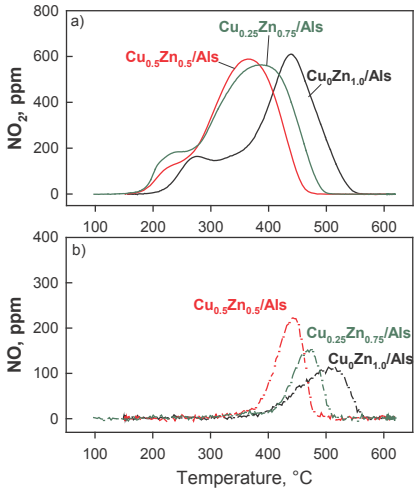

Fig. 4. TPD-NO_x results for Cu_xZn_{1-x}/Als sorbents after calcination in N_2 at 250 °C.

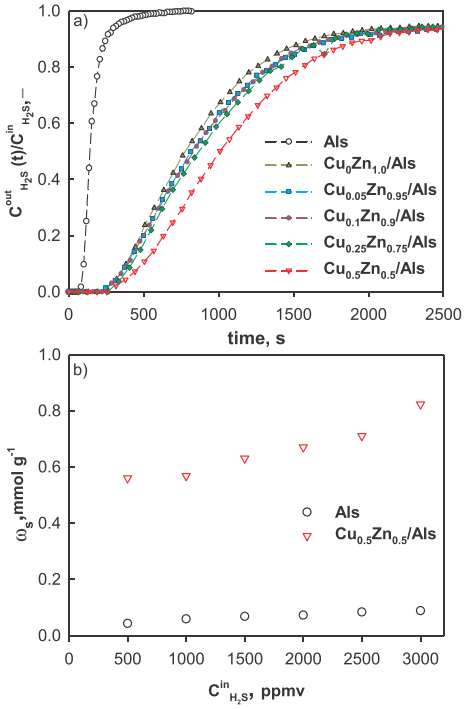

Fig. 5. a) H_2S breakthrough curves for Cu_xZn_{1-x}/Als sorbents and raw alumina spheres. Inlet conditions: C^{in}_{H2S} = 3000 ppmv, T = 30 °C, P = 1 bar. b) H_2S adsorption isotherms on raw alumina and $Cu_{0.5}Zn_{0.5}$/Als sorbent. T = 30 °C, P = 1 bar.

functionalized alumina sorbents after calcination. Fig. 4 shows the NO_2 and NO concentration patterns of selected alumina-based sorbents under N_2 flux during TPD-NO_x tests. In the case of $Cu_0Zn_{1.0}$/Als it is possible to observe that the NO_2 desorption pattern is made by a lower peak centred at approximately 270 °C and a second main peak with a maximum at approximately 450 °C. A minor production of NO is also detected (peak at 510 °C). The presence of copper in the active phase determines a clear shift of TPD-NO_x profiles towards lower temperatures together with a broadening of the main NO_2 peak, likely ascribable to the overlapping of signals associated with the decomposition of Zn and Cu (hydroxy)nitrates. The experimental results confirm that Cu and Zn (hydroxy)nitrates formed on alumina display a significantly higher stability than previously reported, requiring temperatures in excess of 350 °C and 450 °C, respectively, to be fully decomposed.

Fig. 5a reports the breakthrough curves at 3000 ppmv of H_2S and 30 °C obtained for Cu_xZn_{1-x}/Als and Als raw sorbents. Values of breakpoint time t_{br} (for which $C^{out}_{H2S}/C^{in}_{H2S} \approx 0.05$) and saturation adsorption capacity ω_s determined from dynamic concentration profiles are summarized in Table 1, in which the data obtained for representative activated carbon-based sorbents (cf. Balsamo et al. [9]) are also included for comparison. The experimental data show that the functionalization treatment significantly enhances the adsorption capacity of the raw alumina, and the performance improvement is monotonic with the Cu content in the active phase under the investigated compositional range, in accordance with our recent findings concerning the dispersion of mixed Cu–Zn onto Darco® activated carbon [9]. In more detail, for the $Cu_{0.5}Zn_{0.5}$/Als sorbent the adsorption capacity is 9 times greater than the corresponding of raw alumina, while $Cu_0Zn_{1.0}$/Als exhibits a ω_s value 7.5-folds the one retrieved for Als. Moreover, a higher value for ω_s was found with respect to other Cu-containing inorganic based sorbents such as Cu-3DOM [13] under dry conditions. In addition, adsorption tests carried out with a pre-humidified feed stream (50% relative humidity at 30 °C) did not show any significant effect of water vapour on the H_2S capture mechanism and capacity of the $Cu_{0.5}Zn_{0.5}$/Als sorbent.

The increase in the adsorption capacity along with the copper content in the Cu_xZn_{1-x}/Als sorbents could be partially ascribable to the formation of Cu hydroxyde and hydroxynitrate species which are more reactive phases for H_2S capture, as testified by a comparison of XRD patterns between the $Cu_{0.5}Zn_{0.5}$/Als sorbent before and after adsorption (cf. Fig. 3). The effect of the functionalization can be also observed in terms of the breakpoint time, which increased from 65 s for the raw alumina to 293 and 362 s for the $Cu_0Zn_{1.0}$/Als and $Cu_{0.5}$ $Zn_{0.5}$/Als sorbents, respectively.

Fig. 5b presents the results in terms of the H_2S saturation capacities measured at 30 °C with an inlet H_2S concentration in the range 500–3000 ppmv, in comparison with the results obtained on the raw alumina. Across the entire investigated range of concentrations, $Cu_{0.5}Zn_{0.5}$/Als showed a much larger H_2S adsorption capacity than the raw alumina support. For both the materials, ω_s increased slightly with the H_2S partial pressure, suggesting a small contribution of physisorption on the alumina support, while most of the H_2S capture on $Cu_{0.5}Zn_{0.5}$/Als can be ascribed to the chemical reactions occurring with the composite Cu–Zn active phase.

Finally, a comparison between the alumina and activated carbon sorbents both containing an equimolar Cu–Zn mixture (Table 1) witnesses a significantly higher H_2S capture performance in the case of the carbonaceous support, with $\omega_s \approx 1.8$ times larger for $Cu_{0.5}Zn_{0.5}$/AC with respect to $Cu_{0.5}Zn_{0.5}$/Als. Considering the minor differences in adsorption capacity values obtained for the parent substrates, a more efficient exploitation of the active phases when dispersed on the activated carbon is likely linked to: i) its remarkably higher surface area allowing a greater dispersion of the active phase nanoparticles, also ending up in reduced H_2S diffusion limitations in the capture process; ii) the exhaustive formation of ZnO and CuO which, in contrast, is hindered on the alumina support due to the stabilization of metal hydroxynitrates species.

TPD tests were carried out in order to study the type of S-bearing species formed during the capture process and the thermal regenerability of functionalized sorbents. It is important to underline that all Cu_xZn_{1-x}/Als sorbents released non-negligible amounts of H_2S, but the total quantity of sulphur desorbed as H_2S compared to SO_2 was much lower (at least one order of magnitude). Consequently, it is confirmed that the capture process involved a minor contribution of physical adsorption (sulphur released as H_2S) coupled with reactive adsorption. Notably, no H_2S desorption was observed from spent Cu_xZn_{1-x}/AC nor by their raw AC support [9], unveiling a higher reactivity of the activated carbon support that also adsorbed twice as much H_2S as the mesoporous alumina. Fig. 6 reports a comparison of TPD patterns obtained for spent $Cu_{0.5}Zn_{0.5}$/Als and $Cu_{0.5}Zn_{0.5}$/AC as best-performing sorbents for each support investigated. It is herein recalled that the peaks observed for $Cu_{0.5}Zn_{0.5}$/AC and centred at around 330 °C and 500 °C can be ascribed to the decomposition of $CuSO_4$ and $ZnSO_4$ dispersed onto the activated carbon, respectively [9]. The SO_2 TPD profile obtained for $Cu_{0.5}Zn_{0.5}$/Als appears more complex and characterized by different decomposition peaks starting from ca. 80 °C and occurring in the whole temperature range investigated. The main signal extending in the 500–800 °C temperature range is likely to embody the partial decomposition of copper and zinc sulphates, as suggested by the TPD patterns obtained for the reference bulk materials (Fig. 6). The oxidation of H_2S to form several S-bearing compounds can occur in absence of molecular oxygen during the reactive capture process and/or the thermal treatment stage, and is possibly promoted by various oxygen sources from the sorbent including Cu/Zn (hydro)oxides, metal

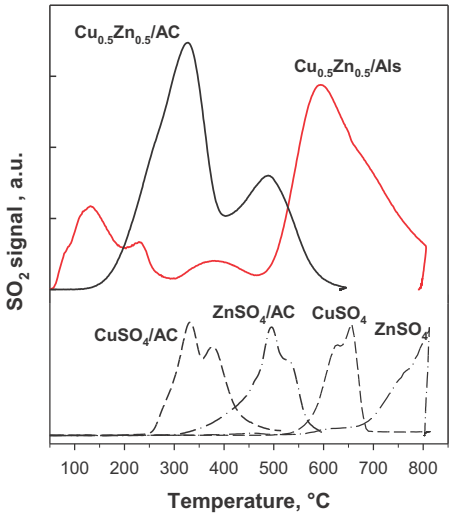

Fig. 6. SO_2 release from spent $Cu_{0.5}Zn_{0.5}$/Als and $Cu_{0.5}Zn_{0.5}$/AC sorbents previously saturated with H_2S (3000 ppmv in N_2, $T = 30$ °C, $P = 1$ bar) during TPD tests under N_2 flow. SO_2 TPD profiles for reference samples of $CuSO_4$ and $ZnSO_4$ in bulk or supported on activated carbon are also included for comparison purposes (dashed lines).

(hydroxy)nitrates and surface hydroxyl groups of the alumina substrate. In particular, the TPD signal at lower temperature could be ascribed to the desorption of SO_2 directly formed in the capture stage [9] or produced during the thermal treatment by oxidation of more reduced S species (such as sulphides or elemental sulphur). It is highlighted that other authors in the literature have recently verified the formation of metal sulphates (besides sulphides and elemental sulphur) upon low temperature desulphurization [10 and Refs. therein, 13]. For example, Wang et al. detected the presence of $CuSO_4$ by means of XPS analysis for spent CuO dispersed onto 3DOM sorbents [13].

Table 1 reports the total amounts of sulphur released from Cu_xZn_{1-x}/Als sorbents during the TPD under inert flow (ω_{des}) that were calculated by integration of the corresponding TPD profiles.

It is observed that all the materials released most of the adsorbed sulphur (between 80 and 90%) after thermal treatment at 800 °C. The value $\omega_{des}^{800\,°C}$ generally increases along with the copper content, in good agreement with the easier thermal decomposition of bulk $CuSO_4$ with respect to $ZnSO_4$ (Fig. 6). However, limiting the thermal treatment up to 600 °C to prevent a significant formation of metal aluminates, only half of the sulphur content can be removed from the best performing $Cu_{0.5}Zn_{0.5}$/Als sorbent, and even less from Zn-richer materials ($\omega_{des}^{600\,°C}$), once again due to the stability of the corresponding metal sulphates.

For the same regeneration temperature (600 °C) the carbon-based $Cu_{0.5}Zn_{0.5}$/AC sorbent released a significantly higher amount of sulphur (Table 1). This is due to a strong interaction of the activated carbon support with the metal sulphates formed during the reactive adsorption of H_2S, that reduces the stability of both $CuSO_4$ and $ZnSO_4$ [10] thus lowering their decomposition temperatures by as much as 300 °C (Fig. 6).

Fig. 7 shows the results of TPO tests in the presence of 5000 ppmv of O_2 in N_2 or in air, and TPD test carried out on the spent $Cu_{0.5}Zn_{0.5}$/Als sample. Results testify that the presence of O_2 in the desorbing flow causes an evident decrease of the amount of sulphur released as SO_2, and the effect is more pronounced for an increase in the oxygen concentration. The major differences in SO_2 profiles for TPO and TPD tests occur for the high temperature band (500–800 °C), previously ascribed

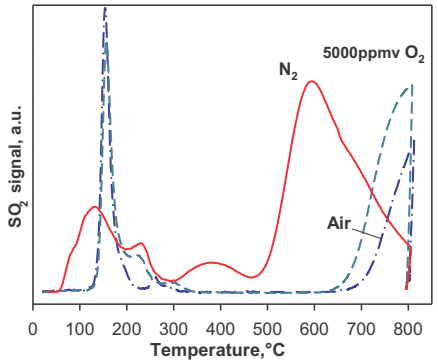

Fig. 7. SO_2 release from H_2S-saturated $Cu_{0.5}Zn_{0.5}$/Als during TPD and TPO tests (run under 5000 ppmv of O_2 in N_2 or under air flow).

to the metal sulphates decomposition. In this context, the presence of O_2 is likely to thermally delay the decomposition of sulphates (with an onset temperature shifted towards 700 °C), being oxygen one of the decomposition products [16]. Additionally, the formation of more thermally stable products due to the reaction of sulphates with the alumina substrate under oxidizing conditions cannot be ruled out.

Wang et al. [13] also detected two SO_2 emission peaks at low (~200 °C) and high (> 600 °C) temperature in their TG-MS experiments under air on Cu-based 3DOM sorbents. They assigned the first SO_2 emission to the restoration of CuO through CuS oxidation, and the second emission to the decomposition of sulphates, previously formed by sulphides oxidation at about 300 °C, although they observed the presence of sulphates already on the saturated sorbents.

From a quantitative point of view, the amount of sulphur desorbed when adopting 5000 ppmv O_2 in N_2 is more than halved when compared to the value retrieved from the TPD test (cf. ω_{des}^{TPO} and $\omega_{des}^{800\,°C}$ in Table 1). Finally, it is highlighted that in the case of Cu_xZn_{1-x}/AC sorbents, the presence of oxygen during the desorption test produces a complete release of sulphur with an associated combustion of the substrate, as expected [9].

The stabilization of metal (hydroxy)nitrates on virgin sorbents and the formation of sulphates during the H_2S reactive adsorption was confirmed by DRIFT analysis. In Fig. 8, DRIFT spectra of fresh calcined $Cu_0Zn_{1.0}$/Als and $Cu_{0.5}Zn_{0.5}$/Als sorbents are reported. Indeed, in addition to the large band at 3500–3600 cm^{-1}, typical of hydroxyls of hydrated alumina [17], a sharp band at 1385 cm^{-1}, assigned to nitrate species [18], confirms that the calcination temperature (250 °C) was not high enough to completely decompose nitrates from precursors salts, in agreement with XRD and TPD-NO_x results. Nevertheless, the nitrate band is also ascribable to aluminium nitrate [19] and well matches with the good stability of this compound, which turns into aluminium oxide only at T > 350 °C. Furthermore, the absence of the nitrate band in the AC-supported sorbents with the same copper and zinc loadings [9] suggests that the same calcination temperature was sufficient to form copper and zinc oxides dispersed on active carbon. On the other hand, alumina strongly interacts with the supported transition metals modifying the properties of dispersed nitrate salts. Following H_2S adsorption, the nitrate band appears almost unchanged, whereas new signals appear in the 1050–1200 cm^{-1} region, quite strong for the sorbent with 50% Zn substitution for Cu but weak for $Cu_0Zn_{1.0}$/Als, that can be reasonably attributed to the formation of sulphate groups on metals [18] but also on the alumina support [20,21]. This band is typical of both sulphate reference compounds, and its low intensity in the spectrum of spent $Cu_0Zn_{1.0}$/Als sorbent suggests that the formation of copper sulphate prevails. Nevertheless, some sulphation of alumina

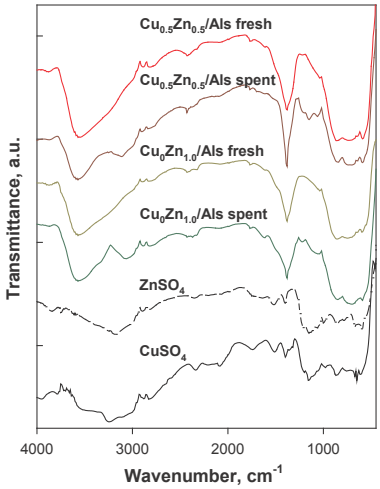

Fig. 8. DRIFT spectra of fresh and spent Cu_xZn_{1-x}/Als sorbents and of bulk $CuSO_4$ and $ZnSO_4$ reference compounds.

surface cannot be ruled out [21]. For both the spent sorbents, a new band is superimposed to that corresponding to alumina hydroxyls in the region 3000–3700 cm^{-1}, being centred at 3065 cm^{-1} for $Cu_0Zn_{1.0}$/Als and at 3110 cm^{-1} for $Cu_{0.5}Zn_{0.5}$/Als, respectively. Reference $CuSO_4$ and $ZnSO_4$ show bands in the same region: basic copper sulphate monohydrate provides signals at 3300–3400 cm^{-1} [22], whilst a band at 3072 cm^{-1} is attributed to the symmetric stretching mode of water molecule for $ZnSO_4{\cdot}7H_2O$ [23], thus confirming that some zinc sulphate is also formed upon H_2S adsorption.

These results generally demonstrate that the copper and zinc sulphate formation occurs directly by oxidation of H_2S during the capture process when alumina is used as support for mixed Cu–Zn active phases, likely at the expense of surface –OH groups from metal hydroxides and Al_2O_3, which are reduced in the spent sorbents compared to fresh samples, whereas residual nitrate groups seem to be poorly affected.

4. Conclusion

Dynamic adsorption tests of H_2S in N_2 were carried out at room temperature in a lab-scale plant based on a fixed-bed column of inorganic sorbents prepared starting from γ-alumina spheres functionalized with mixed Cu and Zn nitrates in different proportions ranging from 0:1 to 1:1. XRD, DRIFT and TPD-NO_x studies on fresh sorbents calcined at 250 °C revealed that the active phase comprised a mixture of metal (hydro)oxides and hydroxynitrates, because of a strong stabilizing effect of the alumina support against the complete decomposition of metal nitrates precursors during the calcination step.

The deposition of the active phase on γ-alumina spheres determined a minor reduction of the pore size distribution and BET surface area, proportional to the weight increase, testifying the high dispersion of the active phase that, on the contrary, strongly enhanced the H_2S adsorption capacity of the raw support. The partial substitution of Zn with Cu induced a progressive increase in the H_2S sorption capacity, which, on the other hand, was poorly affected by the inlet H_2S concentration in the range 500–3000 ppmv. At the maximum copper content explored, $Cu_{0.5}Zn_{0.5}$/Als sorbent provided the best H_2S adsorption capacity (0.82 mmol g^{-1}) under both dry and humid conditions.

Moreover, a comparison with previous published data clearly showed that a homologous sorbent, with identical nominal active phase composition but supported on an activated carbon ($Cu_{0.5}Zn_{0.5}$/AC), had a significantly higher breakpoint time and adsorption capacity at saturation than $Cu_{0.5}Zn_{0.5}$/Als. This was likely due to its remarkably larger surface area enhancing dispersion of the active phase nanoparticles, but also to the stabilization of metal hydroxynitrates on the surface of the alumina support, which turned out to be less reactive than the corresponding oxides formed on the activated carbon.

The reactive adsorption mechanism of H_2S was investigated through DRIFT analysis and TPD of H_2S and SO_2 from spent sorbents. Apart from small quantities of H_2S physisorbed on the alumina, most of the H_2S captured at room temperature is oxidized to Cu and Zn sulphate species, showing decomposition temperatures comparable to those of their reference bulk sulphates. As a consequence, the complete desorption of sulphur from spent materials in the form of SO_2 requires temperatures ≥800 °C under inert flow, which poses serious issues on the thermal regenerability of the Cu_xZn_{1-x}/Als sorbents, due to costs and undesired transformation of the active phase into metal aluminate species. Furthermore, TPO tests showed that the presence of O_2 in the atmosphere tends to inhibit the thermal decomposition of the metal sulphates, being oxygen one of the decomposition products.

References

[1] Stirling D. The sulfur problem: cleaning up industrial feedstocks. Cambridge: Royal Society of Chemistry; 2000.
[2] Nam S, Hur KB, Lee NH. Effects of hydrogen sulfide and siloxane on landfill gas utility facilities. Environ Eng Res 2011;16:159–64.
[3] Yuan W, Bandosz TJ. Removal of hydrogen sulfide from biogas on sludge-derived adsorbents. Fuel 2007;86:2736–46.
[4] Ryckebosch E, Drouillon M, Vervaeren H. Techniques for transformation of biogas to biomethane. Biomass Bioenergy 2011;35:1633–45.
[5] Elyassi B, Al Wahedi Y, Rajabbeigi N, Kumar P, Jeong JS, Zhang X, et al. A high-performance adsorbent for hydrogen sulfide removal. Micropor Mesopor Mater 2014;190:152–5.
[6] Jiang D, Su L, Ma L, Yao N, Xu X, Tang H, et al. Cu–Zn–Al mixed metal oxides derived from hydroxycarbonate precursors for H_2S removal at low temperature. Appl Surf Sci 2010;256:3216–23.
[7] Bezverkhyy I, Skrzypski J, Safonova O, Bella JP. Sulfidation mechanism of pure and Cu-doped ZnO nanoparticles at moderate temperature: TEM and in Situ XRD studies. J Phys Chem C 2012;116(27):14423–30.
[8] Montes D, Tocuyo E, González E, Rodríguez D, Solano R, Atencio R, et al. Reactive H_2S chemisorption on mesoporous silica molecular sieve-supported CuO or ZnO. Micropor Mesopor Mater 2013;168:111–20.
[9] Balsamo M, Cimino S, de Falco G, Erto A, Lisi L. ZnO-CuO supported on activated carbon for H_2S removal at room temperature. Chem Eng J 2016;304:399–407.
[10] de Falco G, Montagnaro F, Balsamo M, Erto A, Deorsola FA, Lisi L, et al. Synergic effect of Zn and Cu oxides dispersed on activated carbon during reactive adsorption of H_2S at room temperature. Micropor Mesopor Mater 2018;257:135–46.
[11] Dhage P, Samokhvalov A, Repala D, Duin CE, Bowman M, Tatarchuk BJ. Copper-promoted ZnO/SiO_2 regenerable sorbents for the room temperature removal of H_2S from reformate gas streams. Ind Eng Chem Res 2010;49(18):8388–96.
[12] Girard V, Baudot A, Chiche D, Bazer-Bachi D, Bounie C, Geantet C. Rational selection of single oxide sorbents for syngas desulfurization regenerable at reduced temperature: thermochemical calculations and experimental study. Fuel 2014;128:220–30.
[13] Wang J, Wang L, Fan H, Wang H, Hu Y, Wang Z. Highly porous copper oxide sorbent for H_2S capture at ambient temperature. Fuel 2017;209:329–38.
[14] Iamarino M, Chirone R, Lisi L, Pirone R, Salatino P, Russo G. Cu/γ-Al_2O_3 catalyst for the combustion of methane in a fluidized bed reactor. Catal Today 2002;75:317–24.
[15] Małecka B, Łącz A, Drożdż E, Małecki A. Thermal decomposition of d-metal nitrates supported on alumina. J Therm Anal Calorim 2015;119:1053–61.
[16] Dunn JG, Muzenda C. Thermal oxidation of covellite (CuS). Thermochim Acta 2001;369:117–23.
[17] Al-Abadleh HA, Grassian VH. FT-IR Study of water adsorption on aluminum oxide surfaces. Langmuir 2003;19:341–7.
[18] Miller FA, Wilkins CH. Infrared spectra and characteristic frequencies of inorganic ions. Anal Chem 1952;24:1253–94.
[19] Myronyuk IF, Mandzyuk VI, Sachko VM, Gun'ko VM. Structural and morphological features of disperse alumina synthesized using aluminum nitrate nonahydrate. Nanoscale Res Lett 2016;11:153.
[20] Saur O, Bensitel M, Mohammed Saad AB, Lavalley JC, Tripp CP, Morrow BA. The structure and stability of sulfated alumina and titania. J Catal 1986;99:104–10.
[21] Kloprogge JT, Ruan H, Frost RL. Near-infrared spectroscopic study of basic aluminum sulfate and nitrate. J Material Sci 2001;36:603–7.
[22] Uzunov I, Klissurski D, Teocharov L. Thermal decomposition of basic copper sulphate monohydrate. J Therm Anal 1995;44:685–96.
[23] Saha JK, Podde J. Crystallization of zinc sulphate single crystals and its structural, thermal and optical characterization. J Bangladesh Acad Sci 2011;35:203–10.

V

Carbon 138 (2018) 283–291

Contents lists available at ScienceDirect

Carbon

journal homepage: www.elsevier.com/locate/carbon

Role of sulfur and nitrogen surface groups in adsorption of formaldehyde on nanoporous carbons

Giacomo de Falco [a, b, c], Wanlu Li [a], Stefano Cimino [b], Teresa J. Bandosz [a, *]

[a] Department of Chemistry and Biochemistry, The City College of New York, New York, NY 10031, USA
[b] Institute of Research on Combustion, National Research Council, IRC-CNR, Piazzale Vincenzo Tecchio 80, 80125 Napoli, Italy
[c] Department of Chemical Sciences, University of Naples Federico II, Complesso Universitario di Monte Sant'Angelo, 80126 Napoli, Italy

ARTICLE INFO

Article history:
Received 16 April 2018
Received in revised form
22 May 2018
Accepted 29 May 2018
Available online 7 June 2018

ABSTRACT

S-doped nanoporous carbon, and commercial activated carbons, as received or modified by an incorporation of sulfur and nitrogen functional groups to their surface, were tested as low concentration formaldehyde (1 ppmv) adsorbents. The breakthrough capacities, in dry and wet conditions, were measured. The surface properties of the samples were evaluated using nitrogen sorption, potentiometric titration, thermal analysis, and XPS. The incorporation sulfur and/or nitrogen functional groups led to an increase in the amount of HCHO removed from air. These group (pyridines, amines, thiophenes, sulfones) when located in large pores increase the utilization of the carbon surface for formaldehyde adsorption providing chemical reactivity. In this aspect, rich in sulfur carbon of a relatively low surface was found as the most efficient formaldehyde adsorbent. Its HCHO adsorption capacity was 7.15×10^{-4} mg m^{-2} whereas on melamine modified carbon of a high surface area 4.23×10^{-4} mg m^{-2} were adsorbed. On the microporous carbon of basic nature reactions of HCHO with phenols block this carbon porosity and thus excluded the adsorption centers in ultramicropores for physical adsorption decreasing the adsorption capacity. Water in the system decreases the HCHO capacity between 10 and 30%, owing to its competitive adsorption on polar centers.

1. Introduction

An efficient removal of formaldehyde (HCHO) from indoor air remains one of the big industrial challenges of these days. For example, only in the USA up to 2 million workers are exposed every day to it [1]. HCHO is considered as one of the most dangerous gases for the respiratory system [2]. In indoor air, formaldehyde is found in carpet cleaners, medicines, cosmetics, adhesives, paper and plastics. Moreover, pressed wood products containing formaldehyde resins are often a significant source of formaldehyde in homes. Exposure to only 4 ppm HCHO causes irritation of a nose, throat, and eyes.

Formaldehyde has been classified as a human carcinogen, as it causes nasopharyngeal cancer, pulmonary damage and probably leukaemia [3]. As a consequence, the World Health Organization (WHO) has established its exposure limit at 0.08 ppm for 30 min [4].

Various approaches have been developed to purify air from HCHO including photo- and thermal catalytic oxidation [5–7], plasma technologies [8], and adsorption [9–11]. The removal of HCHO from air via adsorption offers numerous advantages related to the operating flexibility of this purification technology coupled with generally low costs. In particular, activated carbons (AC) are extensively used as adsorbents for removing HCHO from air because of their properties, such as a high surface area and surface chemistry that play an important role. As an example, Kumagai et al. studied the removal of 1 ppm of formaldehyde at room temperature using AC derived from heat treated rice husks [12]. The results showed that an increase in the carbonizing temperature, from 250 °C to 800 °C, led to an increase in the HCHO adsorption rate. In the case of sample treated at lower temperature (250 °C), it required more than 100 min to reduce the HCHO concentration to 0.5 ppm while the sample treated sample at 800 °C decreased the HCHO concentration to 0.5 ppm after 10 min. Wen et al. evaluated the adsorption performance of three commercial activated carbons, derived from coconut shells, wood and coal [13]. The measured formaldehyde adsorption capacities were between 7 and 8 mg g^{-1} at a HCHO concentration of 0.41 mg m^{-3}.

* Corresponding author.
E-mail address: tbandosz@ccny.cuny.edu (T.J. Bandosz).

https://doi.org/10.1016/j.carbon.2018.05.067
0008-6223/

In general, the introduction of N-groups to a carbon matrix was found to increase the HCHO adsorption capacity of commercial activated carbons [14–17]. As an example, An et al. explored the adsorption of 1 ppmv HCHO in N_2 at 30 °C on mesoporous activated carbon functionalized with sulfuric acid or ammonia [18]. The best adsorbent material was the activated carbon modified by NH_3. Its good performance was linked to the combined effects of nitrogen and oxygen functional groups formed on the surface after the functionalization treatment. Ma et al. investigated the removal of 2.2 ppmv formaldehyde from air using coal based AC modified by introducing hexamethylene diamine in various amounts to the surface [19]. The amount of HCHO adsorbed was 0.08 and 3.8 mg g^{-1} on as received carbon and on the best functionalized sample, respectively. Lee et al. studied the HCHO removal on seven different activated carbons [20]. The measured adsorption capacities were in the range between 0.01 and 0.478 mmol g^{-1}. Also in this case, the high adsorption capacities were attributed to the surface functionalization and in particular to the presence of nitrogen groups. The importance of nitrogen groups, and especially pyrrolic or pyridonic nitrogen, pyridinic nitrogen, and quaternary nitrogen, was also pointed out as enhancing HCHO adsorption on activated carbon fibers [21].

In our recent work we modified highly porous carbon textiles by an incorporation of various surface functionalities [22]. It was found that S- and N-containing functional groups (pyridines, amines, and sulfones/sulfonic acids) significantly enhanced the HCHO adsorption capacity at ambient conditions from air of HCHO concentration of about 1 ppm. Following this path, this paper extends the previous investigation and focuses on the evaluation of the role of sulfur or sulfur and nitrogen groups incorporated to porous activated carbons in HCHO removal from air. Our intent is to show that surface chemistry, especially that related to sulfur species, can lead to high adsorption capacity or even can result in the adsorption capacity exceeded that provided by strong adsorption forces in pores similar in size to adsorbate molecule. HCHO adsorption tests in dynamic conditions were carried out at room temperature at fixed concentration of formaldehyde (1 ppmv) in dry and humid conditions. The novelty aspect is on focusing on the effects of sulfur and/or nitrogen groups on the enhancement of formaldehyde adsorption. At this stage of our study we do not focus on finding an exact correlation between the performance of adsorbents and the surface features but we rather direct our attention on finding which features can enhance markedly the performance of porous carbons as HCHO removal media at ambient conditions.

2. Experimental

2.1. Materials

Commercial activated carbons S208 (coconut shell-based carbon-Waterlink Barnabey and Sutcliffe, indicated as S208) and BAX-1500 (wood -based carbons-Westvaco, indicated as BAX) were used in this study. While the former is a predominantly microporous material of a basic surface, the latter is micro/mesoporous carbon obtained at ~600 °C and therefore its surface is considered as susceptible to further modification at higher temperatures. BAX was dispersed in a melamine suspension, mass ratio = 1.5:1, in 25 mL of ethanol for 5 h under stirring at room temperature. Then, the mixture was boiled until a complete evaporation of the ethanol and dried in an oven at 100 °C. The next step was a thermal treatment of the sample at 950 °C in an inert atmosphere (nitrogen) for 30 min. The heating rate was set to 10 °C min^{-1}. Then the sample was washed in a Soxhlet apparatus to remove all water-soluble compounds and dried in oven at 100 °C. This carbon is referred as BAX-M. To modify with thiourea, BAX was dispersed in a thiourea solution obtained by dissolving thiourea in 25 mL of water; mass ratio = 1:1. After stirring overnight at room temperature, the same steps were carried out as for the preparation of BAX-M. The obtained carbon is referred to as BAX-T.

The sulfur-containing polymer derived carbon, referred to as PSC, was obtained from poly (sodium 4-styrene sulfonate) carbonized at 800 °C, heating rate 10 °C min^{-1}, for 40 min under nitrogen flow (300 mL min-^{1}) in a horizontal furnace. The carbon was extensively washed after the synthesis to remove the excess of sodium.

2.2. Methods

2.2.1. HCHO dynamic adsorption test

Dynamic adsorption tests of HCHO were carried out at room temperature (T = 25 °C) and atmospheric pressure using a lab-scale fixed bed reactor already described elsewhere [22]. 1.3 cm^3 of samples equivalent to about 300 mg for the activated carbons (functionalized and not) and to 130 mg in case of PSC, of a particle size of 1–2 mm, were placed in a 9 mm glass column. The differences in the weight are related to the differences in the packing density of the carbons tested. Formaldehyde gas flow was obtained from a calibrated formaldehyde permeation tube (Metronics, Inc.) using a Dynacalibrator® (Model 150, Metronics, Inc.) operated at 80 °C with 100 mL min^{-1} nitrogen as a carrier gas. The outlet gas from the generator was mixed with 400 mL min^{-1} of dry air passed through $CaSO_4$ to totally remove any humidity, or moist air (passed through a water bed). Before adsorption tests under moist conditions, the samples were prehumidified with moist air (500 mL min^{-1}, for 1 h) and then weighted, in order to determine the amount of water preadsorbed on the surface. The initial concentration of formaldehyde (C^{IN}_{HCHO}) was fixed approximately to 1 ppmv. Gas analysis was performed with a continuous analyzer equipped with an electrochemical sensor (RM 16 Interscan Corporation) with an accuracy of 2% (working range of analyzer 0–2 ppmv of formaldehyde).

The breakthrough adsorption capacity of HCHO, ω_{ads} [mg g^{-1}], was calculated by an integration of the area above the breakthrough curve using the flow rate, concentration of HCHO, time and mass of the adsorbent material. In particular, all the adsorption tests were stopped at $C^{OUT}_{HCHO}(t)/C^{IN}_{HCHO} = 0.8$, where $C^{OUT}_{HCHO}(t)$ is the outlet concentration of formaldehyde. This value was arbitrary chosen for the comparison of the data since the saturation was not reached for some carbons even after very long experimental time.

2.2.2. Sorption of nitrogen

The porosity of the samples was determined from N_2 adsorption isotherms measured on an ASAP 2020 (Micromeritics) at −196 °C. All the samples were degassed at 120 °C to a constant vacuum (10^{-4} Torr). BET method was used to determine the specific surface area (S_{BET}), while the total pore volume, V_{tot}, was calculated from adsorption isotherms at $p/p_o = 0.998$. The micropore volume, V_μ, and pore size distributions were calculated using nonlinear density functional theory, 2D-NLDFT, which assumes the heterogeneity of the pore sizes [23,24].

2.2.3. Thermal analyses

Thermogravimetric (TG) and differential TG (DTG) curves were measured on a Q600 thermal analyzer (TA Instruments). The samples were heated up to 1000 °C at a rate of 10 °C min^{-1} in helium flow (100 mL min^{-1}). The m/z thermal profiles of the exhausted gases/vapors, for m/z 17 (NH_3), 18 (H_2O), 28 (CO), 29 (HCO), 30 (HCHO/NO), 44 (CO_2) and 48 (SO) were collected using a mass spectrometer (MS, Omnistar GSD 320, Pfeiffer Vacuum).

2.2.4. Potentiometric titration

Potentiometric titration was performed on an 888 Titrando automatic titrator (Metrohm). A mass of 0.1 g of carbon was placed in a vessel and dispersed in $NaNO_3$ 0.1 M solution. The solution was maintained at a constant stirring overnight and purged with N_2 to eliminate the effect of CO_2. The pH was recorded and adjusted to about 3.2 by adding HCl 0.1 M and the suspension was titrated with NaOH (0.1 M) up to pH ≈ 10. In order to eliminate the influence of atmospheric CO_2, the suspension was continuously saturated with N_2 during the experiment. The proton binding curves, Q [25], were derived from the titration data. The pK_a distributions [26], $f(pK_a)$, of the surface acidic groups were calculated by finding a stable solution of the Fredholm integral equation that relates Q to $f(pK_a)$. For this, SAIEUS procedure was used [27].

2.2.5. X-ray photoelectron spectroscopy (XPS)

The XPS spectra were collected using the Physical Electronics PHI 5000 VersaProbe II spectrometer with a monochromatic Al Kα (1486.6 eV) radiation operating at 15 kV and 50 W in the analyzer chamber. Prior to analysis, all samples were outgassed until 10^{-8} Torr at room temperature. High-resolution spectra of powdered samples were detected with the constant pass energy values of 29.35 eV and a 200 μm diameter analysis area with a take-off angle of 45°. 117.4 eV pass energy was used for the survey spectra. The detailed amounts of each element were calculated from the individual spectra. The spectrometer energy scale was calibrated using Cu $2p_{3/2}$, Ag $3d_{5/2}$, and Au $4f_{7/2}$ photoelectron lines at 932.7, 368.3, and 84.0 eV, respectively. The SmartSoft-VP2.6.3.4 software package was used for acquisition and data analysis and Multipack software was used to fit photoelectron spectra. A Shirley-type background was subtracted from the signals and recorded spectra were fitted using Gauss–Lorentz curves in order to determine the binding energy of the different element core levels accurately.

3. Results and discussion

The HCHO breakthrough curves measured at room temperature in dry (A) and wet (B) conditions on the carbons tested are presented Fig. 1. From them, the adsorption parameters were calculated and they are listed in Table 1, in which t_{br} [min/g] is the time of the breakthrough point (assumed as the time for which $C^{out}_{HCHO}(t)/C^{in}_{HCHO} = 0.05$) divided by the mass of samples used. Table 1 also lists the amounts of water adsorbed [g g^{-1}] during the prehumidification step. The measurements under dry condition were repeated (Fig. S1 of the Supplementary Information). The comparison of the data obtained is presented in Table S1. The results show good reproducibility of the results which differ in the range 1.5–6% between two measurements.

The HCHO breakthrough curves, in dry condition on the initial BAX and S208 are steep, which indicates fast kinetics of the adsorption process (Fig. 1A). Even though S208 has a lower breakpoint time than has BAX (almost 27% less), ca. 20% more HCHO is adsorbed on that carbon than on BAX. PSC and S208 have similar breakthrough capacities but t_{br} of the former is 3 times longer compared to that of S208. The treatment of BAX with thiourea or melamine resulted in a significant increase in both quantitative parameters of HCHO adsorption, compared to those on BAX. Thus, the breakthrough point time increased from 44 min g^{-1} to 87 and 215 min g^{-1}, respectively, and the HCHO breakthrough capacities reached values equal to 0.4 and 0.66 mg g^{-1} for BAX-T and BAX-M, respectively.

The presence of moisture on the carbon and in the feed gas decreased t_{br} and the adsorption capacities for all samples (Fig. 1B, Table 1). This is likely caused by the adsorption of water on the active sites of the adsorbents. It occurs as a competitive process during the reactive adsorption and during the prehumidification process [22,28]. Even though the carbons adsorb large quantities of water (Table 1), that water doesn't contribute to an increase in the adsorption capacity

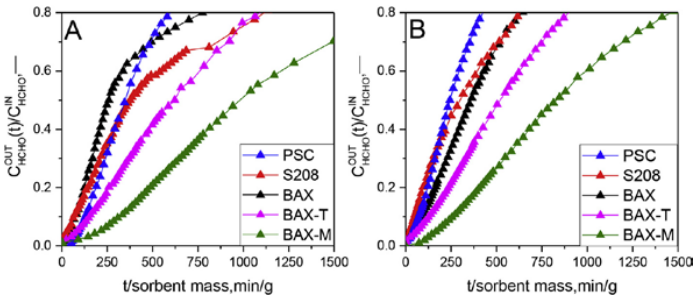

Fig. 1. HCHO breakthrough curves measured in the dry (A) and moist conditions (B). (A colour version of this figure can be viewed online.)

Table 1
HCHO adsorption parameters in the dry and moist conditions on the carbons studied.

Sorbent	C^{IN}_{HCHO} [ppmv] Dry	ω_{ads} [mg g^{-1}] Dry	t_{br} [min g^{-1}] Dry	C^{IN}_{HCHO} [ppmv] Moist	Water adsorbed [g g^{-1}]	ω_{ads} [mg g^{-1}] Moist	t_{br} [min g^{-1}] Moist
PSC	1.22	0.31	96	1.22	0.21	0.20	44
S208	0.94	0.31	32	0.94	0.21	0.19	23
BAX	1.18	0.25	44	0.99	0.61	0.23	35
BAX-T	0.94	0.40	87	1.01	0.58	0.34	72
BAX-M	0.94	0.66	215	1.02	0.64	0.57	185

considering the possibility of HCHO dissolution in a water film. On the other hand, water likely blocks the pore entrances and/or occupy the polar centers on which HCHO would be otherwise adsorbed. In particular, the most marked decrease in the amount of HCHO adsorbed is found for S208 and PSC. For both carbons ω_{ads} decreased of about 38%. t_{br} decreased of 28 and 54% for S208 and PSC, respectively. Interestingly, for BAX, BAX-T and BAX-M in the moist conditions ω_{ads} decreased only 8, 15 and 14% and t_{br} of 20, 17 and 14%, respectively, which suggests differences in the adsorption mechanisms between the BAX series and other two carbons tested.

To understand differences in the performance of the carbons studied and to identify surface features important for the HCHO retention, the porosity and surface chemistry of our carbon were extensively studied. To evaluate former, nitrogen adsorption isotherms were measured (Fig. S2) and from them the parameters of the pore structure and pore size distributions, PSDs, were calculated (Table 2 and Fig. 2). The porosity of the exhausted samples used in dry conditions was also evaluated.

BAX is a micro/mesoporous carbon ($\frac{V_\mu}{V_{tot}}$=55%) with the most developed surface area equal to 2175 $m^2 g^{-1}$. Its main pore sizes are 0.65, 1.1, 1.9 and 3.6 nm (Fig. 2 C–D). After modifications with thiourea and melamine the porosity changes and the surface area decreased to 1288 and 1588 $m^2 g^{-1}$ for BAX-T and BAX-M AC, respectively. Interestingly, the volume of ultramicropores, V < 0.7 nm, almost doubled, while those pores in BAX with mean size around 1.1 nm almost disappeared, which might be related to the incorporation of thiourea and melamine onto the carbon matrix and to an increase in the carbonization level (BAX was synthesized at about 600 °C). Even though both modifications resulted in similar trends in the porosity changes, the thiourea treatment decreased the porosity to slightly greater extent than that of the melamine treatment. Among all carbons tested PSC has the smallest surface area (1/4 of that of BAX and about 1/2 of that of S208). Its volume of ultramicropores is similar to that of BAX but three times smaller than that of S208. From the point of view of physical adsorption via dispersive forces these pores are expected to be the most active in the HCHO retention. S208 is the most microporous ($\frac{V_\mu}{V_{TOT}}$=94%) among all carbons tested.

Table 2
Parameters of the porous structure calculated from nitrogen adsorption isotherms.

Carbon	S_{BET} [$m^2 g^{-1}$]	V_{tot} [$cm^3 g^{-1}$]	$V\mu$ [$cm^3 g^{-1}$]	$V < 0.7$ nm [$cm^3 g^{-1}$]	$V < 1$ nm [$cm^3 g^{-1}$]
Initial carbons					
PSC	433	0.40	0.17	0.08	0.14
S208	1042	0.50	0.47	0.24	0.34
BAX	2175	1.32	0.73	0.10	0.26
BAX-T	1288	0.72	0.50	0.17	0.29
BAX-M	1558	0.90	0.58	0.19	0.32
Spent carbons in dry conditions					
PSC	376	0.35	0.16	0.09	0.13
S208	509	0.26	0.25	0.17	0.21
BAX	1979	1.20	0.67	0.08	0.24
BAX-T	1260	0.70	0.49	0.16	0.28
BAX-M	1475	0.86	0.55	0.18	0.30

After HCHO adsorption in the dry conditions the parameters of the porous structure decreased. Since the samples were outgassed under the high vacuum at 120 °C before the measurement and all physically adsorbed HCHO was expected to be removed under those conditions, the observed decrease in the surface area and porosity might be related to either HCHO polymerization or its reaction with the carbon functional groups. As a result of this some pores could be blocked to N_2 molecules. More specifically, the BET surface areas decreased of 9, 51, 13, 2 and 5% for BAX, S208, PSC, BAX-T and BAX-M. This implies that on S208 and PSC surface chemistry in micropores or at their entrances was most involved in the HCHO reactive adsorption process. Interestingly, for PSC after HCHO adsorption the volume of ultramicropores slightly increased and it might suggest the deposition of some reaction products in larger pores decreasing their sizes.

Since the results obtained suggest that the porosity is not the only factor determining the performance of our carbons, their surface chemistry was analyzed in detail. Fig. 3 collects the TG and DTG curves measured in helium for the initial and spent samples in the dry conditions.

The DTG peaks represent the extent of the weight loss linked to the decomposition of distinct surface species. The total weight loss

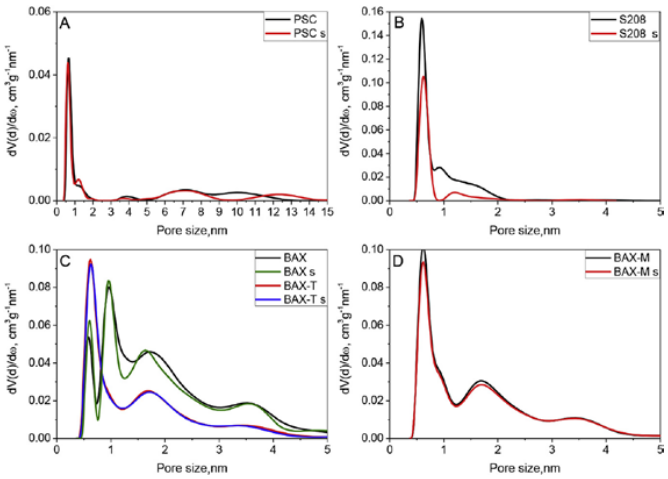

Fig. 2. Pore size distributions of the initial and spent sorbents in the dry conditions (designated with letter s): A) PSC, B) S208, C) BAX and BAX-T, D) BAX-M. (A colour version of this figure can be viewed online.)

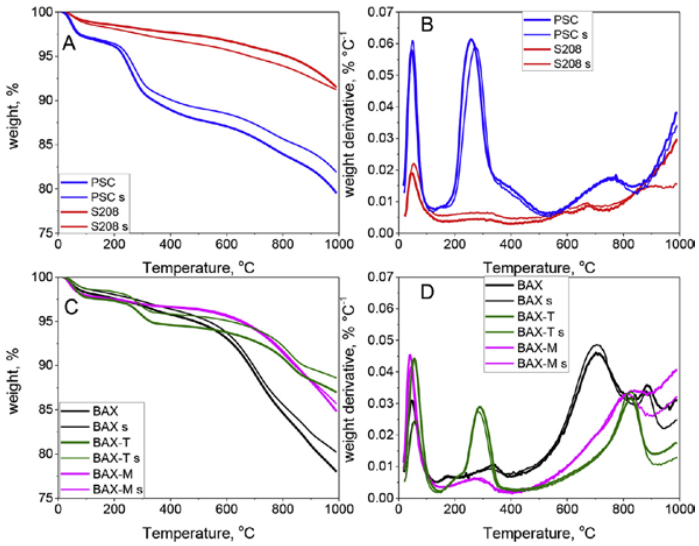

Fig. 3. TG curve (A, C) and DTG curves (B, D) for the initial and spent carbons in dry conditions (designated with letter s): A-B) PSC and S208, C-D) BAX, BAX-T and BAX-M. (A colour version of this figure can be viewed online.)

for all initial samples was between 7 and 25% (Fig. 3 A and C), which is related to the differences in the content of heteroatoms and their chemical environment. The weight loss below 150 °C represents the removal of physically adsorbed water/formaldehyde. The weight loss over 800 °C, and for BAX after 600 °C, should not be analyzed since the samples were originally not exposed to these temperatures. S208 appears as most thermally stable with weight loss about 7%. Its groups decompose mainly over 500 °C, and assuming that mainly oxygen is present on the surface of this commercial carbon, this weight loss represents the removal of phenols [29]. BAX is richer in the surface groups than is S208 and its carboxylic acids decompose between 200 and 400 °C. By the modification with melamine these groups were apparently decomposed/consumed. As a result of this process, a marked number of groups decomposing between 500 and 800 °C was incorporated to the surface. The thiourea treatment introduced groups decomposing between 200 and 350 °C and at about 800 °C. Since they overlap with those on the DTG curves of PSC, which is expected to be rich in sulfur, we link these temperature weight losses mainly to the decomposition of oxidized sulfur species. Apparently, the amount of these species and also their chemical nature is more diverse on the surface of PSC than on that of BAX-T. The weight loss for BAX-T and BAX-M at temperatures below 950 °C, even though these carbons were exposed to the high temperature, can be explained by instability of their surface after the treatment and its reactivity with atmospheric oxygen.

After exposure to HCHO no marked changes in the weight loss pattern were found, likely owing to the fact that rather small amounts of HCHO were adsorbed and the changes, if any, were below the sensitivity of the method. Nevertheless, a decrease in the weight loss, especially for S and N containing carbons, suggest an improved thermal stability of the surface, likely due to their interactions/reactions with HCHO.

To further study the chemistry of our adsorbents, the thermal decomposition products were analyzed by mass spectrometry and relevant m/z thermal profiles are collected in Figs. S3 and S4 of the Supplementary Information. For the analysis only thermal profiles of m/z 18, 28, 29, 30, 44 and 48, which represent H_2O, CO, HCO, HCHO/NO, CO_2 and SO, respectively, were chosen owing to their relevance to surface chemistry and the changes in these features. For BAX-M m/z 17 representing NH_3 was also selected. The detection of m/z 48 and its thermal profiles for PSC and BAX-T confirm the presence of sulfur on their surface and some similarities and differences in their chemical nature. Formaldehyde apparently interacted with those species, which is demonstrated by an increase in the peaks' intensity and changes in their patterns. For S208 after HCHO exposure, the profile for CO (m/z 28), representing the decomposition of OH groups at high temperature changed, suggesting the involvement of these groups in the formaldehyde adsorption and/or a release of CO as a result of HCHO retained on the surface. Those m/z also markedly changed after HCHO adsorption for the BAX series of carbons. For BAX-M and S208 also the thermal profiles of m/z 44 representing CO_2 showed some alterations as a result of carbon surface interactions with HCHO. Generally, the changes are not dramatic owing to, as indicated above, the small amounts of formaldehyde adsorbed from which a significant portion is expected to be adsorbed in pores through dispersive interactions.

The surface chemistry of the carbons studied was also investigated by the potentiometric titration method. Fig. 4 shows the proton binding curves. Calculated from them pK_a distributions for the initial and spent samples are presented in Fig. S5 of the Supplementary Information. The numbers of groups in the category of strongly acidic ($3<pK_a<5$), close to neutral ($5<pK_a<8$), and weakly acidic ($8<pK_a<11$) are listed in Table 3. An increase in the acidity of the sample modified with thiourea is found and the one modified with melamine became more basic. Moreover, the functionalization treatments led to a reduction in the number of dissociating groups (Table 3) due to the introduction of new chemical species (N groups, S groups and N/S groups) that modified the surface of BAX. While

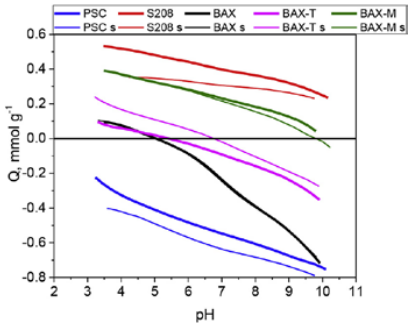

Fig. 4. Proton bindings curves of the initial and spent (in dry conditions) carbons (The latter are denoted with s). (A colour version of this figure can be viewed online.)

Table 3
Amounts of functional groups (in mmol/g) in various acidity ranges on the surface of the carbons studied before and after exposure to HCOH in dry conditions.

Carbon	pH[a]	Strongly acidic $3<pK_a<5$	Neutral $5<pK_a<8$	Weakly acidic $8<pK_a<11$	All
Fresh adsorbent					
PSC	3.3	0.33	0.17	0.24	0.84
S208	8.4	0.10	0.09	0.19	0.39
BAX	5.5	0.10	0.41	0.6	1.11
BAX-T	4.4	0.19	0.16	0.34	0.69
BAX-M	7.3	0.10	0.10	0.29	0.49
Spent adsorbent in dry conditions					
PSC	3.1	0.11	0.18	0.19	0.48
S208	8.4	0.00	0.04	0.09	0.13
BAX	5.1	0.11	0.39	0.47	0.97
BAX-T	4.4	0.26	0.18	0.29	0.73
BAX-M	7.2	0.08	0.10	0.23	0.41

[a] In an electrolyte solution ($NaNO_3$).

S208 presents a basic character with the initial pH equal to 8.4, PSC is very acidic (pH = 3.3). The proton binding curves displays the strong acidic character for PSC whereas all other carbons studied are amphiprotic.

The XPS analysis results on our samples are collected in Table 4. BAX-M contains the smallest amount of oxygen and, as expected, the highest content of nitrogen on the surface. The most chemically heterogeneous is BAX-T that is rich in sulfur and nitrogen and contains the highest amount of oxygen. While on the surface of PSC a marked amount of sulfur is present, S208 appears as the most chemically homogenous and the potentiometric titration analysis showed that it has the smallest amount of acids on the surface, which dissociate in our experimental window (its average surface pH is 8.4).

The results of the XPS analyses are summarized from Refs. [30–33] where the reader can find the detailed deconvolution of specific core energy level spectra. Fig. 5 shows the deconvolution results for BAX-T, as an example. The deconvolutions of C 1s combined with O 1s suggest that on S208 the majority of oxygen groups is in phenols and on BAX carboxylic acids are also present in a marked quantity. Based on the deconvolution of S 2*p*, on PSC and BAX-T, and especially on the former, a marked amount of oxygen is in oxidized sulfur species. After the thiourea modification, the majority of sulfur is in the reduced forms. Even though on the surface of BAX some small amount of nitrogen is present, the treatment with thiourea and melamine, and especially with the latter, introduced marked amounts of nitrogen that is relatively evenly distributed between pyridones, pyroles/amines/amides and quaternary nitrogen with a small contribution of pyridine N-oxides. On BAX-T, on the other hand, the majority of nitrogen species is present in pyroles/amines/amides and pyridine N-oxides. The latter, and a relatively high contribution of sulfonic acids, can explain its average low pH value.

Combining all textural and chemical characterization results will help us to explain the differences in the performance between

Table 4
Results of the deconvolution of the XPS spectra of C 1s, O 1s, N 1s and S 2*p* (in bold -atomic % of specific elements).

Bond assignment	PSC[a] [%]	S208[b] [%]	BAX[c] [%]	BAX-T [%]	BAX-M[d] [%]
C 1*s*	**85.1**	**92.6**	**89.2**	**86.1**	**90.4**
C–C sp^2	72.6	83.7	77.9	76.6	68.7
C–O (phenol, alcohol, ether), C–N (amine, amide)	15.4	11.6	12.1	14.0	16.1
C=O (carbonyl, quinone), O=C–N (amide)	5.8	4.7	5.0	5.9	6.7
O=C–O (carboxyl)	3.8		3.42	3.5	5.0
$\pi\rightarrow\pi^*$, π-electrons in aromatic rings	2.3		1.72	---	3.4
O 1*s*	**9.8**	**7.4**	**9.1**	**11.6**	**5.2**
C=O	65.2	43.5	44.4	88.5	36.3
C–O	25.1	56.5	55.6	11.5	58.5
Water or chemisorbed O_2, CO_2	9.7		---	---	5.2
N 1*s*	**0**	**0**	**0.6**	**1.6**	**3.9**
Pyridine			41.3	22.4	33.3
pyrrole, amine, amide			36.6	33.1	33.3
quaternary nitrogen/ammonium			---	18.7	22.3
pyridine-N-oxide, $C–N^+O–C$, NO_x			---	25.8	11.1
$C–N^+$ O–C, Ph–NO_2, R–NO_2 and NO_3			22.1	---	---
S 2$p_{3/2}$	**5.1**	**0**	**0**	**0.6**	**0**
R–S— in thiol, bisulfides, thiophenes	52.4			83.3	
R_2–SO in sulfoxides	14.0			---	
R-S(O_2) in sulfones	26.3			---	
HSO_3^- (sulfonic acids)	7.4			16.7	

[a] Ref.[30], [b] Ref. [31], [c] Ref. [32], [d] Ref. [33]

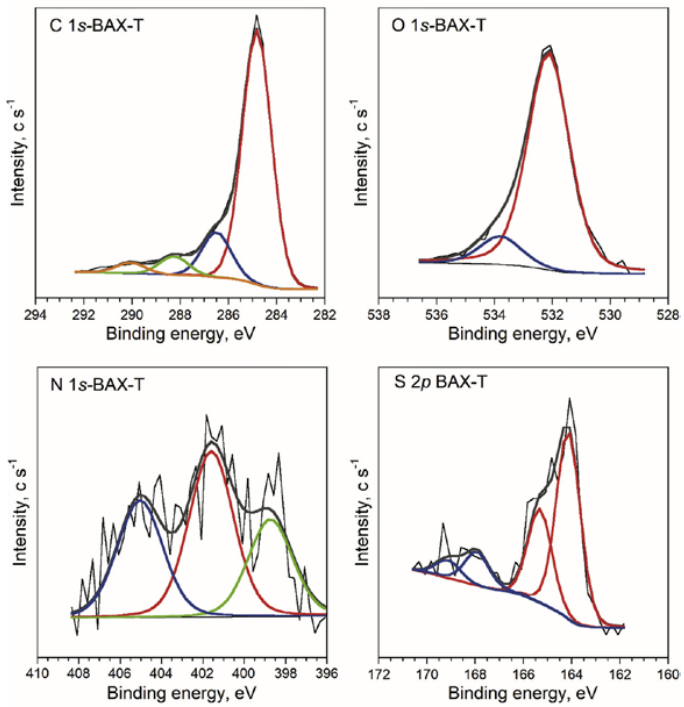

Fig. 5. Deconvolution of C 1s, O 1s, N 1s and S 2*p* spectra for BAX-T. (A colour version of this figure can be viewed online.)

the carbons tested in terms of the amount adsorbed and the utilization degree of their surface, that is directly linked to the surface activity (Fig. 6). The most basic carbon with the marked amount of phenols on the surface is S208. For this carbon the most pronounced changes in the porosity were found after HCHO adsorption, which was reflected in the significant blocking of its pores (Fig. 2, Table 2). On the other hand, the changes in the porosity of BAX are much less visible, in spite of more oxygen in phenols. Here the differences in the performance might be caused by the differences not only in the volume of small pores promoting HCHO physical adsorption in favor of S208, but also by the differences in the chemical environment. Basic environment of the S208 carbon likely catalyzes the reactions of formaldehyde with phenolic groups in which hydroxybenzyl alcohols are formed and retained on the surface [34]. This reaction can explain a marked decrease in the surface area and the micropore blocking in this carbon after HCHO exposure. This might also explain higher "utilization" of this carbon porosity (Fig. 6) compared to that of BAX, and a marked decrease in the number of dissociating species after HCHO adsorption.

From the viewpoint of surface utilization for HCHO adsorption, PSC is the most active, even though its volume of pores in which HCHO could be strongly adsorbed is twice smaller than that in

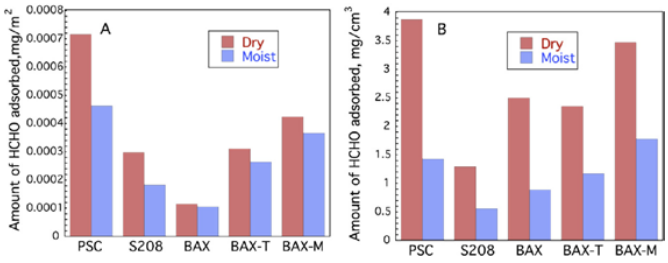

Fig. 6. Normalized amounts of HCHO adsorbed per unit surface area (A) and per unit volume of pores smaller than 0.7 nm (B). (A colour version of this figure can be viewed online.)

S208. Interestingly, these pores appear as almost unchanged after HCHO adsorption, suggesting that a significant part of formaldehyde was physically adsorbed there. Nevertheless, the porosity changes are seen in the disappearance of pores with sizes between 9 and 11 nm for the exposed samples. HCHO is not expected to be physically adsorbed in these pores but some bulky sulfonic groups might exist there and react with formaldehyde resulting in hydroxymethanesulfonates [35–37]. Moreover, that carbon has a significant amount of sulfur in reduced configurations, which might react with HCHO in condensation reactions [38] or in reactions analogous to Mannich reactions [39] forming thiomethanols. This resulted in a decrease in the amounts of acids detected on the surface from the potentiometric titration experiments.

The explanation of the adsorptive behaviors of BAX- M and BAX-T is more complex. From the viewpoints of surface and pore volume utilizations BAX-M is second to PSC and it is followed by BAX-T. The modifications significantly improved the performance compared to that of the unmodified counterpart and the results indicate that the incorporation of nitrogen was more beneficial than that of N and S combined. Interestingly, the changes in the porosity after HCHO adsorption are minimal suggesting that formaldehyde was only physically adsorbed, or the species formed in reactive adsorption were decomposed during outgassing at 120 °C and at high vacuum. Changes in the acid-base chemistry are also not visibly marked, especially for the best performing BAX-M. However, in the case of BAX-T the population of strong acids increased slightly after exposure to HCHO and the amount of weak acids-decreased suggesting some subtle changes. Even though the primary and secondary amines are known to undergo the chemical condensation reaction with formaldehyde and Mannich reaction is an example, the chemistry of follow-up-reactions and transformations of the formed compounds have been indicated as very complex processes depending on the nature of amines and their chemical environment [40]. In the case of chemically heterogeneous carbons, even though various techniques can be used to present the complementary views of their surface, the exact description of the surface chemical environment is rather impossible. Therefore, in this discussion we can only present the plausible hypotheses on the role of nitrogen and sulfur surface chemistry along with that of the porosity in enhancing HCHO adsorption on BAX-M and BAX-T. Since the volume of the pores smaller than 1 nm is very similar in these two carbons, about 30% better performance of BAX-M must be linked to its nitrogen groups which either chemically (pyridines and amines) or via providing surface polarity (pyridine N-oxides) retain HCHO in larger pores. Supporting for this is larger total pore volume of BAX-M than that of BAX-T. Those interactions, when occurring in larger pores, might not affect visibly their sizes seen by very small nitrogen molecule. Moreover, HCHO retained via polar forces, as that through dispersive forces, is expected to be removed during outgassing. The mechanism on BAX-T should be similar that on BAX-M, however, here the volume of pores with sizes similar to HCHO molecule is smaller and the total number of groups containing heteroatoms is smaller. These groups are distributed in the smaller surface of large pores. In a rough evaluation, if one assumes that only chemistry is important, BAX-T has 44% less S + N in at % and its HCHO capacity is 34% smaller. Obviously, in this consideration the physical adsorption of formaldehyde in small pores should not be neglected.

Interestingly, on the BAX series the effects of the presence of water on the surface/in the air stream on the amount of HCHO adsorbed per gram of the adsorbent or that normalized per unit surface area are the smallest. That insensitivity compared to that of PSC or S208 might be caused by the adsorption water formed in the condensation reactions in larger pores than on S208 or PSC, which are more microporous than are the BAX series. Even though that water might occupy the polar centers where formaldehyde could be otherwise adsorbed and thus limits the adsorption of HCHO via specific interactions, the net effect of surface chemistry on the HCHO retention is positive, compared to the performance of the surface without these specific chemical features. When the amount adsorbed is normalized per unit volume of pores smaller than 0.7 nm the differences between the amounts adsorbed in dry and moist conditions are more or less 50% smaller for each carbon, which suggests that indeed these pores are very important for HCHO adsorption and their blocking by water during prehumidification limits markedly the number of the adsorption centers.

4. Conclusions

The results collected in this paper show that the chemical heterogeneity of a carbon surface is a very important factor which governs the surface activity of nanoporous carbon towards HCHO retention. Even though, following the physical adsorption principles, the volume of ultramicropores was expected to markedly influence the amount adsorbed, we have shown that decorating the surface of carbon in larger pores with sulfur and nitrogen containing functional groups, being able to chemically/specifically interact with HCHO, enhances the capacity. The key factor leading to the maximum utilization of the carbon surface is a combination of a high volume in ultramicropores with highly reactive with HCHO groups located in larger pores. This combination of both, besides proving a high adsorption capacity will also result in an efficient mass transport of HCHO to the adsorption sites. When the condensation reactions in which water is formed take place, the surface is apparently less sensitive for a detrimental effect of moisture in air on the HCHO removal on these particular carbons and the capacity measured is a net effect of *insitu* conditions. Even though the effect of nitrogen containing groups on HCHO adsorption has been discussed [14–17] and the combined effect of nitrogen and sulfur has been pointed out recently [22], the novelty of this work is in presenting the sulfur groups incorporated to carbon matrix as those which significantly increase the carbon surface activity towards HCHO adsorption. On such carbon the degree of surface utilization is even greater than that on only N-modified carbon. Moreover, we have shown that on very microporous carbon rich in phenolic groups and having basic pH, reactive adsorption of HCHO on phenols blocks the porosity and thus limits the performance even though the high volume of small pores would suggest an excellent adsorption capacity. Even though our results are collected in the dynamic conditions, we believe that they also reflect on the behavior of carbons in the static conditions, when these adsorbents would be exposed to indoor HCHO.

Acknowledgement

G.d.F thanks the support of the Short term Mobility Program of CNR (CUP B53C17001430005) for his research at the City College of New York.

Appendix A. Supplementary data

Supplementary data related to this article can be found at https://doi.org/10.1016/j.carbon.2018.05.067.

References

[1] L. Zhang, C. Steinmaus, D.A. Eastmond, X.K. Xin, M.T. Smith, Formaldehyde exposure and leukemia : a new meta-analysis and potential mechanisms, Mutat. Res. Rev. Mutat. Res. 681 (2009) 150–168, https://doi.org/10.1016/j.mrrev.2008.07.002.

[2] M.A. Medinsky, J.A. Bond, Sites and mechanisms for uptake of gases and

vapors in the respiratory tract, Toxicology 160 (2001) 165–172, https://doi.org/10.1016/S0300-483X(00)00448-0.
[3] R. Golden, Identifying an indoor air exposure limit for formaldehyde considering both irritation and cancer hazards, Crit. Rev. Toxicol. 41 (2011) 672–721, https://doi.org/10.3109/10408444.2011.573467.
[4] World Health Organization, WHO Guidelines for Indoor Air Quality: Selected Pollutants, WHO Regional Office of Europe, 2010, https://doi.org/10.1186/2041-1480-2-S2-I1.
[5] C. Li, Y. Shen, M. Jia, S. Sheng, M.O. Adebajo, H. Zhu, Catalytic combustion of formaldehyde on gold/iron-oxide catalysts, Catal. Commun. 9 (2008) 355–361, https://doi.org/10.1016/j.catcom.2007.06.020.
[6] D. Chen, Z. Qu, S. Shen, X. Li, Y. Shi, Y. Wang, et al., Comparative studies of silver based catalysts supported on different supports for the oxidation of formaldehyde, Catal. Today 175 (2011) 338–345, https://doi.org/10.1016/j.cattod.2011.03.059.
[7] J.Q. Torres, S. Royer, J.P. Bellat, J.M. Giraudon, J.F. Lamonier, Formaldehyde: catalytic oxidation as a promising soft way of elimination, ChemSusChem. 6 (2013) 578–592, https://doi.org/10.1002/cssc.201200809.
[8] Y. Wan, X. Fan, T. Zhu, Removal of low-concentration formaldehyde in air by DC corona discharge plasma, Chem. Eng. J. 171 (2011) 314–319, https://doi.org/10.1016/j.cej.2011.04.011.
[9] W.D.P. Rengga, A. Chafidz, M. Sudibandriyo, M. Nasikin, A.E. Abasaeed, Silver nano-particles deposited on bamboo-based activated carbon for removal of formaldehyde, J. Environ. Chem. Eng 5 (2017) 1657–1665, https://doi.org/10.1016/j.jece.2017.02.033.
[10] J.P. Bellat, I. Bezverkhyy, G. Weber, S. Royer, R. Averlant, J.M. Giraudon, et al., Capture of formaldehyde by adsorption on nanoporous materials, J. Hazard Mater. 300 (2015) 711–717, https://doi.org/10.1016/j.jhazmat.2015.07.078.
[11] V. Boonamnuayvitaya, S. Sae-Ung, W. Tanthapanichakoon, Preparation of activated carbons from coffee residue for the adsorption of formaldehyde, Separ. Purif. Technol. 42 (2005) 159–168, https://doi.org/10.1016/j.seppur.2004.07.007.
[12] S. Kumagai, K. Sasaki, Y. Shimizu, K. Takeda, Formaldehyde and acetaldehyde adsorption properties of heat-treated rice husks, Separ. Purif. Technol. 61 (2008) 398–403, https://doi.org/10.1016/j.seppur.2007.12.006.
[13] Q. Wen, C. Li, Z. Cai, W. Zhang, H. Gao, L. Chen, G. Zeng, et al., Study on activated carbon derived from sewage sludge for adsorption of gaseous formaldehyde, Bioresour. Technol. 102 (2011) 942–947, https://doi.org/10.1016/j.biortech.2010.09.042.
[14] H. Rong, Z. Ryu, J. Zheng, Y. Zhang, Influence of heat treatment of rayon-based activated carbon fibers on the adsorption of formaldehyde, J. Colloid Interface Sci. 261 (2003) 207–212, https://doi.org/10.1016/S0021-9797(03)00099-7.
[15] Y. Matsuo, Y. Nishino, T. Fukutsuka, Y. Sugie, Removal of formaldehyde from gas phase by silylated graphite oxide containing amino groups, Carbon 46 (2008) 1162–1163, https://doi.org/10.1016/j.carbon.2008.04.015.
[16] K. László, Characterization and adsorption properties of polymer-based microporous carbons with different surface chemistry, Microporous Mesoporous Mater. 80 (2005) 205–211, https://doi.org/10.1016/j.micromeso.2004.12.013.
[17] E.M. Carter, L.E. Katz, G.E. Speitel, D. Ramirez, Gas-phase formaldehyde adsorption isotherm studies on activated carbon: correlations of adsorption capacity to surface functional group density, Environ. Sci. Technol. 45 (2011) 6498–6503, https://doi.org/10.1021/es104286d.
[18] H.B. An, M.J. Yu, J.M. Kim, M. Jin, J.K. Jeon, S.K. Park, et al., Indoor formaldehyde removal over CMK-3, Nanoscale Res. Lett. 7 (2012) 1–14, https://doi.org/10.1186/1556-276X-7-7.
[19] C. Ma, X. Li, T. Zhu, Removal of low-concentration formaldehyde in air by adsorption on activated carbon modified by hexamethylene diamine, Carbon 49 (2011) 2873–2875, https://doi.org/10.1016/j.carbon.2011.02.058.
[20] K.J. Lee, J. Miyawaki, N. Shiratori, S.H. Yoon, J. Jang, Toward an effective adsorbent for polar pollutants: formaldehyde adsorption by activated carbon, J. Hazard Mater. 260 (2013) 82–88, https://doi.org/10.1016/j.jhazmat.2013.04.049.
[21] Y. Song, W. Qiao, S.H. Yoon, I. Mochida, Q. Guo, L. Liu, Removal of formaldehyde at low concentration using various activated carbon fibers, J. Appl. Polym. Sci. 106 (2007) 2151–2157, https://doi.org/10.1002/app.26368.
[22] G. de Falco, M. Barczak, F. Montagnaro, T.J. Bandosz, A new generation of surface active carbon textiles as reactive adsorbents of indoor formaldehyde, ACS Appl. Mater. Interfaces 10 (9) (2018) 8066–8076, https://doi.org/10.1021/acsami.7b19519.
[23] J. Jagiello, J.P. Olivie, Carbon slit pore model incorporating surface energetical heterogeneity and geometrical corrugation, Adsorption 19 (2013) 777–783, https://doi.org/10.1007/s10450-013-9517-4.
[24] J. Jagiello, J.P. Olivie, 2D-NLDFT adsorption models for carbon slit-shaped pores with surface energetical heterogeneity and geometrical corrugation, Carbon 55 (2013) 70–80, https://doi.org/10.1016/j.carbon.2012.12.011.
[25] T.J. Bandosz, J. Jagiello, C. Contescu, J.A. Schwarz, Characterization of the surfaces of activated carbons in terms of their acidity constant distributions, Carbon 31 (1993) 1193–1202, https://doi.org/10.1016/0008-6223(93)90072-I.
[26] J. Jagiello, Stable numerical solution of the adsorption integral equation using splines, Langmuir 10 (1994) 2778–2785, https://doi.org/10.1021/la00020a045.
[27] J. Jagiello, T.J. Bandosz, J.A. Schwarz, Carbon surface characterization in terms of its acidity constant distribution, Carbon 31 (1994) 1026–1028, https://doi.org/10.1016/0008-6223(94)90066-3.
[28] J. Li, Z. Li, B. Liu, Q. Xia, H. Xi, Effect of relative humidity on adsorption of formaldehyde on modified activated carbons, Chin. J. Chem. Eng. 16 (2008) 871–875, https://doi.org/10.1016/S1004-9541(09)60008-2.
[29] T.J. Bandosz, C.O. Ania, Activated carbon surfaces in environmental remediation, Interface sci. Technol. 7 (2006) 159–229, https://doi.org/10.1016/S1573-4285(06)80013-X.
[30] M. Seredych, S. Łoś, D.A. Giannakoudakis, E. Rodríguez-Castellón, T.J. Bandosz, Photoactivity of g-C_3N_4/S-doped porous carbon composite: synergistic effect of composite formation, ChemSusChem. 9 (2016) 795–799, https://doi.org/10.1002/cssc.201501658.
[31] L. Nielsen, M.J. Biggs, W. Skinner, BandoszTJ. The effects of activated carbon surface features on the reactive adsorption of carbamazepine and sulfamethoxazole, Carbon 80 (2014) 419–432, https://doi.org/10.1016/j.carbon.2014.08.081.
[32] N.A. Travlou, M. Seredych, E. Rodríguez-Castellón, T.J. Bandosz, Activated carbon-based gas sensors: effects of surface features on the sensing mechanism, J. Mater. Chem. A 3 (2015) 3821–3831, https://doi.org/10.1039/C4TA06161F.
[33] W. Li, B. Herkt, M. Seredych, T.J. Bandosz, Pyridinic-N groups and ultramicropore nanoreactors enhance CO_2 electrochemical reduction on porous carbon catalysts, Appl. Catal. B Environ. 207 (2017) 195–206, https://doi.org/10.1016/j.apcatb.2017.02.023.
[34] G.R. Sprengling, J.H. Freeman, The reaction of phenol with formaldehyde, J. Am. Chem. Soc. 72 (1950) 1982–1985, https://doi.org/10.1021/ja01161a029.
[35] D. Möller, Chemistry of the Climate System, Walter de Gruyter, Berlin, 2010.
[36] J.G. Papalos, Condensation Products of Aromatic Sulphonlc Acids with Formaldehyde, Europen Patent Application 0073606 A, 1982.
[37] R.E. Law, Sulfonated Aromatic-formaldehyde Condensation Products, US patent 3954677 A, 1976.
[38] P.D. Caesar, A.N. Sachanen, Thiophene-formaldehyde condensation, Ind. Eng. Chem. 40 (1948) 922–928, https://doi.org/10.1021/ie50461a030.
[39] F. Poppelsdorf, S.L. Holt, Reaction of Thiols and Thiosters. part I. An analogue of the Mannich reaction involving thiols, formaldehyde, and active methylene or methylidine compounds, J. Am. Chem. Soc. (1954) 1124–1130.
[40] M.M. Sprung, A summary of the reactions of aldehydes with amines, Chem. Rev. 26 (1940) 297–338, https://doi.org/10.1021/cr60085a001.